

Thesis submitted in the fulfillment
of the requirements for the degree of

Doctor of Philosophy

in

Physics

at

École Polytechnique

by

Alexander Serov

Modeling oxygen transport in the human placenta

Thesis defended on the 10th of July 2015 in front of the scientific jury:

Dr.	Rohan LEWIS	FM, University of Southampton	Reviewer
Prof.	Jean-Frédéric GERBEAU	INRIA Paris-Rocquencourt	Reviewer
Prof.	James GROTBERG	BME, University of Michigan	Examiner
Prof.	Abdul BARAKAT	LadHyX, École Polytechnique	Examiner
Prof.	Mickaël TANTER	INSERM, Institut Langevin, ESPCI	Examiner
Dr.	Denis GREBENKOV	PMC, École Polytechnique	Thesis supervisor
Prof.	Marcel FILOCHE	PMC, École Polytechnique	Thesis supervisor

English abstract

The efficient functioning of the human placenta is crucial for the favorable outcome of the pregnancy. This thesis aims at developing a mathematical model of respiratory gas exchange in the human placenta, which would improve our understanding of the relation between the structure and the function of the organ. Taking advantage of the precise 2D placental structure provided by the placental histology, we construct a 3D model of oxygen transport in the placenta by extending 2D histological cross-sections along the third dimension. The model simultaneously accounts for both diffusion and convection of oxygen in the intervillous space and allows us to predict the oxygen uptake of a placentone.

In the first part of the thesis, the diffusion-convection equation governing oxygen exchange is numerically solved for different densities of circular fetal villi in a placentone. These calculations provide estimations of the oxygen uptake of a placentone with an arbitrary villi density and demonstrate the existence of an optimal villi density maximizing the uptake. This optimality is explained as a trade-off between the incoming oxygen flow and the absorbing villous surface.

As a next step, the assumption of circular villi is relaxed and an approximate analytical solution is proposed for the diffusion-convection equation. It is shown that only two geometrical characteristics — the villi density and the effective villi radius — are required to predict the fetal oxygen uptake. Two combinations of physiological parameters that determine oxygen uptake in a given placenta are also identified: (i) the maximal oxygen inflow of a placentone, and (ii) the Damköhler number defined as the ratio of the transit time of the maternal blood through the intervillous space to a characteristic oxygen extraction time in a cross-section. Analytical formulas for fast and simple calculation of oxygen uptake are derived, and two diagrams of oxygen transport efficiency in an arbitrary placental cross-section are provided. The theory also suggests a method of how the results of artificial placenta perfusion experiments performed with no-hemoglobin blood can be recalculated to account for oxygen-hemoglobin dissociation.

Finally, an automatic image analysis method is developed allowing one to analyze large histological human placenta cross-sections and to determine areas, perimeters and shapes of villous, intervillous space and fetal capillary compartments. These data can then be used as input data for the model. This method is applied to 25 cross-sections from 22 healthy and 3 pathological pregnancies. By combination of the obtained data with the described efficiency diagrams, it is demonstrated that the villi density of a healthy human placenta lies within 10% of the optimal value. The overall geometry efficiency of a healthy placenta was found to be rather low (around 30–40%).

In a perspective, the presented model can constitute the base of a reliable tool of assessment of oxygen exchange efficiency in the human placenta from histological measurements *post partum*, or, in a longer term, from non-invasive *in utero* measurements.

French abstract

L'efficacité de fonctionnement du placenta humain joue un rôle crucial dans la santé du nouveau né. L'objectif principal de cette thèse est de développer un modèle mathématique de l'échange des gaz respiratoires au sein du placenta humain, afin d'améliorer la compréhension de la relation entre la structure et la fonction de cet organe. En exploitant la structure détaillée du placenta fournie par les méthodes d'histologie placentaire, nous construisons un modèle 3D du transport d'oxygène dans le placenta en prolongeant la géométrie des coupes histologiques 2D le long de la troisième dimension. Ce modèle est capable de prendre en compte simultanément la diffusion et la convection de l'oxygène dans l'espace intervillaire.

Dans la première partie de la thèse, l'équation de diffusion-convection qui détermine l'échange d'oxygène est résolue numériquement pour diverses valeurs de densités de villosités à l'intérieur du placentone. Ces calculs fournissent une estimation de l'absorption d'oxygène d'un placentone pour une densité arbitraire de villosités, et permettent de mettre en évidence l'existence d'une densité optimale de villosités maximisant l'absorption d'oxygène. Cette optimalité peut être vue comme le résultat d'un équilibre entre l'arrivée d'oxygène par le flux entrant du sang maternel et l'absorption à la surface des villosités.

À l'étape suivante, l'on s'affranchit de l'hypothèse d'une forme circulaire des villosités, et l'on propose une solution analytique approchée de l'équation de la diffusion-convection. Il est ensuite démontré que deux caractéristiques géométriques — la densité de villosités et le rayon efficace de villosités — suffisent à prédire l'absorption fœtale d'oxygène dans une géométrie donnée. La théorie identifie également deux combinaisons de paramètres physiologiques qui déterminent l'absorption d'oxygène : (i) le flux entrant maximal d'oxygène dans un placentone, et (ii) le nombre de Damköhler défini comme le rapport entre le temps de passage du sang maternel dans l'espace intervillaire et un temps caractéristique d'extraction d'oxygène dans une coupe transversale du modèle. Des formules analytiques permettant de calculer l'absorption d'oxygène d'une façon simple et efficace en sont déduites, et deux diagrammes d'efficacité du transport d'oxygène dans une coupe arbitraire de placenta sont tracés. La théorie analytique propose également une méthode permettant d'exploiter les résultats d'expériences sur la perfusion artificielle du placenta par un sang ne contenant pas d'hémoglobine, afin de prédire l'efficacité de transfert en intégrant cette fois l'interaction entre l'oxygène et l'hémoglobine.

Au final, nous présentons une méthode d'analyse de grandes coupes histologiques de placenta humain, dans le but de mesurer de façon automatique les aires, les périmètres et la morphologie des régions de villosités, de l'espace intervillaire et des capillaires fœtaux. Ces données peuvent ensuite être introduites dans le modèle afin d'estimer l'efficacité du placenta. La méthode est appliquée à 25 coupes placentaires provenant de 22 grossesses saines et de 3 grossesses pathologiques. La combinaison des données obtenues avec les diagrammes d'efficacité montre que toutes les valeurs mesurées de la densité de villosités se retrouvent en écart relatif à moins de 10 % de la valeur optimale. En revanche, l'efficacité globale correspond à une valeur assez basse (autour de 30–40 %).

Dans l'avenir, le modèle présenté peut constituer la base d'un outil fiable de l'évaluation de l'efficacité d'échange d'oxygène au sein du placenta humain à partir de mesures histologiques *post partum*, ou, à plus long terme, à partir de mesures non-invasives *in utero*.

Acknowledgements

The three and a half years of my Ph.D. studies at the PMC lab of École Polytechnique were an interesting challenge. The way I arrived here was not simple, and I have considered for a significant time the life-changing choices I had to make. However, I have to admit that finally I have never regretted the decisions made. Here I would like to thank all those without whom this experience would not have been so instructive, pleasant and diverse.

First of all, I would like to acknowledge the scientific as well as personal efforts Denis and Marcel have put into this project and into my development as a scientist. The progress of this placenta project is in a great part due to these two quite different researchers. I hope that this project is only a start of our long and fruitful collaboration.

I would also like to thank all the members of the jury for having accepted to participate in the evaluation of the manuscript and in my Ph.D. defense, as well as for their instructive remarks. In particular, the two reviewers, Dr. Rohan Lewis and Dr. Jean-Frédéric Gerbeau, have performed a great amount of work analyzing the thesis manuscript and have provided very helpful and important suggestions.

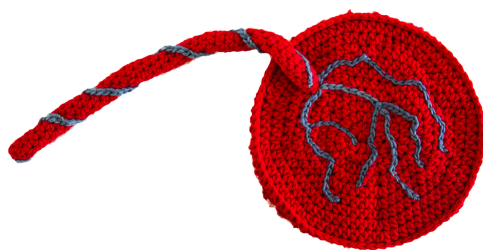
I would like to thank Carrie for her patience in answering numerous basic biological questions (not at all evident for a physicist) and for introducing me to the field of experimental placental studies and to the international placenta community. I have also much enjoyed the scientific discussions we have had with Paul Brownbill and Rohan Lewis. This project also owes to the efforts of the three interns, Zhenzhen You, Nguyễn Đăng Khoa and Junior Goubalan, who have made great contribution to bringing this initially theoretical and computational project closer to practice.

The successful defense of the thesis would also not have been possible without the advice and support of the members of the PMC lab. I would especially like to thank the directors of the lab, Mathis and François, for having created and maintaining a good working atmosphere in the lab, as well as for their help with administrative questions and valuable discussions. Solving the administrative problems has also been made much easier for me thanks to the efforts of Anne-Marie, Eve, Élodie, Florence, Mme Cécile Vigouroux and the staff of the Direction des Relations Internationales (formerly Direction des Relations Extérieures who has funded this Ph.D. thesis). I would also like to express my gratitude to Anne and Yves for having made my moving to the new office smooth and pleasant, as well as for several delicious madeleines. The bug-shaped cookies of Anne L. were also great. Many other people of the lab (interns, Ph.D. students, post-docs and permanent staff of the lab), as well as friends outside the lab (Matthieu, Barbara, Salim, Jonghoon, Mahsa, Kami and many others) have contributed to making PMC, École Polytechnique and Paris a very pleasant place to work and stay.

Certainly, it would be hard to imagine the realization of the project without the support of my family who have closely followed all my progress and participated in the discussion of all important decisions. The “pot de thèse” would not have been so well organized, if it had not been for the careful selection of the products by my mother and for the preparation of the dishes by Галя, Серёжа, Kami and all the volunteers of the PMC.

Finally, there are some more people whom I would like to thank in particular:

- Maud, pour avoir été une super collègue de bureau et pour m'avoir parlé le plus de toutes les personnes du labo pendant son stage ;
- Julien, pour son soutien avec la partie informatique, pour les petites optimisations du code qu'il proposait au fil du projet, pour m'avoir accompagné pendant l'achat de la nourriture pour le barbecue et le repas de Noël du labo, ainsi que pour son aide avec le remplacement du disque dur de mon portable, ce qui l'a mis en panne pour un mois ;
- Наташу, за обучение секретам музыки, таким как умение слушать диалог двух рук, корректно определять музыкальные голоса или правильно писать слова мизинец, стаккато и мордент;
- Juliette, pour des discussions infinies des règles et des exceptions du français, des leçons de biologie, pour un accueil chaleureux septentrional, une balade dans la berdouille, ainsi que pour JJG et de savoureux thés goûtés et offerts ;
- Mahsa, pour les nombreux déjeuners ensemble, sa gaité et sa personnalité débordantes, ainsi que pour des idées exceptionnelles de post-doc ;
- Matthieu, pour des discussions de la science et du français, pour des balades insolites, ainsi que pour un week-end tout viril dans la Creuse ;
- Finally, Pani Kami, za to, że litery moich słów wychodowały ogonki, za miły czas wspólnego burczenia w takim ciekawym języku, za spacery bez smyczy i po miastach europejskich, oraz za to, że nie dała mi Pani umrzeć bez słodkiego ani od czosnku.



Contents

English abstract	2
French abstract	3
Acknowledgements	4
Contents	7
Preface	11
1 Introduction	13
1.1 Introduction	13
1.1.1 Importance of placental studies and goals of the thesis	13
1.1.2 Structure of this chapter	14
1.2 Placental structure	15
1.2.1 Placental classification by shape	15
1.2.2 Placental classification by histological structure	17
1.3 Human placenta structure	21
1.3.1 Healthy pregnancies	21
1.3.2 Pathological conditions	24
1.4 Placental functions	26
1.4.1 Placental transport function	26
Passive and active transport	26
Transferred substances	29
1.4.2 Endocrine function	30
1.4.3 Protective function	31
1.4.4 Concluding remarks	31
1.5 Experimental methods of placental studies	31
1.6 Review of theoretical models of placental transport	41
1.6.1 Overview of placenta modeling	41
1.6.2 Respiratory gas exchange models	42
1.6.3 Capillary-scale models. Flow patterns	43
1.6.4 Morphometric diffusing capacity models	46
1.6.5 Distributed parameters models	48
1.6.6 Models based on histological placental sections	51
1.6.7 Experimental validation of mathematical models of respiratory gas exchange in the placenta	53
1.6.8 Concluding remarks	53
1.7 Objectives and structure of the thesis	54

2	Stream-tube placenta model	57
2.1	Model outline	58
2.1.1	Model assumptions	59
2.1.2	Dimensionless hydrodynamic numbers	61
	The Reynolds number (Re)	61
	The Péclet number (Pe).	63
	The Schmidt number (Sc)	63
	The Damköhler number (Da).	64
2.2	Diffusion-convection equation	65
2.2.1	Characteristic time scales of transfer processes in the human placenta	65
2.2.2	Equilibrium between the bound and the dissolved oxygen	65
2.2.3	Diffusive-convective transport of oxygen	66
2.2.4	Linearization of the Hill equation	67
2.2.5	Boundary conditions	68
2.2.6	Conversion to a 2D eigenvalue equation	69
2.2.7	General expression for oxygen uptake	69
2.3	Model parameters	70
2.3.1	Calculation of the model parameters	70
2.3.2	Concluding remarks	77
2.4	Numerical simulation	77
2.4.1	Circular villi. Solution convergence and validation	77
2.4.2	Results	80
2.4.3	Comparison to the experimental data	82
2.4.4	Comparison to the porous medium model	83
2.4.5	Other ways of comparison	86
2.4.6	Additional remarks	87
2.5	Conclusions	87
3	Approximate analytical solution	89
3.1	Mathematical formulation	90
3.1.1	Form of the approximation	90
3.1.2	Uptake at the infinite length	90
3.1.3	Average concentration decay rate	91
3.1.4	Dimensionless geometrical parameters	93
3.1.5	The optimal cross-sectional geometry	93
3.1.6	Optimal villi density	95
3.1.7	Villi density efficiency	97
3.2	Analytical results	97
3.2.1	Oxygen uptake for circular villi	97
3.2.2	Typical values of the parameters Da and F_0	99
3.2.3	The parameter Da	100
3.2.4	Advantages of the analytical theory	101
3.3	Concluding remarks	104

4	Analysis of Histological Placental Cross-Sections	105
4.1	Manual placental histomorphometry	106
4.1.1	Application of the STPM to histological placental cross-section . .	106
	Geometrical parameters	106
	Physiological parameters	107
	Summary	108
4.1.2	Histological placental cross-sections	108
4.1.3	Point–intersection counting techniques	110
4.2	Automatic placental segmentation	112
4.2.1	“Ideal” segmentation and main segmentation challenges	112
4.2.2	Thresholding and the initial segmentation	114
4.2.3	Refining the segmentation	117
	Filtering out noise	117
	Discriminating fetal capillaries from the IVS.	118
	Smoothing out the contours	118
4.2.4	Accuracy of the segmentation algorithm	120
4.2.5	Histomorphometrical measurements	122
4.2.6	Code execution time as a function of image size	124
4.3	Algorithm application to placental cross-sections	125
4.3.1	Samples description	125
4.3.2	Comparison of segmentation results for healthy and pathological placentas with the results obtained with manual histomorphome- trical techniques	126
4.3.3	Efficiency diagrams	128
4.4	Concluding remarks	130
5	Conclusions and Further Development	133
5.1	Results summary	133
5.2	Further development	136
5.2.1	Development of the model	136
5.2.2	Development of the field	137
	Appendices	141
A	Hormones secreted by the placenta	142
B	Typical parameters of placenta models	144
C	Error estimation	148
D	Typical problems of histomorphometrical placental studies	150
D.1	Inhomogeneity of the fetal villous tree	150
D.1.1	Intraplacentone structural variations	150
	Villi density φ and the effective villi radius r_e	150

Trophoblast layer thickness.	152
D.1.2 Intraplacental structural variations	157
D.2 Immersion fixation vs. perfusion fixation of placental samples	157
D.3 Influence of the fixative on histomorphometrical measurements	159
E Comparison of oxygen exchange efficiency at low and high altitudes	161
Bibliography	163

Preface

*There's nothing wrong with
putting animal afterbirth in
your hair*

Customer recommendation of
a placental shampoo
(Power and Schulkin, 2012)

While working on this project, I was surprised to discover the multiple ways in which the placenta can be used after delivery. Those include ingestion of the placenta in the dried, frozen or ground into powder forms. Recipes can be found on the Internet instructing on how to make the most delicious placenta lasagne, placenta stew, placenta smoothie, placenta pizza, or a placentaburger, and do-it-yourself placenta encapsulation kits can be ordered on Amazon. The placenta can also be burned, buried with a tree planted above it, converted into a teddy bear, or applied to different parts of the body to help you cope with the “baby blues”, make your hair lustrous and thick, your skin dry and improve the overall health and beauty.


This thesis is an attempt to demonstrate that in addition to all these options, a delivered placenta can also serve scientific purposes and help diagnose newborn health risks.

This thesis has a digital object identifier (DOI) that can be used to cite it. All remarks and questions about this work can be sent to alexander.serov@polytechnique.edu.

Chapter 1

Introduction

1.1 Introduction

HE placenta is the only link between the mother and the growing fetus. It supplies the fetus with water, nutrients and oxygen, eliminates carbon dioxide and other wastes, performs barrier, metabolic and endocrine functions, thus fulfilling functions of multiple organs. Understanding the placental function is thus important to understand the fetal development *in utero*.

While studying the placenta may help the assessment of baby health risks, this valuable and unique source of information about the development of the baby for the first nine months is usually discarded after birth as medical waste. At the same time, it is the only organ that the body does not need after birth and which can thus be extensively examined.

1.1.1 Importance of placental studies and goals of the thesis

The information the placenta may provide has been shown to be crucial for understanding the reasons of fetal maldevelopment and the main causes of fetal death (reported at the level of 6.05 fetal deaths / 1000 pregnancies after the 20th week of gestation in the US in 2006, see [MacDorma et al., 2012](#)). For instance, [Baergen \(2007\)](#) has demonstrated that studying the placenta may not only reveal pregnancy-related problems that are due to an inherent placental abnormality, but often also lets ascertain the etiology of the injury and the corresponding time frame. [Korteweg et al. \(2009\)](#) analyzed 750 cases of singleton intrauterine fetal death (after 20 weeks of gestation) and have concluded that 64.9% of death cases can be attributed to placental pathologies. [Hutcheon et al. \(2012\)](#) have shown that low placental weight at birth significantly increases the risk of stillbirth, while high placental weight was related to a high probability of adverse neonatal outcomes.

Interestingly, the placenta does not only provide information on the fetal development *in utero*, but also allows one to make prediction on the future development of the newborn. For instance, [Misra et al. \(2012\)](#) have correlated the children intelligence coefficient at the age of 7 years with placental thickness and chorionic plate diameter. Other studies have provided evidence of correlation between the risk of hypertension and

coronary heart disease in adults and the placental weight, diameter and cross-sectional area (Barker, 1994, 1995, Eriksson et al., 2010). So understanding the placental function may not only shed light on adverse pregnancy outcomes, but also help identify children with increased health risks.

Past studies have shown that the transport function of the placenta is in significant part determined by the structure of the organ (Guilbeau et al., 1972, Hill et al., 1972, Erian et al., 1977, Faber, 1977, Mayhew et al., 1984, Chernyavsky et al., 2010, Gill et al., 2011). The main goal of this thesis is to further extend our understanding of the relation between the placental structure and the transport function by constructing a mathematical model based on the details of placental morphology that can be obtained in a histological examination. This 3D model considers a part of the maternal blood flow in the intervillous space — a stream tube — crossed by fetal villi. In this stream-tube model, we will not only quantitatively estimate oxygen uptake, but will also determine an optimal geometry of the stream-tube that provides the maximal oxygen uptake. Starting with simple villi shapes, we will then advance to villi of arbitrary shape. Finally, we will thoroughly analyze how this model can be converted into a tool of medical diagnostics of placental exchange efficiency that would take 2D histological placental cross-sections as input.

1.1.2 Structure of this chapter

In the present chapter we provide an introduction to the placental studies for a reader who may be new to the subject. For this purpose, we first discuss the great variability of the placental shape and structure among the placental mammals. Two main principles of placental classification are considered: classification by shape and classification by histological structure of the organ.

Having provided an overview of inter-species placental differences, we further focus on the human placenta, which is of primary medical interest and which arguably has the most complicated pattern of maternal circulation. We briefly describe the structural organization of the human placenta and its main functions (transport, endocrine and protective). Special attention is given to its transport function, which is the principal topic of the present thesis.

After that, we review experimental techniques developed for placenta investigation including macroscopic and microscopic histological examination, micro-CT, T_1 - and T_2 -weighted contrast MRI, confocal laser scanning microscopy and ultrafast ultrasound techniques. We discuss the data that can be obtained with each method and the corresponding limitations. Our analysis will demonstrate that due to ethical reasons and the fact that histological and physiological placental features commonly co-vary, the experimental techniques are not able to provide a complete picture of intraplacental transport processes. A complementary point of view on this question is offered by mathematical models. In the vast field of placenta models, we direct our attention to the models of respiratory gas exchange. On one hand, it is explained by the short time within which the adverse effects of compromised respiratory gas exchange are observed in the fetus. On the other hand, we are interested in the special focus of this kind of models on the geometry

of the placenta as an exchanger (rather than on transport-related biochemical reactions). Other directions of the placenta modeling (such as modeling of the placenta shape, villi branching or glucose and amino acid exchange) are also listed.

The first models of respiratory gas exchange in the human placenta date back to [Barron \(1951\)](#) and [Lamport \(1954\)](#). To let the reader understand the positioning of the present study in the context of the previous models, we analyze the main directions of the placental respiratory gas exchange modeling, of which we distinguish four:

- capillary-scale models and flow patterns studies,
- morphometric diffusing capacity models,
- distributed parameters models,
- models based on histological sections.

After a short review of the models, we discuss the possible ways of validation of the models and analyze their main limitations. This analysis of placental models was published in [Filoche et al. \(2015\)](#). In the last section, the structure of subsequent chapters is outlined.

1.2 Placental structure

The placenta is an organ developed only by mammals during pregnancy. It is formed when the fetal membranes (blue and black in Fig. 1.1) come into close contact with the endometrial lining of the uterus (red in Fig. 1.1). However, not all mammals can produce a placenta, which is one of the basic criteria for distinguishing three classes of mammals: *eutherians* (placental mammals), *metatherians* (or marsupials, nonplacental mammals having abdominal pouches) and *monotremes* (nonplacental egg-laying mammals like the platypus and the echidna). Although eutherian mammals share many similar features, there exist considerable interspecies differences (especially with regards to the placental structure and morphology), which yielded multiple placenta classification schemes. In this section we will review the two basic classifications (by the placental shape and by histological structure) following [King \(1992\)](#), [Wooding and Burton \(2008\)](#), [Power and Schulkin \(2012\)](#). For the details of other classifications, the reader is referred to [Ramsey \(1982\)](#).

1.2.1 Placental classification by shape

The growing fetus is surrounded by four fetal membranes: the chorion, the amnion, the allantois and the yolk sac (Fig. 1.1). The chorion is the external embryonic membrane in direct contact with the maternal tissue. It often forms chorionic folds or villi that significantly increase the exchange surface. The placenta classification by shape is based on the distribution of outgrowths of the chorion on the mature gestation sac. According to this criterion, four major placental categories are recognized (Fig. 1.2):

1. A *diffuse placenta* completely surrounds the fetus, and the chorion is distributed over most of the surface of the gestation sac. As a consequence, almost all the

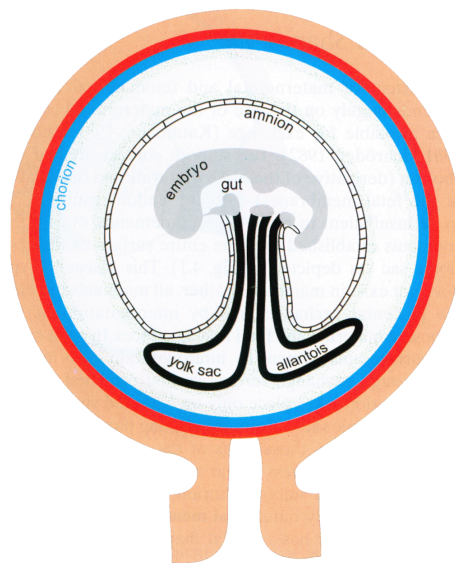


Figure 1.1. Synoptic representation of the fetal membranes (black and blue) that may contribute to the formation of the placenta. The maternal tissues are shown in red (the endometrial lining in contact with the fetal chorion) and brown (the rest of the uterus). Reproduced from Benirschke et al. (2006)

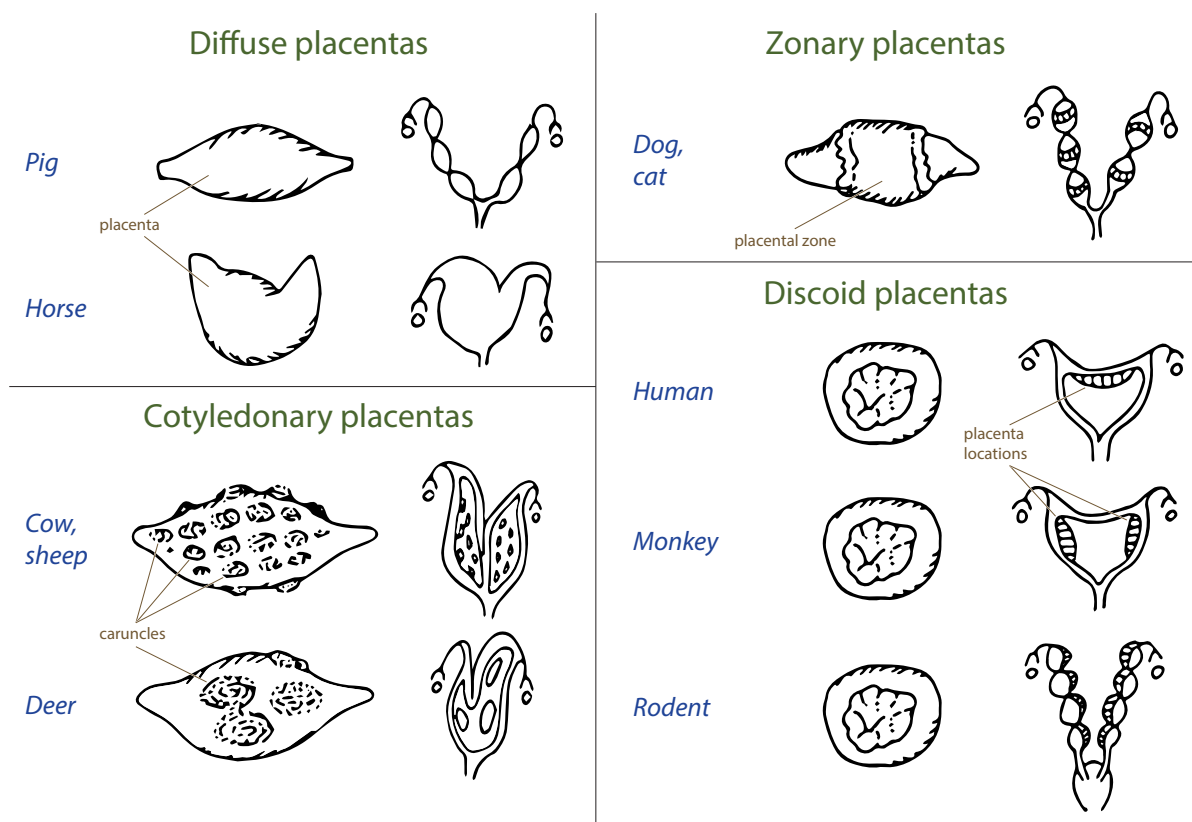


Figure 1.2. Major categories of placentas according to their shape (second column). The corresponding shape of the uterus and placental location in it (third column) in it are also shown. Modified from Wooding and Burton (2008)

placental surface attaches to the uterine wall. This placenta type is seen in pigs, horses, whales, dolphins, hippopotamuses and some primitive primates (lemurs and lorises).

2. A *cotyledonary placenta* attaches to the uterus in multiple discrete locations, which form circular or oval patches on the chorionic sac. The maternal attachment sites are called caruncles, and the placental sections which attach to the uterine wall are termed cotyledons. A maternal attachment site together with a corresponding placental cotyledon form what is called a placentome (Power and Schulkin, 2012). Note however that nowadays the terms cotyledons, placentones (-omes) or lobules are often used interchangeably (Chernyavsky, 2011), especially in application to the human placenta. In this thesis we will mainly use the term placentone. The cotyledonary placental organization can be found in ruminants (e.g., cows, sheep), deer, sloths, armadillos. Horses have microcotyledons in discrete sections of their diffuse placenta (Power and Schulkin, 2012). Placentones are also found in the discoid human placenta (Benirschke et al., 2006).
3. A *zonary placenta* forms a band or a girdle around the fetus usually located in the equatorial plane. In some species it completely encircles the fetus, while in others the band is incomplete or forms two half-bands. Zonary placenta is found in all carnivores (e.g., canines, felines, bears, seals), elephants, rock hyraxes and armadillos. Among these species, dogs and cats have complete bands, while ferrets and raccoons have two half bands.
4. A *discoid* (or discoidal) *placenta* has a shape close to a disk, in which chorionic villi are distributed. This placenta type is found in rodents, bats, tenrecs, giant anteaters, red panda and anthropoid primates, including humans.

The placental classification by shape is straightforward and convenient, but it does not describe four *functionally* different categories, since numerous functional variations exist within the same shape categories (King, 1992, Wooding and Burton, 2008, Power and Schulkin, 2012).

1.2.2 Placental classification by histological structure

An alternative placental classification, by histological structure, is based on the number and origin of tissue layers separating the maternal and fetal circulations. These characteristics are closely related to the exchange properties of the placenta, which makes such categorization more functional. This classification was originally proposed by Grosser (1909, 1927) and later modified by Mossman (1937), Owers (1960).

The maximal number of different tissue layers separating the maternal and fetal blood circulation is six: *maternal* endothelial, connective and epithelial tissue layers and *fetal* endothelial, connective and epithelial tissue layers (Fig. 1.3). However, with the evolutionary progress, some species have lost one, two or three (i.e. all) maternal tissue levels. The Grosser's classification distinguishes four main placental types which arise as a consequence of this tissue layers reduction (Fig. 1.4). The names of the categories are

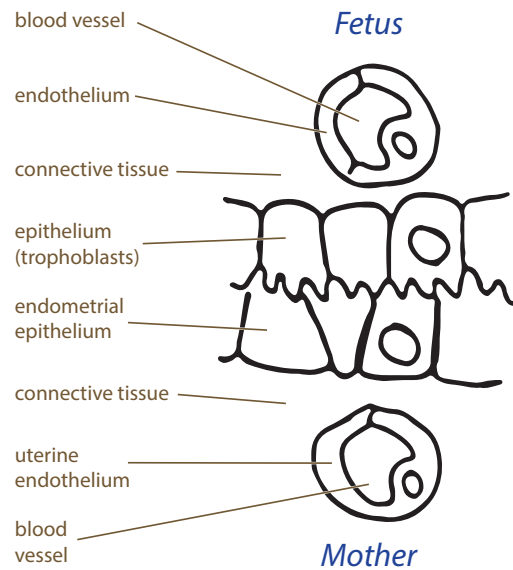


Figure 1.3. Illustration of the six potential tissue layers separating the maternal and fetal circulations: *maternal* endothelial, connective and epithelial tissue layers and *fetal* endothelial, connective and epithelial tissue layers. Modified from Wooding and Burton (2008)

defined by the maternal tissue layer, which is in contact with the fetal chorion after the placental implantation and early differentiation of fetal organs are completed (see also Fig. 4.5 and Table 4.1 in Benirschke et al., 2006):

1. In *epitheliochorial* placentas no tissue layers have been lost, so that the uterine epithelium is in contact with the chorion. Such placental organization is observed in pigs, horses, deer, dolphins and whales.
2. In *synepitheliochorial* (*syndesmochorial*) placentas the uterine epithelium is removed, and the maternal connective tissue is in contact with the chorion. Such placentas are typical for ruminants.
3. In *endotheliochorial* placentas the uterine epithelium and the maternal connective tissue are removed, and the maternal capillary endothelium is apposed to the chorion. Such placentas can be seen in carnivores (e.g., cats and dogs).
4. In *hemochorial* placentas, all intervening maternal tissues are removed, and the maternal blood directly bathes fetal trophoblasts. Such placentas are found in rodents, rabbits, insectivores and anthropoids (including humans).

Having proposed this histological classification, Grosser suggested that the number of tissue layers separating the maternal and fetal circulations determines the thickness of the placental membrane and therefore the placental transport properties. However, with the discovery of active, facilitated and endocytic transport (discussed later), this hypothesis became oversimplified. For instance, immunoglobulin is transferred differently from the mother to the fetus in humans and guinea pigs (see King, 1992).

It was also reported that more tissue layers do not necessarily make the placental membrane thicker: for example, in the epitheliochorial placenta of the pig, maternal capillaries indent the uterine epithelium and fetal capillaries indent fetal trophoblasts, so

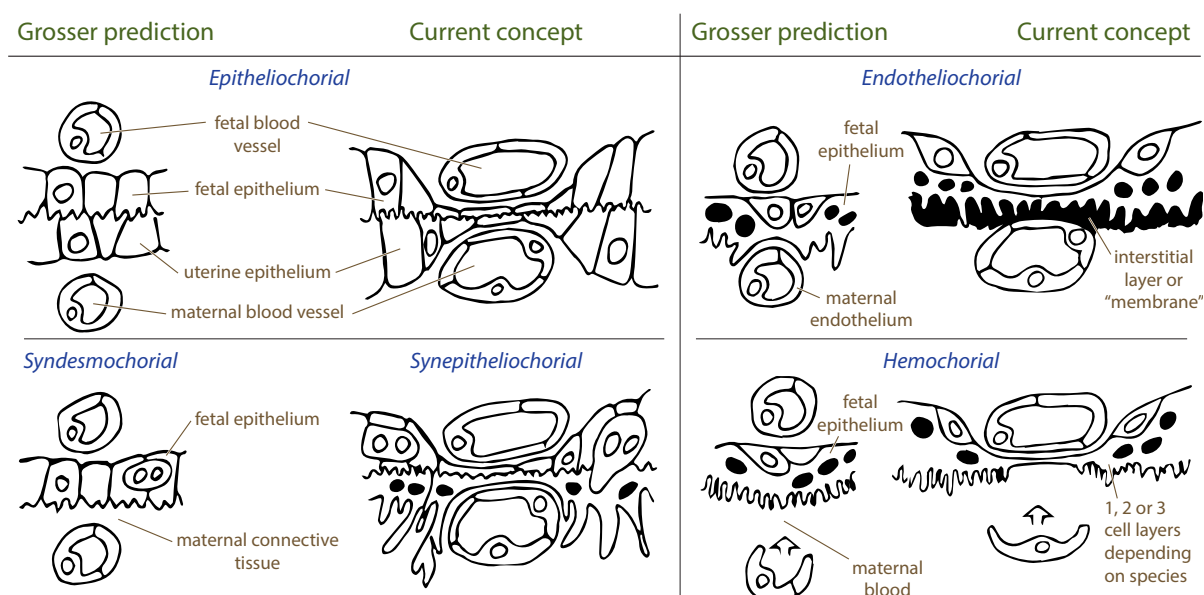


Figure 1.4. Major categories of placentas according to histological placental structure. The original suggestion of Grosser (1909, 1927) is accompanied to the right by a revised version (Wooding and Burton, 2008). The revised version takes into account the fact that fetal and maternal capillaries indent into the chorionic and uterine epithelium respectively during growth, which significantly decreases the diffusion distance between the two circulations. Modified from Wooding and Burton (2008)

that the diffusional distance between the two circulations is significantly reduced (King, 1992). With these restrictions kept in mind, the Grosser's classification still stays a convenient reminder of which placental tissue layers should be taken into account while working with one or another species.

The differences in the histological structure of the placenta across species find their reflection in the organization of the maternal and fetal circulations in the placenta. In many species, the maternal blood and the fetal blood pass through the placenta in blood vessels which come into close contact in the exchange region to allow for substance transfer. Such organization of the organ is natural for epitheliochorial (Fig. 1.5a), syndesmochorial and endotheliochorial placentas, where at least one maternal tissue layer separates the maternal and fetal placental vascular systems (King, 1992). In hemochorial placentas, there are no maternal blood vessels in the exchange region. In labyrinthine hemochorial placentas, the maternal space is organized in a kind of labyrinth, the architecture of it resembles that of blood vessels (Figs 1.5b, 1.6a, see Battaglia and Meschia, 1986, King, 1992). However, the structure of the non-labyrinthine anthropoid primate placenta (monkeys, apes and humans, see Figs 1.6b, 1.7a) is quite different with maternal blood forming a blood basin into which fetal chorionic villi are immersed. Such structural organization significantly complicates the description of transport properties of the human placenta due to the intricate maternal blood flow pattern and chorion arrangement. This thesis focuses on the human placenta because of its primary medical interest, and also because of the greater complexity of its structure compared to other species.

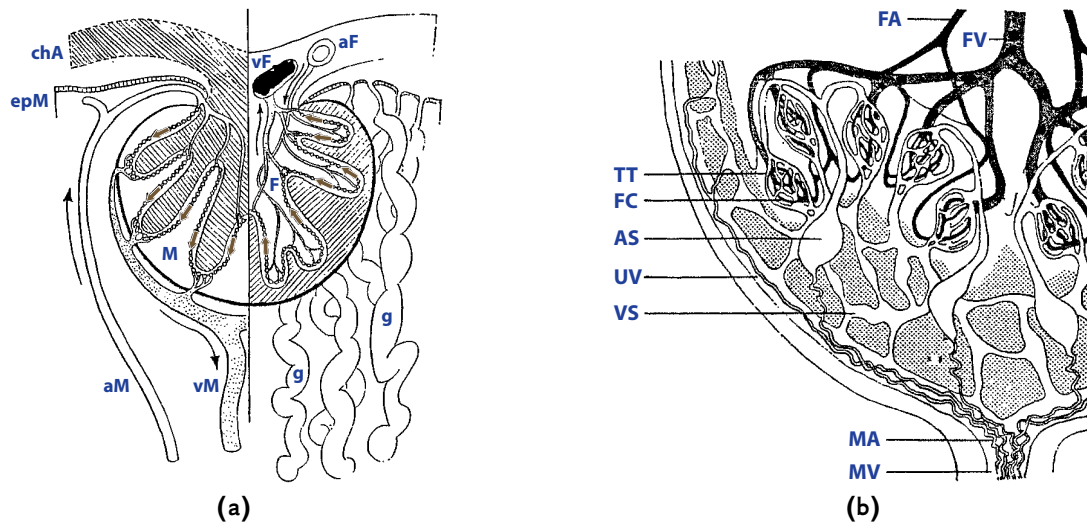


Figure 1.5. (a): Arrangement of the maternal and fetal blood vessels in microcotyledons of the epitheliochorial placenta of the horse. Small brown arrows mark the countercurrent organization of the maternal and fetal blood flows, currently supposed in the horse placenta. Notations: maternal (M), fetal (F), maternal artery (aM), maternal vein (vM), fetal artery (aF), fetal vein (vF), chorioallantois (chA), uterine epithelium (epM), endometrial glands (g). Modified from Silver et al. (1973), Battaglia and Meschia (1986), based on the data by Tsutsumi (1962). (b): Arrangement of the maternal and fetal blood vessels in the rabbit placenta. Maternal blood enters the exchange area via maternal arteries (MA) that feed large arterial sinuses (AS). Efferent arteries proceed from these sinuses toward the fetal surface of the placenta and open into trophoblastic tubules (TT) of the placental labyrinth. In these tubules the blood flows towards the decidua, where it collects in venous sinuses (VS) that are drained by large veins in the uterine wall (UV) and mesometrium (MV). Fetal arteries (FA) penetrate deep into the placenta and then break up into fetal capillaries (FC) in which fetal blood runs back towards fetal umbilical veins (FV). Modified from Carter (1975), based on the original drawing by Mossman (1926)

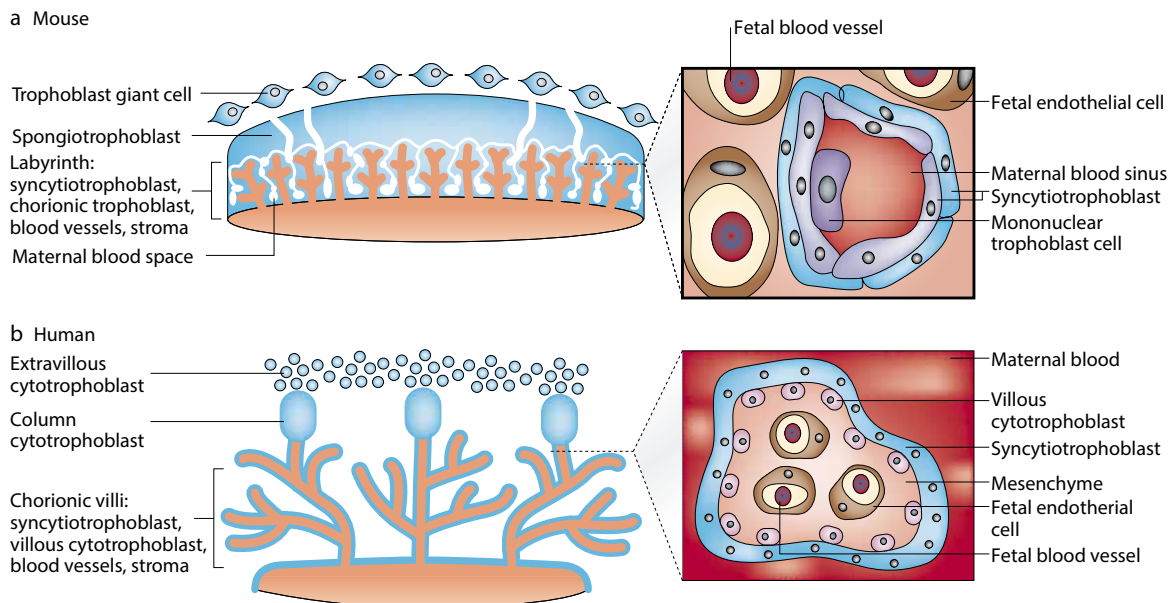


Figure 1.6. Comparative anatomy of the mouse and the human placenta. (a) Structure of the mouse placenta. The details of the fetal-maternal interface in the labyrinth are provided in the inset. (b) Structure of the human placenta. The inset image shows a cross-section of a fetal villus. One can see that in the mouse placenta the maternal blood and the fetal blood are confined to capillaries, while in the human placenta fetal villi are directly immersed in a basin of maternal blood. Reproduced from Rossant and Cross (2001)

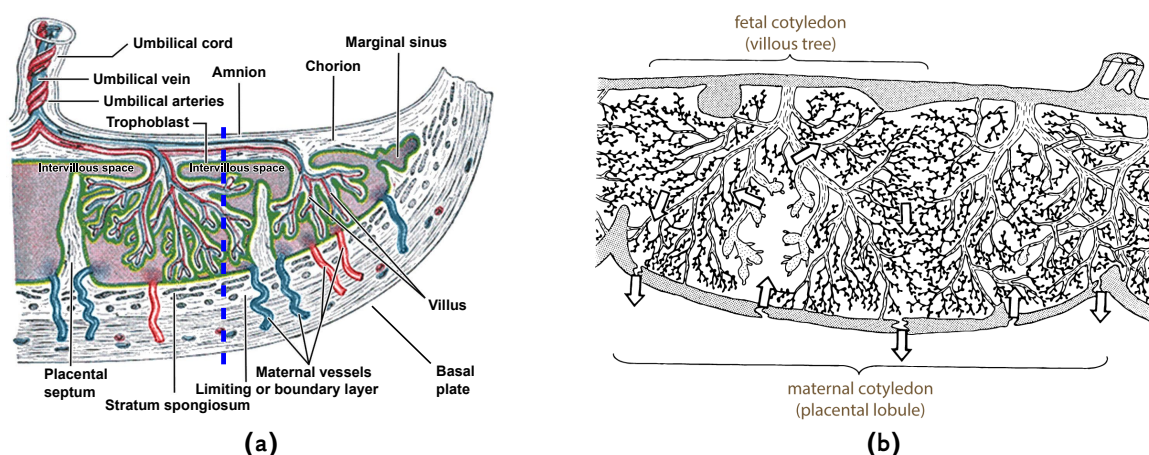


Figure 1.7. (a): Structure of the human placenta (modified from Gray, 1918). The bottom side is the basal plate which attaches to the uterus; the upper side is the chorionic plate, where the umbilical cord connects to the placenta. Typical location and orientation of a histological placental section is marked by a dashed blue line. (b): Location and structure of villous trees inside the human placenta. The chorionic plate is facing up. The direction of the maternal blood flow is marked by arrows. According to the modern views, the maternal blood enters the placenta near the center of a villous tree and leaves the intervillous space between the villous trees (Benirschke et al., 2006). The adjacent villous trees may overlap. Reproduced from Kaufmann (1985b), Benirschke et al. (2006)

1.3 Human placenta structure

1.3.1 Healthy pregnancies

A healthy human placenta is a disk with an average diameter of 22 cm (Benirschke et al., 2006, p. 13). The two faces of the disk are called the chorionic plate (the one from which the umbilical cord stems, Fig. 1.8a) and the basal plate (the one which attaches to the uterus wall, Fig. 1.8b). The average thickness of the delivered organ is 2.5 cm and the average weight is 470 g (Benirschke et al., 2006, p. 13).

In what concerns the internal structure, the maternal portion of a term human placenta is a basin into which maternal blood is brought by numerous spiral arteries and which is drained by decidual veins (Fig. 1.7a; Benirschke et al., 2006). It is remarkable that after many years of human placenta studies, the exact number of spiral arteries and decidual veins perfusing the placenta is still unknown. The review by Panigel and Pascaud (1968) cites the following numbers: spiral arteries — from 50 to 120 and orifices of spiral arteries — from 100 to 500. There are also around 30 (Klein, 1890) decidual veins, which form around 80 venous openings (Franken, 1954). The low precision of these numbers is explained by the difficulty to find the orifices of the vessels and to distinguish between arteries and veins after the delivery (see Haller, 1968, Benirschke et al., 2006, p. 251–2).

The fetal portion of the human placenta is a tree of villi immersed into the maternal blood. As a tree, it has many generations of branches (up to 30, mean value around 10, see Benirschke et al., 2006) which differ by their caliber, stromal structure, vessel structure and location within the villous tree (Fig. 1.9). According to these criteria, five villi types are distinguished: stem villi, immature intermediate villi, mature intermediate villi, terminal villi and mesenchymal villi (for the details of classification see Kaufmann et al., 1979,

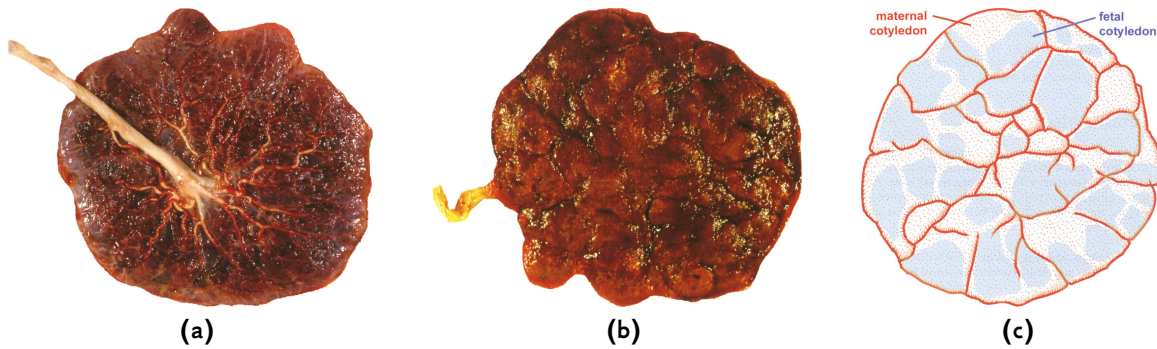


Figure 1.8. (a), (b): Appearance of the human placenta: the chorionic plate (a) and the basal plate (b). It can be seen that the basal surface is subdivided into placental lobules of various size by an interrupted net of dark grooves. Reproduced from Benirschke et al. (2006). (c): Subdivision of the human placenta into maternal and fetal lobules. The borderlines of the maternal lobules are marked by red lines (drawn from the grooves at the basal surface), 29 fetal trees are shaded in blue (obtained by a radiograph of the placenta after injection of a radiopaque medium into the fetal vessels). Although there is a good agreement in the locations of the fetal and the maternal lobules, one to three fetal lobules can project on the same maternal lobule. Reproduced from Kaufmann and Scheffen (1992), Benirschke et al. (2006), based on the photographs by Boyd and Hamilton (1970)

Sen et al., 1979). Scanning electron photographs of mature intermediate and terminal villi are shown in Fig. 1.10. The characteristic diameters (calibers) of the villi are: stem villi, 300–3000 μm ; immature intermediate villi, 60–200 μm ; mature intermediate villi, 40–80 μm ; terminal villi, 30–80 μm .

Inside each villus, fetal capillaries conduct fetal blood from the umbilical arteries to the umbilical vein, without admixture with the maternal blood stream (Fig. 1.11). All exchange processes between the mother and the fetus take place at the surface of the fetal villi. It mainly occurs in the smallest branches of the tree — terminal and mature intermediate villi, — in which capillaries are located close to the villous membrane and the membrane itself is thin (Benirschke et al., 2006, p. 121).

The human placenta is normally considered as subdivided into functional units (placentones, also called lobules or cotyledons, Fig. 1.8c). It is estimated that a healthy human placenta counts from 40 to 60 placentones (Benirschke et al., 2006, p. 161). Fetal trees tend to overlap, and placental septa do not completely separate one placentone from another, but rather mark their approximate boundaries (Figs 1.7b and 1.8c). Each placentone normally has a villi-free central part (a central cavity, with a characteristic diameter of 1 cm, as estimated from figure 4 of Aifantis, 1978), which, as some researches believe, is formed by the mechanical force of a “jet” of maternal blood spurting from the spiral arteries (Ramsey et al., 1963, Borell et al., 1958, Benirschke et al., 2006, p. 163–4). However, recent calculations predict that due to trophoblast invasion and remodeling of the spiral arteries, the velocity of the “jet” is significantly lower ($\sim 10 \text{ cm/s}$) than 1–2 m/s estimated earlier (Burton et al., 2009). So the mechanisms of formation of the central cavity are as yet unclear.

The intervillous space (IVS) is drained by decidual veins which tend to be located at the periphery of the placentone (at the basal plate or in the lower one-third of placental septa; see Benirschke et al., 2006, p. 161, p. 252 and Fig. 1.7a). The ideal arrangement with one spiral artery opening near the center of the villous tree is

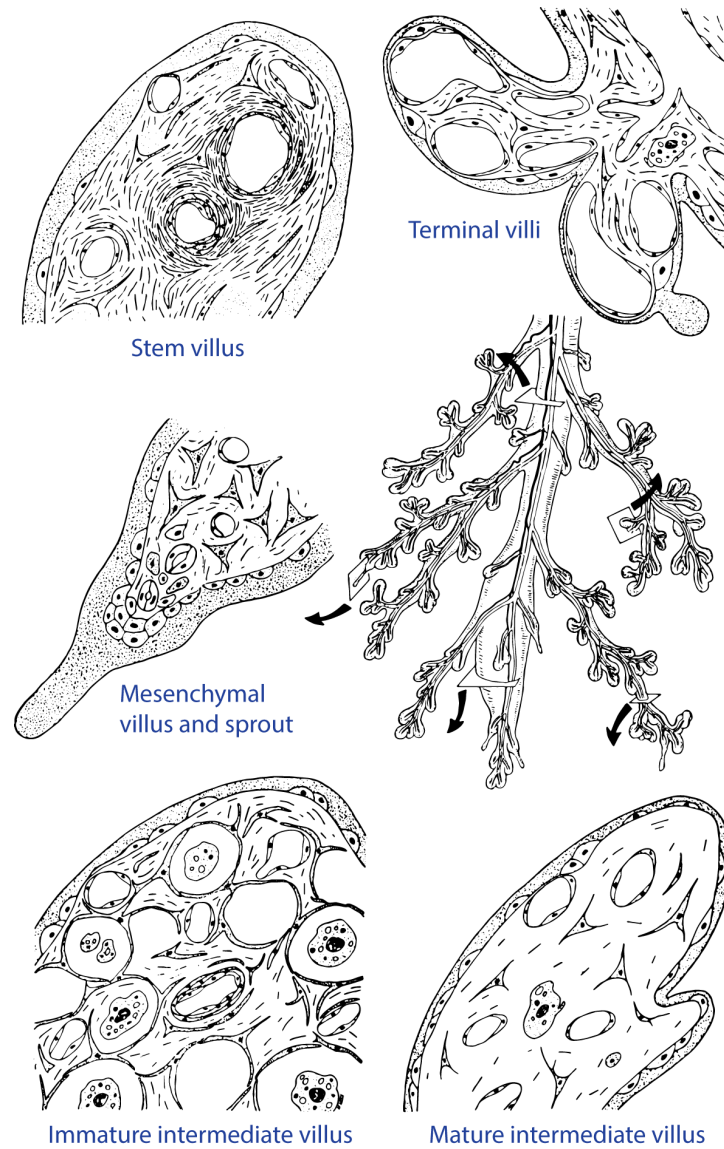


Figure 1.9. Schematic representation of the cross-sections of the main types of fetal villi (stem villi, immature intermediate villi, mature intermediate villi, terminal villi and mesenchymal villi) and their location in the villous tree. Note that villi cross-sections are shown at different magnifications. Reproduced from Kaufmann and Scheffen (1992)

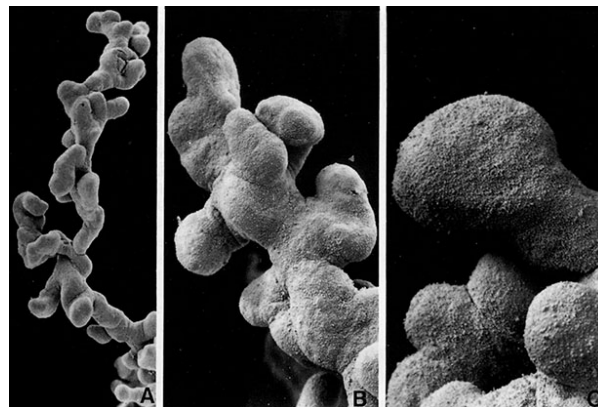


Figure 1.10. Scanning electron photographs of different villous regions. (A): A single mature intermediate villus. (B): A tip of a mature intermediate villus featuring rich branching into terminal villi. (C): A group of terminal villi, with the central one showing a typical constricted neck region and a dilated final portion. Reproduced from Kaufmann et al. (1979), Benirschke et al. (2006)

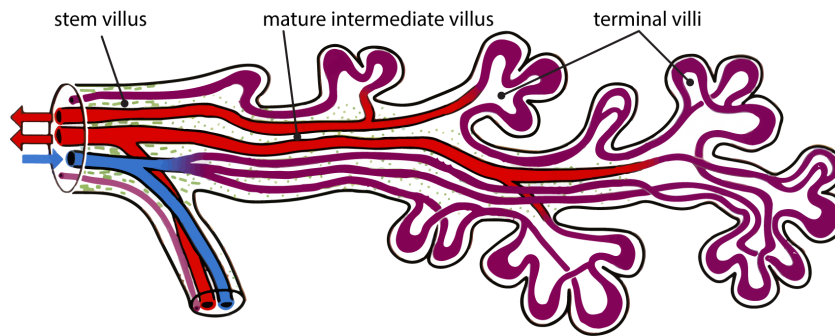


Figure 1.11. Location of fetal vessels inside a branch of a villous tree. Color code: blue — fetal arteries and arterioles (with low oxygen content), lilac — fetal villous capillaries and sinusoids (terminal dilations), red — fetal venules and veins (with high oxygen content), green — stroma of the parent mature intermediate villus. Reproduced from Benirschke et al. (2006)

however rarely observed. It normally occurs only near the periphery of the placental disk, where placentones are small, and one maternal lobule approximately corresponds to one villous tree (Benirschke et al., 2006, p. 252). Near the center of the placental disk, maternal lobules visible from the basal plate normally contain one to four overlapping villous trees (Fig. 1.7b), and the precise location of maternal vessels in these lobules is unclear.

The maternal circulation starts in the human placenta only around 10th–12th week of gestation, after the maternal spiral arteries have been invaded and remodeled by fetal trophoblasts (see Fig. 1.12 and Benirschke et al., 2006, Burton et al., 2009). The delayed onset of the maternal circulation is believed to protect the developing fetal tissues from the high velocity of the maternal blood flow and high partial pressures of oxygen. In the human placenta, the volumetric blood flow in the umbilical vein (i.e., the total fetal placental blood flow) is reported to be around 36 ml/min at 20 weeks of gestation, and around 265 ml/min at 40 weeks (Acharya et al., 2005). Per 1 kg of fetal weight these numbers give 88 ml/(min · kg) at 20 weeks and 66 ml/(min · kg) at 40 weeks. Analysis of umbilical blood samples provides the approximate arterial (0.11 ± 0.06 ml O₂/ml blood) and venous (0.21 ± 0.07 ml O₂/ml blood) oxygen content of the fetal blood at term (Acharya and Sitras, 2009). Combination of these data yield fetal oxygen uptake at term around 5.6 ± 3.2 ml O₂/(min · kg) or, equivalently, $(4.2 \pm 2.4) \cdot 10^{-6}$ mol/(s · kg) in SI units (Acharya and Sitras, 2009). At the same time, the maternal uterine blood flow at term (to the uterine and placental tissues) is reported to be 500 ± 200 ml/min (Metcalf et al., 1955). The uterine oxygen consumption was then estimated at the level of 25 ± 13 ml O₂/min or 7.5 ± 3.8 ml O₂/(min · kg) per kilogram of fetal weight. In SI units it amounts to $(19 \pm 10) \cdot 10^{-6}$ mol/s or $(5.6 \pm 2.8) \cdot 10^{-6}$ mol/(s · kg) respectively. Therefore, fetal oxygen uptake corresponds to around 75 % of the uterine oxygen consumption at term.

1.3.2 Pathological conditions

Numerous studies have reported alterations in the structure of the human placenta in pathological cases. The most typical pathologies and pathological conditions are (Benirschke et al., 2006):

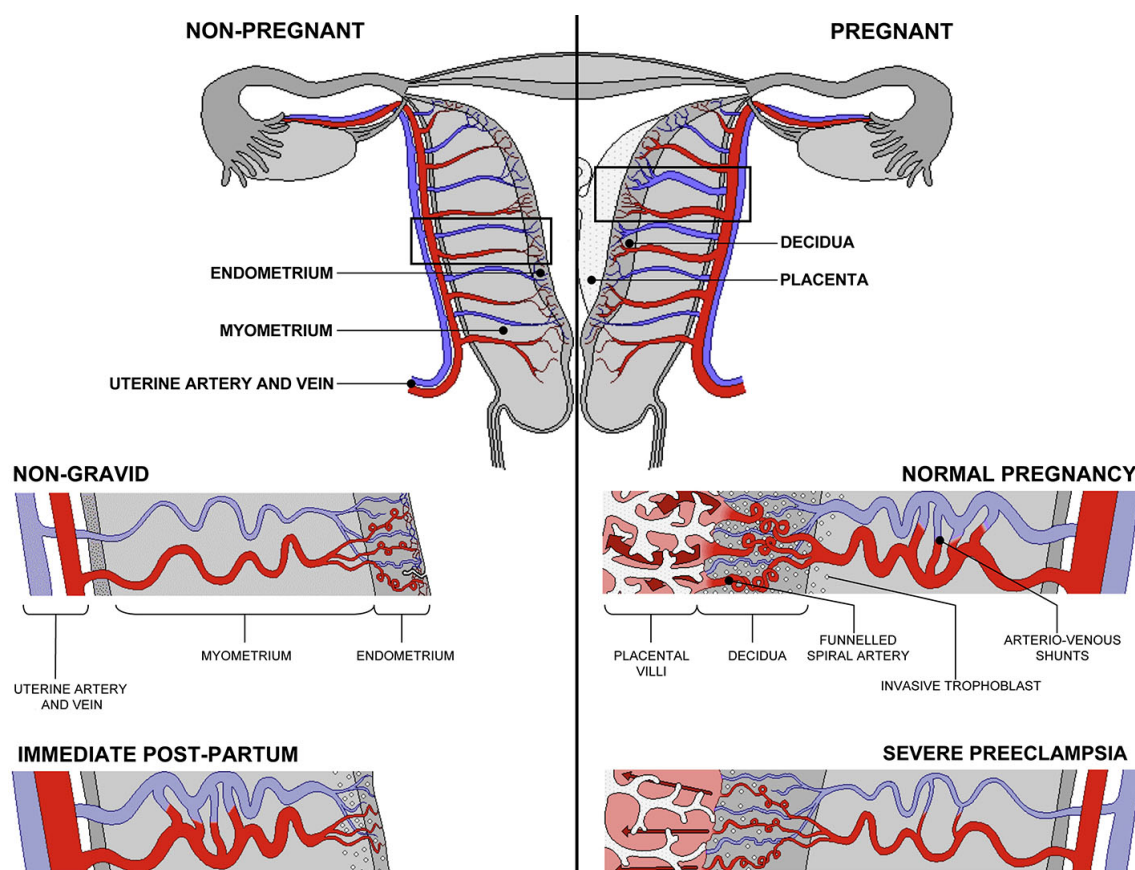


Figure 1.12. Remodeling of the maternal spiral arteries in pregnancy. Note the dilation and the funneled outlets of the spiral arteries as well as the formation of arterio-venous shunts that persist in the immediate *post-partum* period. Non-dilated spiral arteries of severe pre-eclampsia are also shown. Color code: arteries — red, veins — blue. See also Fig. 1.20. Reproduced from Burton et al. (2009)

- Diabetes mellitus: a group of diseases characterized by abnormalities of glucose metabolism.
- Pre-eclampsia, also called pregnancy-induced hypertension (PIH): a pregnancy disorder characterized by high maternal blood pressure and increased amount of protein in the urine.
- Placenta accreta, placenta increta, placenta percreta: cases of abnormally strong attachment of the placenta to the uterine myometrium (the uterine muscular level), which may cause heavy bleeding after the delivery. The three pathological conditions are distinguished by the depth of placenta invasion into the uterine wall.
- Placenta previa: an abnormality when the placenta overlies the internal cervical os of the uterus, effectively obstructing the birth canal, which may cause bleeding before the delivery.
- Placental abruption: a pregnancy complication, when the placental lining separates from the uterus before the labor.
- Umbilical cord abnormalities.
- Placental infections.

- Pathologies of placental membranes usually associated with abnormal vascularization of the chorionic plate.
- Maternal anemia: low maternal RBCs count.
- Maternal smoking, alcohol abuse or drug addiction.

To this list should be added the intra-uterine growth restriction (IUGR) and small for gestational age (SGA fetus) condition, which are symptoms which can result from numerous pathologies, rather than pathologies themselves. Typical placental structure variations reported for some of these pathologies are collected in Table 1.1. Note that it is often hard to distinguish whether these alterations are directly caused by a pathology or are rather a placental adaptation to it.

1.4 Placental functions

Placenta is a multifunctional organ combining transport, endocrine, protective and metabolic functions, each of which is briefly reviewed below. For more details, the reader is referred to the reviews by Gude et al. (2004), Desforges and Sibley (2010). Note also that there exist many interspecies differences in the placental function.

1.4.1 Placental transport function

The placental transport function much depends on the organization of the blood flow in the placenta. Since the circulation of the maternal blood in the placenta is established only at the end of the first trimester of pregnancy (Benirschke et al., 2006), the transport function in early pregnancy significantly differs from that in late pregnancy. During the first trimester, the nutrition of placental and embryonic tissues is histiotrophic with trophoblast phagocytosis of endometrial glandular secretions including glycogen and a variety of glycoproteins (Burton et al., 2002). In other words, the nutriment (proteins and carbohydrates) are absorbed by the surface of the developing embryo. After the formation of the placenta and the onset of the maternal circulation, the maternal blood comes into contact with terminal fetal villi, the nutrition becomes hemotrophic and all transport occurs across the placental membrane (which comprises the membranes and the cytoplasm of all tissue layers making it up, see Section 1.2.2).

Passive and active transport

According to energy requirements and the ability of the transported substance to diffuse through the membrane, all transmembrane transport processes are divided into passive and active transport processes (Sadava et al., 2007, pp. 105–125). *Passive transport* does not require input of chemical energy and comprises diffusion, facilitated diffusion, filtration and osmosis:

- *Diffusion* follows the concentration gradient and is possible only for those substances to which the membrane is permeable. Since the phospholipids that make up the bilayer of biological membranes have hydrophilic heads and hydrophobic fatty acid

Table 1.1. Reported alterations of the human placenta structure in some pathological cases. The up arrow denotes the increase of the area, perimeter or branching of a structural component, while the down arrow marks their decrease. The up and down arrows put together mean that variation in both directions was observed or that the direction of change was not reported

	Placenta size	Villous tissue	IVS	Exchange surface	Villous membrane thickness	Villous tree branching	Fetal capillary bed	References
Diabetes	↑	↑	↑	↑	↑	↑		Teasdale (1981, 1983, 1985a), Boyd et al. (1986), Teasdale and Jean-Jacques (1986), Jirkovská et al. (1994), Mayhew (1996), Mayhew and Burton (1997), Jirkovská et al. (2002, 2012), Jauniaux and Burton (2006), Nelson et al. (2009), Higgins et al. (2011), Dubova et al. (2011)
Well-controlled diabetes				↑			↑/↓	Mayhew et al. (1994), Mayhew and Sisley (1998), Mayhew and Jairam (2000), Maly et al. (2005)
Pre-eclampsia	↓			↓		↑	↑	Boyd and Scott (1985), Teasdale (1987), Resta et al. (2006), Rainey and Mayhew (2010)
Maternal anemia				↓	↓	↓		Mayhew and Burton (1997)
High altitude placentas		↓	↑					Lee and Mayhew (1995), Mayhew (1996), Mayhew and Burton (1997)
IUGR	↓	↓	↓	↓		↓	↓	Teasdale (1984), Teasdale and Jean-Jacques (1988), Mayhew et al. (2003, 2004b), Egbor et al. (2006), Rainey and Mayhew (2010), Almasry and Elfayomy (2012)
Smoking mothers				↓	↑/↓		↓	van der Velde et al. (1983), Mayhew (1996), Mayhew and Burton (1997)

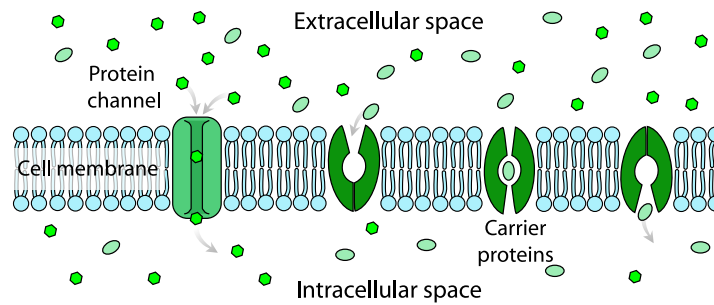


Figure 1.13. Facilitated diffusion across the cell membrane. Both ion channels and carrier proteins are shown. Image taken from the public domain

tails, only small non-polar and non-charged molecules (e.g., oxygen or carbon dioxide) can freely cross the membrane.

- *Facilitated diffusion* is a spontaneous process of transport of molecules and ions across a biological membrane via specific integral transmembrane proteins, which follows the concentration gradient. Small molecules pass through channels in transmembrane proteins (ion channels), large molecules bind to transmembrane proteins and cause conformation changes (carrier proteins, Fig. 1.13). Most of the integral transmembrane proteins are gated, i.e. they can open and close under the influence of special chemical signals. Facilitated diffusion has been observed for sodium and chloride ions, glucose, amino acids and lipids, as well as for other substances.
- *Filtration* is the process of crossing the membrane by water and solutes under the hydrostatic pressure produced by the cardiovascular system and can occur against the concentration gradient.
- *Osmosis* refers to the process of spontaneous crossing of a semi-permeable membrane by solvent molecules from the region of low solute concentration into the region of high solute concentration, which tends to equalize solute concentrations on both sides of the membrane. In particular, in osmosis solvent molecules can spontaneously cross the membrane against the solvent concentration gradient. The physical nature of osmosis lies in the repulsion of the solute by the membrane which then transfers its momentum to the solvent. This repels the solvent and diminishes the solvent flux across the membrane from the compartment where solute concentration is high (see Joos and Freeman, 1951, Kramer and Myers, 2013). Water being the main solvent in the living organisms, the term osmosis is generally used in biological sciences to describe osmotic transport of water.

Active transport describes the movement of molecules across a biological membrane, which either requires energy in the form of adenosine triphosphate (ATP) molecules (primary active transport, Fig. 1.14a) or relies on electrochemical potential difference at the membrane created by ion pumps (secondary active transport, Fig. 1.14b). Active transport is typically associated with substances that cell needs in high concentrations, such as sodium and potassium ions, glucose and amino acids.

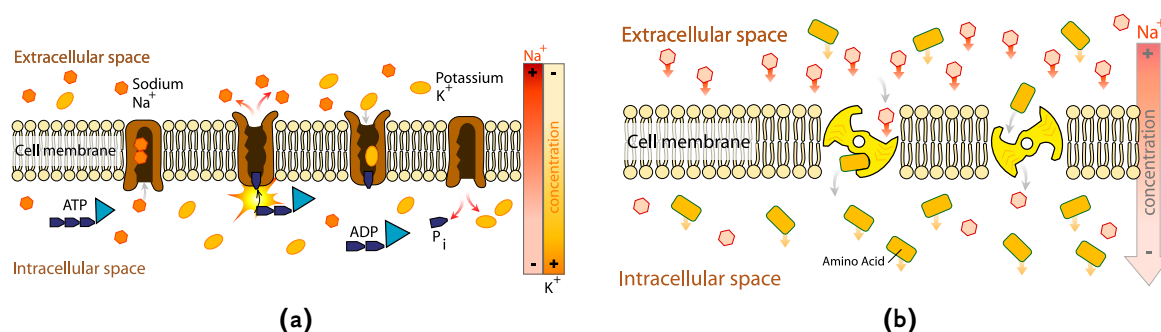


Figure 1.14. Active transport across a biological membrane. (a): Primary active transport requires an ATP molecule for moving molecules across the membrane (example of the sodium–potassium pump). (b): Secondary active transport relies on electrochemical potential difference across the membrane created by ion pumps (example of a sodium ion pump moving an amino acid against the concentration gradient). Images taken from the public domain

Transferred substances

A short review of the main substances crossing the human placenta barrier and the corresponding transport mechanisms (passive or active) is provided below:

- *Respiratory gases.* The placental membrane is highly permeable to respiratory gases (oxygen, carbon dioxide), which are transferred passively by diffusion. Due to the high membrane permeability, the transfer rate may be limited by the availability of the gases at both sides of the membrane (flow-limited) rather than by the permeability of the membrane itself (diffusion-limited, see discussion in [Faber, 1995](#)). One should also take into account that 99 % of oxygen in blood is transported bound to hemoglobin (Hb), and association-dissociation processes also contribute to the effective permeability of the placental membrane. Interestingly, in human the oxygen affinity of the fetal hemoglobin is higher than that of the maternal hemoglobin (the phenomenon also called a shift in oxygen dissociation curves), which some researchers believe to facilitate oxygen transport from the mother to the fetus and carbon dioxide transfer from the fetus to the mother ([Gude et al., 2004](#)). However, it has been argued that under the conditions of flow-limited transfer (which seem to hold for respiratory gases in the human placenta), the shift in the dissociation curves does not give a significant transport advantage (see discussion in [Faber, 1995](#)).
- *Glucose.* Glucose is the main source of energy for the growing fetus. Since little glucose is synthesized by the fetus, it is mainly transferred from the maternal circulation. Glucose transport across the placenta occurs via protein-mediated facilitated diffusion involving a number of membrane-located glucose transporters (GLUTs). Glucose molecules are first transferred across syncytiotrophoblast membranes facing the maternal circulation, then across syncytiotrophoblast basement membranes, then to fetal endothelial cells and finally to the fetal blood. The passage of syncytiotrophoblasts is believed to be the rate-limiting step for this process ([Baumann et al., 2002](#)).

- *Amino acids.* The growing fetus requires over 20 different amino acids, which are used by the fetus as building blocks for proteins or are metabolized. It was demonstrated that the concentration of many amino acids is up to 4 times higher in the fetal circulation than in the maternal indicating active transport (Yudilevich and Sweiry, 1985). Multiple amino acid transporters can be classified into two large families of heterodimeric and monodimeric transporters (Gude et al., 2004).
- *Lipids.* Lipids (including free fatty acids, triacylglycerols, phospholipids, glycolipids, sphingolipids, cholesterol, cholesterol esters and fat-soluble vitamins) can be transported across the placental membrane by both passive and active transport. In the maternal plasma, most of the lipids are transported bound to proteins, from which they should be released before crossing the membrane. For instance, fatty acids are bound to serum albumin in the maternal blood, but at the maternal surface of the placenta they are released from the complexes by lipoprotein lipase. Free fatty acids, being lipophilic, can then passively diffuse through the syncytiotrophoblast membranes. Alternatively, they can cross it by binding to membrane-located cytosolic fatty acid binding proteins, which allow for regulation of the net flux of fatty acids (Haggarty, 2002). Once in the trophoblast cytoplasm, the free fatty acids can bind to cytosolic binding proteins, be transported out of the trophoblast, or be oxidized or esterified (Gude et al., 2004).
- *Water.* Water is believed to passively cross the placenta by filtration and osmosis, with the transfer rate defined by the hydrostatic and osmotic pressures (Stulc, 1997). However, water transfer may be facilitated by water-channel-forming integral protein expressed in the trophoblasts (Stulc, 1997).
- *Inorganic ions, minerals and vitamins.* Most of these substances are actively transported across the placental membrane (Shennan and Boyd, 1987, Sibley et al., 2002, Gude et al., 2004), although passive transport has been reported, for instance, for sodium and chloride at least in some species (Stulc, 1997).

Note finally that the placenta should not be considered as a simple conduit for the exchanging substances: it also consumes oxygen, nutriment and excretes metabolic waste products.

1.4.2 Endocrine function

The placenta secretes endocrine, paracrine and autocrine factors which may be released both into the maternal and fetal circulations. The main of them are progesterone, estrogens, human chorionic gonadotrophin, human placental lactogen, placental growth hormone, chorionic thyrotropin, chorionic corticotropin, cytokines, chemokines, eicosanoids, autacoids and acetylcholine. More details on synthesis and function of these hormones can be found in Appendix A.

1.4.3 Protective function

Although some xenobiotics can be transferred by some of the placental transport mechanisms, the placenta disposes of several protective mechanisms which diminish fetal exposure to dangerous substances. On one hand, special export pumps can be found in the maternal-blood-facing membrane of the fetal trophoblasts, which include multidrug resistance protein 1, several members of the multidrug resistance-associated protein family, placenta-specific ATP-binding cassette proteins, breast cancer resistance protein and mitoxantrone resistance-associated protein (Marin et al., 2003, Gude et al., 2004). On the other hand, the placenta contains a number of cytochrome P450 and other phase I and phase II enzymes that can metabolize xenobiotics (Pasanen, 1999). However, there are many substances (such as alcohol, thalidomide, many anticonvulsants, lithium, warfarin and isotretinoin) that can still cross the placenta and have adverse effects on the fetus (Gude et al., 2004). The placenta also lets maternal immunoglobulin G class antibodies cross the placental barrier, which provides the baby with passive immunity (Gude et al., 2004).

Interestingly, no generally accepted answer has yet been found to the question of why the placenta and the baby are not rejected by the immune system of the mother (Moffett and Loke, 2004). It is however clear that separation of the maternal and fetal circulations considerably simplifies this function since the maternal immune cells are mainly in contact with only fetal trophoblast cells, which allows these cells to develop special strategies to evade maternal immune attack (including expression of non-typical antigens and complement regulatory proteins, see Bulla et al., 2003).

1.4.4 Concluding remarks

One can see that the sophisticated internal structure of the human placenta is related to its complex function. For instance, the combination of the protective and transport functions requires separation of the fetal and maternal circulations and at the same time a capacity for a high exchange rate. This naturally leads to a large exchange surface, which is organized in a form of a tree (like in the lungs). Thus, our understanding of physiological processes taking place in the placenta may be incomplete as long as we do not account for the role of the geometrical structure of the organ.

1.5 Experimental methods of placental studies

Modern technologies provide numerous ways to study the placenta. However, few measurements are ethical in the human placenta, to the extent that even oxygen content in the umbilical arteries and vein (which is a general and imprecise characteristic of the placental oxygen transport function) is rarely available. Moreover, the internal placental structure has as yet been only obtained after birth, but even for a delivered human placenta no high-resolution 3D structure is available. In what follows, we summarize experimental techniques and experimental data they can provide on the placentas of different species, which were obtained in special setups or can be gathered on a regular basis:

1. Macroscopic measurements, such as placenta weight, placenta-to-fetus weight ratio, placental diameter and thickness can be obtained after birth (see for example [Salafia et al., 2005, 2012](#), [Misra et al., 2012](#)). These measurements, however, do not provide complete information on the placental functions.
2. Histological placental sections can be obtained after birth and be microscopically analyzed to diagnose pathologies. Histomorphometrical measurements can also be manually performed on these sections (see [Aherne and Dunnill, 1966](#), [Laga et al., 1972, 1973](#), [Teasdale, 1978, 1980, 1981, 1982, 1983, 1984, 1985a,b, 1987](#), [Teasdale and Jean-Jacques, 1985, 1986, 1988](#), [Sen et al., 1979](#), [van der Velde et al., 1983](#), [Boyd, 1984](#), [Boyd and Scott, 1985](#), [Boyd et al., 1986](#), [Jackson et al., 1987a,b](#), [Barker et al., 1988](#), [Karimu and Burton, 1993](#), [Mayhew et al., 1993b, 1994, 2003, 2004a,b](#), [Mayhew, 2002, 2006a,b, 2008, 2009](#), [Mayhew and Wadrop, 1994](#), [Mayhew, 1996](#), [Mayhew and Burton, 1997](#), [Mayhew and Sisley, 1998](#), [Mayhew and Jairam, 2000](#), [Jirkovská et al., 1994](#), [Lee and Mayhew, 1995](#), [Maly et al., 2005](#), [Egbor et al., 2006](#), [Huppertz et al., 2006](#), [Jauniaux and Burton, 2006](#), [Nelson et al., 2009](#), [Rainey and Mayhew, 2010](#), [Dubova et al., 2011](#), [Higgins et al., 2011](#), [Samson et al., 2011](#), [Almasry and Elfayomy, 2012](#), and references therein). Typical values of the measured histological characteristics are collected in Table 1.2. These studies have convincingly demonstrated that the placental structure plays an important role in the organ's function. Figure 1.15 illustrates the basic idea: a typical sample taken from a healthy placenta (Fig. 1.15b) contains intervillous space (IVS) and villous tree sections in "healthy" proportions (which allow efficient function), whereas pre-eclamptic (Fig. 1.15a, disproportionally large IVS, rare villi) and diabetic (Fig. 1.15c, denser and larger villi) cases exhibit very different geometries.

Theoretically, a stack of serial 2D placental cross-sections could be taken with a small step from the same region of a placenta, and these sections could then be reconstructed in 3D to provide the 3D arrangement of the villi. Although such reconstruction has been performed on a scale of a single or several villi with the confocal laser scanning microscopy (see Fig. 1.16 and [Jirkovská et al., 2012](#)), to the best of our knowledge, no studies have reported performing this operation on a large scale, using histological placental cross-sections.

Note however that the placental morphometry obtained after birth may not exactly represent the situation *in vivo* because of the detachment of the placenta from the uterine wall, cease of maternal blood circulation, mechanical stress of the vaginal delivery and fixation procedures ([Bouw et al., 1976](#), [Sisson, 1978](#), [Kaufmann, 1985a](#), [Illsley et al., 1985](#), [Burton et al., 1987](#), [Burton and Palmer, 1988](#), [Mayhew and Burton, 1988](#), [Mayhew et al., 1993b](#), [Luckhardt et al., 1996](#), [Mayhew, 2008](#)). These problems are reviewed in more details in Appendix D on p. 150. For these reasons, the placental histology cannot provide complete information on the organ functions, although it can yield valuable indications.

3. Placental corrosion casts can be prepared ([Leiser et al., 1997](#), [Leiser and Kohler,](#)

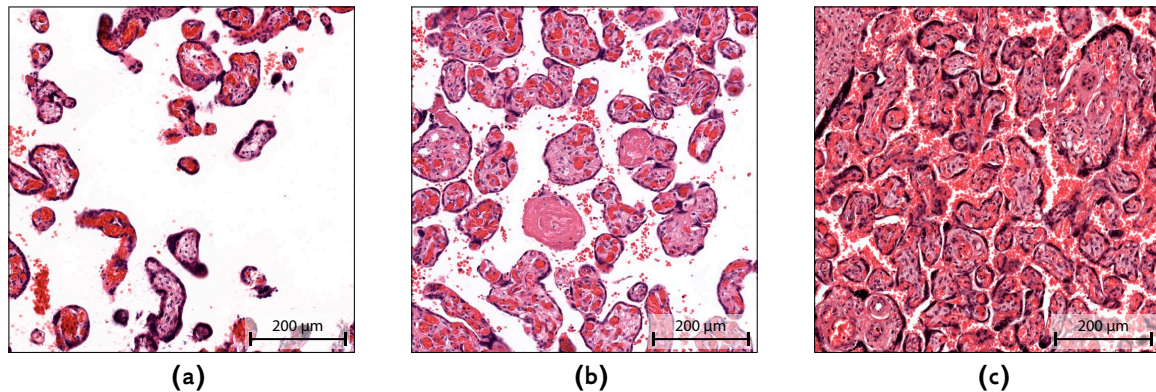


Figure 1.15. Typical microphotographs of the human placenta: (a) pre-eclamptic placenta (rarefied villi, reduced exchange surface); (b) healthy placenta; (c) diabetic placenta (dense villi, reduced surface accessibility). White space is the intervillous space (IVS), normally filled with the maternal blood, which has been washed away during the preparation of the slides (some residual red blood cells are still present). The dark shapes are cross-sections of fetal villi. The lighter regions inside them correspond to fetal capillaries, and the darker regions at their boundaries are the syncytiotrophoblast boundary layer. The sections are H&E stained and have been taken in the direction from the basal to the chorionic plate (see Fig. 1.7a). For more details on the components of placental cross-sections refer to Fig. 4.2 on p. 109

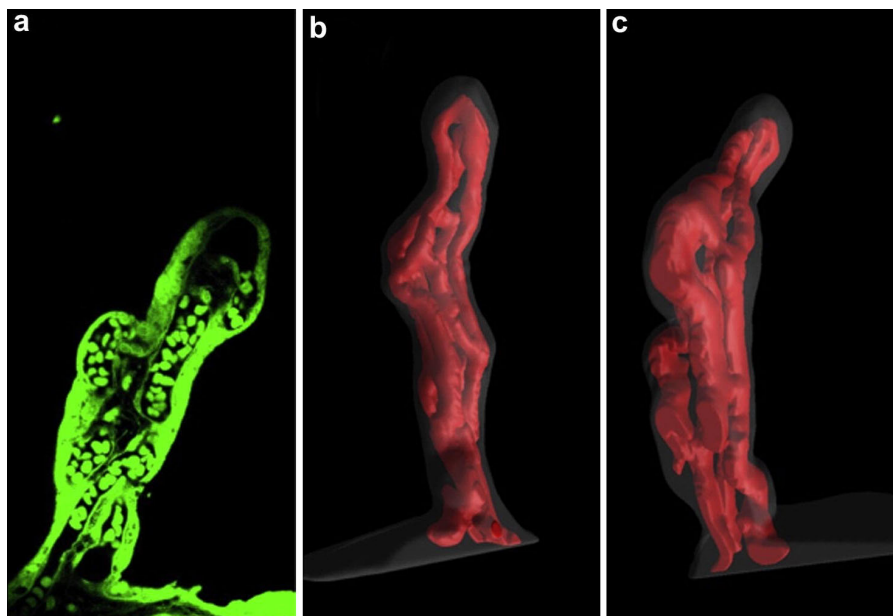


Figure 1.16. Three dimensional reconstructions (b, c) of the villous capillary bed in a healthy human placenta based on a set of confocal laser scanning microscopy images like the one shown in (a). The images (b) and (c) are two different views of the same reconstructed 3D structure (a) taken at different angles. Reproduced from Jirkovská et al. (2012)

Table 1.2. Quantitative data for the human placenta at term obtained by histological measurements. The values were rounded up according to the uncertainties of the measurements. The minus sign marks the data that were not available. Notations: *a* — calculated from the placental weight under the assumption that the placenta density is 1.05 g/cm^3 (see Nelson et al., 2009); *b* — calculated under the assumption that small villi (terminal and mature intermediate) represent 66.5 % of the total villi volume (see Sen et al., 1979); *c* — calculated under the assumption that small villi (terminal and mature intermediate) represent 77.3 % of the total villi surface (see Sen et al., 1979). Small villi density and the effective villi radius are discussed in Section 3.1.4 on p. 93. Note that the used raw data of Mayhew et al. (1993a) are actually reported in Lee and Mayhew (1995). Only 10 placentas at 40 weeks of gestation are taken for calculations from the 21 placentas studied by Aherne and Dunnill (1966)

	Mayhew and Jairam (2000)	Nelson et al. (2009)	Aherne and Dunnill (1966)	Lee and Mayhew (1995)	Mayhew et al. (1993a)	Laga et al. (1973)
Number of placentas in the study	8	39	10	24	34	18
Feto-placental weight ratio	-	5.70 ± 0.15	-	-	7.0 ± 0.3	7.3 ± 0.4
Corrections for changes during fixation (Yes/No)	Y	N	Y	Y	Y	N
Placenta volume, cm^3	420 ± 40	610 ± 20^a	488	430 ± 20	475 ± 15^a	450 ± 20
IVS volume (V_{IVS}), cm^3	170 ± 25	220 ± 65	170	177 ± 12	170	110 ± 7
Villi volume ($V_{\text{sm.v}}$), cm^3	200 ± 20	325^b	285	158 ± 11	230	204 ± 10
Small villi volume, cm^3	130^b	220 ± 70	190^b	110 ± 7^b	150^b	160 ± 8
Total capillary volume, cm^3	-	-	-	-	-	30 ± 4
Capillary volume in small villi, cm^3	-	24 ± 16	-	-	-	28.6 ± 3.5
Trophoblast volume, cm^3	-	50 ± 20	-	-	-	54.8 ± 2.8
Arithmetic mean trophoblast thickness, μm	-	9.3 ± 1.2	-	-	-	-
Harmonic mean trophoblast thickness, μm	-	-	-	-	-	10
Total villi surface area, m^2	8.5 ± 0.8	18.1^c	11	6.8	9	16.7 ± 0.5
Small villi surface area ($A_{\text{sm.v}}$), m^2	7^c	11 ± 7	9^c	5^c	7^c	16.1 ± 0.5
Total capillary surface area, m^2	-	-	-	-	-	12.4 ± 1.3
Capillary surface area in small villi, m^2	-	14 ± 9	-	-	-	12.0 ± 1.3
Small villi density ($\phi = V_{\text{sm.v}} / (V_{\text{sm.v}} + V_{\text{IVS}})$)	0.43	0.50	0.53	0.38	0.47	0.59
Surface-to-volume ratio for small villi ($\epsilon_{\text{sm.v}} = A_{\text{sm.v}} / V_{\text{sm.v}}$), mm^{-1}	54	50	47	45	47	101
Effective villi radius ($r_e = 2V_{\text{sm.v}} / A_{\text{sm.v}}$), μm	37	40	43	44	42	20
Index of small villi surface elaboration ($A_{\text{sm.v}} / V_{\text{sm.v}}^{2/3}$)	2700	3000	2700	2200	2500	5500

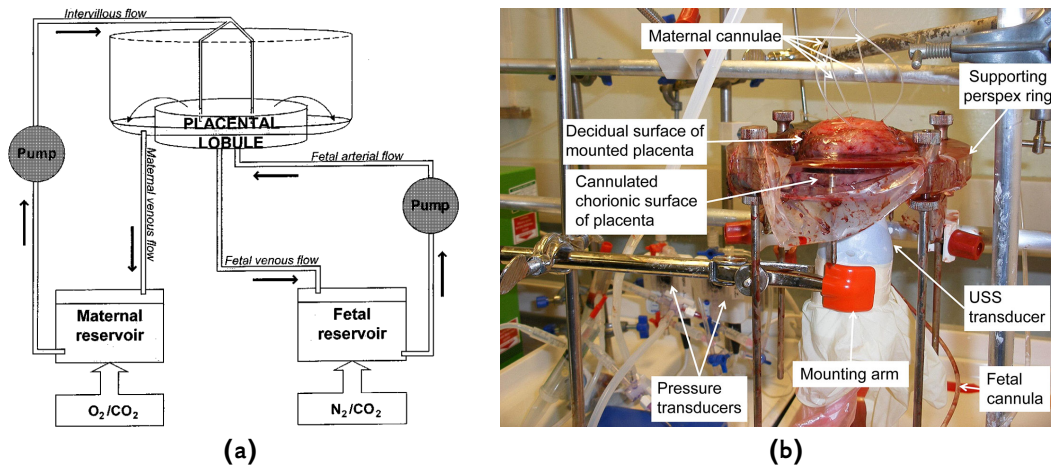


Figure 1.17. Artificial perfusion of the human placenta *in vitro*. A simplified scheme (a) and a photo of the experimental setup (b) are reproduced from Ala-Kokko et al. (2000) and Jones et al. (2009) respectively

1983, 1984, Gordon et al., 2007a, Detmar et al., 2008, Hafez et al., 2010, Rennie et al., 2012) providing several first generations of the fetal villous tree branches, which can then be analyzed, in particular by means of the scanning electron microscopy (see Fig. 1.10 and Herbst and Multier-Lajous, 1972, Kaufmann et al., 1979, Burton, 1987, Pfarrer et al., 1999, 2001, Konje et al., 2003, Detmar et al., 2008, Hafez et al., 2010, Rennie et al., 2012).

4. Confocal laser scanning microscopy with 3-D reconstruction can be used to qualitatively and quantitatively compare the terminal villi structure in healthy and pathological placentas (see Fig. 1.16 and Jirkovská et al., 2002, 2007, 2008, 2012, Resta et al., 2006, Jirkovská, 2013, and references therein).
5. The placenta can be artificially perfused after birth to imitate the *in vivo* placental blood flow and exchange characteristics (see Fig. 1.17 and Longo and Bartels, 1972, Longo et al., 1973, Jones et al., 2009, Schneider, 2009). Although this manipulation method is allowed by ethical norms and can provide the time course of the analyzed processes, it has several disadvantages (Ala-Kokko et al., 2000):
 - Not all the placentas or placentones can be artificially perfused since the artificial perfusion is possible only if the placental membrane is intact and there is no leakage between the circulations. However, macroscopic placental tissue injuries (including membrane ruptures) are common during the vaginal delivery.
 - A unique perfusion protocol is not yet established, which does not allow to compare the results of different studies.
 - The degree to which the recreated feto-maternal circulation reproduces the *in vivo* situation is as yet unknown.
 - In artificial perfusion experiments, the placental tissue is viable for 14 hours at maximum, which does not allow one to use long perfusion times or to reproduce the experiment later.

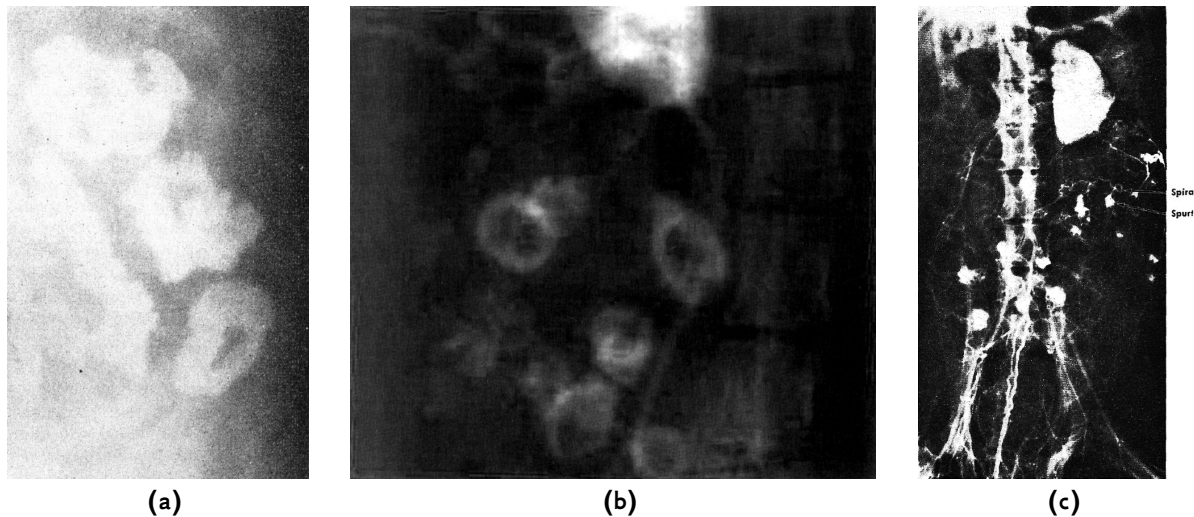


Figure 1.18. X-ray images of a radiopaque dye diffusion in the intervillous space of the human (a) and monkey placentas (b, c). (a), (b): The observed doughnut shape of the dye clouds is explained by the radial diffusion of the dye from a spiral artery orifice at the center of a placentone to decidual veins at its periphery. (c): White clouds in the middle portion of the image (marked as *Spurt*) are also the entry sites of the maternal blood in the intervillous space (the absence of the doughnut cloud shape is probably due to the low resolution of the image). Spiral arteries (marked *Spiral*) leading to these entry sites can also be seen. Images reproduced from Burchell (1967) (a), Freese (1968) (b), and Ramsey (1962) (c)

6. Partial pressures of oxygen, carbon dioxide and concentrations of other solutes, as well as volumetric blood flows in the uterine and umbilical arteries and veins can be obtained in multiple species in both *in vivo* and *in vitro* preparations (see Faber, 1977, 1995, and references therein).
7. X-Ray photographs of the *in vivo* placenta perfusion by the maternal blood were obtained with a contrast dye in normal and pathological human pregnancies (see Fig. 1.18 and Burchell, 1967). The obtained data not only provided evidence for the existence of a central cavity, but also allowed one to estimate a characteristic size of a placentone, the transit time of blood through the IVS, and a characteristic velocity of the maternal blood flow (see also the discussion of the maternal blood velocity on p. 75). Radiographic images of the *in vivo* placenta perfusion in primates and human were also obtained by Ramsey (1962), Ramsey et al. (1963), Freese et al. (1966), Freese (1968, 1972). However, X-ray-involving techniques are currently unethical and are used in humans only in serious pathological conditions.
8. Standard ultrasound techniques can give the placental size, shape and volume *in utero* (Fig. 1.19). Typical values of the linear maternal blood velocity and pulsatility indices in the umbilical and uterine arteries and veins can also be obtained (see Fig. 1.20 and Jauniaux et al., 1995). Such measurements can be used for diagnosis of pre-eclampsia at the early stages of pregnancy (Poon and Nicolaides, 2014). However, the sensitivity threshold of these techniques to linear flow velocities is around 0.1 cm/s, which is insufficient to measure the linear blood velocity expected in the IVS (around 0.05 cm/s on the average, see discussion of the maternal blood velocity on p. 75). Thus, these techniques cannot be currently efficiently used either in the dense exchange region, or in central cavities. Note that the use of

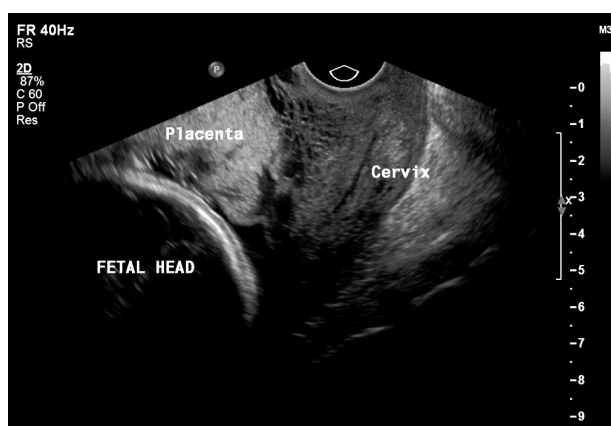


Figure 1.19. Ultrasound techniques used for diagnosis of placenta increta: note the invasion of the cervix by the placental tissue (a sponge-like zone in the upper central part of the image). See also the discussion of placental pathologies in Section 1.3.2. Reproduced from Abramowicz and Sheiner (2007)

potentially safe contrast agents (e.g., microbubbles of inert gas) may enhance their resolution (Ragavendra and Tarantal, 2001).

9. 3D color/power Doppler angiography can provide a low-resolution villous tree structure and patterns of blood flow in the vicinity of central cavities of the human placenta at different stages of pregnancy (see Fig. 1.21 and Konje et al., 2003). It can also be used for reproducible quantification of placental and myometrial vascularization, in particular for diagnosis of the pre-eclampsia and intra-uterine growth restriction (Morel et al., 2010, 2011, Hafner et al., 2013). Note that *color* Doppler sonograms show linear blood velocity and its direction (to or from the sensor), while the *power* Doppler signal is proportional to the sum of velocities of all scatterers in a region (with a resolution up to 0.1 cm/s) and is independent of the angle of insonation (Dymling et al., 1991). Based on the power Doppler method, 2D and 3D *fractional moving blood volume* techniques were developed to assess the fraction of moving blood in the placenta (Rubin et al., 1995, Stevenson et al., 2015).
10. Ultrafast ultrasound techniques are likely to allow high-sensitivity mapping of blood flows simultaneously in the whole placenta in analogy to brain studies (see Fig. 1.22 and Dmené et al., 2014). It may even be possible to discriminate between fetal and maternal blood by analyzing the pulsatility index.
11. T_1 - and T_2 -weighted contrast MRI techniques can be used to determine the placenta location *in vivo* and the main blood circulation regions inside it (see Figs 1.23a,b and Yeh, 2006, Linduska et al., 2009, Nguyen et al., 2012, Masselli and Gualdi, 2013). Greater precision could be gained by the use of contrast agents, which allow for visualization of the placental perfusion in animal models (Salomon et al., 2005), but they have not yet been proved safe in humans. Alternatively, diffusion of water molecules in the placenta can be observed with diffusion-weighted MRI (see Figs 1.23b,c and Bonel et al., 2010, Manganaro et al., 2010). The obtained data can be further analyzed with the help of Intra-Voxel Incoherent Motion (IVIM) models, which are able to provide estimates of the placental blood volume and can thus be used as a tool to diagnose pre-eclampsia (see Fig. 1.23d

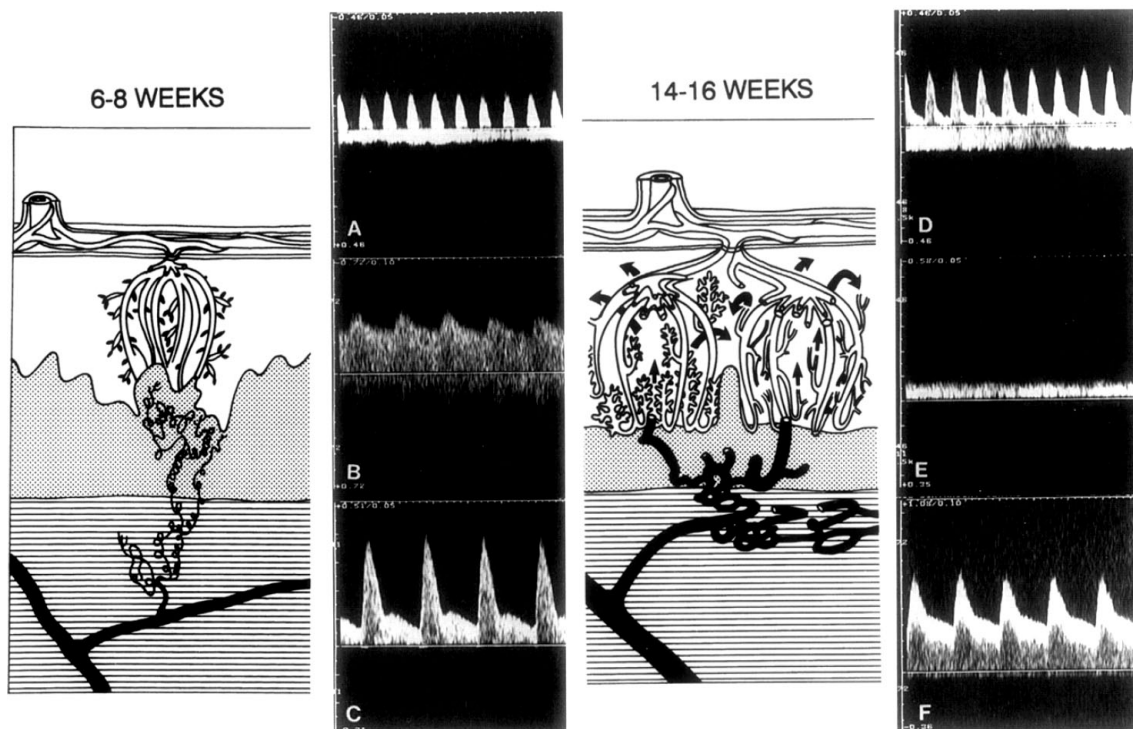


Figure 1.20. Ultrasound techniques demonstrating the change in pulsatility patterns caused by the trophoblast remodeling of the spiral arteries and the onset of the maternal intervillous circulation: before (on the left) and after (on the right). The ultrasound measurement were made in: A, D — the umbilical cord, C, F — the main uterine artery, B — the spiral artery, E — the intervillous space. The horizontal and vertical axes in all plots correspond to time and linear blood velocity respectively. Although not all the pulsatility figures have the same scale, note the change in the shape of flow velocity waveforms. See also discussion in Section 1.3.1 and Fig. 1.12. Reproduced from Jauniaux et al. (1995)

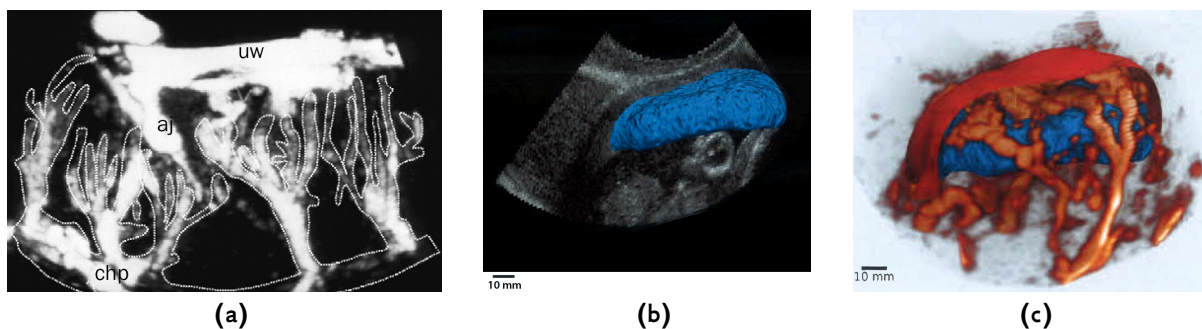


Figure 1.21. (a): 3-D power Doppler scan of a placentone of a healthy human placenta at 38 weeks of pregnancy. In the figure: the chorionic plate and the villous tree (chp, outlined in white), the uterine wall (uw) and jets of maternal arterial blood entering the IVS (aj). Reproduced from Konje et al. (2003). (b): 3D segmentation of the placental volume based on 3D B-mode (brightness mode) ultrasonographic pictures. (c): 3D rendering of the moving blood volume obtained with 3D Power Doppler ultrasound (orange) plotted over the segmented placental volume of (b). The fraction of moving blood volume is then estimated as the ratio of the volumes of the orange and blue components. The uteroplacental interface is shown in red. Both pictures reproduced from Stevenson et al. (2015)

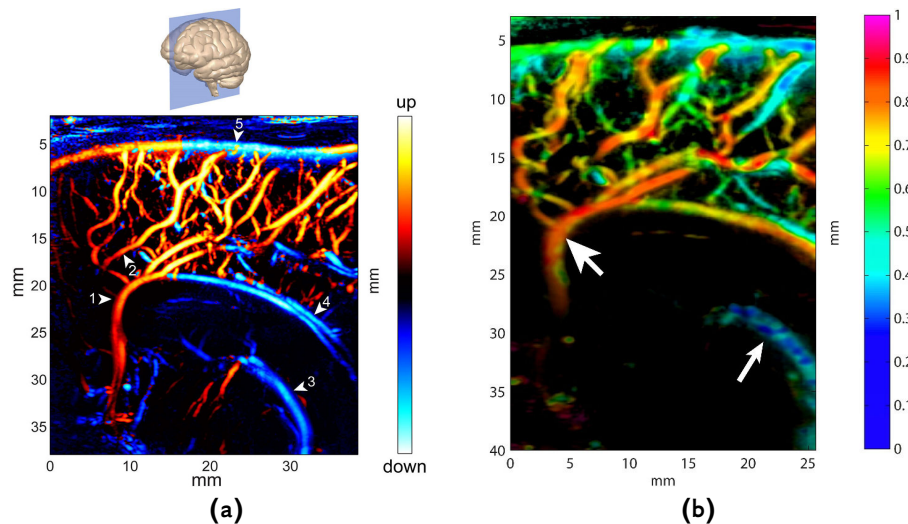


Figure 1.22. Ultrafast ultrasound studies of the brain. (a): A directional ultrafast Power Doppler sonogram showing the direction of the blood flow in the neonate brain and the plane in which the sonogram has been taken. (b): A map of resistivity of brain vessels (the definition of resistivity is based on cyclic variations of the velocity of the blood flow), which allows one to distinguish arteries from veins. It is demonstrated that arteries normally have a resistivity index between 0.75 and 0.9 (red and orange, the large-head arrow), while the resistivity index of veins is below 0.45 (blue, the small-head arrow). Note that clear discrimination between the arteries and veins is achieved even when they lie close to or overlay each other. Reproduced from [Demené et al. \(2014\)](#)

and [Alison et al., 2013](#), [Moore et al., 2000a,b](#)). Alternatively, an Arterial Spin Labeling (APL) method can be used to study placental micro-flow patterns (see [Fig. 1.24a](#) and [Avni et al., 2012](#)), while oxygen-enhanced MRI and blood-oxygen-level-dependent MRI (BOLD MRI) techniques allow one to estimate placental blood oxygenation *in vivo* (see [Figs 1.24b,c](#) and [Huen et al., 2013](#), [Sørensen et al., 2013a,b](#)). Additionally, high resolution *ex vivo* MRI angiography is able to provide the 3D structure of the human placenta up to the 6th generation of villous trees branches (see [Fig. 1.25](#) and [Rasmussen et al., 2010](#)). The same method was used to demonstrate a positive correlation between the volume of the fetal placental blood vessels and the size of the fetus ([Rasmussen et al., 2014](#)). However, a general analysis of the sensitivity of MRI techniques shows that the spatial resolution of MRI methods of about 1 mm is enough to provide the main vessel structure of the placenta, but would not resolve the villi architecture in dense exchange regions (where villi have a characteristic size of 50–500 μm , see [Section 1.3.1](#)).

12. Micro-CT techniques can be used to obtain 3D spatial organization of placental fetal arteries and veins, as demonstrated on small rodents placentas (see [Figs 1.26a,b](#) and [Rennie et al., 2007, 2012](#)) and in humans (see [Fig. 1.26c](#) [Langheinrich et al., 2004, 2008](#)).

The provided summary shows that although there exist multiple techniques for experimental placental studies, at the moment, none of them can provide a high-resolution 3D structure of the organ. In the absence of the fully resolved 3D placental structure, studies of structure–function correlation in the placenta have to rely on high resolution (but only 2D) histological placental cross-sections.

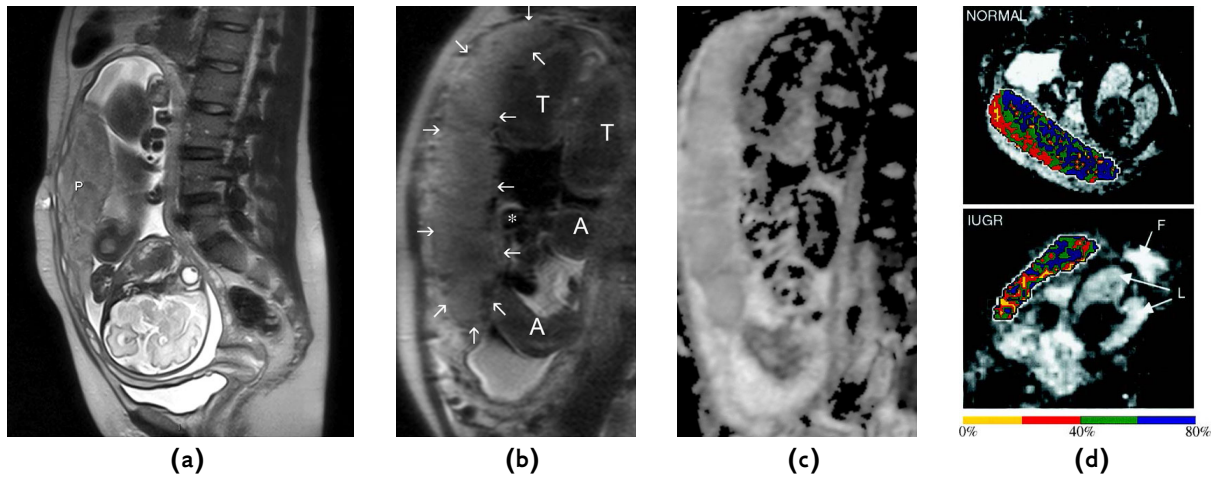


Figure 1.23. (a): The human fetus and its placenta (P) *in utero* as seen at 24 weeks with T_2 -weighted contrast MRI (reproduced from Masselli and Gualdi, 2013). (b), (c): T_2 -weighted MRI of a placenta (b) and the corresponding apparent diffusion coefficient (ADC) map (c) obtained by diffusion-weighted MRI in a normal placenta at 33 weeks of gestation (reproduced from Bonel et al., 2010). The outline of the placenta is marked by the white arrows. Fetal thighs (T) and arms (A) can also be seen. (d): Perfusion fraction maps of the placenta in a normal and an IUGR-complicated pregnancy obtained with intra-voxel incoherent motion models (IVIM, reproduced from Moore et al., 2000b). Two separated zones of blood movement are clearly visible in the normal pregnancy, but are less distinct in the IUGR case. The locations of the fetal lungs (L) and the amniotic fluid (F) are marked

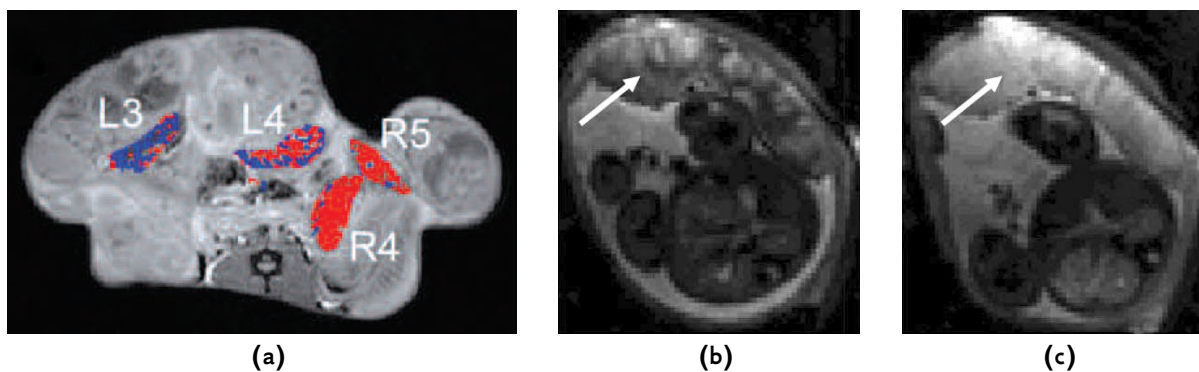


Figure 1.24. (a): Arterial spin labeling used to demonstrate the maternal blood circulation in four mouse placentas (L3, L4, R4, R5, shown in red and blue) of the same litter (reproduced from Avni et al., 2012). (b): BOLD MRI used to visualize placental oxygenation *in vivo* under normal conditions (reproduced from Sørensen et al., 2013a). The placenta is marked by the white arrow. (c): Same measurements performed on the same placenta, but under hyperoxic conditions (higher oxygen content of the air inhaled by the mother). Increase of brightness corresponding to a higher intraplacental oxygen level can be seen

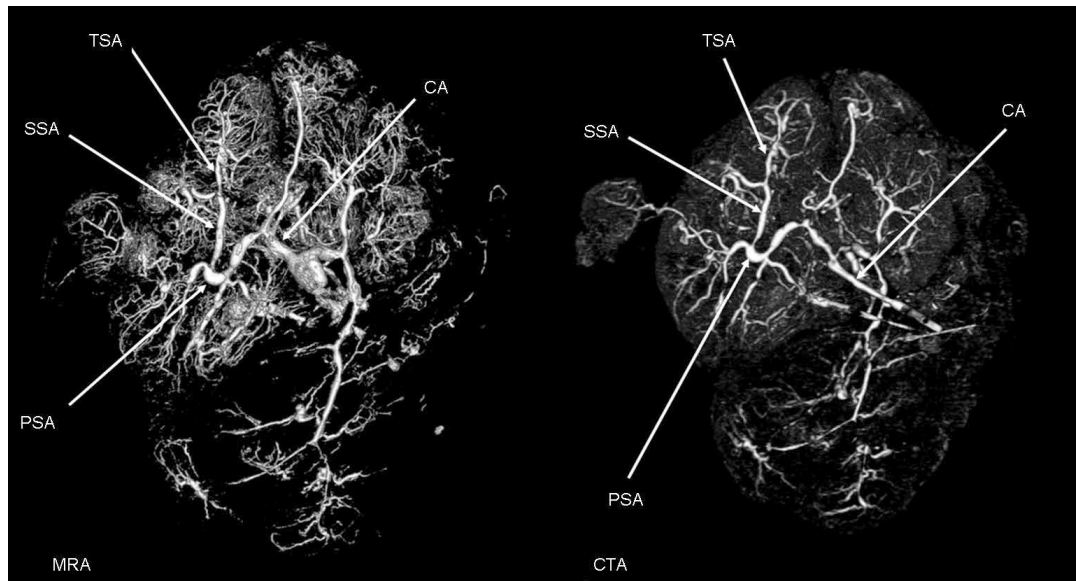


Figure 1.25. Comparison of reconstructions of the fetal placental vascular system based on magnetic resonance angiography (MRA) and computed tomography angiography (CTA) of the same human placenta. As can be seen, MRA is capable to distinguish much more small vessels than CTA. Key: CA, chorionic artery; PSA, primary stem artery; SSA, secondary stem artery; TSA, tertiary stem artery. Reproduced from Rasmussen et al. (2010)

1.6 Review of theoretical models of placental transport

1.6.1 Overview of placenta modeling

Besides the absence of the high-resolution 3D placental structure, assessing the relation between the placental structure and function is also problematic because it is unethical to manipulate the human placenta *in vivo*, and histological and physiological features commonly co-vary (e.g. changes in villi distribution alter the maternal blood flow). Mathematical modeling and numerical simulations are in this case valuable tools to gain deeper insights into the placental function *in vivo*.

Since the placenta is a multifunctional organ combining transport, endocrine, protective and metabolic functions, mathematical models of the placenta encompass numerous directions, including:

- Placental development and placental shape (Rejniak et al., 2004, Yampolsky et al., 2008, 2009, Cotter et al., 2014, Xia and Salafia, 2014).
- Villous tree structure, fetal placental circulation and umbilical cord circulation (Morrison et al., 1970, Thompson and Trudinger, 1990, Guettouche et al., 1992, Todros et al., 1992, Guiot et al., 1992, Surat and Adamson, 1996, Ménigault et al., 1998, Kleiner-Assaf et al., 1999, Myers and Capper, 2002, Franke et al., 2003, Rejniak et al., 2004, Sebire et al., 2004, Talbert and Sebire, 2004, Gordon et al., 2007b,c, van den Wijngaard et al., 2007, Alastruey et al., 2009, Kaplan et al., 2010).
- Maternal blood flow and respiratory gas exchange (Faber, 1969, Erian et al., 1977, Chernyavsky et al., 2010, Gill et al., 2011).

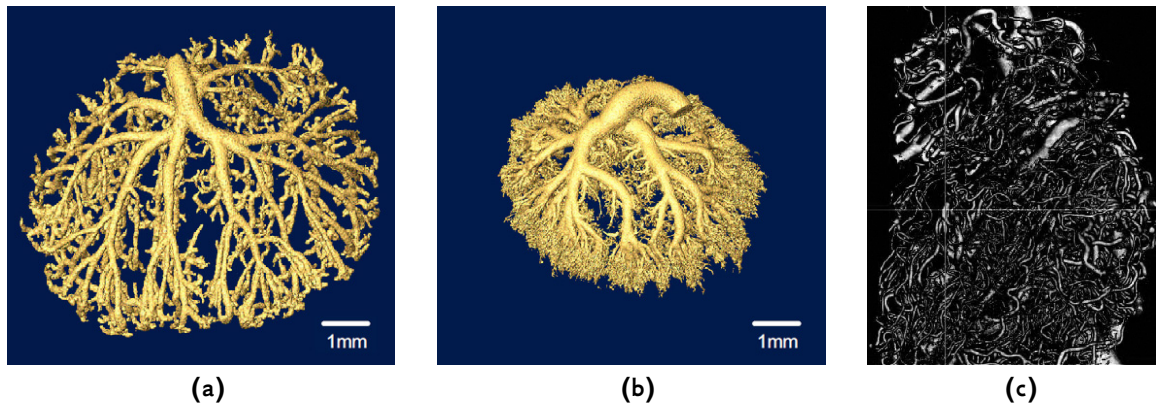


Figure 1.26. (a), (b): Micro-CT images of the arteries (a) and veins (b) of the same fetal villous tree in mouse at 18.5 weeks of pregnancy (same scale, reproduced from Rennie et al., 2007). (c): Micro-CT photograph of the fetal villous tree in human (reproduced from Langheinrich et al., 2004)

- Spiral arteries flow (Sengupta et al., 1997, Burton et al., 2009).
- Mechanical properties of the placenta (Moorcroft et al., 2003).
- Amino acid exchange (Sengers et al., 2010, Lewis et al., 2013, Panitchob et al., 2014).
- Glucose exchange (Barta and Drugan, 2010).
- Water exchange (Wilbur et al., 1978, Faber and Anderson, 1990, Sebire et al., 2004, Talbert and Sebire, 2004).
- Signaling pathways and placental biochemistry (Thoumsin et al., 1978, Mac Gabhann and Popel, 2004).
- Risks of placental infections (Bakardjiev et al., 2006, Walker et al., 2014).

1.6.2 Respiratory gas exchange models

In what follows, the models of respiratory gas exchange in the placenta will be reviewed in greater details. This choice is explained not only by the fact that adverse effects of compromised respiratory gas exchange are the fastest to be observed in the fetus, but also by the special focus of this kind of models on the geometry of the placenta as an exchanger. Indeed, the capacity of the placenta to supply about $16 \text{ cm}^3/\text{min}$ of oxygen at term to the fetus and placental tissues (Mayhew et al., 1984) significantly relies on the efficiency of its geometrical structure. Such mathematical models may yield insights comparable to those obtained for the gas exchange in the lung model of Roughton and Forster (1957) or the concept of diffusional screening discovered by Sapoval et al. (2002), Felici et al. (2005). Combined with experimental techniques, such models may provide powerful tools for diagnostics of newborn health risks.

A specific feature of respiratory gas exchange is oxygen binding to hemoglobin. The relation between oxygen partial pressure and concentration in blood can be used in its experimental non-linear form (Reneau et al., 1974), in a linearized form (Opitz and

Thews, 1952, Bartels and Moll, 1964, Faber and Hart, 1966, Heilmann et al., 1979, Costa et al., 1992) or disregarded (Chernyavsky et al., 2010). Although some of the results obtained in respiratory gas exchange models can be directly applied to the transfer of other substances, accounting for substance-specific transport mechanisms is required in many cases (see Section 1.4.1).

Mathematical models of respiratory gas exchange across the placenta have been proposed for more than six decades. These models mainly consider the exchange of oxygen, carbon dioxide (Longo et al., 1972b, Power et al., 1972a,b, Hill et al., 1973), carbon monoxide (Hill et al., 1977) or a passive inert solute (with no specific transport mechanisms). The following main questions were addressed:

- How does the organization of the maternal and fetal blood flows affect the placental respiratory gas exchange across species?
- How can the placental exchange rate be calculated?
- What parameters do quantitatively characterize the exchange efficiency?

We will now review placental respiratory gas exchange models that were developed to answer these questions. These models can be subdivided into four principal classes:

- *capillary-scale models and studies of flow patterns,*
- *morphometric diffusing capacity models,*
- *distributed parameters models (including porous-medium models)*
- *models based on histological placental sections.*

Previous reviews of respiratory gas exchange placenta models were restricted to capillary-scale models only (Battaglia and Meschia, 1986, Wilkening and Meschia, 1992, Faber, 1995, Schröder, 1982). In the following, a separate section is devoted to each of these model types. To introduce the language of placenta modeling, a summary of the parameters commonly used in mass-transport placenta models is given in Appendix B.

1.6.3 Capillary-scale models. Flow patterns

The earliest models of respiratory gas exchange capitalized on anatomical observations that placentas of different species feature different co-orientations of the maternal and fetal blood flows (see p. 19), and explored how this factor may influence the exchange properties of the organ. In the earliest models only two capillaries (one maternal and one fetal) were used (Lampert, 1954), while later models operated with a larger number of capillaries.

These compartmental models distinguished five principal flow patterns (Fig. 1.27a, Faber, 1969):

- concurrent flow,
- counter-current flow,

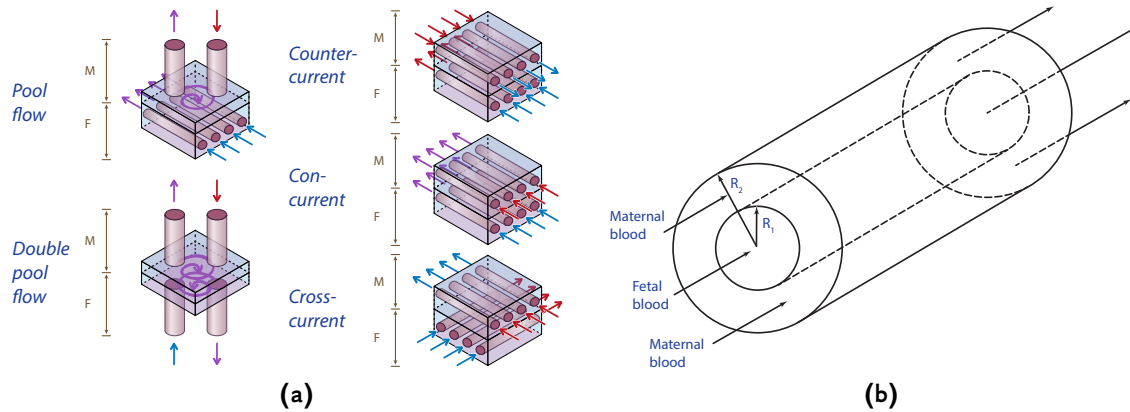


Figure 1.27. (a): Five principal patterns of blood flow based on the original scheme by Faber (1969). The letters F and M mark the fetal and the maternal parts of the exchangers respectively. Arrows show the direction of the blood flows. Their color indicates high (red), intermediate (violet) and low (blue) blood oxygenation (for more details see (Faber, 1969) and references within). (b): Krogh-type cylindrical layers model of placental circulation of Guilbeau et al. (1972)

- cross-current flow (or multivillous flow: maternal capillaries perpendicular to fetal capillaries),
- pool flow (uniform solute concentration along the length of maternal or fetal capillaries)
- double pool flow (uniform solute concentration in both maternal and fetal capillaries).

Anatomical studies suggest that guinea pig, rabbit and horse placentas represent the counter-current pattern (Figs 1.5a,b), goat and sheep placentas are venous equilibrators sharing features of the concurrent and pool flow patterns (Faber, 1977, Wilkening and Meschia, 1992, Faber, 1995), and the non-labyrinthine human and primate placentas can be approximated by the cross-current flow pattern (although maternal blood is not confined into capillaries in these hemochorial placentas, see Section 1.3). Discussions of the applicability of different flow patterns to the modeling of the mass transport in the human placenta can be found in Wilkin (1958), Bartels et al. (1962), Bartels and Moll (1964), Metcalfe et al. (1964), Guilbeau et al. (1972), Schröder (1982), Wilkening and Meschia (1992). Some studies also represented the maternal and fetal blood flows as concentric Krogh-type cylindrical layers, rather than circular capillaries running in parallel (see Fig. 1.27b and Guilbeau et al., 1972, Heilmann et al., 1979).

The efficiency of the concurrent, counter-current and multivillous flow patterns was first compared by Mossman (1926), Lamport (1954), Wilkin (1958). Greater efficiency of the counter-current flow pattern was demonstrated by numerical and analytical calculations of oxygen concentration profiles in the maternal and fetal capillaries in sheep and human placentas. Oxygen–hemoglobin dissociation was taken into account, and cases of finite and infinite exchanger lengths were considered.

Further advances of the placental flow–patterns studies were due to the application of a theoretical description of flow patterns developed for heat transfer problems (Hausen, 1950) to the placenta (Bartels et al., 1962, Bartels and Moll, 1964, Metcalfe et al., 1964, Shapiro et al., 1967). The oxygen dissociation curve was linearized, Henry’s law

was assumed for oxygen dissolved in the blood plasma, and an effective oxygen solubility was introduced. Fetal blood oxygenation was analyzed as a function of the membrane permeability and the materno-fetal flow ratio, and it was concluded that the multivillous flow pattern is more efficient than the concurrent one and less efficient than the counter-current one. Greater efficiency of the counter-current flow pattern over other flow patterns was discussed in terms of "maternal advantage" or "fetal advantage" by Battaglia and Meschia (1986).

Three dimensionless parameters: a *transport fraction*, a *flow ratio* and a *permeability variable* were proposed by Faber and Hart (1966), Faber (1969) and then used for an analysis of experimental data in rabbit (Faber and Hart, 1966) and goat (Rankin and Peterson, 1969). The proposed method required no assumptions on the placental geometry to interpret experimental data, and could predict transfer rates under various experimental conditions. Uptake diagrams plotted in these three parameters allowed for comparison of experimental results for respiratory-gas and inert-solute exchange in different species (Bartels and Moll, 1964, Middleman, 1972, Power et al., 1972a, Rankin, 1972, Faber, 1977, Schröder, 1982, Faber, 1995). Additionally, *placental clearance* was introduced to distinguish between two limiting exchange regimes: *permeability-limited* (or *diffusion-limited*) clearance and *flow-limited* placental clearance (Battaglia and Meschia, 1986, Meschia et al., 1967a). It was demonstrated that the flow-limited clearance is the maximal clearance of a given placenta regardless of the transferred solute. Comparison of the ratio of the diffusing capacity and a fetal transport capacity for different flow patterns was also proposed by Bartels and Moll (1964).

Longo et al. (1972b) extended the concurrent oxygen and carbon dioxide exchange model of Hill et al. (1972, 1973) and provided a graphical method of analysis of fluctuations of the venous materno-fetal oxygen pressure difference due to variation in model parameters (Power and Longo, 1969, Power et al., 1972a). The same model (Hill et al., 1973) was further significantly extended by Butler et al. (1976), who added amniotic fluid pressure and studied the effect of uterine contractions on the fetal oxygen supply.

Flow-patterns models were used to study the influence of different physiological and geometrical parameters on the placental of respiratory gases and other substances (Lamport, 1954, Bartels et al., 1962, Metcalfe et al., 1964, Shapiro et al., 1967, Faber, 1969, 1977, 1995, Kirschbaum and Shapiro, 1969, Longo and Power, 1969, Longo et al., 1972a,b, 1973, Longo, 1987, Power and Longo, 1969, 1975, Power et al., 1972a,b, Rankin and Peterson, 1969, Rankin, 1972, Guilbeau et al., 1972, 1973, Guilbeau and Reneau, 1973, Hill et al., 1972, 1973, Middleman, 1972, Moll, 1972, Reneau et al., 1974, Lardner, 1975, Butler et al., 1976, Heilmann et al., 1979, Schröder, 1982, Battaglia and Meschia, 1986, Schmid-Schönbein, 1988, Groome, 1991, Costa et al., 1992, Talbert and Sebire, 2004, Sengers et al., 2010). More details on flow-patterns models can be found in the review of Battaglia and Meschia (1986), where experimental data are also summarized.

Later, the capillary-scale models were significantly extended to describe water ex-

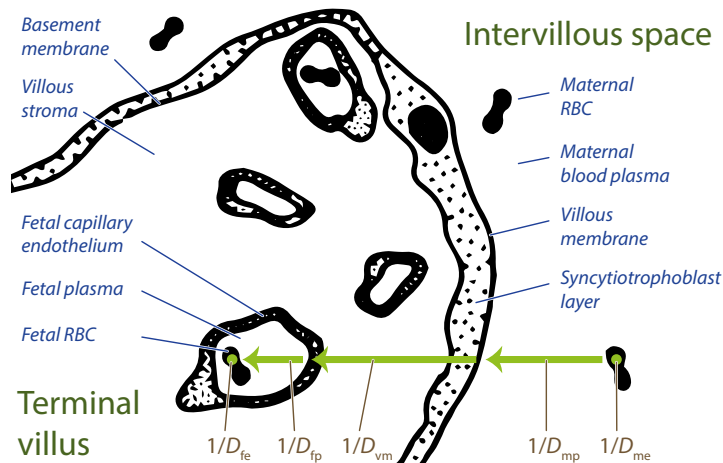


Figure 1.28. A schematic cross-section of one fetal terminal villus illustrating the components of the complex respiratory gas diffusion path. The notations are explained in the text. The internal part of the fetal villus and red blood cell distributions are simplified. Based on the original scheme by Mayhew et al. (1984)

change (Wilbur et al., 1978, Faber and Anderson, 1990, Talbert and Sebire, 2004) and glucose exchange (Barta and Drugan, 2010, Sengers et al., 2010).

1.6.4 Morphometric diffusing capacity models

The capillary-scale models oversimplify the geometry of the placenta, concentrating on the dynamics of oxygen concentration changes in the fetal and maternal blood, while separating them by a simple membrane. However, for respiratory gases this single effective membrane substitutes a complex gas diffusion path (see Fig. 1.28 and Section 1.2.2) that includes:

1. Diffusion within the maternal erythrocytes (*me*),
2. Diffusion within the maternal blood plasma (*mp*),
3. Diffusion across the villous membrane, comprising a syncytiotrophoblast layer, the trophoblast basement membrane, villous connective tissue and fetal capillary endothelium (*m*),
4. Diffusion within the fetal blood plasma (*fp*),
5. Diffusion within the fetal erythrocytes (*fe*).

To account for other passively transported solutes bound by other blood proteins than hemoglobin, binding to these proteins should be substituted into steps 1 and 5. For solutes that do not bind to blood components, only steps 2–4 should be taken into account. In any case, the complex diffusional paths require a separate calculation to estimate the effective membrane permeability before the capillary-scale models of the previous section can be used. Such calculations allow to interpret structural changes of the placenta in terms of altered exchange performance.

Before the review of the results, some definitions need to be discussed. A *membrane permeability* is defined as the proportionality constant between the rate of transfer per unit of membrane surface and solute concentration difference on both sides of the membrane.

The permeability is hence a local characteristic defined per unit of surface, which is well suited for a single membrane separating the exchanging compartments. However, for a multistage process with a different exchange surface at each step, it is more convenient to introduce a quantity characterizing the exchange in the placenta as a whole, such as a *placental permeability*, which is defined as the exchange rate of the placenta as a whole per unit of mean concentration difference in the exchanging compartments (Faber, 1995). For respiratory gases, the exchange rate is traditionally measured in ml/min and the concentration difference is replaced by the partial pressure difference (in mmHg). The resulting quantity is called a *placental diffusing capacity* D_p . Positive correlations between the diffusing capacity and the fetal weight have been reported (Aherne and Dunnill, 1966, Mayhew et al., 1984).

First calculations in the human placenta yielded $D_p \approx 0.5 \text{ ml}/(\text{min} \cdot \text{mmHg})$ (Bartels et al., 1962, Bartels and Moll, 1964) with the main contribution to the diffusive resistance of the entire oxygen path $1/D_p$ due to the villous membrane (about 90 %). However, these estimations oversimplified the diffusion path and did not rely on precise morphometric data, so they were later refined by Longo et al. (1969), Hill et al. (1972), Longo et al. (1972a), Laga et al. (1973). The diffusing capacity was then calculated with a serial resistance model in analogy to lungs (Roughton and Forster, 1957, Weibel, 1967, 1970) by the following formula (Laga et al., 1973):

$$1/D_p = 1/D_{me} + 1/D_{mp} + 1/D_m + 1/D_{fp} + 1/D_{fe}, \quad (1.1)$$

where the reciprocal of the total diffusing capacity for oxygen is assumed to be the sum of reciprocals of the diffusive capacities of each of the path components described above in analogy to electrical circuits. For each of the components, Laga et al. (1973) provided an approximate expression in terms of the following histomorphometrical parameters:

- volume of the intervillous space (IVS) excluding fibrin deposits,
- volume of the fetal capillary bed,
- surface area of the chorionic villi excluding stem villi,
- surface area of the fetal capillaries,
- the harmonic mean diffusion distance across the maternal plasma,
- the harmonic mean diffusion distance across the villous membrane,
- the harmonic mean diffusion distance across the fetal plasma.

Oxygen flow was thus related to geometrical characteristics of the villi and the IVS. For typical values of these quantities, the diffusing capacity was estimated to be $D_p \approx 3.1 \text{ ml}/(\text{min} \cdot \text{mmHg})$ with the following relative contributions of the components to the $1/D_p$: me – 1.1 %, mp – 0.6 %, m – 92.9 %, fp – 1.3 % and fe – 4.1 %. So the villous membrane was confirmed to provide the main diffusive resistance to oxygen exchange in the placenta. It should be noted that independent physiological experiments indicate that oxygen exchange in the human placenta and placentas of other species is

flow—limited rather than diffusion—limited (Faber et al., 1992, Faber, 1995), suggesting that the obtained value of D_p is large enough to allow for the transfer of practically all oxygen brought by the maternal circulation across the placental barrier. However, this point of view is not shared by all investigators (Wilkening and Meschia, 1992).

These calculations were later repeated yielding $D_p \approx 3 \text{ ml}/(\text{min} \cdot \text{mmHg})$ for the oxygen diffusing capacity (Mayhew et al., 1986) and explaining the discrepancy with other calculations ($D_p \approx 5.1 \text{ ml}/(\text{min} \cdot \text{mmHg})$, Mayhew et al., 1984). Correspondence of these values to physiologically obtained ones and some of those calculated by other groups (Ah-erne and Dunnill, 1966, Laga et al., 1973, 1974, Teasdale, 1982, 1983) was also discussed (Mayhew et al., 1984). It has also been found that the diffusion path components have the following relative contributions to the whole diffusive resistance $1/D_p$: me — 0.9 %, mp — 3.4 %, m — 89.3 %, fp — 2.9 % and fe — 3.5 %, which agreed with the results of Laga et al. (1973). Additionally, it was proposed to assess the influence of placental structural changes on the efficiency of oxygen exchange by calculating the sensitivity of the diffusive resistance to variations of directly measurable morphometric parameters. Calculations showed that variations of the harmonic mean thickness of the villous membrane had the greatest impact; variations of the surface area of the chorionic villi and that of the fetal capillaries had a medium impact; and variations of all other parameters had minimal impact on the D_p . It was concluded that the placental exchange performance can be assessed and compared in different placentas by monitoring only three structural quantities: the harmonic mean thickness of the villous membrane and the surface areas of the villi and of the fetal capillaries.

The definition (1.1) of morphometric placental diffusing capacity (D_p) is similar to the formula that describes the morphometric diffusing capacity of the lung (D_L) earlier introduced by Roughton and Forster (1957) and Weibel (1967, 1970). Since both the lung and the placenta supply the same living organism with oxygen at different stages of its development, it might be instructive to compare their diffusing capacities. The diffusing capacity D_{LO_2} of an adult human lung at rest is reported to be around $30 \text{ ml}/(\text{min} \cdot \text{mmHg})$, reaching as much as $100 \text{ ml}/(\text{min} \cdot \text{mmHg})$ at heavy exercise (Weibel, 1984, 2009). Recalculated per kilogram of body tissue, D_{LO_2} values give a diffusing capacity around $0.45 \text{ ml}/(\text{min} \cdot \text{mmHg} \cdot \text{kg})$ at rest and $1.4 \text{ ml}/(\text{min} \cdot \text{mmHg} \cdot \text{kg})$ under exercise for a 70-kg adult. For the placenta, recalculation of $D_p \approx 3\text{--}5 \text{ ml}/(\text{min} \cdot \text{mmHg})$ per kilogram of fetal weight at term (3.2 kg on average, see Salafia et al., 2008), gives $0.95\text{--}1.55 \text{ ml}/(\text{min} \cdot \text{mmHg} \cdot \text{kg})$. This value is similar to that of the adult human lung under exercise conditions. Note finally that oxygen transport in the lung under normal conditions is also flow-limited (West, 2008).

1.6.5 Distributed parameters models

To account for large-scale mass—transport effects, distributed parameters models were proposed. One of the first models of this class was proposed by Aifantis (1978) who treated the mass transport in the human placenta as a mixture problem. The placental tissue was considered as a solid constituent while the fetal blood and the maternal blood were modeled as two fluid constituents. These three components were allowed to interact

in a general way chemically, mechanically and thermally according to the laws of mass, momentum and energy conservation. This model is however only a general framework, and case-specific calculations are required to relate the model to the experiment. In other words, one needs to assume specific properties of the solid and the fluid constituents. Such calculations were performed as an example for some basic cases, but they were too general to provide quantitative results.

One of the possible ways of introducing properties of the solid and fluid constituents is to consider the placenta as a porous medium with the maternal blood percolating through it. Mathematically, such description can take the form of Darcy's law, which assumes a linear relation between the velocity of the maternal flow, the hydrostatic blood pressure and the porosity of the solid component (Bejan, 1984). A theoretical discussion of the applicability of porous-medium models to the human placenta from the hydrodynamic point of view can be found in Schmid-Schönbein (1988), Chernyavsky et al. (2010, 2011), Chernyavsky (2011). A way of calculation of porous-medium parameters from histological placental sections is also discussed (Chernyavsky et al., 2011, Chernyavsky, 2011).

The first calculation of the distribution of the maternal blood flow in a porous-medium human placenta model was performed by Erian et al. (1977). This model encompassed a whole placentone with a square cross-section filled with an isotropic porous medium, through which the maternal blood percolated following Darcy's law (Fig. 1.29a). At the basal side of the placentone, two maternal venous and one arterial openings were placed (a geometry which corresponds to the current anatomical views, see Section 1.3.1). Three permeability options have been studied:

- a uniform permeability,
- two zones of different fixed permeabilities, one of them modeling the central cavity (shown in Fig. 1.29a),
- a velocity-dependent permeability (to account for deformation of the villous tissue due to the blood flow) defined by an *ad hoc* formula, with no central cavity.

A generalization of the model to 2D+1D by assuming an *axial symmetry* along the line passing through the spiral artery was also proposed (Erian et al., 1977, central dotted line in Fig. 1.29a). Velocities of the maternal blood were assumed to be low, so that the inertia of the flow could be disregarded.

Interestingly, in all considered model configurations, the perfusion of the placentone by the maternal blood was significantly non-uniformly (with the central-cavity case showing slightly better performance). In particular, direct flow of a part of the maternal blood from the spiral artery to the decidual veins without penetrating deep into the placentone (short-circuiting) was observed. These results led the authors to conclude that the inertia (neglected by Darcy's law) and the pulsatility of the maternal blood flow cannot be disregarded. However, other explanations of the observed short-circuiting can be proposed:

- the *ad hoc* form of the dependence of the permeability of the porous medium on

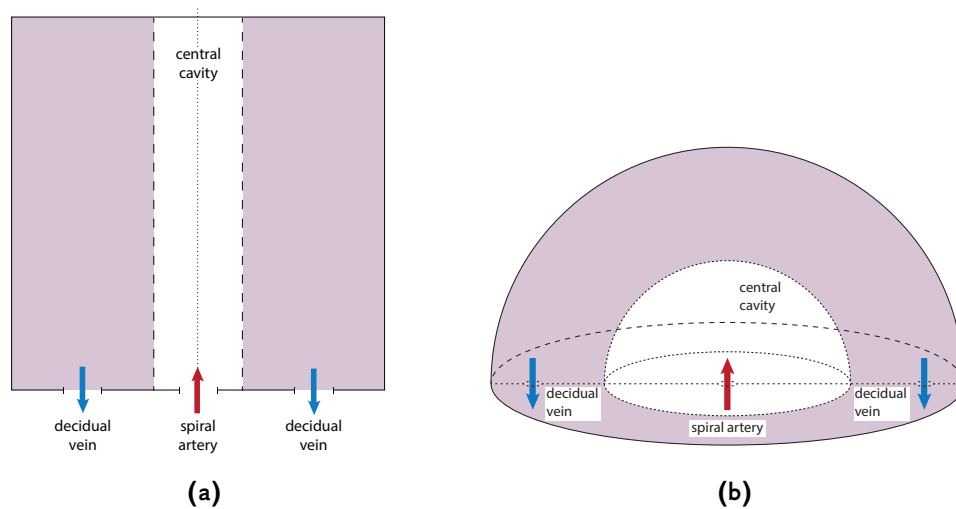


Figure 1.29. (a) Scheme of the square 2D placentone filled with a porous medium as proposed by Erian et al. (1977). One spiral artery and two decidual veins were placed at the bottom of the placentone. Boundaries of the central cavity are marked by two dashed lines. An extension to a cylindrical 2D+1D model by rotation around the central “vertical” axis (the dotted line) was proposed. (b) Scheme of the hemispherical 3D porous–medium placentone model of Chernyavsky et al. (2010). The dotted line delimits the central cavity. The same number and location of maternal vessels were used. A rotational symmetry was assumed around a “horizontal” axis passing through the three vessels

the maternal blood flow velocity chosen by Erian et al. (1977) may not correctly represent villi properties,

- or the placenta cannot be adequately described by a porous medium model.

It should be noted that Erian et al. (1977) wrongly assessed the diameter of the spiral arteries supplying the IVS as 0.03 cm, whereas recent calculations show that to the end of the pregnancy, they are dilated up to 0.3–1.2 cm in diameter due to the trophoblast invasion (Burton et al., 2009, see also Section 1.3). This mismatch yielded higher blood velocity in the IVS in the calculations of Erian et al. (1977) than is normally expected. However, diminishing the maternal blood velocity would reduce the blood penetration into the placentone even further and only enhance the short-circuiting.

To understand the negative conclusions of Erian et al. (1977) on the applicability of a porous–medium description to the placenta, a modified 3D placentone model was constructed, and the influence of the position and the size of the maternal veins, as well as the influence of the presence of a central cavity on the blood flow distribution in the placentone were studied (Chernyavsky et al., 2010). Rotational symmetry was assumed not along the “vertical” axis proposed by Erian et al. (1977), but along a “horizontal” axis passing through the maternal vessels, while the square placentone cross-section of Erian et al. (1977) was replaced by a semicircular one (Fig. 1.29b). The porous medium was considered non-deformable, which allowed for an analytical calculation of the maternal blood flow distribution. The central cavity was modeled as being free of the porous medium. To model not only the blood flow distribution (as done by Erian et al., 1977), but also mass transport, a uniform volumetric absorption coefficient was assumed everywhere outside the central cavity. Since no account for specific transport kinetics of a solute (e.g., oxygen-hemoglobin dissociation) was given, applications of the model were

limited to the transport of inert solutes (the authors' choice of oxygen dissolved in the blood plasma as an illustration of inert solute transport is slightly confusing). Also, only convective transport was taken into account, while the diffusive transport of solute was disregarded (an assumption which may not be valid in small IVS pores). Additionally, the effects of the deformability of the villous tissue and of the presence of red blood cells and of a central cavity have been considered (Chernyavsky, 2011).

Several conclusions were obtained:

- If the distance between the maternal artery and veins is small compared to the placentone radius, the maternal blood flow pattern is localized near the vessels, yielding short-circuiting of blood from the arteries to the veins. However, if the veins are located near the periphery of the placentone, the maternal blood flow penetrates deeper into the IVS and perfuses it more efficiently.
- The maternal vessels caliber is one of the main determinants of the maternal blood flow rate through the placentone if there is a fixed hydrostatic pressure difference between the spiral artery and the decidual veins.
- The main pressure drop occurs in the vicinity of the maternal vessels, while low resistance to the flow is observed far from the vessels.
- There is an optimal size of the central cavity as a compromise between the resistance to the maternal flow and the amount of villous tissue participating in solute uptake.
- There is also an optimal volume fraction $\varphi_0 = V_{\text{vil}}/V_{\text{IVS}}$ of the "villous material" in the IVS as a result of a trade-off between the flow resistance and the uptake capacity of a placentone. However, the obtained value of the optimal villi density corresponds to experimental values observed in high-altitude and pre-eclamptic placentas rather than in healthy ones (as discussed later in Section 2.4.4 on p. 83).

In summary, even with no account for the flow inertia, an efficient perfusion of the placentone can be obtained by right positioning of the venous outlets with respect to the arteries. The porous–medium approach was proved valuable in the analysis of the maternal blood distribution in the placentone and of the effects of the shear stress and flow resistance. At the same time, the main drawbacks of the porous–medium models are:

- the difficulty of modeling the solute uptake due to the absence of a clearly defined uptake surface,
- and representation of the human placental geometry as being random thus ignoring the structure of the fetal villous tree (Fig. 1.7a).

1.6.6 Models based on histological placental sections

Geometrical models reviewed below are based on 2D histological placental sections (Fig. 1.15) and feature a clearly defined uptake surface. These models can be considered as a further development of the morphometric diffusing capacity models of Section 1.6.4,

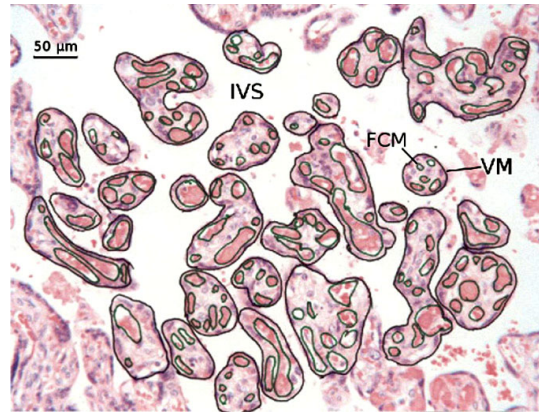


Figure 1.30. One of the histological cross-sections of a healthy human placenta segmented by Gill et al. (2011). Villous membranes (VM) and fetal capillary membranes (FCM) were traced. The maternal IVS is also marked

since oxygen uptake is computed in the same 2D structures that were used before to calculate the diffusing capacity.

To our knowledge, the only model of this type, a model of intravillous mass transport, was proposed by Gill et al. (2011, see Fig. 1.30), who used 2D spatial distributions of capillaries in several dozens of villi obtained from histological cross-sections of the human placenta. In this model, a uniform oxygen concentration was assumed on the perimeter of all villi, while perfect sink conditions were set on the fetal capillary boundaries. Purely diffusive oxygen transport from the villous perimeter to the capillaries was then simulated. The internal structure of the fetal villi was thus studied independently from the maternal oxygen supply to the villi. Expectedly, the calculations showed that fetal capillaries located close to the center of a villus have smaller contribution to the uptake of the villus than those located close to its boundary. This effect was named *screening of capillaries* in analogy to a screening concept described earlier in the human lung (Sapoval et al., 2002, Felici et al., 2005). *Villus efficiency* was then introduced based on a measure of screening of individual capillaries, which was defined as the ratio between the oxygen uptake of a given capillary in the presence of other capillaries and the oxygen uptake of the same capillary if no other capillaries were present in the villus. The villus efficiency was shown to be correlated to independent indicators of the placental function, such as the placenta–fetus birth weight ratio.

The model of intravillous transport by Gill et al. (2011) assessed the role of spatial distribution of fetal capillaries inside a villus and the efficiency of individual villi. However, the concentration of oxygen in the maternal blood and at the villous boundaries may vary significantly in different regions of the IVS as a function of the villi density and the spatial arrangement of the villi. In order to compute the oxygen uptake of the whole placentone, one also needs to simulate oxygen transport in the IVS. However, the model by Gill et al. (2011) cannot be directly applied to the oxygen transport in the IVS since convective transport should be considered in addition to the diffusion. Describing the combination of the two transport mechanisms will be the main focus of the first part of the present thesis.

1.6.7 *Experimental validation of mathematical models of respiratory gas exchange in the placenta*

The only sure way to validate a mathematical model and to evaluate the new insights it gives is to confront model predictions to medical observations and experimental measurements. Based on the available experimental techniques, the following ways of comparison of the respiratory gas exchange placenta models to experimental data have been proposed:

- Faber (1969) proposed uptake diagrams which allowed to analyze blood flow patterns in multiple species based on experimental data (Rankin and Peterson, 1969, Faber, 1977). It was shown that in all considered species oxygen transfer is flow-limited, demonstrating a nearly complete equilibration of oxygen concentrations between the maternal and fetal circulations (Faber, 1995).
- Battaglia and Meschia (1986) proposed that to integrally characterize the placenta of a particular species as an exchanger, one needs to measure the maternal and fetal placental blood flows, transplacental diffusion rates of various test molecules and their concentrations in the arteries and veins of both the mother and the fetus. This experimental program was later completed in sheep (Meschia et al., 1967a,b).
- Results of the placental model of Longo et al. (1972a, 1973) were compared to partial pressures of oxygen and carbon dioxide measured during *in situ* perfusion of an isolated placentone (Longo et al., 1972b, Power and Jenkins, 1975).
- Morphometrically calculated oxygen diffusing capacity was shown to correspond to physiologically measured values (Mayhew et al., 1984).
- It was demonstrated that ring-like radioactive dye diffusion patterns of Freese (1968) observed in the human placenta, can be explained in a porous-medium placenta model (Chernyavsky et al., 2010).
- Comparison with histological sections showed that the optimal villous material density of around 30 % calculated by Chernyavsky et al. (2010) corresponded to high-altitude or pathological rather than healthy placentas.

1.6.8 *Concluding remarks*

The provided analysis shows that more than 60 years of mathematical modeling of the placenta have significantly contributed to our understanding of the placental respiratory gas exchange. Starting with a pair of capillaries conducting all fetal and maternal blood, the models have evolved to the description of the placenta as a porous medium, and to predictions of the placental exchange efficiency based on 2D histological cross-sections. Mathematical modeling has allowed to estimate the blood flow distribution and respiratory gas exchange rates across the placenta in different species.

However, our understanding of the placental respiratory gas exchange still remains incomplete:

1. As yet, no placenta model has been proposed that would account for the complicated 3D structure of the organ and for both convective and diffusive transport of respiratory gases in the intervillous space of the human placenta. Such models may give new insights into the role that the geometrical structure plays in the transport function of the organ.
2. The absence of such placental models is partly due to that the high-resolution 3D geometrical structure of the placenta is yet unavailable for large placental regions (with at least 1000 villi), especially in dense exchange regions. Meanwhile, models can be based either on high-resolution 2D histological sections, on low-resolution 3D structures from *ex vivo* MRI angiography or micro-CT, or on local high-resolution 3D villi geometry (about dozens of villi) provided by the confocal laser microscopy.
3. High resolution blood flow patterns in the human placenta have not yet been experimentally determined either *in vivo*, or *ex vivo*.
4. Oxygen, carbon dioxide and other substances concentrations in the human placenta are not available on a regular basis either in the IVS, or in the umbilical and uterine arteries and veins. Some advances may be expected with the development of the BOLD MRI techniques.
5. There exists no automatic image-processing technique of analysis of placental cross-sections that could provide large histomorphometrical statistics and supply them as input data to the models based on histological sections.
6. The degree to which fixed histological sections faithfully represent the *in vivo* placenta structure and the methodology of how to correct for the possible discrepancies are yet to be established.

1.7 Objectives and structure of the thesis

The work presented in this thesis aims to provide a model of diffusive and convective transport of oxygen in the IVS of the human placenta. This model allows one to predict the oxygen exchange rate and the efficiency of a given placental geometry based on the histomorphometrical data from placental cross-sections. It gives new insights into the relevant geometrical and physiological placental parameters that govern oxygen exchange efficiency. It also provides predictions on the optimal placental geometry that maximizes oxygen exchange for a given set of physiological parameters.

The subsequent chapters of the thesis are organized in the following way.

In **Chapter 2**, a geometrical stream-tube placenta model (STPM) is described and mathematical equations defining oxygen exchange in this model are developed. Model assumptions and location of the stream tubes in the human placenta are discussed. Physiological values of model parameters and standard dimensionless hydrodynamic numbers are calculated. Oxygen concentration distribution and oxygen uptake are then obtained by numerical calculations for circular villi. The observed optimal villi density and the

dependence of the results on model parameters are discussed. The optimal geometry predictions are compared to experimental data.

In Chapter 3, an approximate analytical solution of the STPM is developed, which extends the results of Chapter 2 to villi of arbitrary cross-sectional shape. Moreover, we identify the main geometrical characteristics defining the oxygen exchange performance, and demonstrate that all model parameters do not influence the results independently, but form only two parameter combinations. Also, the analytical approach allows us to introduce two measures of efficiency to characterize a non-optimal geometry, for which analytical formulas and efficiency diagrams are provided.

In Chapter 4, a computer algorithm is proposed to automatically segment and perform histomorphometrical measurements on histological placental slides. The algorithm is then applied to 25 histological cross-sections (taken from 22 healthy and 3 pathological pregnancies). The resulting histomorphometrical data are then plotted on the efficiency diagrams, which allows us to discuss the efficiency of oxygen exchange in these placentas.

In Chapter 5, we summarize the obtained results, and analyze them from a physiological perspective. Possible ways of future development of the presented model are outlined.

Chapter 2

Stream-tube placenta model

In the present chapter we introduce a stream-tube placenta model (STPM) of oxygen exchange in the human placenta. This model has several features which were missing or never combined in the previous models:

- It is 2D+1D.
- It accounts for both diffusion and convection of oxygen in the IVS.
- The model is based on histological placental cross-sections and can use histological measurements as input data.

The chapter will start with a description of the geometry and the location of the model in the human placenta. Geometrical and physiological assumptions of the model will be discussed. The standard dimensionless hydrodynamic numbers characterizing the maternal blood flow and oxygen transport will be then reviewed. This analysis will allow to identify the characteristic features of the studied transport process and justify some of the stream-tube model assumptions. After that, we will be ready to develop a mathematical description of oxygen transport in the model. For this purpose, we will first consider the relevant transport processes in the human placenta and their characteristic time scales. The calculations will yield that oxygen-hemoglobin dissociation can be considered instantaneous as compared to oxygen diffusion and convection in the maternal blood. The high speed of oxygen-hemoglobin dissociation will further enable us establish a one-to-one relationship (a “mirror” relationship) between the hemoglobin-bound and free oxygen concentrations. Then, from the mass conservation law, we will develop a 3D convection-diffusion equation for oxygen in the maternal blood (including both bound and dissolved oxygen concentrations), and will use the mirror relationship to reduce the number of unknown functions to only one (the concentration of oxygen dissolved in the blood plasma). At the same time, the model assumptions will be converted into mathematical form to provide boundary conditions for the diffusion-convection equation.

The obtained equation will include the Hill saturation function and will therefore be non-linear in oxygen concentration, which significantly hinders its resolution. To simplify the equation, we will linearize the saturation function in the physiological range of oxygen partial pressures observed in the human placenta. We will then take advantage of the system’s symmetry in the direction of the maternal blood flow and convert

the 3D convection-diffusion equation into a 2D+1D one by a standard separation of variables. The obtained 2D equation for Laplace operator eigenvalues in the stream-tube cross-section can then be numerically solved and the oxygen uptake of a stream tube computed. At this point, we will review the values of the model parameters necessary for the numerical solution of the equation (such as the permeability of the effective placental membrane, the maternal blood flow velocity and the oxygen diffusivity in blood plasma).

Although the 2D eigenvalues equation can be solved for arbitrary villi shapes and sizes, we will start the investigation of the model properties with a simple case of identical circular villi in a circular stream tube. This restriction will be relaxed in Chapter 3 with the development of an approximate analytical oxygen exchange theory. The numerical solution of Chapter 2, however, will be obtained with a finite elements method and will be validated by comparison with an exact analytical solution for the case of one villus. Results convergence will be numerically studied for arbitrary villi densities and stream-tube lengths.

In the next section of the chapter, the numerical results will be discussed. In particular, it will be shown that the stream-tube placenta model exhibits an optimal villi density maximizing the oxygen uptake, which is different for different stream-tube lengths. The explanation of the optimality will then be provided, and the optimal villi density predicted by the model for the physiological values of model parameters will be compared to the published histomorphometrical data. Other options for the experimental validation of the model will also be discussed. Finally, we will provide a comparison of the optimal villi density predictions of the present model and those of the porous medium placenta model of Chernyavsky et al. (2010), and will discuss the advantages and the drawbacks of each approach. The investigation of the optimal stream-tube geometry will continue in Chapter 3 with the development of an approximate analytical theory of placental oxygen exchange.

2.1 Model outline

Maternal blood arrives into the intervillous space (IVS) of the human placenta by spiral arteries (see Section 1.3.1 and Fig. 1.7a). It then percolates through the branching structure of the tree of fetal villi and leaves the IVS by decidual veins. The whole pattern of the maternal blood flow (MBF) can be virtually subdivided into small regions (stream tubes), each following the flow and extending from a spiral artery to a decidual vein (Fig. 2.1a). Each stream tube is crossed by numerous fetal villi, at the surface of which mass exchange between the maternal and fetal blood takes place.

Our 3D stream-tube placenta model (STPM) is inspired by the observation that the human placenta resembles "a closed cubical room supported by cylindrical pillars running from floor to ceiling" (Lee and Mayhew, 1995). The model describes one *unfolded* stream tube of maternal blood, which is represented by a large straight cylinder (Fig. 2.1c). This cylinder contains multiple smaller parallel cylinders which correspond to small fetal villi (terminal and mature intermediate) filled with fetal blood (Fig. 2.1b). At first, we will consider these small cylinders to be of identical sizes and shapes, while their lateral spacings will be randomly distributed (with no cylinders overlap). This technical assumption

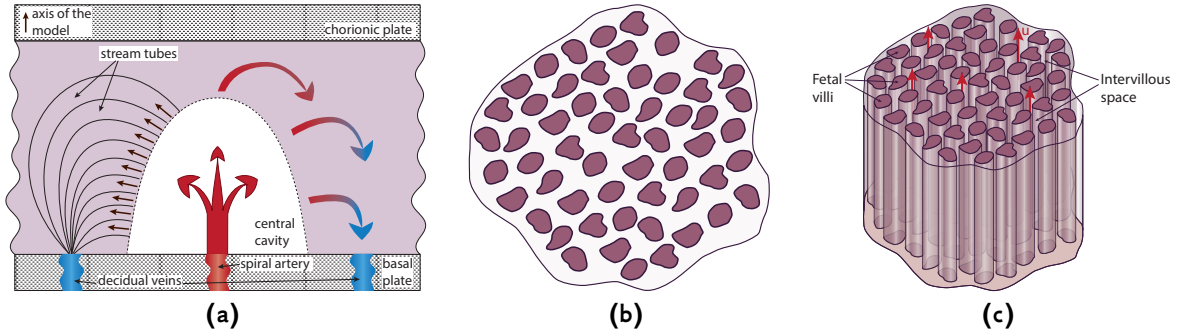


Figure 2.1. (a): Scheme of a placentone and location of stream tubes in the placenta. The dashed line outlines the central cavity. The curved arrows on the right show the maternal blood losing oxygen while going from the central cavity to the decidual veins. The curved lines on the left show the stream tubes. The STPM corresponds to one such tube unfolded; small straight arrows show the entrance points of the model. The exchange is not modeled in the central cavity, but only outside it. The concept that spiral arteries open into the IVS near the central cavity corresponds to the current physiological views (see Section 1.3.1). (b): A cross-section of the STPM featuring arbitrary cross-sections of fetal villi, which imitate villi cross-sections seen in histological slides (Fig. 1.15). As shown in Section 2.2.1, the shape of the external boundary of the stream tube can be chosen arbitrary. (c): A translationally symmetric extension of the cross-section (b) into 3D, which yields the STPM. Red arrows show the direction of the maternal blood flow

will be relaxed in subsequent chapters to allow model application to histological placental sections with villi of arbitrary sizes and shapes (Fig. 2.1b).

2.1.1 Model assumptions

Our model relies on the following assumptions:

1. *The large cylinder corresponds to an idealized unfolded stream tube of maternal blood*, extending from the boundary of the central cavity to a decidual vein (Fig. 2.1a). Every portion of arterial blood coming into placenta has its own stream tube, along which blood exchanges oxygen with fetal villi and gradually becomes venous. The contorted axis of each stream tube follows the maternal blood flow. The length of a tube can vary from one region to another, but is expected to be of the order of placental disk thickness (see Section 2.3 for more details).
2. *The stream-tube has the same cross-section along its axis.* In fact, we aim to base our STPM on histological slides (like those shown in Fig. 1.15), which give us only one section of a stream tube without any information about how this section evolves along it. We then suppose that the same average characteristics, such as the density or the perimeter of the villi, are preserved along the same tube. This is obviously an oversimplification of the irregular 3D structure of the placenta, but it is the most straightforward assumption given the lack of the complete 3D geometrical data with all spatially resolved terminal and mature intermediate villi. The effect of the co-orientation of the villi and the maternal blood flow is not negligible, but is likely to give only a correction to the main part of the result defined by the total villi volume and the total villi surface, on which we will focus in this work.
3. *In any cross-section perpendicular to the MBF, oxygen is only redistributed by dif-*

fusion. The gradient of oxygen dissolved in the blood plasma, not the gradient of oxygen bound to hemoglobin, determines the rate of oxygen diffusion in blood (Bartels et al., 1962). Since oxygen has low solubility in blood, linear solubility (Henry's law, Prausnitz et al., 1998) is assumed.

4. *Fetal blood is considered to act as a perfect oxygen sink*. This technical assumption means that when we will be talking about the partial pressure of oxygen in the maternal blood, we will mean the partial pressure difference between the maternal and the fetal blood. Additionally, this assumption suggests that the fetal circulation is efficient enough to rapidly carry away all oxygen that is transferred from the maternal blood.

If villi are considered to be perfect sinks, there is no difference between fetal arterial and venous blood, between concurrent and counter-current blood flow patterns, or any other organization of the flow in this specific geometry. Fetal blood flow can therefore be disregarded, as long as the fetal blood flow rate is assumed to be sufficient to maintain steep oxygen gradients for diffusion. In other words, the STPM separates the IVS geometry from the capillary geometry inside the villi. The diffusive resistance to oxygen transfer across the fetal trophoblasts, the connective tissue, the fetal endothelium and the fetal blood plasma is modeled by one effective feto-maternal interface of finite permeability calculated from the placental diffusing capacity (see Section 2.3).

5. *Oxygen uptake occurs at the feto-maternal interface*, i.e. at the boundaries of small villi in Fig. 2.1b. *It is directly proportional to the interface permeability and to the concentration of oxygen dissolved in the blood plasma on the maternal side of the interface* (Fick's law of diffusion). Note that oxygen partial pressure (p_{O_2}) can be used in this definition instead of oxygen concentration in the blood plasma (c_{pl}), since according to Henry's law of solubility the two variables are directly proportional. The validity of Fick's law for the description of a flux of mass across a membrane can be demonstrated by combination of the first and second laws of thermodynamics, Onsager linear theory of irreversible thermodynamics, the expression for the chemical potential of a gas dissolved in a liquid and microscopic-scale theories (for more details see Kjelstrup and Bedeaux, 2008, Lebowitz and Spohn, 1982, Deng, 1989, Benes and Verweij, 1999, van Milligen et al., 2005, Koide, 2005, Sattin, 2008) in the case of a static non-absorbing interface without a temperature gradient across it.
6. *The maternal blood flow is considered to be laminar with no liquid–walls friction (slip boundary conditions at all surfaces)*, so that *the velocity profile in any cross-section is flat*. This assumption is supported by the calculations obtained for capillary-tissue cylinders in brain (Reneau et al., 1967). The brain model has been used to compare the effect of non-slip boundary conditions (and thus a non-flat velocity profile) and slip boundary conditions (and thus a flat velocity profile) on the distribution of p_{O_2} in a Krogh's type cylindrical tissue layer. The difference in p_{O_2} distribution between the two cases was less than 10%. The strong assumption of slip boundary conditions is

further discussed in Section 2.1.2 (see the discussion of the Schmidt number) and in Section 2.4.4 on p. 84.

7. *Oxygen-hemoglobin dissociation curve is linearized* in the physiological range of oxygen partial pressures (0–60 mmHg) observed in the human placenta (further discussed in Section 2.2.4 on p. 67).
8. *Red blood cells (RBCs) are uniformly distributed in the IVS.*
9. *Oxygen bound to hemoglobin does not diffuse* and is transported only by convection (RBCs being too large); only oxygen dissolved in the blood plasma does.
10. *The solution is stationary*, i.e. the placental oxygen flow remains constant over time. Pulsatility of maternal blood is not taken into account.
11. *Blood flow matching does not occur*, i.e. there is no influence (feedback) of the oxygen uptake on the parameters of the model (such as the MBF velocity, see Talbert and Sebire, 2004). No redundancy of some of the fetal cylinders when the maternal blood flow is reduced is taken into account.

2.1.2 Dimensionless hydrodynamic numbers

Before writing the diffusion-convection equation, it is important to understand the basic features of the blood flow and oxygen transport in the human placenta and evaluate how well the assumptions of the previous section describe the physical phenomena occurring in the placenta. A standard approach to this problem is to estimate several universal dimensionless quantities that characterize the flow and transport phenomena in the given system (Incropera and Dewitt, 2001). In the following, four such numbers will be considered:

- the Reynolds number (Re),
- the Péclet number (Pe),
- the Schmidt number (Sc),
- the Damköhler number (Da).

The results of the calculations of these dimensionless numbers and their physical meaning are summarized in Table 2.1.

The Reynolds number (Re)

The Reynolds number characterizes the flow of a fluid and is defined as the ratio of inertial forces to viscous forces per volume of fluid (Incropera and Dewitt, 2001). It therefore quantifies the relative importance of these forces. In the case of domination of viscous forces over the inertial ones (low Reynolds numbers: $Re \lesssim 10^3$), the flow is *laminar*, i.e. smooth and continuous (see Potter et al., 2012, p. 105). Otherwise, at large Reynolds numbers ($Re \gtrsim 10^3$), the flow is dominated by inertial forces and is

Table 2.1. Dimensionless hydrodynamic numbers and their typical values characterizing the human placenta (see calculations in the text). The consequences for oxygen transport in the human placenta are summarized

Name	Symbol	Value	Physical interpretation
Reynolds number	Re	0.17	Domination of viscous forces over inertial forces. Laminar, smooth and steady flow of maternal blood in the IVS
Péclet number	Pe	5600	Convective transport is much faster than diffusive transport along the maternal blood flow
Schmidt number	Sc	$2 \cdot 10^6$	Boundary-induced velocity gradients are much larger and much more localized than concentration gradients, which justifies slip boundary conditions
Damköhler number	Da	1.4	Discussed in Section 3.2.3

turbulent, featuring flow instabilities, such as vortices or eddies. In the systems with the same Reynolds number, the flows are similar, although in practice small perturbations of the flow parameters or boundary conditions may result in considerable differences in the flow features (especially for the turbulent flow), but small differences in Reynolds number. Mathematically, the Reynolds number can be defined as

$$\text{Re} = \frac{ud}{\nu} = \frac{\rho ud}{\mu}, \quad (2.1)$$

where u is the characteristic velocity of a liquid, d is a characteristic linear size of the duct or the pipe, ρ is the density of the liquid, ν is the kinematic viscosity (in m^2/s) and μ is the dynamic viscosity (in $\text{kg}/(\text{m} \cdot \text{s})$, see [Incropera and Dewitt \(2001\)](#)). The characteristic linear size d is often estimated as the hydraulic diameter $d = d_h \equiv 4A/P$ of the pipe, where A is the cross-sectional area of the pipe and P is its wetted perimeter.

For the human placenta, d_h can be calculated in the following way. Experimental studies indicate that the fraction of the cross-sectional area occupied by the fetal villi (φ) is around 0.5 (see [Table 2.5](#) and [Fig. 2.1b](#)). It is also known that the effective radius of one terminal villus is around $r_e \approx 41 \mu\text{m}$ ([Table 2.2](#)). In such cross-section, A corresponds to the total area of the IVS cross-section S_{IVS} , and $P = 2\pi r_e N$, with $N = S_{\text{IVS}}\varphi/(\pi r_e^2(1 - \varphi))$ being the number of terminal villi. These data then allow one to estimate d_h as

$$d_h = \frac{4S_{\text{IVS}}}{2\pi r_e N} = \frac{4S_{\text{IVS}}}{2\pi r_e} \cdot \frac{\pi r_e^2(1 - \varphi)}{S_{\text{IVS}}\varphi} = \frac{2r_e(1 - \varphi)}{\varphi} \approx 82 \mu\text{m}.$$

The typical values of other variables entering the definition (2.1) are: $\rho \approx 10^3 \text{ kg}/\text{m}^3$ (as close to the density of water), $u \approx 6 \cdot 10^{-4} \text{ m}/\text{s}$ ([Table 2.2](#)) and $\mu \approx 3.5 \text{ kg}/(\text{m} \cdot \text{s})$ ([Dor-mandy, 1970](#)). This yields

$$\text{Re} \approx 0.17$$

in the IVS of the human placenta under normal conditions. This value of the Reynolds number indicates that viscous forces dominate over the inertial forces. The flow is

thus expected to be laminar, with smooth and constant fluid motion (compare with assumption 6 of the previous section).

The Péclet number (Pe)

The Péclet number is defined as the ratio of the rates of convective and diffusive transport in a given direction (Incropera and Dewitt, 2001). High values of the Péclet number ($Pe \gg 1$) imply domination of the convective transport, while low values ($Pe \ll 1$) mean that molecular diffusion is the main transport mechanism. It is clear that in a direction perpendicular to the flow (for instance, in a cross-section of a stream-tube in Fig. 2.1), $Pe = 0$ and only diffusive transport takes place (compare with assumption 3 of the previous section). Along the flow, the Péclet number can be calculated as

$$Pe \equiv \frac{uL_0}{D},$$

where for oxygen transport the human placenta, $u \approx 6 \cdot 10^{-4}$ m/s is the average velocity of the blood flow in the IVS, $D \approx 1.7 \cdot 10^{-9}$ m²/s is the diffusivity of oxygen, and the length of a stream tube $L_0 \approx 1.6$ cm is the transport distance along the blood flow (Table 2.2). Combination of these data gives the following estimation for the Péclet number:

$$Pe \approx 5600.$$

This value indicates that convective oxygen transport along the blood flow is much faster than the diffusive transport, and the latter can probably be ignored.

The Schmidt number (Sc)

The Schmidt number is defined as the ratio of momentum and mass diffusivities in a given liquid (Incropera and Dewitt, 2001). For convective mass transfer in laminar flows it allows to compare the thicknesses of the concentration and velocity boundary layers. High values of the Schmidt number ($Sc \gg 1$) indicate that the velocity boundary layer is much thinner than the concentration one and the boundary-induced velocity gradients are much larger than the concentration gradients. This situation favors the use of the slip boundary conditions for the velocity field (non-zero boundary velocity), since velocity changes are localized in a relatively small region next to the boundary. Low values of the Schmidt number ($Sc \ll 1$) describe the opposite situation.

The definition of the Schmidt number does not contain a characteristic linear scale, and is hence a property of the liquid and of the diffusing substance. It can be calculated by the following formula:

$$Sc = \frac{\mu}{\rho D},$$

where for the human placenta $\mu \approx 3.5$ kg/(m · s) is the dynamic viscosity of blood (Dor-mandy, 1970), $\rho \approx 10^3$ kg/m³ is the density of blood (as close to the density of water) and $D \approx 1.7 \cdot 10^{-9}$ m²/s is the diffusivity of oxygen (Table 2.2). Substitution of these

values in the last formula yields

$$Sc \approx 2 \cdot 10^6.$$

Such a large value of Sc suggests that in the human placenta boundary-induced velocity gradients are much larger and much more localized than the concentration gradients, which justifies the use of the slip boundary conditions in the stream-tube placenta model (assumption 6).

The Damköhler number (Da)

The Damköhler number is a dimensionless number used in chemical engineering which is defined as the ratio of the reaction rate of a substance to the rate of its convective transfer in a chemical reactor (Fogler, 2005). The Damköhler number provides an estimate on the fraction of substance entering the chemical reactor in a unit of time which undergoes chemical transformation. High Damköhler numbers ($Da \gg 1$) indicate that most of the substance will undergo the chemical transformation after passing through the reactor, while under low Damköhler numbers ($Da \ll 1$) most of the substance will leave the reactor in the unchanged form. The balance between the two processes is achieved, when $Da \approx 1$.

In application to oxygen transport in the human placenta, Da can be introduced as the ratio of the rate of oxygen extraction by the fetal villi ($1/\tau_e$) to the rate of the maternal blood flow in the IVS ($1/\tau_{tr}$):

$$Da \equiv \frac{\tau_{tr}}{\tau_e}, \quad (2.2)$$

where τ_e and τ_{tr} are respectively the characteristic time of oxygen extraction and the transit time of the maternal blood through the placenta. Applied to the placenta, the Damköhler number was first introduced for inert solutes by Chernyavsky et al. (2010), although some similar coefficients have been proposed before (like *permeability variable*, *maternal/fetal transport fractions* or *coefficient of oxygen utilization*, see Table B.1 in Appendix B on p. 144).

The transit time τ_{tr} can be estimated either by direct measurements of from known transit path and the average maternal blood velocity in the IVS, and its characteristic values will be discussed in Section 2.3. However, it is for the moment unclear how τ_e should be defined. It will be demonstrated later that the correct introduction of this variable requires the development of an approximate analytical theory of oxygen transport in the stream-tube model (discussed in Chapter 3). The notation Da for the Damköhler number will appear early in that chapter, but only in Section 3.2.3 it will be shown that it has a physical meaning of the Damköhler number, and a formula for a characteristic time of oxygen uptake τ_e will be extracted from it. It will be also demonstrated that the Damköhler number for a healthy human placenta is around 1.4 suggesting optimization of the human placenta to oxygen transport.

2.2 Diffusion-convection equation

2.2.1 Characteristic time scales of transfer processes in the human placenta

To calculate the oxygen exchange rate in the STPM, we first need to identify the relevant physical processes. We identify three different physical transport processes in the human placenta, each of which operates on its own characteristic time scale: the hydrodynamic blood flow through the IVS characterized by an average velocity u and a transit time τ_{tr} ; the diffusion of oxygen with a characteristic time τ_D ; and equilibration between the oxygen bound to hemoglobin and the oxygen dissolved in the blood plasma, with a characteristic time τ_p . The three characteristic times can be estimated as follows:

- τ_{tr} , the transit time of blood through the IVS, is of the order of **27 s** from the results of angiographic studies at term (see discussion of the MBF velocity on p. 75).
- τ_D , the time of oxygen diffusion over a length δ in the IVS is $\tau_D \sim \delta^2/D$, where D is the oxygen diffusivity in the blood plasma. The average size of an IVS pore in healthy human placentas was estimated to be $\delta \sim 80 \mu\text{m}$ (Mayhew and Jairam, 2000). Together with the diffusivity of oxygen in blood $D \approx 1.7 \cdot 10^{-9} \text{ m}^2/\text{s}$, it yields $\tau_D \sim 4 \text{ s}$.
- τ_p , an equilibration time scale includes a characteristic diffusion time for oxygen to reach Hb molecules inside a red blood cell ($\sim 10 \text{ ms}$, see Fouquier et al., 2013) and a typical time of oxygen-hemoglobin dissociation ($\sim 20 \text{ ms}$ for the slowest process, see Yamaguchi et al., 1985). Together these times sum up to $\tau_p \sim 30 \text{ ms}$.

The three characteristic times are therefore related as follows: $\tau_p \ll \tau_D \lesssim \tau_{tr}$. This relation suggests that oxygen-hemoglobin dissociation can be considered instantaneous as compared to diffusion and convection; the latter two, by contrast, should be treated simultaneously.

Note that the values of τ_D and τ_{tr} suggest that during the time the maternal blood spends in the stream tube, the oxygen can only diffuse to a distance equal to approximately 2.6 times the size of an IVS pore ($\sqrt{27 \text{ s}/4 \text{ s}} \approx 2.6$). In particular, this means that the internal regions of the stream tube will not “feel” the presence or the shape of the external stream-tube boundary if they are more than about 2.6 IVS pores far from it. In other words in the calculations, the shape of the stream tube can be chosen arbitrary as long as its characteristic radius is significantly larger than $2.6 \times 80 \mu\text{m} \approx 0.21 \text{ mm}$.

2.2.2 Equilibrium between the bound and the dissolved oxygen

The very fast oxygen-hemoglobin reaction can be accounted for by assuming that the concentration of the oxygen dissolved in the blood plasma (c_{pl}) and that of the oxygen bound to hemoglobin (c_{bnd}) instantaneously mirror each other's changes. The thermodynamic equilibrium between the two concentrations is described by an equal partial pressure of oxygen in both states.

Oxygen dissolved in the blood plasma. Because of the low solubility of oxygen in blood, the partial pressure of the dissolved oxygen (p_{O_2}) can be related to its concentration (c_{pl}) by means of Henry's law:

$$p_{O_2} = \frac{k_{hn}}{\rho_{bl}} \cdot c_{pl}, \quad (2.3)$$

where $\rho_{bl} \approx 1000 \text{ kg/m}^3$ is the density of blood. The coefficient k_{hn} can be estimated from the fact that the concentration $c_{pl} \approx 0.13 \text{ mol/m}^3$ of the dissolved oxygen corresponds to the oxygen content of 3 ml O_2 /l blood, or the partial pressure of 13 kPa under normal conditions (Law and Bukwirwa, 1999), yielding $k_{hn} \sim 7.5 \cdot 10^5 \text{ mmHg} \cdot \text{kg/mol}$ for oxygen dissolved in blood.

Hemoglobin-bound oxygen. The partial pressure of the hemoglobin-bound oxygen p_{O_2} depends on its concentration through the Hill equation:

$$c_{bnd} = c_{\max} S(p_{O_2}), \quad S(p_{O_2}) \equiv \frac{(bp_{O_2})^\alpha}{1 + (bp_{O_2})^\alpha}, \quad (2.4)$$

where c_{\max} is the oxygen content of the maternal blood at full saturation, S is the oxygen-hemoglobin dissociation function, and $b \approx 0.04 \text{ mmHg}^{-1}$ and $\alpha \approx 2.65$ are coefficients of the Hill equation, whose values are obtained by fitting the experimental curve of Severinghaus (1979, Fig. 2.2).

The equilibrium relation between c_{pl} and c_{bnd} can then be obtained by substituting Eq. (2.3) into Eq. (2.4):

$$c_{bnd} = c_{\max} S\left(\frac{k_{hn}}{\rho_{bl}} c_{pl}\right). \quad (2.5)$$

2.2.3 Diffusive-convective transport of oxygen

Now that we have established the relationship between the bound and the dissolved oxygen in the maternal blood, we are ready to describe its transport. The diffusive-convective transport of oxygen is governed by the mass conservation law for the total concentration of oxygen in a volume of blood:

$$\frac{\partial(c_{pl} + c_{bnd})}{\partial t} + \text{div} \vec{j}_{c_{\text{tot}}} = 0. \quad (2.6)$$

Here $\vec{j}_{c_{\text{tot}}}$ is the total flux of oxygen, transported both by diffusion and convection for the dissolved form and only by convection (RBCs being too large objects) for the bound form:

$$\vec{j}_{c_{\text{tot}}} = -D \vec{\nabla} c_{pl} + \vec{u}(c_{pl} + c_{bnd}), \quad (2.7)$$

where \vec{u} denotes the MBF velocity, D is the oxygen diffusivity in blood and $\vec{\nabla} \equiv \left\{ \frac{\partial}{\partial x}; \frac{\partial}{\partial y}; \frac{\partial}{\partial z} \right\}$ is the gradient operator. Omitting the time derivative in the stationary regime, substituting Eq. (2.7) into Eq. (2.6) and choosing z as the direction of the MBF, we get

$$\Delta c_{pl} = \frac{u}{D} \frac{\partial(c_{pl} + c_{bnd})}{\partial z},$$

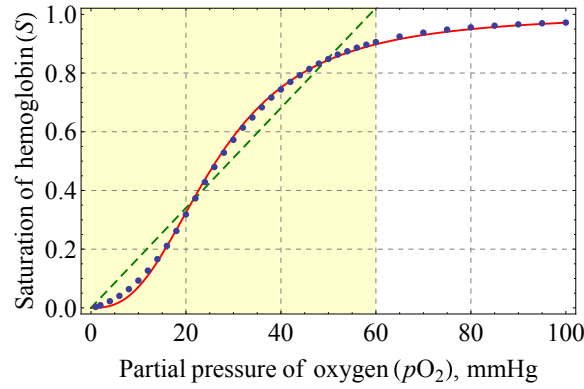


Figure 2.2. Oxygen-hemoglobin dissociation curve. In the figure: (i) the dots are the experimental data under normal conditions as obtained by Severinghaus (1979); (ii) the solid curve shows a fit of these data with the Hill equation (2.4), the coefficients being $\alpha = 2.65$, $b = 0.04 \text{ mmHg}^{-1}$; (iii) the straight dashed line is a linear approximation of the curve in the 0–60 mmHg region (shaded in yellow) as discussed in Section 2.2.4. The slope of the line is $\beta_{60} \approx 0.017 \text{ mmHg}^{-1}$

where $\Delta \equiv \frac{\partial^2}{\partial x^2} + \frac{\partial^2}{\partial y^2} + \frac{\partial^2}{\partial z^2}$ is the Laplace operator. Using the relation (2.5) between the dissolved and the bound oxygen concentrations we then derive an equation for the unknown c_{pl} alone:

$$\begin{aligned} \Delta c_{pl} &= \frac{u}{D} \frac{\partial}{\partial z} \left(c_{pl} + c_{\max} S \left(\frac{k_{hn}}{\rho_{bl}} c_{pl} \right) \right) \\ &= \frac{u}{D} \left(1 + \frac{c_{\max} k_{hn}}{\rho_{bl}} S' \left(\frac{k_{hn}}{\rho_{bl}} c_{pl} \right) \right) \frac{\partial c_{pl}}{\partial z}. \end{aligned} \quad (2.8)$$

This equation is non-linear since c_{pl} also appears in the argument of the derivative of the Hill saturation function S' .

2.2.4 Linearization of the Hill equation

However, in a first approximation, S can be linearized by assuming S' to be constant in the range of oxygen partial pressures encountered in the human placenta. The idea of the linearization is simple: to replace the sigmoid saturation function (2.4) with a linear function of p_{O_2} . Although it is natural to make the line pass through the origin, the slope of the line may be chosen differently depending on the range of partial pressures in which we approximate the curve (Fig. 2.2). Data found in the literature indicate that the maternal blood *in the IVS* of the human placenta has a p_{O_2} of about 60 mmHg (see discussion on p. 72). We further suppose that this partial pressure is the maximal value in the IVS and hence delimits the range of the needed linear approximation. Fitting the experimental curve of Severinghaus (1979) in the region 0–60 mmHg with a straight line passing through zero, we obtain a linear approximation

$$S(p_{O_2}) \approx \beta_{60} p_{O_2}, \quad S'(p_{O_2}) = \beta_{60} \approx 0.017 \text{ mmHg}^{-1},$$

displayed in Fig. 2.2.

This approximation leads to the following relation between c_{tot} , c_{pl} and c_{bnd} :

$$c_{\text{tot}} \equiv c_{\text{pl}} + c_{\text{bnd}} = c_{\text{pl}}B$$

or

$$c_{\text{pl}} = \frac{c_{\text{bnd}}}{B-1} = \frac{c_{\text{max}}}{B-1} S(p_{\text{O}_2}), \quad \text{where } B \equiv \left(1 + \frac{c_{\text{max}} \beta_{60} k_{\text{hn}}}{\rho_{\text{bl}}}\right). \quad (2.9)$$

From Eq. (2.7), a linearized version of the corresponding total oxygen flux is then:

$$\vec{j}_{c_{\text{tot}}} = -D \vec{\nabla} c_{\text{pl}} + \vec{u} c_{\text{pl}} B. \quad (2.10)$$

Finally, the partial differential equation (2.8) becomes

$$\Delta c_{\text{pl}} = \frac{uB}{D} \frac{\partial c_{\text{pl}}}{\partial z}. \quad (2.11)$$

We emphasize here that neglecting oxygen-hemoglobin interaction would be equivalent to setting $B = 1$, which would lead to a hundred-fold underestimation of this constant (Table 2.2).

2.2.5 Boundary conditions

To complete the mathematical formulation of the problem, boundary conditions should be imposed on Eq. (2.11). The model assumptions (Section 2.1.1) transform into the following boundary conditions:

- The boundary of the large cylinder represents the boundary of a stream tube. Assuming there is no exchange of oxygen between different stream tubes or that the exchange rate is equal in both directions, we consider zero flux on its wall:

$$\frac{\partial c_{\text{pl}}}{\partial n} = 0,$$

where $\partial/\partial n$ is the normal derivative directed outside the IVS.

- The uptake at the effective feto-maternal interface (villi borders) is proportional to the oxygen concentration in plasma at the maternal side of the membrane:

$$D \frac{\partial c_{\text{pl}}}{\partial n} + w c_{\text{pl}} = 0,$$

where w is the permeability of the interface which accounts for the resistance of fetal epithelial and endothelial layers as well as for the diffusion in the connective tissue layer separating them.

- The oxygen concentration is uniform and constant at the stream tube entrance (at $z = 0$):

$$c_{\text{pl}}(x, y, z = 0) = c_0, \quad \forall (x, y) \in S_{\text{IVS}},$$

where c_0 is the oxygen concentration in the incoming blood plasma.

2.2.6 Conversion to a 2D eigenvalue equation

Resolution of Eq. (2.11) can be simplified by taking into account the translational symmetry of the model along the z axis. To do that, we use a standard method of separation of variables (or spectral decomposition) to separate the coordinate z along the stream-tube axis from the coordinates x and y in the transverse cross-section. The general solution of Eq. (2.11) then takes the following form:

$$c_{pl}(x, y, z) = c_0 \sum_{j=1}^{\infty} a_j v_j(x, y) e^{-\mu_j z}, \quad (2.12)$$

where $\{\mu_j\}$ are the reciprocals of the characteristic oxygen uptake lengths in z direction for each mode, and $\{a_j\}$ are the weights of c_{pl} in the orthonormal eigenbasis $\{v_j(x, y)\}$ of the Laplace operator Δ_{xy} in the transverse cross-section. The functions $\{v_j(x, y)\}$ satisfy the following equations:

$$\left\{ \begin{array}{ll} (\Delta_{xy} + \Lambda_j) v_j = 0 & \text{in the IVS,} \end{array} \right. \quad (2.13)$$

$$\left\{ \begin{array}{ll} \frac{\partial v_j}{\partial n} = 0 & \text{on the stream-tube boundary,} \end{array} \right. \quad (2.14)$$

$$\left\{ \begin{array}{ll} \left(\frac{\partial}{\partial n} + \frac{w}{D} \right) v_j = 0 & \text{on the villi boundaries,} \end{array} \right. \quad (2.15)$$

$$\left\{ \begin{array}{ll} \sum_j a_j v_j = 1 & \text{in the } z = 0 \text{ plane,} \end{array} \right. \quad (2.16)$$

where

$$\Delta_{xy} \equiv \frac{\partial^2}{\partial x^2} + \frac{\partial^2}{\partial y^2}, \quad \Lambda_j \equiv \mu_j^2 + \mu_j \frac{uB}{D}. \quad (2.17)$$

The Laplace operator eigenvalues $\{\Lambda_j\}$, the eigenfunctions $\{v_j(x, y)\}$ and the weights $\{a_j\}$ are determined by Eqs (2.13–2.17) for a given cross-section. Additionally, it follows from Eq. (2.16) that $a_j \equiv \int_{S_{IVS}} v_j dS$, when eigenfunctions are L_2 -normalized ($\int_{S_{IVS}} v_j^2 = 1$). Note that thanks to the translational symmetry of the problem, the characteristic decay rates of the oxygen concentration along the z -axis are defined by the eigenvalues of the Laplace operator in the cross-section Δ_{xy} (Eq. 2.17).

2.2.7 General expression for oxygen uptake

To finish the description of the model, we need to obtain an expression defining the integral oxygen uptake of the stream tube. According to the mass conservation law, the oxygen uptake up to a length L is equal to the difference between the oxygen inflow into the system at $z = 0$ and the oxygen flow at the position $z = L$ in the stream tube. Knowing this and using Eqs (2.10) and (2.12) one can then derive the explicit

dependence of oxygen uptake on the stream-tube length:

$$\begin{aligned}
 F(L) &= \int_{S_{IVS}} (\vec{j}_{\text{ctot}} \cdot \vec{n}_z)|_{z=0} dS - \int_{S_{IVS}} (\vec{j}_{\text{ctot}} \cdot \vec{n}_z)|_{z=L} dS \\
 &= c_0 \sum_{j=1}^{\infty} a_j^2 (D\mu_j + uB) (1 - e^{-\mu_j L}),
 \end{aligned} \tag{2.18}$$

where \vec{n}_z is a unit vector in the z direction and the definition of $\{a_j\}$ (Section 2.2.6) has been used. This is an exact expression for oxygen uptake, into which the geometrical structure of a placental cross-section enters through the spectral characteristics $\{\mu_j\}$ and $\{a_j\}$.

2.3 Model parameters

The model includes the following geometrical and physiological parameters:

- an oxygen-hemoglobin dissociation constant (B),
- the oxygen concentration in the blood plasma at the entrance to the IVS (c_0),
- the maximal hemoglobin-bound oxygen concentration (c_{max}),
- the diffusivity of oxygen in blood (D),
- the average stream-tube length (L_0),
- the average radius of a placentone (R),
- an effective radius of the fetal villi (r_e),
- the MBF velocity (u),
- the permeability of the feto-maternal interface (w).

A relatively small stream-tube radius R_{num} is used to speed up computations, but all results are rescaled to the placentone radius R by multiplying the uptake by R^2/R_{num}^2 . The details of computation of these parameters are described below, while their values are summarized in Table 2.2. The uncertainties in the experimental parameters were estimated in cases when such information was available from the source.

2.3.1 Calculation of the model parameters

Maximal bound oxygen concentration in maternal blood (c_{max}). c_{max} is the maximal oxygen concentration, which a unit of blood volume would contain at the 100 % saturation only due to oxygen binding to hemoglobin molecules. To calculate c_{max} , one needs to multiply the following quantities:

- The concentration of hemoglobin in blood. The pregnant women hemoglobin level at term is 0.1194 ± 0.0007 g Hb/ml blood (Wills et al., 1947).

Table 2.2. Parameters of the human placenta used in the calculations. The calculation of their values is described in Section 2.3. No experimental error estimation was available for u and L_0

Parameter	Symbol	Mean \pm SD
Maximal Hb-bound oxygen concentration at 100 % Hb saturation, mol/m ³	c_{\max}	7.30 ± 0.11
Oxygen-hemoglobin dissociation constant	B	94 ± 2
Concentration of oxygen dissolved in blood at the entrance to the IVS, 10^{-2} mol/m ³	c_0	6.7 ± 0.2
Oxygen diffusivity in blood, 10^{-9} m ² /s	D	1.7 ± 0.5
Effective villi radius, 10^{-6} m	r_e	41 ± 3
Permeability of the effective materno-fetal interface, 10^{-4} m/s	w	2.8 ± 1.1
Placentone radius, 10^{-2} m	R	1.6 ± 0.4
Radius of stream tube used in numerical calculations, 10^{-4} m	R_{num}	6
Velocity of the maternal blood flow, 10^{-4} m/s	u	6
Stream-tube length, 10^{-2} m	L_0	1.6

- The oxygen binding capacity of hemoglobin. The adult person hemoglobin binding capacity is 1.37 ± 0.02 ml O₂/g Hb (Dijkhuizen et al., 1977).
- The amount of substance in 1 l of oxygen. A liter of any gas taken at normal conditions contains $1/22.4$ mol of substance.

Using these data we obtain

$$c_{\max} = 0.1194 \frac{\text{g Hb}}{\text{ml blood}} \cdot 1.37 \frac{\text{ml O}_2}{\text{g Hb}} \cdot \frac{1}{22.4} \frac{\text{mol}}{\text{l O}_2} = 7.30 \pm 0.11 \text{ mol/m}^3$$

Oxygen-hemoglobin dissociation constant (B). The oxygen-hemoglobin dissociation constant B represents the interaction of oxygen with hemoglobin in Eq. (2.11) after the Hill equation is linearized:

$$B \equiv 1 + \frac{c_{\max} \beta_{60} k_{\text{hn}}}{\rho_{\text{bl}}}.$$

With $c_{\max} = 7.30 \pm 0.11$ mol/m³, Henry's law coefficient $k_{\text{hn}} \approx 7.5 \cdot 10^5$ mmHg · kg/mol (Section 2.2.2), the slope of the linearized Hill equation $\beta_{60} = 0.0170 \pm 0.0003$ mmHg⁻¹ (Section 2.2.4 and Fig. 2.2), and the density of blood $\rho_{\text{bl}} \approx 10^3$ kg/m³ (as close to the density of water), one obtains $B = 94 \pm 2$.

Concentration of oxygen dissolved in the blood plasma at the entrance to the IVS (c_0).

The concentration c_0 is derived from the oxygen saturation of the maternal blood entering the placenta through a formula, which follows from the Hill equation (2.9):

$$c_0 = c_{\text{pl}}(z = 0) = \frac{1}{B - 1} \cdot S(p_{\text{O}_2}) \cdot c_{\max},$$

where S is the oxygen-hemoglobin dissociation function of Hill and the z -axis follows the axis of the stream tube, with $z = 0$ located at the entry plane of the model.

After the 12th week postmenstruation, the p_{O_2} was found to be 90 mmHg in the uterine artery, 61 mmHg in the IVS and 47 mmHg in the decidual vein (Rode-

sch et al., 1992, Jauniaux et al., 2000, Challier and Uzan, 2003). Taking the IVS value of 61 mmHg (no error estimation available) together with the hemoglobin dissociation curve (Fig. 2.2), one gets the hemoglobin saturation $S(61 \text{ mmHg}) \approx 85\%$. Supposing that it is equal to the hemoglobin saturation at the entrance to the IVS, one then obtains $c_0 = (6.7 \pm 0.2) \cdot 10^{-2} \text{ mol/m}^3$ (error estimation for c_0 stems from the known error for B).

Oxygen diffusivity in blood plasma (D). The oxygen diffusivity in the blood plasma has been measured under different conditions with the average value being $D = (1.7 \pm 0.5) \cdot 10^{-9} \text{ m}^2/\text{s}$ (Wise and Houghton, 1969, Moore et al., 2000a).

Effective villi radius (r_e). Histological slides of the human placenta show that the cross-sections of the fetal villi are not circular. Traditionally in the literature, the mean diameter (or caliber) of a villus is estimated either by averaging the length of all line segments with both ends lying on the villus boundary and passing through the barycenter of the villus¹ or just as the largest diameter of the villus. Such measurements yield a mean villi radius of 25–30 μm for terminal and mature intermediate villi, which are known be the main sites of oxygen exchange (Sen et al., 1979). However, such calculation ignores the fact that due to the complicated shape of the villous boundary, the perimeter of a villus is larger than that of a circle with the radius calculated this way. The surface area of the villi is one of the main determinants of the exchange rate.

To account for both the area ($S_{\text{sm.v}}$) and the absorbing perimeter ($P_{\text{sm.v}}$) of small villi cross-sections in our model, an effective villi radius (r_e) is introduced to give the same perimeter-to-area ratio for villi cross-sections ($\varepsilon_{\text{sm.v}} \equiv P_{\text{sm.v}}/S_{\text{sm.v}}$, also called surface density) as in histological slides. Since for N cylinders of radius r , $\varepsilon_{\text{sm.v}} = 2\pi r N / (\pi r^2 N) = 2/r$, by analogy, we define the effective villi radius r_e for arbitrary villi shapes as $r_e \equiv 2/\varepsilon_{\text{sm.v}} \equiv 2S_{\text{sm.v}}/P_{\text{sm.v}}$. The value of $\varepsilon_{\text{sm.v}}$ is taken from histomorphometrical studies.

Experimental values of the perimeter-to-area ratio $\varepsilon_{\text{sm.v}}$ and the effective radii calculated from them are given in Table 2.3. The area ($S_{\text{sm.v}}$) and the perimeter ($P_{\text{sm.v}}$) of small villi cross-sections are traditionally reported in terms of small villi volume ($V_{\text{sm.v}}$) and small villi surface area ($A_{\text{sm.v}}$) respectively obtained by scaling them to the size of the whole placenta. In spite of this recalculation procedure, the same formula remains valid for $\varepsilon_{\text{sm.v}}$: $\varepsilon_{\text{sm.v}} = A_{\text{sm.v}}/V_{\text{sm.v}}$. Averaging the table data, one gets $r_e = 41 \pm 3 \mu\text{m}$ for the effective villi radius. Note that this value is slightly larger than the traditionally measured average villi radius as it accounts for the correct perimeter-to-area ratio of the villi cross-sections.

Permeability of the effective feto-maternal interface (w). The permeability of the effective feto-maternal interface is a local transfer characteristic, which has been studied before under the form of *oxygen diffusing capacity* (D_p). We show below how both characteristics are related and how one can be recalculated into the other. Following Bartels et al. (1962), Mayhew et al. (1984), we define D_p as a volume of gas (measured

¹It is not explicitly stated, but most probably, the caliber was not measured for villi whose barycenter lies outside the villus.

Table 2.3. Estimations of the effective villi radius r_e . The average small villi fractions in all villi volume (66.5%) and surface area (77.3%) (Sen et al., 1979) were used for calculations, when these data were not directly available from the experiment. Note that the used raw data of Mayhew et al. (1993a) are actually reported in Lee and Mayhew (1995). Only 10 placentas at 40 weeks of gestation are taken for calculations from the 21 placentas studied by Aherne and Dunnill (1966)

	Mayhew and Jairam (2000)	Nelson et al. (2009)	Aherne and Dunnill (1966)	Lee and May- hew (1995)	Mayhew et al. (1993a)
Small villi volume ($V_{sm.v}$), cm^3	130	220	190	110	150
Small villi surface area ($A_{sm.v}$), m^2	7	11	9	5	7
Perimeter-to-area ratio ($\varepsilon_{sm.v}$), mm^{-1}	54	50	47	45	47
Effective villi radius (r_e), μm	37	40	43	44	42

under normal conditions) transferred per minute per average oxygen partial pressure difference between the maternal and the fetal blood: $D_p = V_{O_2} / (t(\overline{p_{mat}} - p_{fet}))$, where the horizontal bar denotes averaging over the surface of the fetomaternal interface. The oxygen diffusing capacity has been calculated for the placenta as a whole, but the details of calculations (namely, rescaling) demonstrate its local nature (Aherne and Dunnill, 1966, Laga et al., 1973, Teasdale, 1982, 1983, Mayhew et al., 1984). The following points need to be clarified:

1. Our model assumption that the fetal blood is a perfect sink for oxygen implies that the partial pressure of oxygen (p_{O_2}), appearing in our model, is not its absolute value in the maternal blood, but the difference in oxygen partial pressures on both sides of the membrane: $p_{O_2} = p_{mat} - p_{fet}$. This partial pressure can be recalculated into the concentration of oxygen dissolved in the blood plasma (c_{pl}) using Henry's law (Section 2.2.2): $p_{O_2} = c_{pl}k_{hn}/\rho_{bl}$. The volume of the transferred oxygen V_{O_2} measured under normal conditions can be recalculated into the amount of substance: $V_{O_2} = \nu_{O_2}V_m$, where $V_m = 22.4 \text{ l/mol}$. For the diffusing capacity one then obtains

$$D_p = \frac{\nu_{O_2}}{t} \frac{V_m \rho_{bl}}{k_{hn} \bar{c}_{pl}} \quad \text{or} \quad \frac{\nu_{O_2}}{t} = \frac{D_p k_{hn} \bar{c}_{pl}}{V_m \rho_{bl}}, \quad (2.19)$$

where the horizontal bar denotes averaging over the surface of the fetomaternal interface.

2. Using boundary conditions (2.15), we can write the total oxygen uptake as

$$F = - \int_{A_{sm.v}} D \frac{\partial c_{pl}}{\partial n} dS = w \int_{A_{sm.v}} c dS = w \bar{c}_{pl} A_{sm.v},$$

where $A_{sm.v}$ is the total absorbing surface of the fetal villi. The permeability w can then be rewritten as $w = F / (A_{sm.v} \bar{c}_{pl})$. By definition, the oxygen uptake F is the amount of oxygen transferred to the fetus (ν_{O_2}) divided by the time of exchange t ,

so for w one gets

$$w = \frac{\nu_{O_2}}{t} \frac{1}{\bar{c}_{pl} A_{sm.v}}. \quad (2.20)$$

Substituting Eq. (2.19) into Eq. (2.20), one relates the permeability w to the experimental diffusing capacity:

$$w = \frac{D_p k_{hm}}{V_m \rho_{bl} A_{sm.v}}. \quad (2.21)$$

According to morphometric diffusing capacity models, the diffusing capacity of the human placenta lies in the 3–5 ml/(min · mmHg) range (see discussion in Section 1.6.4 on p. 46). The average value is then $D_p \approx 4.0 \pm 1.0$ ml/(min · mmHg). The absorbing surface is that of the small villi (terminal and mature intermediate), $A_{sm.v} = 7.8 \pm 2.3$ m² (Table 2.3), since they correspond to the main site of the exchange. Using these data, we finally get $w = (2.8 \pm 1.1) \cdot 10^{-4}$ m/s.

Note that this way of calculation of w introduces an error in its value, since the D_p includes a contribution from the diffusion path of oxygen in the maternal blood plasma and from oxygen interaction with the maternal hemoglobin (see Section 1.6.4). However, as discussed earlier (Section 1.6.4), the combined contribution of these two elements of the oxygen diffusion path to the total diffusive resistance $1/D_p$ is less than 5 %. Therefore, the error introduced in the value of w by the provided calculation method must also not exceed 5 %.

The presented calculations can be compared with permeability estimations on the local scale of one villus. For this purpose, oxygen flux across a region of villous membrane j is approximated as a product of local membrane permeability w and concentration difference on both sides of the membrane. If villi are considered to be perfect sinks of oxygen, this concentration difference is equal to oxygen concentration in maternal blood plasma c_{pl} , so we get $j = w c_{pl}$. At the same time, the only transport process inside the membrane is 1D diffusion, so the same flux can be written as $j = D c_{pl} / h$, where D is the diffusivity of oxygen, and the concentration gradient is approximated as concentration difference on both sides of the membrane (c_{pl}) divided by its local thickness (h). Combining the two equations for j , one can estimate w as $w = D/h$. Substituting $D = (1.7 \pm 0.5) \cdot 10^{-9}$ m²/s (Table 2.2) and taking h equal to the harmonic thickness of the terminal-villus membrane $h = 3.1 \pm 0.2$ μm (placentone-averaged data of Critchley and Burton, 1987, see also discussion in Section D.1.1 of Appendix D on p. 150), one gets $w = (5.5 \pm 1.7) \cdot 10^{-4}$ m/s. The obtained value has the same order of magnitude, but is twice higher than the previously calculated value of $w = (2.8 \pm 1.1) \cdot 10^{-4}$ m/s. This discrepancy can be explained by inhomogeneous oxygen distribution in the IVS and on villi boundaries (e.g., because of higher exchange speed, there may be less oxygen available in the IVS near thinner membrane regions), by participation of larger villi with thicker membranes (such as immature intermediate villi) in oxygen uptake, by differences in oxygen diffusion coefficient in the membrane and in the blood plasma, or by the error introduced in the calculations by the perfect sink approximations. The morphometric diffusing capacity D_p also includes other components of the oxygen diffusion path (such as villous stroma, fetal capillary endothelium and fetal blood plasma, see discussion in

Section 1.6.4 on p. 46), and is thus likely to yield a value of w more adapted to our stream-tube model (in the model, all oxygen diffusion path components are replaced by a single membrane). We will therefore use the value $w = (2.8 \pm 1.1) \cdot 10^{-4} \text{ m/s}$ in the calculations of this thesis.

Radius of a placentone at term (at least 37 completed weeks of pregnancy) (R). A normal placenta numbers 50 ± 10 (Benirschke et al., 2006, p. 161) placentones, whereas the average radius of the placental disk is $11 \pm 2 \text{ cm}$ (Salafia et al., 2012). Division of the disk area by the number of functional units yields $R = 1.6 \pm 0.4 \text{ cm}$. The cross-section of a placentone of this radius can contain up to $1.5 \cdot 10^5$ fetal villi of radius r_e . Numerical resolution of the problem for such a large number of villi would be too time-consuming. At the same time, for rather uniform distributions of villi, the oxygen uptake is likely to depend on the ratio of the total number of villi and the cross-sectional area of the stream tube, rather than independently on these two variables. This statement will be proved in Chapter 3. This property allows us to perform the numerical calculations in this thesis for a smaller radius $R_{\text{num}} = 6 \cdot 10^{-4} \text{ m}$, and then rescale the obtained oxygen uptake to the placentone radius R by multiplying it by R^2/R_{num}^2 .

Remember also that the analysis of the characteristic time scales of the transfer processes in the human placenta shows that during the time that a small volume of blood spends in a placentone, the characteristic diffusion distance of oxygen in the stream-tube cross-section is of the order of 0.21 mm (Section 2.2.1). This means that the solution of the diffusion-convection equation in the stream tube of the chosen radius $R_{\text{num}} = 0.6 \text{ mm}$ will be effectively independent of the shape of the boundary, and hence, any shape of the external boundary can be chosen.

Maternal blood flow velocity (u). *In vivo* data on the linear maternal blood flow velocity in the IVS of the human placenta is scarce. To our knowledge, no direct measurements with sub-placentone resolution have ever been conducted (see Section 1.5). Among indirect estimations, the following approaches are worth attention:

1. The modeling by Burton et al. (2009) concluded that the linear blood velocity at the outlets of the spiral arteries towards term falls down to 0.1 m/s due to the dilation of the spiral arteries. The MBF velocity in the IVS must be even lower.
2. The order of magnitude of the linear MBF velocity can also be estimated as follows: the total maternal placental blood flow can be divided by the area of a cross-section of the whole placenta (performed parallel to the basal plate), which is occupied by the IVS. The total incoming flow is known to be of the order of 600 ml/min (Assali et al., 1953, Browne and Veall, 1953, Bartels et al., 1962), or 450 ml/min if one considers that 25 % of the flow passes through myometrial shunts (Bartels et al., 1962); the cross-sectional area of the placental disk is $\pi(11 \text{ cm})^2 \approx 380 \text{ cm}^2$; and the fraction of the cross-section occupied by the IVS is around 35 % (Aherne and Dunnill, 1966, Laga et al., 1973, Bacon et al., 1986, Mayhew et al., 1986).² For

²There is no contradiction between this value of 35 % and the optimal villi density of around 50 %

Table 2.4. Radioactive dye diffusion in the human IVS at term (original data taken from Burchell, 1967)

"Diffusion diameter" ($2a$), cm	≤ 3.5
Dye observation time (t_{obs}), s	30
Incoming blood flow per 1 placentone (q), ml/min	24
Transit time of blood through the IVS (τ_{tr}), s	28
Mean velocity of blood in the IVS (u), m/s	$6 \cdot 10^{-4}$

the estimation of the average MBF we then get: $u \sim 450 \text{ ml/min} / (380 \text{ cm}^2 \cdot 0.35) \approx 5.6 \cdot 10^{-4} \text{ m/s}$.

3. A more accurate estimate of the linear maternal blood velocity can be obtained from the results of the experimental study by Burchell (1967), in which angiographic photographs of the human uterus perfused with a radioactive dye at different stages of pregnancy have been obtained by X-ray. This study reported the time during which the radioactive dye was observed in the placenta (t_{obs}) and the corresponding "diffusion diameter" of the dye spot ($2a$) at term (Table 2.4). A "diffusion diameter"³ was defined by Burchell as the mean maximal diameter of the zone of the convective propagation of the radioactive material, and the dye observation time (t_{obs}) as the time elapsed since the appearance of the radioactive dye till its disappearance from the IVS. Burchell's data reproduced in Table 2.4 shows that the "diffusion diameter" (up to 3.5 cm) is of the order of the placentone diameter ($2R \approx 3.2 \text{ cm}$, Table 2.2), which justifies the conclusion of the author that in this study, blood propagation in separate placentones has been observed.

The used dye volume V_{dye} was reported to be 50 cm^3 . For estimations, we neglect the effect of its further dissolution and of increase of the dye volume due to mixing with dye-free blood. We also assume that the dye volume is equally distributed between $n_{\text{cot}} = 50$ placentones of the term placenta (Benirschke et al., 2006). From these data, it is then possible to estimate the total maternal blood flow through one placentone (q , in ml/min), the linear maternal blood flow velocity in the IVS (u) and the transit time (τ_{tr}) of the maternal blood through the placentone. For this purpose, we assume that the IVS has the shape of a hemisphere of radius R , and that blood flows uniformly in radial directions from its center to the hemisphere boundary (this description is supported by the doughnut shape of the dye diffusion clouds reported in this and other studies, see Fig. 1.18). In this case, $q = (2\pi a^3/3 + V_{\text{dye}}/n_{\text{cot}})/t_{\text{obs}}$ and the transit time of the maternal blood through the placentone is $\tau_{\text{tr}} = 2\pi a^3/(3q)$. The average blood velocity in the placentone is $u = a/\tau_{\text{tr}}$.

Calculation results for q , u and τ_{tr} are presented in Table 2.4. The obtained transit time of the maternal blood of around 28 s corresponds to earlier estimates of other

discussed in Section 2.4.3, since the latter is the fraction of small villi in the area of a cross-section containing small villi and IVS only (all other components subtracted), whereas the former also accounts for large villi and non-IVS components of the placental cross-section.

³Since the process observed by Burchell was mainly convection and not diffusion, the term "convective diameter" would be more appropriate

authors (25–30 s, see [Burton et al., 2009](#)). The average IVS blood flow velocity is calculated to be of the order of $6 \cdot 10^{-4}$ m/s.

The three estimates ($u_1 < 0.1$ m/s, $u_2 \approx 5.6 \cdot 10^{-4}$ m/s and $u_3 \approx 6 \cdot 10^{-4}$ m/s) are compatible, and for the calculations we will use the value $u = 6 \cdot 10^{-4}$ m/s obtained from the third, the most precise method. We emphasize that MBF velocity may significantly vary between and within placentas, and the value $u = 6 \cdot 10^{-4}$ m/s should be treated as a mean value.

Stream-tube length (L_0). The stream-tube length L_0 is fixed to provide the same transit time of blood through the IVS as calculated from [Burchell \(1967\)](#), $\tau_{tr} = 28$ s (Table 2.4). If the velocity of the flow is $u \approx 6 \cdot 10^{-4}$ m/s, the calculations give $L_0 \approx 1.6$ cm (no error estimation available). Note that this value is comparable to, but smaller than the basic estimate as a doubled placenta thickness (for the idealized case when the maternal blood goes from the basal plate to the chorionic plate and then back). Possible explanations (such as the presence of the central cavity, the basal and the chorionic plate) will be discussed in details later in Section 4.1.1 on p. 106.

2.3.2 Concluding remarks

Note that besides the parameters traditionally used for modeling 1D exchange in the human placenta (namely, c_0 , c_{\max} , D , k_{hn} , β_{60} , ρ_{bl} , L , R , w and D_p), the construction of the STPM required several additional parameters to account for the 2D placental section structure (compare, for example, with [Power et al., 1972b](#)). These are:

- The linear maternal blood flow velocity in the exchange region (u , in m/s), since the usual integral flow (in ml/min) does not suffice.
- The volumetric density (φ) of small fetal villi in a given region.
- The effective radius of the fetal villi (r_e) that accounts for the non-circular shape of the fetal villi by providing the right perimeter-to-area ratio for the modeled villi cross-sections.

2.4 Numerical simulation

2.4.1 Circular villi. Solution convergence and validation

The obtained diffusion-convection equation (2.11) can now be numerically solved to yield the oxygen uptake in stream tubes of arbitrary geometry. We start the investigation of the relation between the structure and the function of the placenta with simple circular geometries (Fig. 2.3), while more sophisticated morphologies will be discussed in the next chapter. Distributions of circular villi are generated in the range of villi densities φ from 0.005 to 0.75, where the villi density is defined as the ratio of the cross-sectional area of the small villi ($S_{sm.v}$) to the total area of the stream tube cross-section (S_{tot}): $\varphi = S_{sm.v}/S_{tot}$. For the stream-tube of the radius $R_{num} = 600 \mu\text{m}$ (Table 2.2), these villi densities correspond to a range of villi numbers N from 1 to 160. The upper boundary

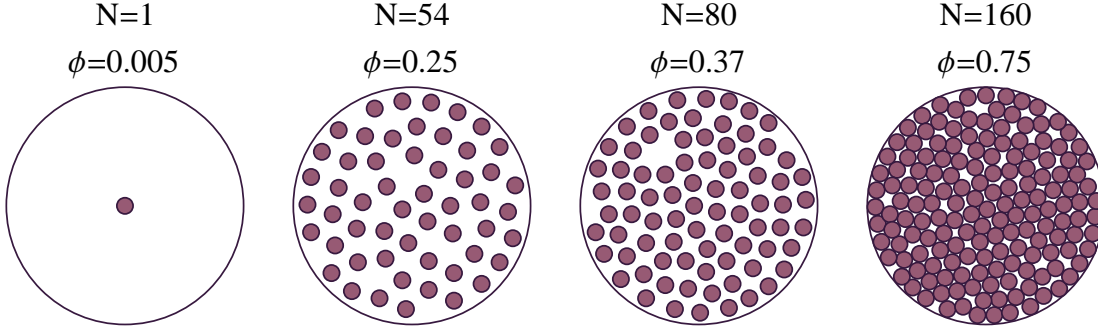


Figure 2.3. A range of villi densities for which the oxygen uptake has been calculated. The number of villi and the corresponding villi density is displayed above each case. The simulations have been carried out for all geometries in the range $N = 1-160$

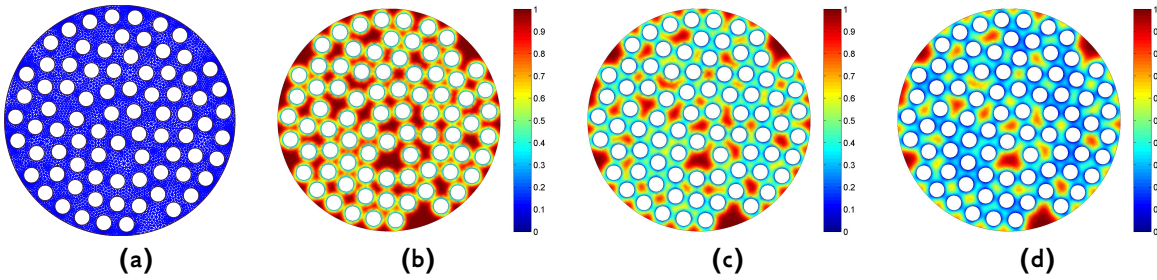


Figure 2.4. (a) A typical calculation mesh for $N = 80$ villi ($\phi = 0.37$). Figures (b), (c), (d) show oxygen concentration distributions at the stream-tube lengths $L = L_0/3$, $L = 2L_0/3$ and $L = L_0$ respectively for the same geometry ($L_0 = 1.6$ cm, see Table 2.2). For this illustration, the incoming oxygen concentration is set to 1, and the color axes represent oxygen concentrations in the range $[0, 1]$. All figures are plotted with 4500 eigenfunctions

of the range is chosen close to the maximal packing density of circles that one can achieve without resorting to special packing algorithms (Specht, 2009). The stream-tube radius R_{num} is used for calculations, but the oxygen uptake is then rescaled to the whole placentone by multiplication by R^2/R_{num}^2 .

The diffusion-convection equation (2.11) is solved by a finite elements method in the PDE Toolbox^R in Matlab^R. 2D IVS meshes necessary for the implementation of the finite elements method are created by Voronoï-Delaunay algorithm (Fig. 2.4a). Figures 2.4b–d illustrate oxygen concentration distributions in the stream-tube cross-section calculated at three different stream-tube lengths.

The convergence of the results has been tested by varying the number of eigenfunctions found and the number of mesh points. Figure 2.5 shows the dependence of the oxygen uptake at length L on the number of eigenfunctions. One can see that a good convergence is achieved with around 3000 eigenfunctions for all geometries in the range of stream-tube lengths expected in the human placenta ($L_0/3 \leq L \leq L_0$).

The following considerations can explain the seemingly large number of eigenvalues required for the convergence. The analysis shows that for the parameter values characterizing the human placenta (namely, the w/D ratio), each eigenfunction is localized in a small part of the cross-section. This means that each small pore of the IVS in the cross-section effectively transports oxygen independently from the other pores. At the same time, to adequately describe the oxygen transport in each small pore, one requires

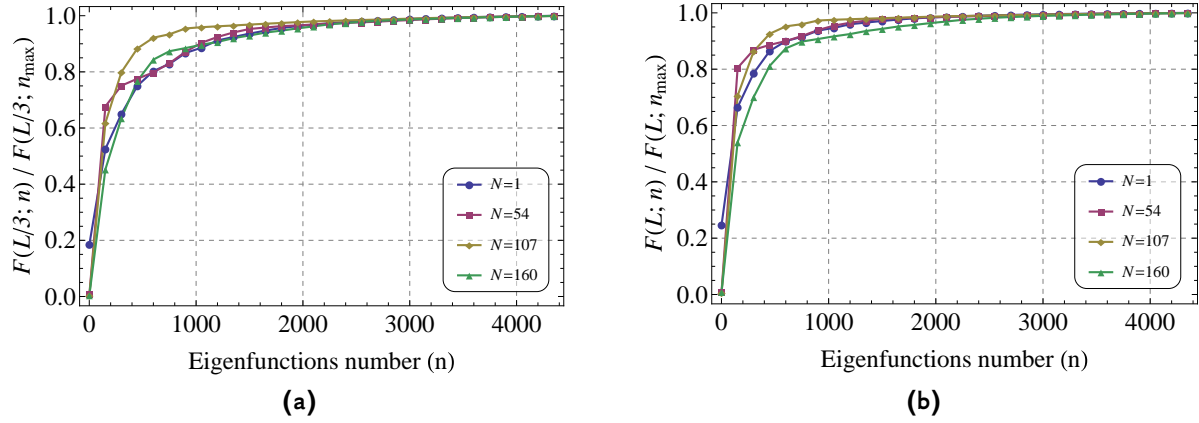


Figure 2.5. Convergence of the oxygen uptake $F(L; n)$ at the stream-tube lengths $L = L_0/3$ (a) and $L = L_0$ (b) with the number of eigenfunctions n for different numbers of villi N . Oxygen uptake for each geometry was normalized to the value $F(L; n_{\max})$ obtained for the maximal calculated number of eigenvalues $n_{\max} = 4500$. The convergence is slower at $L = L_0/3$ (a) than at $L = L_0$ (b), which is seen, for instance, in that the first 500 eigenvalues provide on average around 90 % convergence at $L = L_0$, while giving on average only 80 % convergence at $L = L_0/3$

several first eigenfunctions and relative eigenvalues. The first one or two of these eigenvalues give the main contribution to the transported concentration, while the subsequent modes provide smaller corrections.

The concentration $c_{pl}(r)$ and the oxygen uptake $F(L)$ for the case of one fetal villus (Krogh-type cylinder) have been compared to the exact analytical solution (Lundberg et al., 1963):

$$v_j(r) = A_j \left(J_0(\sqrt{\Lambda_j} r) - \frac{J_1(\sqrt{\Lambda_j} R)}{Y_1(\sqrt{\Lambda_j} R)} Y_0(\sqrt{\Lambda_j} r) \right),$$

$$\mu_j = \frac{\sqrt{B^2 u^2 + 4D^2 \Lambda_j} - Bu}{2D},$$

$$A_j = \left(2\pi \int_{r_0}^R \left(J_0(\sqrt{\Lambda_j} r) - \frac{J_1(\sqrt{\Lambda_j} R)}{Y_1(\sqrt{\Lambda_j} R)} Y_0(\sqrt{\Lambda_j} r) \right)^2 r dr \right)^{-1/2},$$

$$a_j = 2\pi \int_{r_e}^R A_j \left(J_0(\sqrt{\Lambda_j} r) - \frac{J_1(\sqrt{\Lambda_j} R)}{Y_1(\sqrt{\Lambda_j} R)} Y_0(\sqrt{\Lambda_j} r) \right) r dr,$$

where $\{\Lambda_j\}$ are defined as the roots of the equation

$$\left(\frac{w}{D} J_0(\sqrt{\Lambda_j} r_e) + \sqrt{\Lambda_j} J_1(\sqrt{\Lambda_j} r_e) \right) Y_1(\sqrt{\Lambda_j} R) - \left(\frac{w}{D} Y_0(\sqrt{\Lambda_j} r_e) + \sqrt{\Lambda_j} Y_1(\sqrt{\Lambda_j} r_e) \right) J_1(\sqrt{\Lambda_j} R) = 0,$$

$J_m(r)$ and $Y_m(r)$ are the m^{th} order Bessel functions of the first and the second kind respectively, r_e and R are the radii of the internal and the external cylinders respectively, and r is the radial coordinate. The plot of the exact solution (Fig. 2.6) shows that the relative error between the numerical and the exact oxygen uptake for the case of one villus is less than 5 % for all physiologically relevant stream-tube lengths. However, one

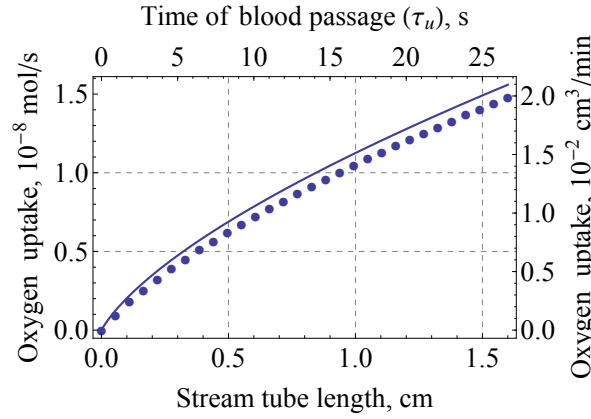


Figure 2.6. Comparison of the oxygen uptake of one villus calculated numerically with 4500 geometrical eigenvalues (points) and analytically (solid line). The seemingly large number of eigenvalues which still does not provide a complete convergence is explained by the fact that no direct account for the system's symmetry is given in the numerical simulations. This means that degenerate eigenvalues are found and counted multiple times, which correspond to the modes with a non-constant angular part, but whose contribution to the oxygen uptake is zero. It can be shown that 4500 numerical eigenvalues correspond to only around 100 non-degenerate eigenvalues of the analytical solution

may expect that the calculations error will be lower for other villi densities than in the one villus case, since in the latter case the symmetry of the geometry makes the Laplace operator eigenvalues degenerate, which effectively lowers the number of independent eigenvalues found (see the caption of Fig. 2.6) and the precision of the calculations.

2.4.2 Results

Figure 2.7a shows the dependence of oxygen uptake on the stream-tube length. One can see that the villi density which provides the maximal oxygen uptake depends on stream-tube length, all other parameters remaining fixed. In other words, *the most efficient geometry* (the one which gives the highest uptake for a fixed length, MBF velocity and incoming oxygen concentration) *is different for different stream-tube lengths*. The villi density corresponding to the maximal uptake will be called "optimal". The fact that there is an optimal villi density can be clearly seen in Fig. 2.7b, which shows the variation of oxygen uptake with villi density for a fixed stream tube length.

Both the maximal oxygen uptake and the corresponding optimal villi density depend on the average MBF velocity and on the stream-tube length L , which are the parameters the most susceptible to variations in different placentas and for which no error estimations were available (see Section 2.3). If the distribution of the MBF velocities in the IVS of the human placenta were known, with the help of Fig. 2.8a, *one could estimate the optimal villi density that would result in the maximal uptake* in any given region. Conversely, if one knew the average villi density in a placental region (e.g., from histological slides) and if the optimal placental function were assumed, *one could estimate the MBF velocity* in that region. The maximal oxygen uptake corresponding to a given villi density can be determined from Fig. 2.8c. The dependence of the optimal characteristics on the stream-tube length is shown in Figs 2.8b,d.

Our calculations show that for a healthy placenta (with the parameters given in Table 2.2), the optimal villi density is $\phi_0 = 0.47 \pm 0.06$ and the corresponding maximal

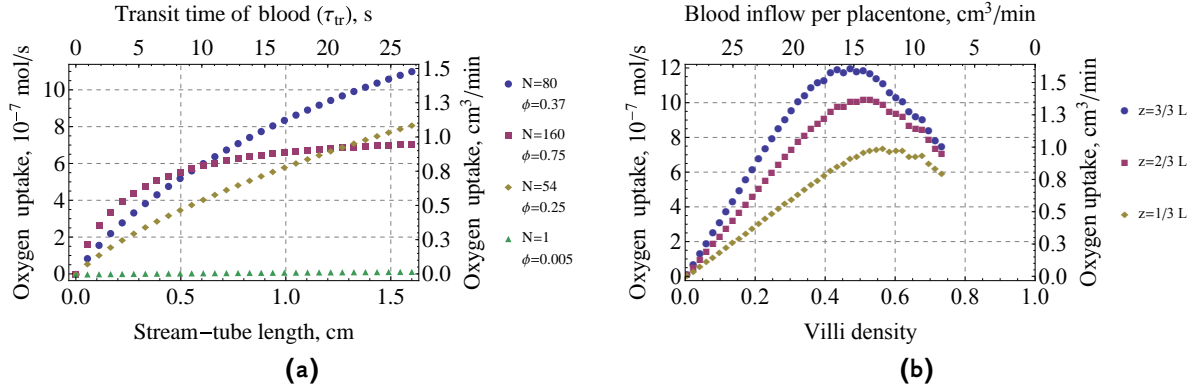


Figure 2.7. Oxygen uptake of a stream tube as a function of two geometrical parameters. (a): Oxygen uptake as a function of stream-tube length L for fixed villi densities ϕ . Various symbols represent the villi densities of Fig. 2.3. (b): Oxygen uptake as a function of villi density ϕ for three lengths L : $L_0/3$, $2L_0/3$, and L_0 . The peak uptake moves to smaller villi densities when the length L increases. Oxygen uptake has been calculated for R_{num} and rescaled to the placentone radius R by multiplying by R^2/R_{num}^2 . The transit time of the maternal blood through the stream tube ($\tau_{\text{tr}} = L/u$), the blood inflow per placentone ($u\pi R^2(1-\phi)$) and oxygen uptake in cm^3/min are shown on additional axes to simplify the comparison with physiological data. Note that in (b) the curves do not reach the expected limit of 1 for the optimal villi density, but rather stop around 0.75, which is explained by the circular villi shapes used in the calculations. The maximal packing density for the used radii ratio of $R_{\text{num}}/r_e \approx 14.63$ is known to be $\phi \approx 0.83$ or $N = 177$ cylinders (Specht, 2009). Without using the optimal packing algorithms, we have carried out the calculations up to the density $\phi = 0.75$, which we believe to be sufficient to represent densely packed regions of placental cross-sections (cf. Figs 1.15 and 2.3)

oxygen uptake is $F_{\text{max}} = (1.2 \pm 0.6) \cdot 10^{-6} \text{ mol/s} \approx 1.6 \pm 0.8 \text{ cm}^3/\text{min}$. The details of the provided error estimations can be found in Appendix C. It is worth noting that, to the precision of the calculations, no results dependence on oxygen diffusivity D was observed. Note that we have not included uncertainty estimations for L_0 and u in the calculations, which means that the uncertainties of ϕ_0 and F_{max} may be significantly underestimated. However, this was only due to the lack of experimental data, and the uncertainties can be corrected once new experimental measurements are performed. Note also that there is no means to estimate the error introduced by the assumptions of the model, which may be comparable to that caused by the uncertainties in the model parameters.

In summary, we have developed a stream-tube model of oxygen exchange in the human placenta that can be used to predict oxygen uptake from the cross-sectional histomorphometry performed on routinely prepared placental slides. For the moment, oxygen uptake was calculated numerically for a cross-section filled with uniformly distributed identical circular villi. The model was found to exhibit an optimal villi density (at which the oxygen uptake is maximal), all other parameters being fixed. *The optimal density is determined by a competition of two factors.* On one hand, larger villi density leads to larger exchange surface and thus larger uptake. On the other hand, larger villi density implies that less blood is coming into the placentone per unit of time, and hence a lower uptake rate. For a given set of placenta-specific parameters (Table 2.2), our model allows one to calculate the optimal villi density for a given placenta or placental region.

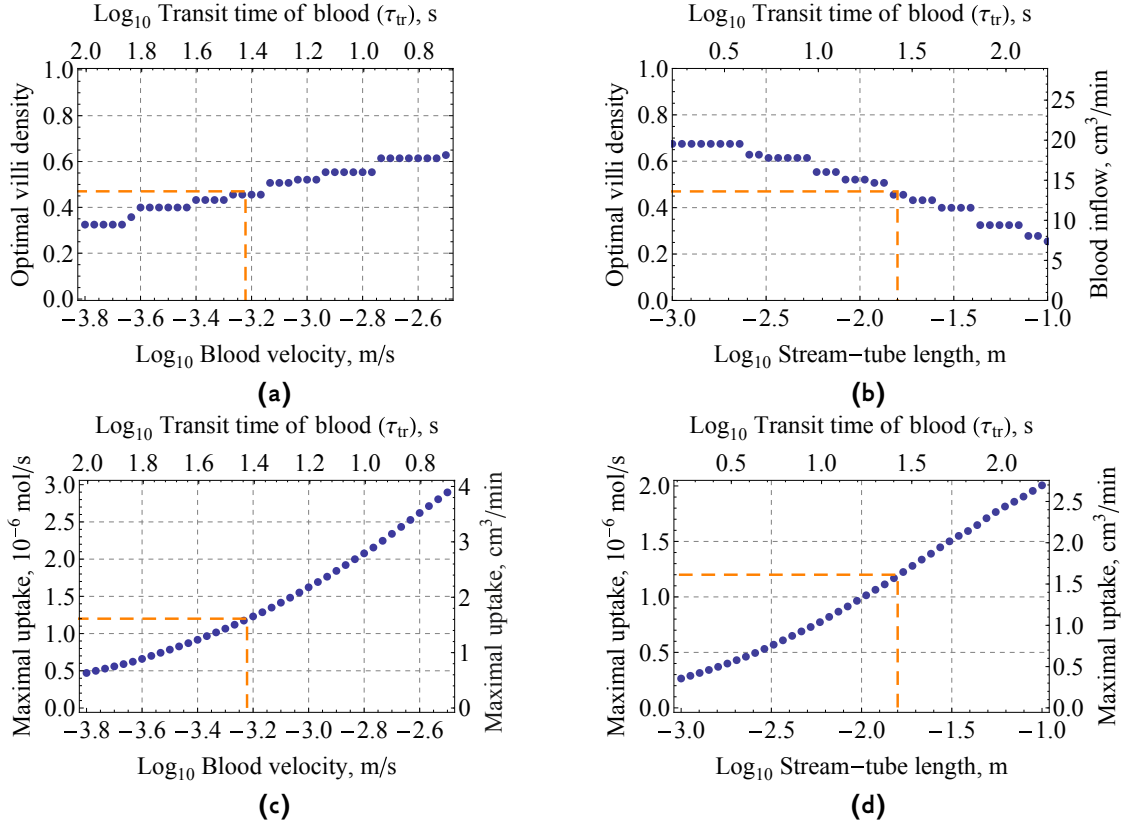


Figure 2.8. (a), (c): Dependence of the optimal villi density (a) and the maximal oxygen uptake (c) on the MBF velocity at the fixed length $L = L_0$ for a single placentone. (b), (d): Dependence of the optimal villi density (b) and the maximal oxygen uptake (d) on stream-tube length L for a single placentone. Dashed lines show the expected average stream tube length $L_0 = 1.6$ cm and the MBF velocity $u = 6 \cdot 10^{-4}$ m/s (Table 2.2). The transit time of the maternal blood through the stream tube ($\tau_{tr} = L/u$), the blood inflow per placentone ($u\pi R^2(1 - \phi)$) and oxygen uptake in cm³/min are shown on additional axes to simplify the comparison with physiological data

2.4.3 Comparison to the experimental data

Our calculated optimal density can be compared to the experimental data. The villi density ϕ can be determined from the published histomorphometrical data according to the formula $\phi = S_{sm.v}/(S_{sm.v} + S_{IVS})$, where $S_{sm.v}$ is the area of a histological cross-section occupied by the terminal and mature intermediate (small) villi, and S_{IVS} is the area of the cross-section occupied by the IVS. In the literature, $S_{sm.v}$ and S_{IVS} are traditionally obtained as surface area fractions of a 2D cross-section and then multiplied by the volume of the placenta to yield the volumes of small villi ($V_{sm.v}$) and of the IVS (V_{IVS}). However, the villi density can be calculated by the same formula from these volumes: $\phi = V_{sm.v}/(V_{sm.v} + V_{IVS})$ (Table 2.5). In cases when the fraction of terminal and mature intermediate villi in the total villi volume was not available, we have used the average fraction $\alpha \approx 0.665$ reported by Sen et al. (1979).

The optimal villi density 0.47 ± 0.06 obtained in our model is consistent with the experimental data which yield $\phi = 0.46 \pm 0.06$ (mean \pm SD). The quantitative agreement of the model predictions with physiological densities allows us to speculate that normal placentas are optimal oxygen exchangers, while pathological placentas (e.g. diabetic or pre-eclamptic) may behave sub-optimally. Although such an argument is plausible, further

Table 2.5. Villi density (ϕ) as calculated from the small villi volume ($V_{\text{sm.v}}$) and the IVS volume (V_{IVS}) measured in healthy term human placentas. Note that the used raw data of Mayhew et al. (1993a) are actually reported in Lee and Mayhew (1995). Only 10 placentas at 40 weeks of gestation are taken for calculations from the 21 placentas studied by Aherne and Dunnill (1966)

$V_{\text{sm.v}}, \text{ cm}^3$	$V_{\text{IVS}}, \text{ cm}^3$	ϕ	Source
130	170	0.43	Mayhew and Jairam (2000)
220	220	0.50	Nelson et al. (2009)
190	170	0.53	Aherne and Dunnill (1966)
110	180	0.38	Lee and Mayhew (1995)
150	170	0.47	Mayhew et al. (1993a)

analysis is required. Evidence from sheep specifically demonstrates a large reserve capacity for fetal oxygen supply, suggesting that variations in villi density and the MBF velocity might be a normal tolerated biological process (Carter, 1989). A similar behavior has been demonstrated earlier in human lungs, where lung geometry is not optimal under normal conditions, but its reserve capacity is used during exercises (Sapoval et al., 2002).

Villi density calculations in the placental cross-sections obtained *post-partum* may not precisely represent the *in vivo* situation due to the mechanical stress of the vaginal delivery (see Sisson, 1978), the cease of the maternal and fetal blood flows and to the formalin fixation. Because of these effects, the histological villi density is likely to provide an overestimation of the *in vivo* villi density. However, at the moment, there is no generally acknowledged method that could provide a correction for these changes (see discussion in Bouw et al., 1976, Sisson, 1978, Burton et al., 1987, Barker et al., 1988, Karimu and Burton, 1994).

2.4.4 Comparison to the porous medium model

The obtained optimal villi density can be compared to the predictions of the porous medium model (PMM, Chernyavsky et al., 2010). Chernyavsky et al. have obtained the value of the optimal fraction of the "villous material" ϕ_{all} close to 0.3. This value has to be translated into ϕ obtained in our stream tube placenta model (STPM) to allow for comparison. By definition, ϕ_{all} is the fraction of all villi in the combined volume of the IVS and the villi, while ϕ is defined as the fraction of *small* villi in the total volume of the IVS and the *small* villi:

$$\phi_{\text{all}} = V_{\text{vil}} / (V_{\text{vil}} + V_{\text{IVS}}), \quad \phi = V_{\text{sm.v}} / (V_{\text{sm.v}} + V_{\text{IVS}}).$$

One can therefore obtain the following translation formula:

$$\phi = \frac{\alpha}{\alpha - 1 + 1/\phi_{\text{all}}}, \quad (2.22)$$

where again $\alpha \equiv V_{\text{sm.v}} / V_{\text{vil}} \approx 0.665$ is the average fraction of small villi in the total villi volume (Sen et al., 1979). Application of this formula to the $\phi_{\text{all}} = 0.3$ of Chernyavsky et al. (2010) gives $\phi \approx 0.22$. Comparison of this value to the average experimental value $\phi = 0.46 \pm 0.06$ demonstrates a twofold underestimation of the observed villi

density in the PMM. The authors themselves admit that this value corresponds to high-altitude or pathological pre-eclamptic placentas rather than to healthy ones (Chernyavsky et al., 2010). A possible reason of this mismatch is that in the PMM, the optimal villi density appears as a trade-off between the blood flow resistance and a uniform uptake capacity of a passively transported substance, which does not bind to blood proteins. We propose a different explanation presenting *the optimal villi density as a trade-off between the absorbing surface of the fetal villi and the incoming flow of oxygen*. In this claim, we underline the role of the absorbing surface (which is hard to define in the PMM), but also suggest the importance of oxygen transport as compared to other substances.

The two models offer two different points of view on the modeling of the human placenta, which we discuss below.

1. Representation of the villi as a uniform and isotropic porous medium in the PMM ignores the placental geometry. The only geometrical parameter left (the volume fraction of the “villous material”, analogous to the villi density) cannot account for the independent roles played by the absorbing surface as well as by villi shapes and sizes. With no uptake surface, the PMM has to introduce a uniform volumetric uptake rate proportional to the IVS volume fraction. At the same time, experimental results show a considerable difference in the absorbing surface between healthy and pathological cases (Mayhew and Jairam, 2000).

Although the full 3D structure of the human placenta at the microscopic scale of individual villi is not available from the experiment, its 2D cross-sections can be obtained (see Section 1.5). Both PMM and STPM can use the villi density measured in these slides, but the STPM also accounts for the absorbing surface by using an effective villi radius (see Section 2.3). In the PMM, the geometry analysis cannot go beyond the villi density.

2. A simple uniform transport kinetics used in the PMM can account for the passive transport of certain metabolites, but is unable to describe the exchange of respiratory gases, since it ignores protein binding (and about 99 % of oxygen comes into the placenta bound to hemoglobin). However, the STPM can be used for oxygen and carbon dioxide transport, as well as for passive transport of other substances.
3. The use of slip boundary conditions yielding a flat velocity profile in the STPM needs further discussion. Ideally, a full model of the placental oxygen transport function would require knowing the full high-resolution 3D placental structure, so that the maternal blood velocity field could be computed by solving the Navier-Stokes equation with non-slip boundary conditions at the villous tree surface. Oxygen uptake could then be calculated using the convection-diffusion equation with the obtained velocity profile. Since modern experimental techniques can neither acquire the placental structure with a sufficient spatial resolution for such calculations, nor provide direct experimental measurements of the blood velocity field (see Sections 1.5 and 2.3), one must resort to simplifications. One way is to ignore the geometrical structure of the organ and substitute it by a uniform isotropic porous medium as in

the PMM. We chose an alternative way using the geometrical information available from 2D histological slides.

From a hydrodynamical point of view, non-slip boundary conditions would be the most natural for modeling the maternal blood flow in the real high-resolution 3D placental structure. Since the blood flow path in the real placenta geometry is rather irregular, *no developed velocity profile* is expected along the flow, and different cross-sections of the placenta may present different velocity profiles. However, these real velocity profiles can be far from that of the *developed* flow with non-slip boundary conditions. As a consequence, the advantage of choosing the non-slip boundary conditions over the slip ones in our already simplified structure is not so evident. In other words, although the slip and the non-slip boundary conditions may lead to different quantitative predictions, it is difficult to say, which prediction will be closer to the results in the real 3D placenta geometry. This statement can be verified either by modeling the blood flow in the full placental geometry (unavailable by now), or indirectly, by confronting models predictions to physiological observations. From the latter point of view, our model with the slip boundary conditions predicts an optimal villi density that is comparable to the experimentally observed one. A comparison with the predictions for the same simplified structure, but calculated with the non-slip boundary conditions presents an interesting perspective. Note also that the blood velocity used in our model should be understood as an *average* velocity across a stream tube or a placental region.

On the contrary, the PMM implicitly takes into account the non-slip boundary conditions (friction at the boundary) by using Darcy's law. However, the PMM has similar limitations as it obtains a developed blood flow that may be far from the real non-developed one. Moreover, the qualitative distribution of the maternal blood flow in the placentone obtained in the PMM remains approximate because:

- Darcy's law has never been proved valid for the human placenta due to the lack of experimental data.
- Darcy's law was argued to ignore the inertia of the flow and can possibly miss important characteristics of the flow in the organ: "given the architecture of a placental circulatory unit, the [maternal blood] jet penetration essential to good utilization of the full villous tree for mass transfer can occur only with appreciable fluid inertia" (Erian et al., 1977). However, the validity of this statement may depend on the location of the maternal vessels (see the discussion in Section 1.6.5). The STPM operates with an average velocity of the maternal blood in the organ which implicitly includes the inertia.

Note finally that our estimations have yielded a Schmidt number $Sc \approx 2 \cdot 10^6$ for convective mass transfer in the human placenta (see discussion in Section 2.1.2 on p. 63). Such a large value suggests that boundary-induced velocity gradients are much larger and much more localized than concentration gradients and justifies the use of the slip boundary conditions.

4. Finally, an appreciable advantage of the PMM is that the results are obtained analytically in a simple form. An approximate analytical solution to the STPM will be constructed in Chapter 3.

2.4.5 Other ways of comparison

Several other ways of validation of the presented model can be suggested. All of them require that some quantitative criteria of oxygen transfer efficiency be experimentally measured, and that histomorphometry be performed on the cross-sections of the analyzed placentas:

1. For each pregnancy, medical doctors possess approximate quantitative criteria of newborns' health, such as the birth-weight (BW) to the placenta weight (PW) ratio. If such information were obtained together with histological sections of the placenta, a correlation could be studied between the observed villi density, the optimal villi density predicted by the model and the BW/PW ratio. Such experiments, however, require the development of image analysis techniques that would allow for automatic segmentation and morphometric measurements to be performed on large histological placental sections. We discuss such techniques in Chapter 4.
2. In the primate placenta (the structure of which is similar to that of the human placenta), more information can probably be obtained from the experiment than it is ethical in the human placenta. Thus, (i) if one measured the average linear MBF velocity in the IVS of a placentone or in spiral arteries supplying it, and (ii) if morphometrical measurements were obtained after birth for the same placentone, then the relation between the blood velocity and the observed villi density could be compared with Fig. 2.8a. If additionally blood oxygenation were measured in the spiral arteries and the decidual veins, the dependence of oxygen uptake of a placentone on the MBF velocity could be compared to Fig. 2.8c. A systematic study of several placentones of the same or different placentas could further improve validation of the model.
3. Artificial perfusion experiments could also provide data comparable to the results of the model. In such setups, one could estimate the oxygen transfer rate of a given placenta, while having control over perfusion parameters. After the perfusion, histomorphometrical measurements could be performed. The fact that in the artificial perfusion experiments no-hemoglobin blood is normally used does not hamper the comparison, since such situation can be simulated in our model by allowing $B = 1$ (see also a discussion in Section 3.2.4 on p. 102). Experimental measurements of the villi density and oxygen uptake as functions of the perfusion parameters can then be compared to the predictions of the model.

These suggestions also represent possible directions of the further development of the experimental techniques.

2.4.6 Additional remarks

The assumption of the fetal villi being a perfect sink for oxygen erases the differences between the concurrent and the counter-current flow organizations (between arterial and venous fetal blood) since this difference essentially arises from the non-uniformity of the oxygen concentration in the fetal blood. The presented STPM can thus describe oxygen transfer in both these flow orientations. As for the cross-current (multivillous) blood flow organization, the model geometry can be changed to account for the angle α between the maternal and fetal flow directions. We have not incorporated such calculations into our model, because (i) there does not seem to exist any fixed co-orientation of the maternal and fetal blood flows in the human placenta, and (ii) the experimentally observed villi density is already a result of sectioning at an unknown (random) angle to fetal villi. If the mean value of this angle were known, the effect of sectioning could be to a first approximation corrected by multiplying the villi density and the villi perimeter used in the model by the factor $1/\cos(\alpha)$ before comparison to the values observed in experimental slides.

2.5 Conclusions

We presented a 2D+1D stream-tube model of oxygen transfer in the human placenta. Our model incorporates only the most significant geometrical and hemodynamic features, enabling it to remain simple, while yielding practical results.

In this chapter, it was shown that the construction of the STPM required several additional parameters to account for a 2D placental section structure as compared to the traditionally used ones. These parameters are the linear maternal blood flow velocity in the exchange region, the volumetric density of the small fetal villi and the effective radius of the fetal villi, which accounts for the non-circular shape of the fetal villi. Although we have indirectly estimated these parameters from the available experimental data, their direct measurement in the human placenta is a promising direction of the further development of the experimental techniques.

In spite of its simplicity, the model predicts the existence of an optimal villi density for each set of model parameters as a trade-off between the incoming oxygen flux and the absorbing villi surface. The predicted optimal villi density 0.47 ± 0.06 is compatible with experimentally observed values. The dependence of the optimal characteristics on the stream-tube length and the MBF velocity was investigated.

As a perspective, one can check the effect of relaxing some of the model assumptions. One direction of the future work could consist in relaxing the slip boundary conditions and comparing the results of the two approaches, which are likely to describe different limiting cases of the real *in vivo* flow. One can also study the effect of distributions of villi shapes and sizes on the predicted optimal villi density and the maximal uptake. Besides, the distribution of MBF velocity in the placenta is likely to be heterogeneous. If this distribution were known (for example, from experimental measurements), it could be combined with Fig. 2.8c to estimate variations of oxygen uptake in different placental regions. The placenta is also a living organ with its own oxygen consumption rate,

which may be considered proportional to the weight of its tissues. Once this effect is taken into account, the amount of oxygen transferred at the same villi density from the mother to the fetus should decrease, shifting the position of the optimal villi density peak in Fig. 2.7b to the left. Another direction is to apply the STPM to 2D histological slides in order to relate the geometrical structure of placental regions to their oxygen uptake efficiency and hence to be able to distinguish between healthy and pathological placentas. In the next chapter, we make a step in this direction by generalizing the developed model to the arbitrary shapes and sizes of the villi cross-sections, and by obtaining an analytical expression for oxygen uptake in such geometries.

Chapter 3

Approximate analytical solution

In this chapter, we derive a simple analytical approximation to the diffusion-convection equation for oxygen and extend the results of the previous chapter to arbitrary cross-sectional stream-tube geometries (Fig. 3.1). For this purpose, we

- note the linear dependence of oxygen uptake on stream-tube length at small lengths (Fig. 2.7a),
- take advantage of the known oxygen uptake at the infinite stream-tube length,
- analyze the dependence of the Laplace operator eigenvalues $\{\Lambda_j\}$ (Eq. (2.17)) on the area and the perimeter of the IVS in the stream-tube cross-section.

These elements are then combined in a single expression, which is shown to give an accurate estimation of oxygen uptake in a range of physiological stream-tube lengths and villi densities, for rather uniform distributions of villi in the cross-section.

The properties of this approximate expression are then explored. Firstly, it turns out that only two geometrical parameters (the villi density and the effective villi radius) suffice to accurately predict the oxygen uptake of a stream tube with an arbitrary (but uniform) cross-sectional geometry (Fig. 3.1). Secondly, all model parameters, geometrical and physiological, enter the final expression for oxygen uptake in only two parameter combinations, each having a clear physical meaning. Thirdly, optimization of oxygen

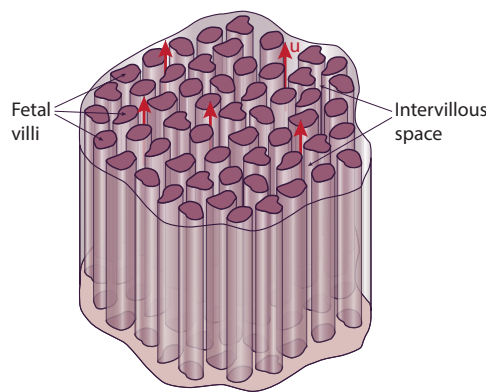


Figure 3.1. Our geometrical model of one unfolded stream tube of maternal blood in a human placentone. The cross-sectional geometry can be either determined from 2D histological slides or chosen arbitrary. Red arrows show the flow of maternal blood

uptake against geometrical parameters allows us to obtain an analytical equation describing the optimal stream-tube geometry that provides the maximal oxygen uptake.

The solution of this transcendental equation is numerically calculated and its explicit asymptotics are analytically deduced. Such analytical description of the optimal geometry further lets us introduce quantitative measures of efficiency for non-optimal geometries. Finally, we discuss the advantages of the analytical approach to the solution of the diffusion-convection equation over the numerical method of the previous chapter.

3.1 Mathematical formulation

3.1.1 Form of the approximation

The analysis of Eq. (2.18)

$$F(L) = c_0 \sum_{j=1}^{\infty} a_j^2 (D\mu_j + uB) (1 - e^{-\mu_j L})$$

shows that $F(L)$ is a smooth monotonous curve which is linear at small lengths¹ and exponentially saturates at large lengths. In a first approximation, Eq. (2.18) can then be replaced by an approximate expression which has the same behavior at these limits:

$$F^{\text{ap}}(L) = A(1 - e^{-\alpha L}), \quad (3.1)$$

where A and α are two parameters: A is the oxygen uptake at $L \rightarrow \infty$ (equal to the total incoming oxygen flow), and α is the average decay rate of oxygen concentration with stream-tube length. We will now relate A and α to the parameters of the model.

3.1.2 Uptake at the infinite length

Large stream-tube lengths are characterized by saturation when all incoming oxygen is transferred to the fetal blood.

The exact expression for the saturation limit can be obtained from Eq. (2.18) by letting $L \rightarrow \infty$:

$$F_{\infty} = c_0 u B S_{\text{IVS}} + c_0 D \sum_{j=1}^{\infty} a_j^2 \mu_j, \quad (3.2)$$

where the identity $\sum_{j=1}^{\infty} a_j^2 = S_{\text{IVS}}$ resulting from Eq. (2.16) was used.

Note that the flow F_{∞} in Eq. (3.2) includes two contributions: the convective flow (the first term) and the diffusive flow along the z -axis (the second term). It turns out that the second term is much smaller than the first one, so that Eq. (3.2) can be simplified by omitting the diffusive term:

$$F_{\infty} \approx A = c_0 u B S_{\text{IVS}}. \quad (3.3)$$

¹Note that this linearity is not granted by the form of Eq. (2.18), but is the consequence of the convergence of the $\sum_{j=1}^{\infty} a_j^2 \mu_j^2$ series

This approximation is justified by the following arguments:

1. The Péclet number for oxygen transport along the MBF in the human placenta is $Pe \approx 5600 \gg 1$ (see Sect. 2.1.2). That means that diffusion in the vertical direction can be neglected as compared to convection. Note however that diffusion in the stream-tube cross-section cannot be ignored in the same way, since it is the only in-plane mechanism of oxygen transport ($Pe = 0$).
2. Since 99 % of oxygen is bound to hemoglobin in the red blood cells (RBC), and RBCs are too large to diffuse, the error from omitting the diffusive transport term in F_∞ does not exceed 1 % in terms of oxygen content.

Mathematically, the simplification we have used can be written as

$$\mu_j \ll uB/D, \quad (3.4)$$

so that Eq. (2.17) becomes $\mu_j \approx \Lambda_j D/(uB)$. It should be noted that statement (3.4) does not contradict the fact that $\{\mu_j\}$ grow to infinity with the eigenvalue number j . In fact, each μ_j contributes to the final expression with a weight a_j , whose absolute value diminishes with j . Eq. (3.4) should be then understood as only valid for all eigenvalues, which have significant contributions a_j .

Oxygen uptake (2.18) can then be approximated as

$$F(L) \approx c_0 u B S_{\text{IVS}} \left(1 - \sum_{j=1}^{\infty} \frac{a_j^2}{S_{\text{IVS}}} \exp \left(-\frac{D}{uB} \Lambda_j L \right) \right). \quad (3.5)$$

3.1.3 Average concentration decay rate

Using Eq. (3.3) and comparing Eq. (3.5) to the approximate form of oxygen uptake (3.1), one obtains the following definition of the average concentration decay rate α :

$$\alpha(L) \equiv -\frac{1}{L} \ln \left(\sum_{j=1}^{\infty} \frac{a_j^2}{S_{\text{IVS}}} \exp \left(-\frac{D}{uB} \Lambda_j L \right) \right). \quad (3.6)$$

In this formula, α depends explicitly on L and implicitly on the cross-sectional geometry. Our goal is now to extract the main part of this implicit dependence. For this purpose, we integrate Eq. (2.13) over the IVS in the cross-section (S_{IVS}). We further apply the divergence theorem to transform the integral over S_{IVS} to an integral over its boundary P_{tot} , which includes the total perimeter P of the villi and that of the outer boundary of the stream tube in a cross-section:

$$\Lambda_j = -\frac{\int_{P_{\text{tot}}} \partial v_j / \partial n \, dP}{\int_{S_{\text{IVS}}} v_j \, dS} = \frac{w}{D} \frac{\int_P v_j \, dP}{\int_{S_{\text{IVS}}} v_j \, dS} = \left(\frac{wP}{DS_{\text{IVS}}} \right) q_j^2, \quad (3.7)$$

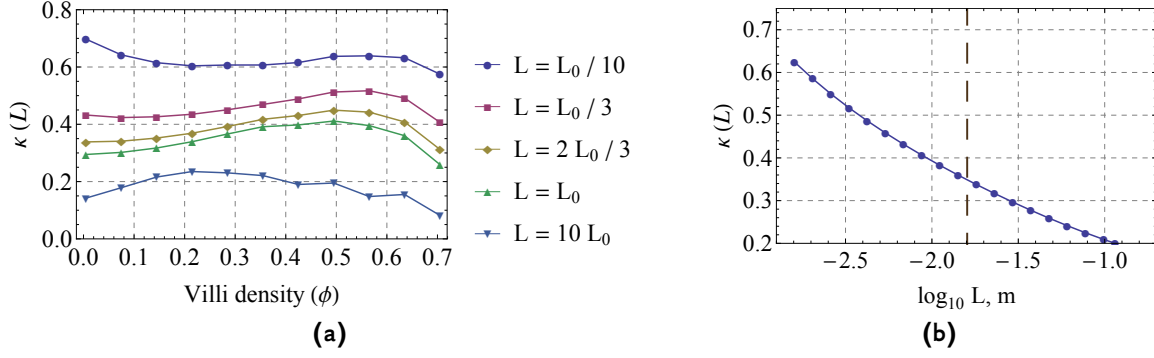


Figure 3.2. Dependence of $\kappa(L)$ on the model cross-sectional geometry for circular villi in a circular stream tube (Fig. 2.3). (a): Dependence of $\kappa(L)$ on the villi density $\phi \equiv S_{vil}/S_{tot}$ in a large range of stream-tube lengths. Here S_{vil} is the area of the cross-section occupied by the fetal villi, S_{tot} is the total area of the cross-section, and L_0 is the average stream-tube length (Table 2.2). One can see that in a first approximation, $\kappa(L)$ may be assumed independent of the villi configuration. (b): Dependence of $\kappa(L)$ on stream-tube length L . The dashed vertical line denotes the average stream-tube length L_0

where boundary conditions (2.14) and (2.15) were used to remove the contribution from the non-absorbing stream-tube boundary, and

$$q_j^2 \equiv \frac{\frac{1}{P} \int_P v_j dP}{\frac{1}{S_{IVS}} \int_{S_{IVS}} v_j dS}$$

is the dimensionless ratio of the mean value of the Laplace operator eigenfunction v_j over the villi boundary to its mean value in the IVS.

In a first approximation, the coefficient $wP/(DS_{IVS})$ in Eq. (3.7) describes the dependence of Λ_j on the cross-sectional geometry. Introduction of q_j and the dimensionless length $\ell(L) \equiv \frac{wP}{uBS_{IVS}}L$ into Eq. (3.6) yields

$$\alpha = \frac{wP}{uBS_{IVS}}\kappa(L), \quad \text{where} \quad \kappa(L) \equiv -\frac{1}{\ell(L)} \ln \left(\sum_{j=1}^{\infty} \frac{a_j^2}{S_{IVS}} e^{-\ell(L)q_j^2} \right) \quad (3.8)$$

is a dimensionless coefficient depending on L and the cross-sectional geometry and containing fine details of the given villi shapes and the distribution of villi, which are ignored by the integral parameters P and S_{IVS} . Figure 3.2a shows the dependence of $\kappa(L)$ on the villi density ($\phi \equiv 1 - S_{IVS}/S_{tot}$, the part of the cross-section occupied by the fetal villi) as calculated numerically for stream tubes of circular cross-section filled with circular villi (Fig. 2.3). One can see that in a first approximation, $\kappa(L)$ can be considered independent of the cross-sectional geometry in a wide interval of biologically relevant stream-tube lengths. For each L , the value of κ can be determined from Fig. 3.2b. For the average stream-tube length ($L_0 = 1.6$ cm, Table 2.2), $\kappa \approx 0.35$. Using Eqs (3.3) and (3.8), the approximate oxygen uptake (3.1) can then be rewritten as

$$F^{ap}(L) = c_0 u B S_{IVS} \left(1 - \exp \left(-\frac{wP}{uBS_{IVS}} \kappa(L) L \right) \right). \quad (3.9)$$

3.1.4 Dimensionless geometrical parameters

In Eq. (3.9), both geometrical cross-sectional parameters P and S_{IVS} depend on the size of the analyzed region. To facilitate the physical interpretation of the approximate solution and its comparison to experimental data, we identify two geometrical characteristics of the placental cross-section that are independent of the size of the region:

- *The fraction of the cross-section occupied by the fetal villi* (villi density), which we define as the ratio of the total area of the (small) villi in a cross-section to the total area of the cross-section:

$$\varphi \equiv \frac{S_{\text{vil}}}{S_{\text{tot}}}. \quad (3.10)$$

- *An effective villi radius*, which we define as

$$r_e \equiv \frac{2S_{\text{vil}}}{P} \equiv \frac{2\varphi S_{\text{IVS}}}{P(1-\varphi)}, \quad (3.11)$$

see also discussion on p. 72. In morphometric studies, the inverse parameter $2/r_e = P/S_{\text{vil}}$ is known as “villi surface density”. For circular villi of radius r , $r_e \equiv r$. The mean value of r_e for the human placenta is reported in Table 2.2.

Substitution of these definitions into Eq. (3.9) gives

$$\zeta(\text{Da}, \varphi) \equiv \frac{F^{\text{ap}}(\text{Da}, \varphi)}{F_0} = (1 - \varphi) \left(1 - \exp \left(-\text{Da}(r_e, L) \frac{\varphi}{1 - \varphi} \right) \right), \quad (3.12)$$

where

$$\text{Da}(r_e, L) \equiv \frac{2w\kappa}{uBr_e}L, \quad F_0 \equiv c_0 u B S_{\text{tot}}. \quad (3.13)$$

The physical meaning of F_0 follows from its definition: it is the maximal oxygen flow entering the stream tube that would be achieved if no villi obstructed the IVS of this stream-tube. In contrast, the incoming flow in the presence of villi is $F_\infty \equiv F_0(1 - \varphi)$.

It will be shown in Section 3.2.3 that the parameter Da can be represented as the ratio of the rate of oxygen extraction in the cross-section and the transit rate of the maternal blood through the placenta, and is thus the Damköhler number for oxygen convection-absorption process.² Note that Da includes information on the average villus shape through the parameter r_e , while F_0 is independent of the cross-sectional geometry. The normalized oxygen uptake $\zeta(\text{Da}, \varphi) \equiv F^{\text{ap}}/F_0$ (which we will call the *overall geometry efficiency*) is plotted in Fig. 3.3a.

3.1.5 The optimal cross-sectional geometry

Looking at Fig. 3.3a and Eq. (3.12) for oxygen uptake, it is natural to ask what are the “optimal” values of the parameters φ and Da that maximize oxygen uptake at a given stream-tube length. Figure 3.3a clearly shows two trends:

²Note that the Damköhler number Da was called parameter γ in an earlier publication (see Serov et al., 2015b)

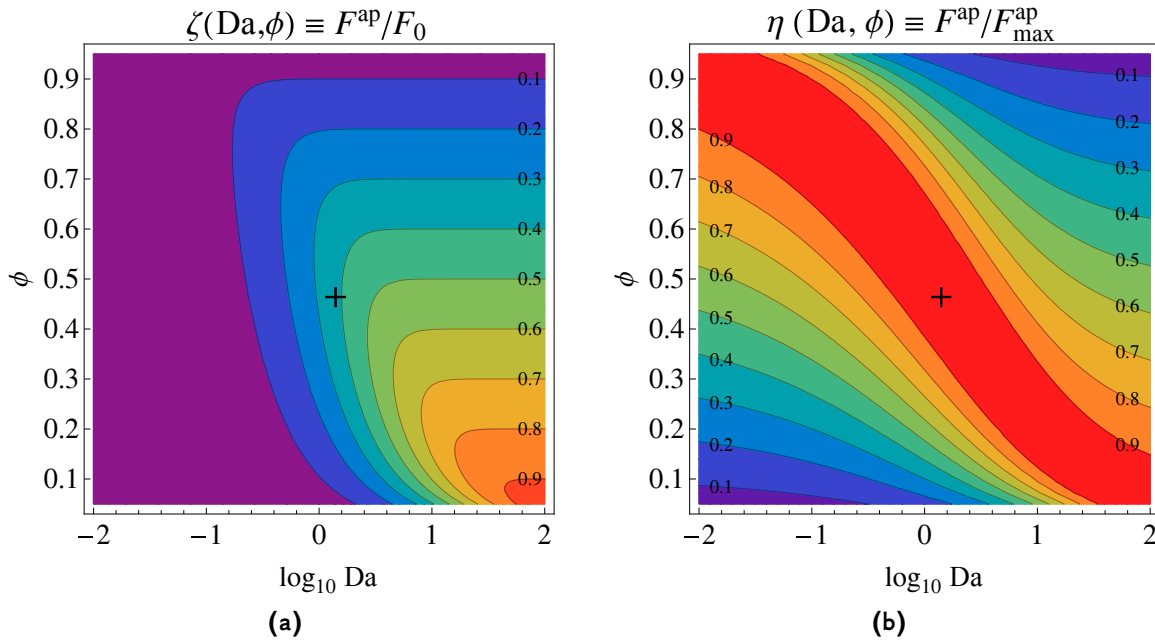


Figure 3.3. Diagrams of the overall geometry efficiency $\zeta(\text{Da}, \phi) \equiv F^{\text{ap}}/F_0$ (a) and the villi density efficiency $\eta(\text{Da}, \phi) = F^{\text{ap}}/F_{\text{max}}^{\text{ap}}$ (b) as functions of villi density ϕ and the Damköhler number Da . The “+” symbol marks the parameters $\text{Da} \approx 1.4$ (see Eq. 3.22 in Section 3.2.2 on p. 99) and $\phi \approx 0.46$ (Section 2.4.3) expected on average in a healthy human placenta ($\kappa = 0.35$). Note the logarithmic scale on the horizontal axis

- for any fixed value of ϕ , larger Da provides larger uptake;
- for any fixed value of Da , there exists some intermediate value of ϕ :

$$0 < \phi_{\text{opt}}(\text{Da}) < 1$$

that maximizes oxygen uptake. This optimal value $\phi_{\text{opt}}(\text{Da})$ tends to decrease with Da .

Note that from the definition (3.13) it follows that in terms of the cross-sectional geometrical parameters, an increase of Da corresponds to a decrease of the effective radius r_e . Figure 3.3a can then be interpreted as follows: it is more efficient to have many small villi than fewer big villi occupying the same area. This prediction can be understood if one considers the fact that small villi have more absorbing surface per unit of cross-sectional area.

However, in the human placenta, r_e cannot be infinitely small (and hence Da infinitely large). Indeed, villi possess an internal structure (e.g., fetal blood vessels), which serves in particular to transport the absorbed oxygen to the fetus. A decrease of r_e below some value is likely to make the villi less efficient in transporting the already absorbed oxygen. This argument is supported by the experimental observation that in the smallest (terminal and mature intermediate) villi of the human placenta, fetal capillaries normally occupy the main part of the internal volume. The mean radius of these villi is $r \approx 25\text{--}30\ \mu\text{m}$ (see Table 28.7 in Benirschke et al., 2006) and is not reported to significantly vary between or within placentas (Benirschke et al., 2006). At the same time, the villi density may

exhibit significant spatial fluctuations within the same placenta as well as between different placentas (see Fig. 1.15 and Bacon et al., 1986).

It is then reasonable to reformulate the initial question of the optimal cross-sectional geometry as “What is the villi density that provides the highest oxygen uptake for a given effective villi radius r_e ?” Mathematically, it is the question of finding the maximum of F against φ , while the fixed value of r_e is determined from external physiological constraints. The other variables entering the definition of Da besides r_e (namely, w , κ , u , B and L , see Eq. (3.13)) will in a first approximation be considered fixed in this optimization problem.

3.1.6 Optimal villi density

Under the constraint of fixed Da , Eq. (3.12) implies the existence of a maximal uptake at a certain villi density. The reasoning is the following (see also optimality discussion in Sections 2.4.2 and 2.4.4):

- $F(\varphi = 0) = 0$, because the condition $\varphi = 0$ means no feto-maternal interface and hence no uptake.
- $F(\varphi = 1) = 0$, because in this case fetal vessels occupy the entire cross-section of the stream tube, and the incoming oxygen flow is zero, since the maternal blood does not have space to flow.
- $F > 0$ for $0 < \varphi < 1$, because the placenta transfers oxygen from the mother to the fetus for intermediate villi densities. Since, by its physical nature, F is a bounded continuous function on the interval $0 \leq \varphi \leq 1$, there always exists a maximal oxygen uptake $F_{\max}(L)$ at a certain villi density $0 < \varphi_{\text{opt}}(L) < 1$ for any $Da(r_e)$.

Here we have used the symbol F and not F^{ap} for the oxygen uptake to underline that these arguments are general and are valid not only for the approximate flow, but for the exact flow as well.

The optimal villi density can then be obtained by solving the equation

$$\left. \frac{\partial F^{\text{ap}}(\varphi, L)}{\partial \varphi} \right|_{\varphi=\varphi_{\text{opt}}} = 0,$$

or

$$\exp\left(Da \frac{\varphi_{\text{opt}}}{1 - \varphi_{\text{opt}}}\right) = 1 + \frac{Da}{1 - \varphi_{\text{opt}}}. \quad (3.14)$$

One can note that both φ_{opt} and Da explicitly appear in Eq. (3.14). As a consequence, solving this equation does not require any eigenvalues calculation.

The substitution $x \equiv Da \varphi_{\text{opt}} / (1 - \varphi_{\text{opt}})$ reduces Eq. (3.14) to the form $Da = g(x)$, where $g(x) \equiv e^x - x - 1$, and its solution can be represented as $x = g^{-1}(Da)$. Although the inverse function $g^{-1}(Da)$ does not have an explicit analytical representation, its form can be numerically calculated once and then the tabulated values can be used in practice.

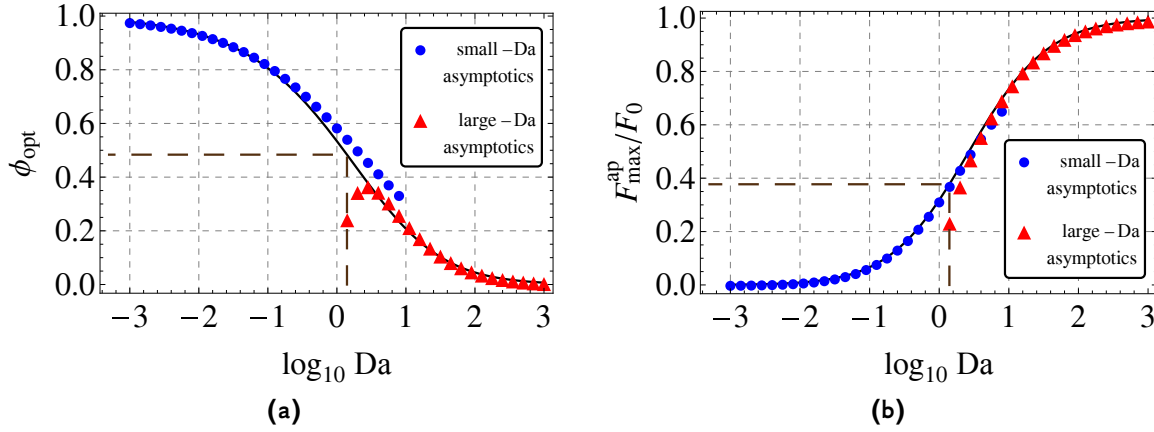


Figure 3.4. Analytical predictions of the optimal villi density (a) and of the normalized maximal uptake (b) as functions of Da (solid black lines). Small- Da asymptotics are shown by circles; large- Da asymptotics are shown by triangles. Dashed lines mark $Da \approx 1.4$ expected in a healthy human placenta (see Eq. 3.22 in Section 3.2.2 on p. 99)

Returning to the definition of x , one obtains ϕ_{opt} as a function of Da :

$$\phi_{\text{opt}}(Da) = \frac{1}{1 + \frac{Da}{g^{-1}(Da)}}. \quad (3.15)$$

The function $\phi_{\text{opt}}(Da)$ (Fig. 3.4a) can be used to calculate the optimal villi density for a placental region if Da is known for it. Substitution of the last result into Eq. (3.12) gives the corresponding maximal uptake (Fig. 3.4b):

$$\frac{F_{\text{max}}^{\text{ap}}(Da)}{F_0} = Da \frac{1 - \exp(-g^{-1}(Da))}{Da + g^{-1}(Da)}. \quad (3.16)$$

From the asymptotic behavior of $g(x)$ at small and large x , we obtain the following asymptotic formulas for ϕ_{opt} and $F_{\text{max}}^{\text{ap}}/F_0$:

$$\phi_{\text{opt}}(Da) \simeq \begin{cases} \frac{1}{1 + \sqrt{Da/2}}, & Da \ll 1 \\ \ln(Da)/Da, & Da \gg 1 \end{cases} \quad (3.17)$$

$$(3.18)$$

$$\frac{F_{\text{max}}^{\text{ap}}(Da)}{F_0} \simeq \begin{cases} \frac{1 - e^{-\sqrt{2Da}}}{1 + \sqrt{2/Da}}, & Da \ll 1 \\ \frac{1 - 1/Da}{1 + \ln(Da)/Da}, & Da \gg 1 \end{cases} \quad (3.19)$$

Figure 3.4 shows that these asymptotics accurately approximate $\phi_{\text{opt}}(Da)$ and $F_{\text{max}}^{\text{ap}}(Da)/F_0$ not only in the limits of $Da \ll 1$ and $Da \gg 1$, but for all Da . For instance, it can be verified that if the small- Da asymptotics is used for $Da \leq 3$ and the large- Da asymptotics is used for $Da > 3$, the maximal relative error of Eq. (3.19) is less than 4%. In other words, we obtained simple explicit approximations for the optimal villi density ϕ_{opt} and the normalized maximal oxygen uptake $F_{\text{max}}^{\text{ap}}/F_0$ as functions of a single parameter Da .

3.1.7 Villi density efficiency

Basing on the analytical expressions for the optimal villi density and the maximal uptake deduced in the previous section, one can define a quantitative measure of optimality of the villi density in a given (non-optimal) geometry.

If the given geometry is characterized by the parameters (Da, φ) , its *villi density efficiency* can be defined as the ratio of the oxygen uptake of this particular geometry to the maximal value, which can be obtained with the same Da :

$$\eta(Da, \varphi) \equiv \frac{F_{ap}(Da, \varphi)}{F_{max}^{ap}(Da)} = \frac{(1 - \varphi) \left(1 - \exp \left(-Da \frac{\varphi}{1 - \varphi} \right) \right)}{(1 - \varphi_{opt}(Da)) \left(1 - \exp \left(-Da \frac{\varphi_{opt}(Da)}{1 - \varphi_{opt}(Da)} \right) \right)}. \quad (3.20)$$

Figure 3.3b presents the villi density efficiency $\eta(Da, \varphi)$ in a physiological range of (Da, φ) and at $L = L_0$.

Following the comment after Eqs (3.17, 3.19), Eq. (3.20) can be rewritten as

$$\eta(Da, \varphi) \simeq \begin{cases} \frac{(1 - \varphi) \left(1 - \exp \left(-Da \frac{\varphi}{1 - \varphi} \right) \right) (1 + \sqrt{2/Da})}{1 - e^{-\sqrt{2}Da}}, & Da \leq 3 \\ \frac{(1 - \varphi) \left(1 - \exp \left(-Da \frac{\varphi}{1 - \varphi} \right) \right) (1 + \ln(Da)/Da)}{1 - 1/Da}, & Da > 3 \end{cases} \quad (3.21)$$

with a maximal relative error of 4 %. Note that the last equation does not require a separate calculation of φ_{opt} and is an explicit function of Da and φ in the entire range of parameters.

Note finally that the optimality indicators ζ and η play different roles. The overall geometry efficiency ζ (Fig. 3.3a) indicates the fraction of the maximal possible incoming oxygen flow F_0 that is absorbed by a given cross-section geometry. The higher is the value of ζ , the higher is the *absolute* value of the fetal oxygen uptake. However, the villi density efficiency η (Fig. 3.3b) shows how far the villi density of a given cross-section is from its optimal value for a fixed Da (and fixed r_e). The higher is the value of η , the closer is the fetal oxygen uptake to the maximal value for the given value of Da (for the given value of the effective villi radius r_e).

3.2 Analytical results

3.2.1 Oxygen uptake for circular villi

Figure 3.5 shows that the fetal oxygen uptake predicted by the analytical Eq. (3.12) agrees well with the numerically calculated results (Chapter 2, Fig. 2.7) in wide ranges of stream-tube lengths (L) and villi densities (φ). For each stream-tube length L shown in Fig. 3.5a, the value of $\kappa(L)$ was determined from Fig. 3.2b. Note that these results were calculated for the same circular geometries as in our earlier numerical simulations (Fig. 2.3). We emphasize however that the numerical simulations with identical circular villi are shown only for the purpose of validation. The proposed analytical theory, which uses only villi density and the effective villi radius as geometrical information,

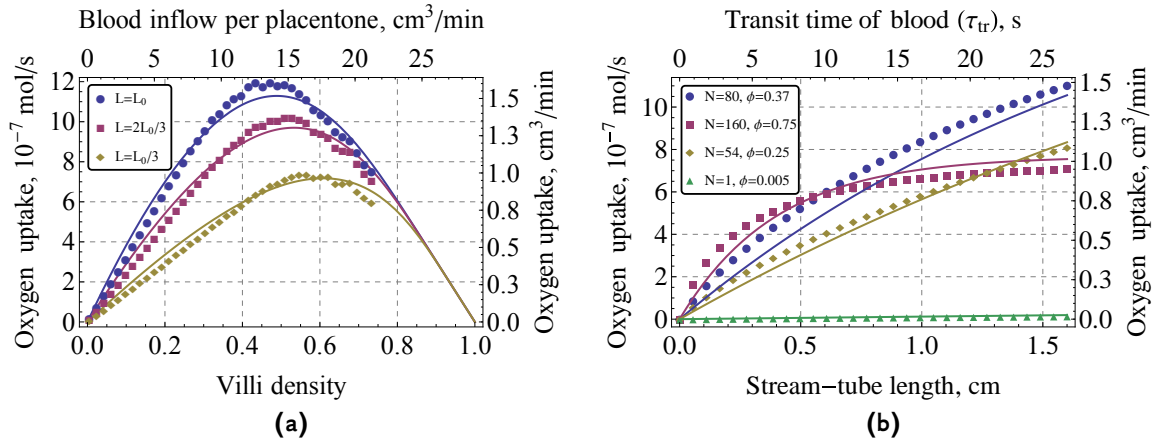


Figure 3.5. Oxygen uptake of a single placentone as a function of geometrical parameters. Solid lines correspond to the analytical approximation; symbols reproduce the results of the numerical simulations of Chapter 2 (Fig. 2.7). (a): Oxygen uptake as a function of villi density ϕ for three stream-tube lengths L : $L_0/3$, $2L_0/3$, and L_0 . For each of these lengths, the corresponding value of κ was determined from Fig. 3.2b: $\kappa \approx \{0.46, 0.39, 0.35\}$ for $L = \{L_0/3, 2L_0/3, L_0\}$ respectively. It can be seen that the peak uptake shifts to smaller villi densities for larger stream-tube lengths L . In all calculations, the MBF velocity $u = 6 \cdot 10^{-4} \text{ m/s}$ was used. In the analytical theory, the oxygen uptake is calculated directly for the placentone radius R , whereas in the numerical simulations the oxygen uptake is calculated for R_{num} and then rescaled to the placentone radius R by multiplying by R^2/R_{num}^2 . Note that the numerical curves do not go beyond the villi density $\phi \approx 0.75$ due to the existence of a maximal packing density of circles in a circle. The numerical results cannot be calculated beyond that density (see discussion in the caption of Fig. 2.7). The analytical theory, on the contrary, does not rely on any specific shapes or distributions of villi, but operates only with the villi density and the effective villi radius, thus allowing the results to be calculated for villi densities beyond this limit. Beyond the maximal packing density, the villi cannot be circular, but the same effective villi radius r_e is maintained. (b): Oxygen uptake as a function of stream-tube length L for several fixed villi densities ϕ . Small deviations of the theory from the numerical results are explained by the fixed $\kappa = \kappa(L_0) \approx 0.35$ used for all lengths. Various symbols represent villi densities of Fig. 2.3

is applicable to villi of arbitrary shapes and sizes (Fig. 3.1). The agreement of the analytical curves with the numerical points demonstrates that it is enough to know the villi density and the effective villi radius to predict the oxygen uptake of a given rather uniform distribution of villi in a given cross-section.

Variations of the parameter Da in the analytical expressions for the optimal villi density and the maximal uptake (Eqs 3.15, 3.16) can be interpreted in terms of changes of individual parameters of the model, other parameters being fixed. For example, the optimal villi density and the maximal uptake can be plotted as functions of the MBF velocity (Figs 3.6a,c) or stream-tube length (Figs 3.6b,d). An agreement between the plotted curves and the numerical results of Chapter 2 (Fig. 2.8) can be observed.

All four plots in Fig. 3.6 feature a dashed black curve representing a fictitious case of blood having no hemoglobin but transporting only oxygen dissolved in the blood plasma. Mathematically, this case is described by the oxygen-hemoglobin dissociation parameter $B = 1$, which is about 100 times smaller than that for the blood containing Hb. As predicted by Eq. (3.15), the no-Hb curves for the optimal villi density have the same shape, but are shifted by two orders of magnitude as compared to those for normal blood. We will discuss later how experimental results obtained in artificial perfusion experiments with no-Hb blood can be recalculated for normal (Hb-containing) blood with the help of the developed analytical theory (Section 3.2.4).

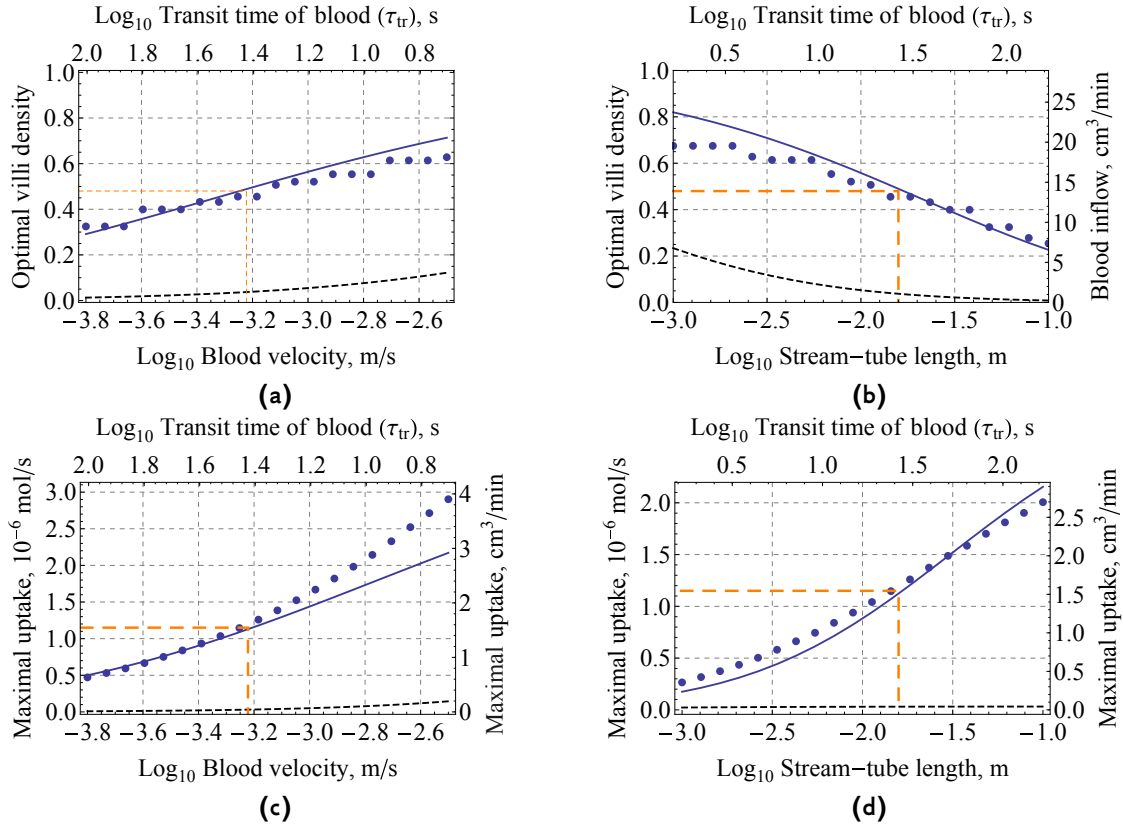


Figure 3.6. (a), (c): Dependence of the optimal villi density (a) and the maximal oxygen uptake (c) on the MBF velocity at a fixed stream-tube length L_0 (Table 2.2) for a single placentone. (b), (d): Dependence of the optimal villi density (b) and the maximal oxygen uptake (d) on stream-tube length at a fixed MBF velocity u (Table 2.2) for a single placentone. Solid curves represent analytical results, while circles correspond to the numerical simulations for circular villi of Chapter 2 (Fig. 2.3). Dashed black curves show analytical results in blood with no hemoglobin ($B = 1$, like in artificial perfusion experiments). Straight dashed orange lines indicate the expected average MBF velocity u and stream-tube length L_0 (Table 2.2). Step growth of numerical results seen in Figs (a), (b) is explained by the discrete changes of villi density in the numerical simulations due to the discrete changes in the number of villi in the cross-section

3.2.2 Typical values of the parameters Da and F_0

Taking πR^2 as the area of the placentone cross-section, parameters from Table 2.2 and $\kappa(L_0) \approx 0.35$ for the average stream-tube length $L_0 \approx 1.6 \text{ cm}$ (Fig. 3.2b), from Eq. (3.13) one can estimate the values of Da and F_0 , which characterize a “healthy” regime of our placenta model:

$$Da \approx 1.4, \quad F_0 \approx 3 \cdot 10^{-6} \text{ mol/s}. \quad (3.22)$$

The obtained average value of the Damköhler number together with the average villi density $\phi \approx 0.46$ (Section 2.4.3) are marked by crosses in the diagrams in Fig. 3.3. One can see that the theory predicts that an average healthy placenta extracts around 35 % of the maximal possible incoming oxygen flow F_0 (Fig. 3.3a), and that the villi density $\phi \approx 0.46$ is close to the optimal one for the given effective villi radius (Fig. 3.3b). Although 35 % seems to be a low value, note that the overall geometry efficiency of 100 % can never be achieved, since (i) in the presence of villi only a part of the flow

unobstructed by villi (F_0) can be transferred to the fetus and (ii) villi cannot be made infinitely small due to physiological restrictions (see discussion in Section 3.1.5).

To have predictive power, Da and ϕ need to be measured over the whole exchange region in a large number of healthy as well as pathological placentas. Such measurements require the development of image analysis techniques that could automatically determine these characteristics in histological placental slides. Such techniques will be discussed in details in the next chapter.

At the same time, because of the lack of consistent experimental information about several other parameters (namely, u , w , L) in each studied placenta, correlations of *variations* of Da and ϕ with *variations* of fetal development characteristics (such as birth-weight, placenta weight or their ratio) are expected to be of more practical use than the absolute values of Da and ϕ . Note finally that the optimal geometry and the maximal uptake may change for the non-slip boundary conditions. Further studies are required to clarify this point (see discussion in Section 2.4.4). Application of the developed analytical theory to the comparison of the efficiency of oxygen exchange in low-altitude and high-altitude placentas can be found in Appendix E on p. 161.

3.2.3 The parameter Da

The two parameters Da and F_0 play different roles. According to Eq. (3.14), Da alone determines the optimal villi density, while F_0 together with Da determines the maximal oxygen uptake (Eq. (3.16)).

It was already noted that F_0 is the maximal oxygen flow entering a stream tube that would be achieved if no villi obstructed the IVS of this stream-tube (p. 93). A clear physical interpretation of the second parameter Da can be obtained by rewriting its definition (Eq. (3.13)) as

$$Da \equiv \frac{L/u}{Br_e/(2w\kappa)} \equiv \frac{\tau_{tr}}{\tau_e}, \quad (3.23)$$

where $\tau_{tr} \equiv L/u$ is the transit time of the maternal blood through the placenta (while it flows along a stream tube of length L with an average velocity u) and $\tau_e \equiv Br_e/(2w\kappa)$ is a characteristic oxygen extraction time in a stream-tube cross-section. Comparison of Eqs (3.23) and (2.2) demonstrates that the obtained parameter combination Da is indeed the Damköhler number for oxygen transport in the stream-tube model describing the ratio of the rates of oxygen absorption rate and its convective transport.

As a consequence, Da can be understood as a quantitative measure of balance between two oxygen transport mechanisms: the longitudinal convective flow and the transverse diffusion. In other words, Da quantifies the level of adaptation of the cross-sectional geometry and the uptake parameters to the incoming MBF. Large values of Da ($Da \gg 1$) mean that oxygen is quickly transferred to the fetal circulation at the beginning of the stream tube and is rapidly depleted, so that poor in oxygen maternal blood flows through the remaining part. Thus, this remaining part of the IVS does not function efficiently (compare with the discussion of the Damköhler number in Section 2.1.2 on p. 64). Small values of Da ($Da \ll 1$) mean that the maternal blood passes too quickly through the placenta as compared to the characteristic cross-sectional oxygen extraction

time, so that a considerable part of incoming oxygen flow may not be transferred to the fetus. One can then speculate that placentas with $Da \sim 1$ are the best adapted for the transport of oxygen. The Damköhler number around 1.4 calculated from the model parameters suggests that a healthy placenta may indeed transfer oxygen optimally. This discussion will continue in the next chapter, when new histomorphometrical data will be obtained.

3.2.4 Advantages of the analytical theory

The advantages of the analytical solution over the numerical solution of Chapter 2 are numerous:

1. Oxygen uptake can be estimated for a histological cross-section of arbitrary geometry (Fig. 3.1).
2. The villi density ϕ and the effective villi radius r_e are shown to be the only geometrical parameters necessary to predict the oxygen uptake of a rather uniform villi distribution in a placental cross-section (see Figs 3.5 and 3.6). These two parameters allow for a simple application of the theory to distributions of villi of arbitrary shapes. The validity of the developed theory in the case of strongly non-uniform villi distributions remains to be investigated.

Finer details of villi distributions which produce the differences between the numerical and the analytical results in Figs 3.5 and 3.6, are “stored” in the coefficient κ . This coefficient not only encompasses the details of villi distributions, but also determines the strength of their influence on the oxygen uptake up to a given length L . In other words, it quantitatively describes the fact that in each geometry, different IVS regions are not equivalent due to the random distribution of villi, and that, with length L , oxygen in some regions is exhausted faster than in other regions. However, the dependence of κ and α (Eq. (3.8)) on L is rather weak as can be seen in Fig. 3.5b, where $F^{ap}(L)$ was plotted for all lengths with the same $\kappa = \kappa(L_0) \approx 0.35$. In a first approximation, κ can hence be considered independent of L in the physiological range of L .

3. The construction of the analytical theory has allowed to deduce from the convection-diffusion equation the characteristic time $\tau_e \equiv Br_e/(2w\kappa)$ of oxygen uptake in the human placenta cross-section. Note that τ_e is directly proportional to the radius of the villus (larger villi slow down the absorption) and is inversely proportional to the permeability of the fetal membranes (thicker membranes also decelerate the absorption). The typical value of τ_e in a healthy human placenta is around 20 s.
4. The efficiency of oxygen transport in a given placental cross-section can be estimated by means of the *overall geometry efficiency* ζ and the *villi density efficiency* η . For these two quantities, the analytical formulas (3.12) and (3.21) and diagrams (Fig. 3.3) are provided, which allow for comparison of different placentas or placental regions once the parameters ϕ and Da are calculated for them. To have predictive power, the efficiency estimations provided by the model need

to be correlated with independent indicators of placental exchange efficiency, such as the placental shape, weight, the placenta-fetus birth-weight ratio (Misra et al., 2010, Hutcheon et al., 2012) or pulsatility indices determined by Doppler velocimetry in the umbilical cord or maternal vessels (Todros et al., 1999, Madazli et al., 2003). These indicators were demonstrated to vary between normal and pre-eclamptic pregnancies, or pregnancies complicated by fetal growth restriction (see also Section 1.5).

5. The analytical theory suggests that oxygen uptake in the human placenta is rather robust to the changes of villi density. Indeed, the diagram in Fig. 3.3a shows that the placental villi density can vary by about 10% around the optimal value, and the villi density efficiency η will still remain in the 90–100% interval. Farther from the optimal villi density, η tends to decrease faster.

In other words, the theory predicts that a healthy placenta “tolerates” deviations of physiological parameters in a certain range without a significant reduction of oxygen uptake. However, beyond these tolerated ranges, the oxygen exchange efficiency rapidly diminishes. Similar trends were reported for the exchange robustness in the lung (Sapoval et al., 2002).

6. One can analyze the consequences of neglecting the oxygen-hemoglobin dissociation on oxygen uptake, as well as on the optimal villi density of a placental region (dashed black lines in Fig. 3.6). The analytical theory gives a method of recalculation of the results obtained for no-Hb blood in artificial placenta perfusion experiments into those for normal blood.

Imagine that at the end of an artificial perfusion experiment with no-Hb blood, one obtains the total oxygen inflow \tilde{F}_{in} into the placenta, the fetal oxygen uptake \tilde{F} and the average villi density ϕ from histomorphometry of the same placenta (note that \tilde{F}_{in} and \tilde{F} differ from F_{in} and F that would have been obtained for normal blood). From these data one can calculate $\tilde{F}_0 = \tilde{F}_{in}/(1 - \phi)$ (see discussion of Eq. (3.13)) and then \tilde{D}_a as the root of Eq. (3.12) (with F^{ap} replaced by \tilde{F}). These values can then be recalculated for Hb-containing blood: $D_a = \tilde{D}_a/B$ and $F_0 = \tilde{F}_0 B$ (where $B \approx 94$, see Table 2.2) and can be substituted into Eq. (3.12) to give the oxygen uptake F in the same placenta for Hb-containing blood. One can see that the oxygen uptake in a no-Hb perfusion experiment gives on average a hundred-times underestimation of the real uptake. Finally, the values of D_a and ϕ for the given placenta can be compared with the diagrams in Fig. 3.3 to determine how far the overall geometry and the villi density of the region are from the optimal ones. Note finally that this recalculation procedure introduces a small error since in no-Hb case the diffusive part of the total flow, which is omitted in Eq. (3.2), becomes important.

7. The computation time is significantly reduced since the calculation of eigenfunctions and eigenvalues of the diffusion equation are not required. Note that due to a long computational time, the numerical simulations of Chapter 2 had to be performed on a smaller stream-tube radius R_{num} and then rescaled to the placenta radius R by

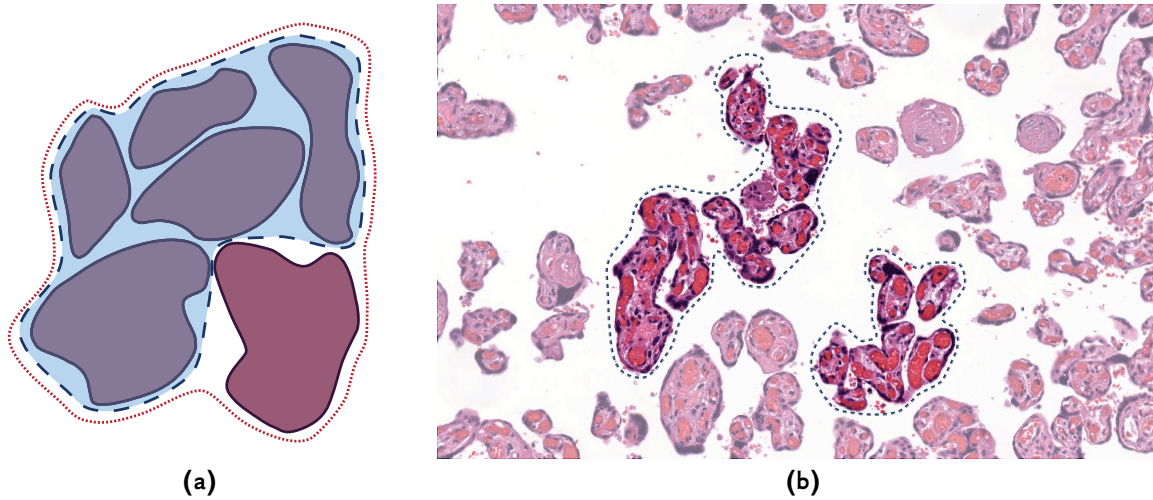


Figure 3.7. Illustration of the difference between the total villous perimeter and the effective absorbing villous perimeter. (a) Example of an isolated group of villi. In the shaded villi group, some parts of the villi boundaries are inefficient as they are screened by other villi from the outside of the isolated group, where the main reservoir of oxygen is supposed to be. The effective absorbing perimeter of the group is close to the perimeter outlined by the dashed line. This perimeter, equivalent to the perimeter of the IVS surrounding this group of villi, can be several times smaller than the total perimeter of the villi in the shaded group. Note also that adding a new villus into such group (the villus outside the shaded perimeter) does not increase the effective absorbing perimeter proportionally to the increase of the total villous perimeter. In the example in the figure, the new perimeter (the dotted contour) has approximately the same length as the old one. (b) Illustration of the same concept in a histological slide of the human placenta. Two dashed contours show the effective absorbing perimeters of two groups of villi, which are considerably smaller than the total perimeters of villi in the groups. Discussion of similar screening concepts can be found in Sapoval et al. (2002), Felici et al. (2005), Gill et al. (2011)

multiplying the oxygen uptake by R^2/R_{num}^2 . This constraint does not apply to the analytical theory. Good agreement between both approaches (Figs 3.5 and 3.6) justifies the rescaling of the results performed in the numerical calculations.

Note that the derivation of Eq. (3.13) implies that, strictly speaking, P is not the total perimeter of the villi, but an *effective absorbing perimeter of the villi* (i.e. only the part of the total perimeter that is directly in contact with the IVS). In the case of well-separated villi, there is no difference between the two definitions. However, it is not always true for the real placental cross-sections. For instance, in Fig. 3.7b one can see several isolated groups of villi, inside which the villi lie so close to each other, that there is virtually no IVS left between them. Parts of the villous boundary which are not in contact with large parts of IVS are then *screened* from participating in oxygen uptake, and hence should not be accounted for in the effective absorbing perimeter of the villi.

This remark can be understood by considering the fact that oxygen diffuses in the IVS, and only parts of the villous boundary that are in contact with the IVS will participate in the uptake. In the case of well separated singular villi, the entire perimeter is absorbing. A schematic description of this situation is shown in Fig. 3.7a. In our model the screening effect is implicitly taken into account by the diffusion equation (2.13). Note finally that the placental structure seen in histological cross-sections may differ from the situation *in vivo* (due to the cease of the maternal blood flow, the mechanical stress at parturition and formalin fixation), and the villi appearing “glued” to each other in histological cross-sections may indeed be separated *in vivo* (see also discussion in Section 1.5).

3.3 Concluding remarks

In this chapter, an analytical solution to the diffusion-convection equation governing oxygen transport in the human placenta has been developed. Oxygen uptake was calculated for an arbitrary cross-sectional geometry of a maternal blood stream tube. It was shown that for a rather uniform spatial distribution of villi in a placental cross-section, only two geometrical characteristics, the villi density and the effective villi radius, suffice to predict the fetal oxygen uptake.


It was also demonstrated that all model parameters do not influence the oxygen uptake independently, but instead form two combinations: (i) the maximal oxygen inflow of one placentone, and (ii) the ratio of the transit time of the maternal blood through the IVS and a cross-sectional oxygen extraction time. These two parameters together with the villi density determine the oxygen uptake. Analytical formulas and diagrams were obtained that allow for oxygen uptake calculation and quantitative estimation of oxygen exchange efficiency in a given placental region based on the measurements of the villi density and the effective villi radius.

Finally, a fictitious case of no-Hb blood was analyzed to study oxygen transport in artificial placenta perfusion experiments. It was demonstrated that artificial perfusion experiments with no hemoglobin tend to underestimate the *in vivo* oxygen uptake by two orders of magnitude. A method of recalculation of the results of artificial perfusion experiments to account for oxygen-hemoglobin dissociation was proposed.

Once combined with image analysis techniques (discussed in Chapter 4), the proposed analytical theory can be the mathematical ground of a future tool for fast diagnostics of placental efficiency based on histological placental slides.

Chapter 4

Analysis of Histological Placental Cross-Sections

HE stream-tube model developed in the previous chapters allows one to estimate the oxygen uptake in an arbitrary placental geometry and the exchange efficiency of a given geometrical placental structure. In the present chapter, we will discuss how case-specific geometrical structure of a given histological cross-section can be used as input data for the model. Using the histological data consists of two stages: (i) identification of the different components of a placental cross-section (segmentation) and (ii) performing histomorphometrical measurements that will provide the total villi area and the total villi perimeter of the given placental cross-section (histomorphometry).

In the first part of this chapter we will describe how the histological cross-sections are prepared, what manual methods are now available for their segmentation and histomorphometry, and what would be the ideal segmentation results. It will be shown that manual methods are time-consuming and thus cannot be used for routine analysis of large placental sections (with more than a thousand villi). Analysis of such cross-sections requires the use of automatic techniques.

In the second part of the chapter, we review standard digital image processing methods that may be applied to this type of images. We then discuss their main drawbacks, which are due to the special features of H&E-stained placental cross-sections, namely, “glued” villi and low contrast between the villi stroma and the villi boundaries, or the villi stroma and the maternal RBCs in the IVS. These problems require that the standard techniques be adapted to the peculiarities of the histological placental cross-sections. We then present one of the possible ways to proceed.

The last part of the chapter is devoted to the application of the developed automatic image analysis algorithm to 25 large histological cross-sections obtained from 22 healthy and 3 pathological placentas by Dr. Carolyn Salafia (Placental Analytics LLC, NY). The obtained histomorphometrical results are then compared with previously published histomorphometrical data and combined with the efficiency diagrams of the previous chapter. Predictions of oxygen exchange efficiency in the analyzed placentas are discussed.

Three internship students have contributed to the work described in this chapter: Zhenzhen You (2014), Khoa Nguyen (2014) and Junior Goubalan (2013). The results

they obtained can be also found in two Master's thesis manuscripts (You, 2014, Goubalan, 2013) and one internship report (Nguyen, 2014). The author would like to especially acknowledge the profound contribution of Zhenzhen You to the elaboration and realization of the segmentation algorithms as well as to the parallelization of the code.

4.1 Manual placental histomorphometry

4.1.1 Application of the STPM to histological placental cross-section

As demonstrated in the previous chapter, application of the developed stream-tube model to placental cross-sections requires calculation of the parameters Da and ϕ . Based on the definitions of these parameters (Eqs (3.10) and (3.13)), the following variables need to be determined for a given placental cross-section:

- the villi density ϕ ,
- the placental membrane permeability w ,
- the maternal blood velocity u ,
- the oxygen-hemoglobin dissociation constant B ,
- the effective villi radius r_e ,
- the stream-tube length L ,
- the parameter κ .

Four of these parameters are geometrical (ϕ , r_e , L and κ), while the other three are determined by the placental physiology (w , u and B).

Geometrical parameters

In this chapter we consider an application of the developed stream-tube placenta model to 2D histological placental cross-sections, in which three of the geometrical parameters can be measured (ϕ , r_e , κ). While ϕ and r_e can be directly assessed from the images, the parameter κ requires solving the eigenvalues problem, which would significantly slow down the algorithm. However, κ was demonstrated to only slightly vary for rather uniform villi distributions (see Fig. 3.2a and discussion in Section 3.1.3). In a first approximation, κ may then be assumed constant, and the cross-sectional geometry may be described by only the villi density and the effective villi radius.

Also, no information on the stream-tube length L can be directly obtained from the 2D cross-sections, since they do not contain any information on the third dimension that is in our model associated with the direction of the MBF. An indirect way of estimating L from 2D sections may consist in cutting the sections through the arterial and venous openings in the basal plate, marking these openings in the sections, and then calculating some kind of average distance between them. Unfortunately, experimental sections passing through the vessels are not yet available (mainly due to the failure to

find maternal vessels in the basal plate *post partum*) and will not be discussed in the present thesis.

In the absence of this information one might assume that the stream-tube length L roughly corresponds to the length of the maternal blood pathway from the spiral arteries in the basal plate, to the chorionic plate and then back to the decidual veins at the basal plate, a path that roughly amounts to the double placenta thickness $2d$ (see also discussion in Section 2.3 on p. 77). The placenta thickness (*post partum*) is known to vary from 1.0 to 3.3 cm between placentas (with the mean value around 1.9 cm), which roughly translates in variations of L from 2.0 to 6.6 cm (and the mean of 3.8 cm, see Salafia et al., 2012).

However, one can see that $L \approx 3.8$ cm calculated as the double placenta thickness is more than two times larger than the value $L_0 = 1.6$ cm calculated from the transit time of the maternal blood through the placenta. This is due to several reasons:

- A part of the placenta thickness corresponds to the basal and the chorionic plates, which do not contribute to the stream-tube length (see Fig. 1.7a).
- The length L calculated as the double placenta thickness includes the flow path of blood through the central cavity, which lies outside the stream tube considered in the model (see Fig. 2.1a).
- The thickness of the placenta *post partum* may be different from the thickness *in vivo* in the presence of the maternal and fetal circulations.

As can be seen, these factors introduce both a scaling factor k and a shift b into the relation between the placental thickness d and the length L , which can be approximately represented as:

$$L + b = 2kd. \quad (4.1)$$

The scaling factor k is determined by the shrinkage of the placenta during the delivery and by the cessation of the blood circulation. The shift b is due to the presence of the decidual plate and the central cavity. Note that the two independent parameters, k and b , cannot be both assessed by substitution of L and d in this single equation. However, it is likely that due to the large diameter of the central cavity (around 1 cm, see figure 4 in Aifantis, 1978) and a considerable thickness of the basal plate (3–6 mm, see Borbely et al., 2014), the shift b gives the dominant contribution to the observed discrepancy in the values. To experimentally estimate the parameters b and k , one needs to measure the transit time of maternal blood through a given human placenta (by measurements *in situ* or by calculations in a high resolution 3D placental structure), estimate from it the stream-tube length L , and measure the placental thickness. Once these data are obtained for several placentas, the resulting points can be fitted with Eq. (4.1) to yield b and k .

Physiological parameters

The MBF velocity u cannot be directly measured from histological cross-sections. It has to be determined by *in vivo* techniques or could be probably calculated *in silico* if the complete highly-resolved 3D placental structure were available. Such information is

not available at the moment. As a consequence, we have to use the same average MBF velocity $u = 6 \cdot 10^{-4} \text{ m/s}$ for all analyzed placentas.

Variations in the permeability of the placental membrane are mainly due to variations of the thickness of the fetal endothelial and epithelial membranes (see [Mayhew and Burton, 1988](#), [Mayhew, 2006b](#)). The placental membrane permeability can either be measured in *in vitro* placental tissue cultures or recalculated from the placental oxygen diffusing capacity. In its turn, the oxygen diffusing capacity can either be measured *in vivo* or estimated from histological data (see discussion in Section 1.6.4). However, the calculations of [Mayhew et al. \(1993a\)](#) demonstrate that, for instance, in diabetic pregnancies, the harmonic membrane thickness and the oxygen diffusive capacity are only 20% higher. This observation suggests that the placental membrane permeability may not vary much between healthy and at least some pathological pregnancies, and may therefore in a first approximation be assumed constant.

Finally, no significant variations of the parameters making up the oxygen-hemoglobin dissociation parameter B (Eq. (2.9)) have been reported, except in cases of maternal anemia (low red blood cells count) or maternal hypoxemia (low blood oxygen level, see [Longo and Power, 1969](#), [Power et al., 1972a](#)).

Summary

To apply the stream-tube placenta model to experimental placental cross-sections we:

- need to measure the villi density ϕ and the effective villi radius r_e in the cross-sections,
- assume that the stream-tube length L , the placental membrane permeability w , the oxygen-hemoglobin dissociation constant B and the parameter κ do not vary significantly and will consider them constant,
- assume a constant uniform maternal blood velocity u .

As discussed earlier (see p. 84), the last assumption is likely to be invalid in general, and should be improved or relaxed by future studies.

4.1.2 Histological placental cross-sections

The modern standard histological preparation of placental cross-sections includes the following stages (see, for instance, [Mayhew, 2006a](#), [Nelson et al., 2009](#)). After the delivery, placental membranes are trimmed and the umbilical cord is shortened to within 1 cm from the chorionic plate. Next, the placenta is cut into slices of 1–2 cm thickness extending from the chorionic to the basal plate (the blue dashed line in Fig. 1.7a). The slices are cut into smaller blocks, which are then fixed in formaldehyde and embedded in paraffin wax. After fixation, the blocks are cut into thin slices with the help of a microtome (with a thickness of several microns), the maternal blood is washed out and the slices are stained. A standard histological stain is hematoxylin and eosin (H&E), which dyes cell nuclei in blue (hematoxylin), and other cell structures in various shades of red, pink and orange (eosin), but other stains are also used. Histological slides obtained by

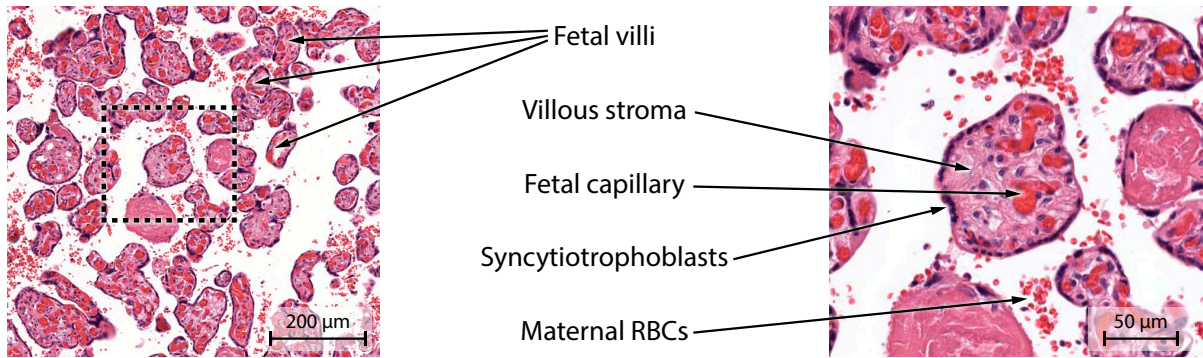


Figure 4.1. A typical H&E-stained histological placental slide. A 3x zoom of the chosen region in the left plate is shown on the right. The main structural components are marked. Compare with Figs 1.3 and 1.4

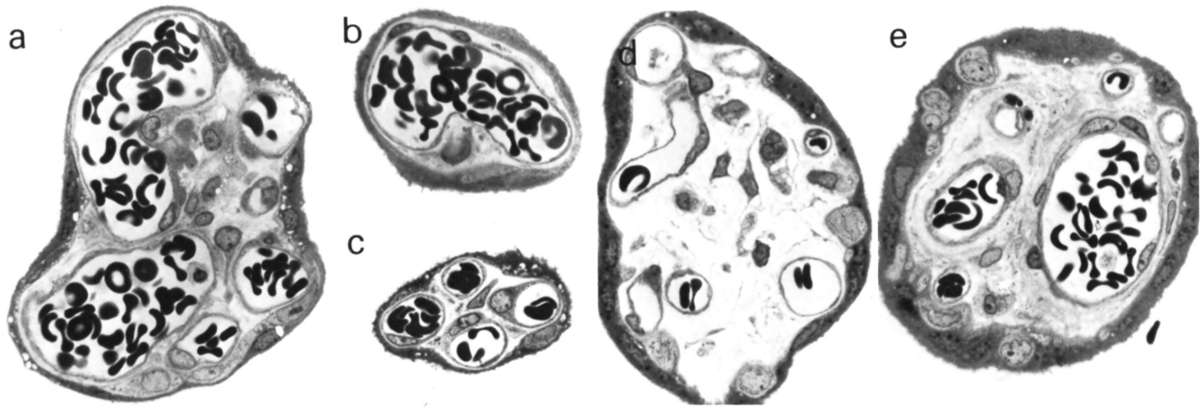


Figure 4.2. Typical cross-sections of different parts of the villous tree reproduced from Kaufmann et al. (1979). (a) A terminal villus containing large sinusoidal capillaries which bulge out the trophoblastic surface. The connective tissue is poorly developed. (b) A tip of a terminal villus with a tangentially sectioned capillary loop. (c) A neck region of a terminal villus with four non-dilated capillaries and little connective tissue. (d) A mature intermediate villus with small fetal vessels and large amount of loose connective tissue. (e) A small stem villus (a ramulus), with an arteriole, a vein, several capillaries and condensed fibrous connective tissue

this procedure are then analyzed by light microscopy. Some groups have studied the effects of the tissue shrinkage during fixation and of the cease of the maternal and fetal circulations, but their quantitative results have not been confirmed by later studies (for a more detailed discussion of the problems of the placental histomorphometry see Appendix D on p. 150). A typical placental cross-section is shown in Fig. 4.1. To allow for the application of the stream-tube model, the villi density ϕ and the effective villi radius r_e have to be measured in these slides.

By definition (p. 77), the villi density is the ratio of the cross-sectional area of the small villi ($S_{sm.v}$) to the total area of the cross-section (S_{tot}): $\phi = S_{sm.v}/S_{tot}$. The class of small villi includes terminal and mature intermediate villi. These villi are mainly distinguished from other villi types (stem and immature intermediate villi) by a small radius (15–40 μm) and dilated (not round) fetal capillaries occupying the main fraction of the villus cross-section (see Fig. 4.2 and Kaufmann et al., 1979). In turn, the effective villi radius is defined as two times the ratio of the total cross-sectional area of the small villi and their total cross-sectional perimeter: $r_e \equiv 2S_{sm.v}/P$ (see Eq. (3.11)). Thus, to calculate both ϕ and r_e from a histological cross-section, one needs to measure $S_{sm.v}$ and P .

4.1.3 Point–intersection counting techniques

The perimeter and the surface area of villous cross-sections are traditionally measured by point–intersection counting techniques (Laga et al., 1973, Howard and Reed, 2005, Mayhew, 2006b). To use such techniques to calculate cross-sectional perimeters of the placental compartments (components), a mesh of randomly-positioned and randomly-oriented lines is superimposed on a placental slide (Fig. 4.3a). It is further assumed that the perimeters of the compartments are proportional to the number of *intersections* of the superimposed lines with the compartments boundaries or membranes. According to the calibration information provided by the producer of the mesh, the number of intersections per length of superimposed lines is interpreted in terms of a “perimeter density” (cm/cm^2), which is defined as the compartment perimeter per cm^2 of the total cross-sectional area. By multiplying the obtained perimeter density by the volume of the placenta, an estimation of the total surface (in cm^2) of the specific compartment is obtained. Note that the obtained result is an overestimation of the surface, since the total placental volume includes parts with a principally different structure (such as the basal plate, see Fig. 1.7a).

A similar *point-counting* technique is used to estimate the cross-sectional areas of the compartments. It consists of superimposing a set of points on the cross-sections and counting the number of hits of specific compartments by these points (Fig. 4.3b). Since for a uniformly distributed set of points the probability of hitting a compartment is proportional to its area, this number can be recalculated into the area fraction of the selected compartment. This area fraction is then multiplied by the placental volume to yield the total volume of the compartment in the placenta, an operation introducing an error similar to the described above. To increase the precision of both point- and intersection-counting techniques, simple or systematic random sampling is used at all stages of the cross-sections preparation (Gundersen and Jensen, 1987, Gundersen et al., 1999, Mayhew, 2006b).

It is interesting to mention some data on the convergence of the point–intersection counting techniques with the number of points provided by Laga et al. (1973). It was reported that volume fractions converged to fixed values after around 1250 points have been counted in the total of 50 fields of view (equivalent to the total analyzed section surface of about 8.3 mm^2). Surface areas were reported to converge to fixed values after the analysis of 100 fields of view (equivalent to the total analyzed section surface of about 16.6 mm^2) and counting around 2000 intersections.

The point–intersection counting techniques have been used in many studies to investigate the placental structure, some of which are cited in Section 1.5 on p. 32. In addition to the evaluation of the placental transport properties (Section 1.6.4), histomorphometrical measurements were shown valuable for the assessment of the fetoplacental angiogenesis, the trophoblast turnover and the villi growth (Mayhew, 2006b). However, the manual implementation of these techniques imposes several restrictions on their use. Thus, to characterize one placenta, one needs to manually count up to 2000 points or intersections (events), which requires a significant amount of work and time. For instance, Longo et al. (1973) in their study have analyzed 18 placentas with 2500 points and

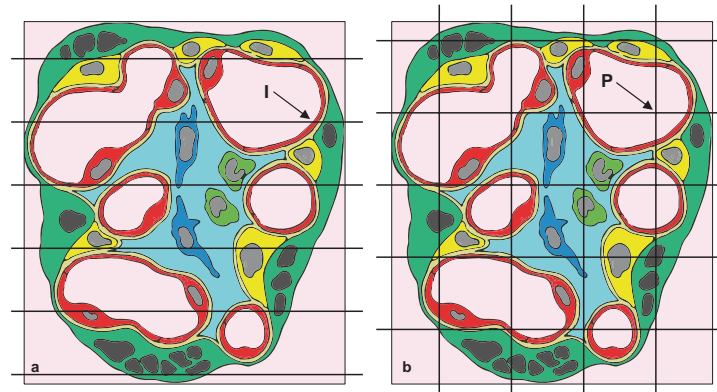


Figure 4.3. Illustration of point–intersection counting techniques, reproduced from Mayhew (2006b). (a) A histological section is overlaid with a set of lines. The number of sites at which these lines intersect the surfaces of interest (e.g., the luminal membrane of the fetal vascular endothelium at point I) can be counted to give estimations on the perimeter of the compartments. (b) A histological section is overlaid with an array of points (mesh nodes). Test point counts inside different tissue compartments (e.g., the capillary lumen at point P) are used to estimate the areas of the compartments. By multiplication by the total placental volume and by using the graduation of the meshes, the 2D perimeters and areas of the compartments are then recalculated to give the surface area and the volume of the compartments in 3D

2000 intersections counted per placenta (81 000 events in total), while Nelson et al. (2009) have restricted themselves to the analysis of 39 healthy and 88 type 1 diabetic placentas with only 200 events per placenta (giving the total of 7 800 events in healthy and 17 600 events in diabetic placentas). The low number of analyzed events per placenta in the latter study may be one of the reasons of the high standard deviation in the results compared to those of Laga et al. (1973): compare the intervillous space volume fraction, $23.29 \pm 0.64\%$ of Laga et al. (1973) and $40 \pm 10\%$ of Nelson et al. (2009), and the total small villi surface, $16.1 \pm 0.5 \text{ m}^2$ of Laga et al. (1973) and $4.0 \pm 7.2 \text{ m}^2$ of Nelson et al. (2009).

The great amount of work required to apply the manual point–intersection counting techniques to histological sections together with considerable interplacental biological variations are some of the reasons why experimental studies focused on using these techniques to obtain average placental data rather than performing case-specific measurements. At the same time, if these techniques were automatized, it should be possible to quickly obtain large statistics for individual placentas. Moreover, they would allow to analyze more points per field of view, which would increase the measurements accuracy. However, the only step made in the direction of automatization is, to our knowledge, the use of computer-assisted measurement systems that (i) automatically overlay sets of points and lines over the sections and store the marked events, but still require a human user to identify the events (Laga et al., 1973, Nelson et al., 2009) or (ii) calculate the perimeters and areas of the compartments manually traced by the operator (Beck, 1991). In the following section, we explore several possible ways of automatic histomorphometrical analysis of placental cross-sections.

4.2 Automatic placental segmentation

4.2.1 “Ideal” segmentation and main segmentation challenges

As mentioned, the analysis of the placental cross-sections consists of two stages: segmentation (identification) of the placental compartments and histomorphometrical measurements. Segmentation is the most difficult part of the two and consists in dividing the given slide into multiple zones, each of which corresponds to one placental compartment. Since the application of the STPM requires knowing only the areas and the perimeters of the villi, we will focus on only two compartments: IVS and villi, but will additionally consider fetal capillaries. We will illustrate the discussion of segmentation concepts and methods on three small placental slides featuring different segmentation conditions, to which we will refer as *sparse*, *dense* and *low-contrast* placental sections (shown in Figs 4.4a,d,g respectively). The names *sparse* and *dense* characterize the density of the villi and residual maternal RBCs in the IVS. The name of the *low-contrast* slide refers to the significantly lower color difference between the villi and the IVS in this cross-section as compared to the *sparse* and *dense* sections, as well as to numerous zones of light-colored villous stroma inside its villi. The difference in slide coloring is best seen in zoomed areas of the slides (Figs 4.4c,f,i). Although the same stain (H&E) was used for all three slides, the color difference of the *low-contrast* slide is probably explained by different settings of the autostainer (e.g., staining time and stain concentration). We will demonstrate below that automatic segmentation techniques are sensitive to staining settings, and that low-contrast slides present significant challenges for an algorithm that efficiently works with high-contrast slides.

To be able to compare the efficiency of different segmentation approaches, we need to define an “ideal” segmentation for the three example slides. This “ideal” segmentation was performed by hand in a graphics editor and is shown in Figs 4.4b,e,h.

The appearance of all three placental slides (Figs 4.4a,d,g) suggests the two main problems encountered with automatic segmentation algorithms: (i) a great similarity in color between the fetal capillaries and the residual maternal RBCs in the IVS, and (ii) the dense packing of villi and maternal RBCs in the IVS, while the syncytiotrophoblast villous boundary (which might be used for distinguishing separate villi) is discontinuous and has a variable thickness. As a consequence, a direct manual application of standard image analysis techniques yields two principal segmentation errors: the maternal RBCs are identified as fetal villi, and fetal villi “glue” to each other and to the maternal RBCs in crowded regions. Although “gluing” between only villi may not be a problem (since we are interested in the total absorbing perimeter of the villi, which is not changed in this process, see discussion on p. 103), “gluing” of villi to the maternal RBCs may significantly diminish the accuracy of histomorphometrical measurements.

For instance, by selecting an appropriate threshold, filtering out small villous and IVS components and performing erosion and dilation, one can achieve good segmentation

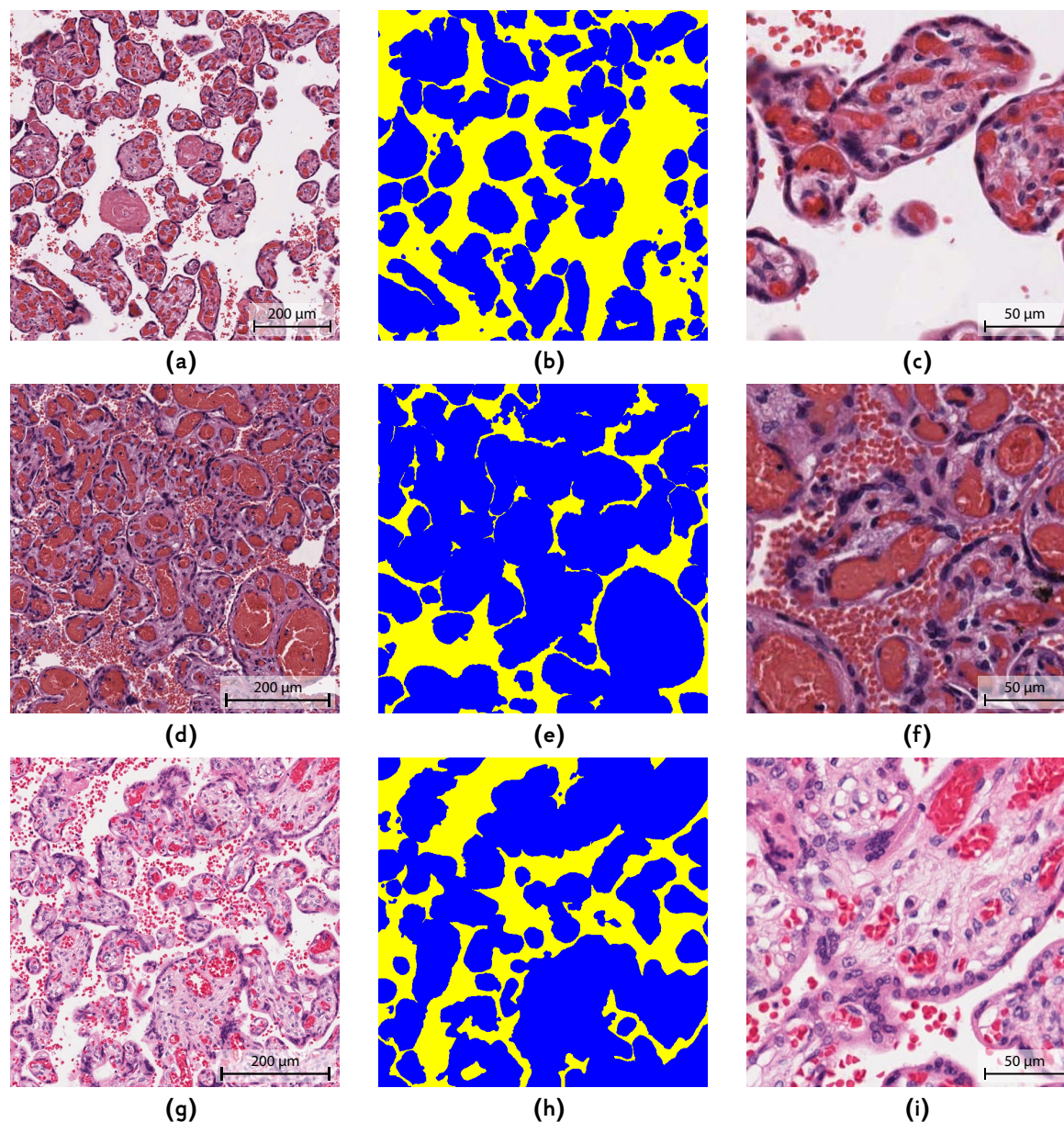


Figure 4.4. Three placental sections, *sparse* (a), *dense* (d) and *low-contrast* (g), which will be used for illustration of the segmentation methods. "Ideal" manual segmentations (b, e and h) of the three placental sections are shown to the right of the original pictures in the second column. Color code: blue — villi, yellow — IVS. The third column (c, f and i) contains a $200\mu\text{m} \times 200\mu\text{m}$ zoom of the upper right corner of the slides (a), (d) and (g) respectively. Note the much smaller color difference between the villi interior and the IVS, and the presence of light colored villous stroma in the *low-contrast* slide (i), as compared to the other slides

for the *sparse* (Figs 4.5a–c) and *low-contrast* (Figs 4.5g–i) sections. Note however the exceptionally high binarization threshold¹ 0.98/1.0 (see figure caption), which is set to eliminate the light stroma regions inside villi in the *low-contrast* cross-section. If the threshold were set to lower values, the initial binarization would create numerous “IVS” regions inside the villi, which would have to be removed before erosion and dilation, or otherwise the final segmentation result would be significantly distorted. Choosing the high threshold for sections containing such light stroma regions, while keeping the threshold values low for high-contrast sections like the *dense* section (where a high threshold would remove real IVS regions) presents a significant challenge for the automatic segmentation. Also, a direct application of the described simple segmentation algorithm to the *dense* section inevitably results in numerous errors, such as identification of the maternal RBCs as villi, their “gluing” to fetal villous regions, or identification of parts of fetal capillaries as IVS (Figs 4.5d–f).

Moreover, all three sections required segmentation parameters to be chosen manually for each case (see caption of Fig. 4.5), which does not allow for automatic batch processing of placental sections and requires human attention. In the following sections, we discuss automatic algorithms allowing to choose segmentation parameters.

4.2.2 Thresholding and the initial segmentation

In this section, we perform an initial segmentation of a placental section based on the compartments color, which will be refined in subsequent sections. The analysis of the placental slides (Fig. 4.4a–c) suggests that villi tend to be a bit bluer and RBCs (maternal and fetal) a bit redder than the other compartments. To use this color difference, we need to quantify how red or blue is a given pixel. Although using red and blue channels of the RGB images is a straightforward idea, it may not be the one that would give the best result. This is explained by the fact that what our eye interprets as the RBCs being redder than the villi, actually means that the intensity of the red channel is the same for the RBC and villous pixels, but it is the intensity of the other channels (blue, in the case of villi and RBCs) that is different (Fig. 4.6). With this in mind, we define RBCs as pixels containing much red and little blue, while pixels, both red and blue channels of which are strong, correspond to the villi.

To quantify this notion, we introduce a measure M_r of how red is a given pixel:

$$M_r \equiv (r^2 - g^2 - b^2 + 2)/3,$$

where $0 \leq r, g, b \leq 1$ are the values of the red, green and blue channels of the pixel respectively. Thus introduced M_r will lie in the interval $[0; 1]$. Note that we have also added the green channel in the definition of M_r , since we have noticed that it further amplified the difference between M_r values of the villi, RBCs and IVS.² Calculated for all

¹A *binarization threshold* is the intensity (the brightness) of a pixel, above which the pixel is considered as white and below which it is considered as black in the process of binarization

²Certainly, there exist many alternative ways to introduce M_r . Different formulas were tested, and the provided one has given the best results so far. However, it may be interesting to further analyze alternative definitions looking for those giving even better contrast between cross-sectional components.

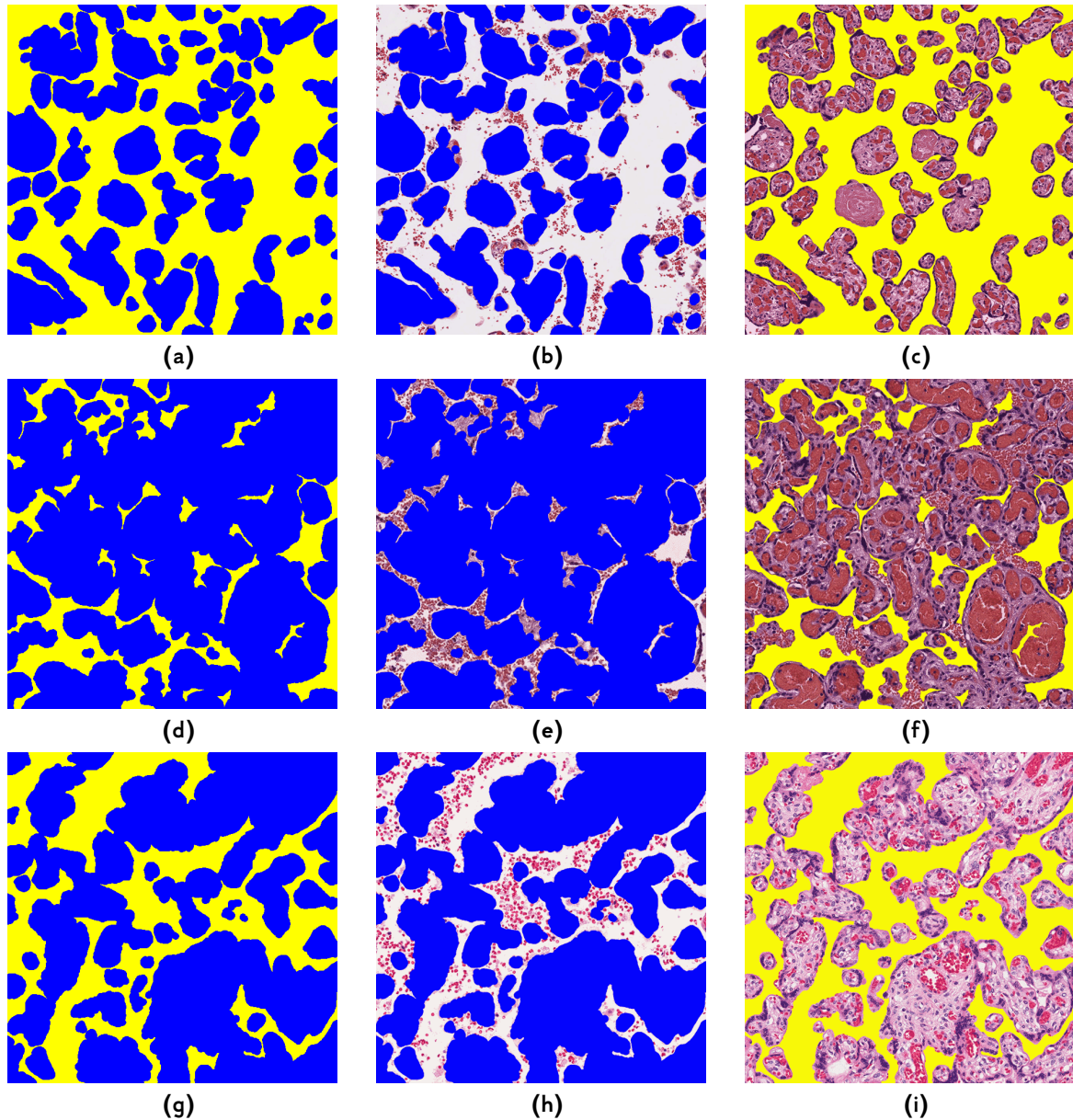


Figure 4.5. Application of basic image segmentation techniques to the *sparse* (a–c), *dense* (d–f) and *low-contrast* (g–i) placental sections with manually selected parameters. The *sparse* section ($1693 \text{ px} \times 1693 \text{ px}$, or $843 \mu\text{m} \times 843 \mu\text{m}$) is first binarized with the pixel intensity threshold set to 0.7/1.0. After that, small villous and IVS regions are removed as noise with area thresholds set to 1000 px ($248 \mu\text{m}^2$) and 20 000 px ($4960 \mu\text{m}^2$) respectively. Finally, villous compartments are eroded and then dilated with a circular structuring element (Fig. 4.10a) with a radius of 20 px ($10 \mu\text{m}$) (a). Good segmentation quality can be noticed from the projections of the IVS (b) and the villi (c) through the segmentation mask. The *dense* section ($1259 \text{ px} \times 1259 \text{ px}$, or $627 \mu\text{m} \times 627 \mu\text{m}$) is first binarized with the pixel intensity threshold set to 0.7/1.0. After that, small villous and IVS regions are removed as noise with area thresholds set to 4000 px ($992 \mu\text{m}^2$) and 1000 px ($248 \mu\text{m}^2$) respectively. Finally, villous compartments are eroded and then dilated with a circular structuring element with a radius of 14 px ($7 \mu\text{m}$) (d). Numerous segmentation errors (viz., identification of the maternal RBCs as villi, their “gluing” to fetal villi, or identification of parts of fetal capillaries as IVS) can be noticed from the projections of the IVS (e) and villi (f) through the segmentation mask. The *low-contrast* section ($1200 \text{ px} \times 1200 \text{ px}$, or $598 \mu\text{m} \times 598 \mu\text{m}$) is first binarized with the pixel intensity threshold set to 0.98/1.0. After that, small villous and IVS regions are removed as noise with area thresholds set to 2000 px ($496 \mu\text{m}^2$) and 300 px ($74 \mu\text{m}^2$) respectively. Finally, villous compartments are eroded and then dilated with a circular structuring element with a radius of 12 px ($6 \mu\text{m}$) (g). Good segmentation quality can be observed in the projections of the IVS (h) and the villi (i) through the segmentation mask. Color code: blue — villi, yellow — IVS. The resolution of all pictures is $0.498 \mu\text{m}/\text{px}$

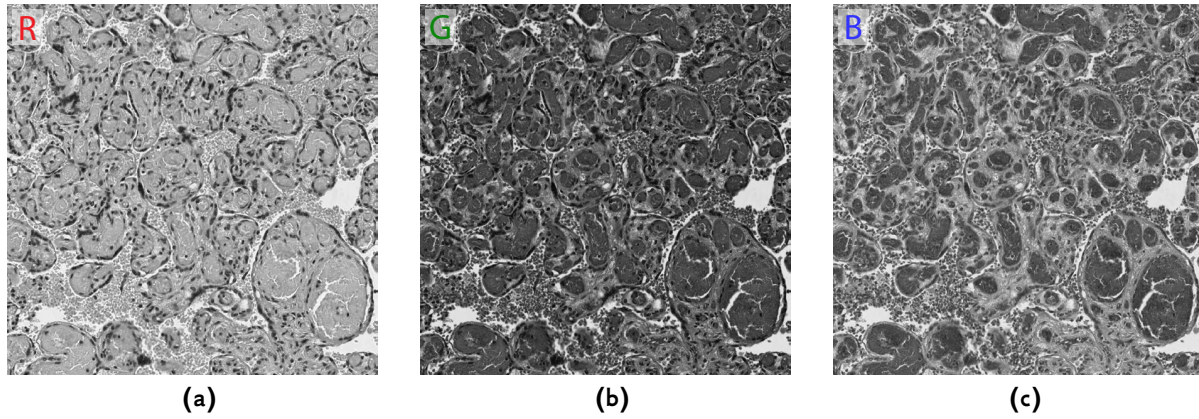


Figure 4.6. RGB channels of the *dense* placental section from Fig. 4.4d: red (a), green (b) and blue (c). The intensity of each channel (from 0 to 1) is shown in grayscale with 0 corresponding to the minimal intensity (black color) and 1 corresponding to the maximal intensity (white color)

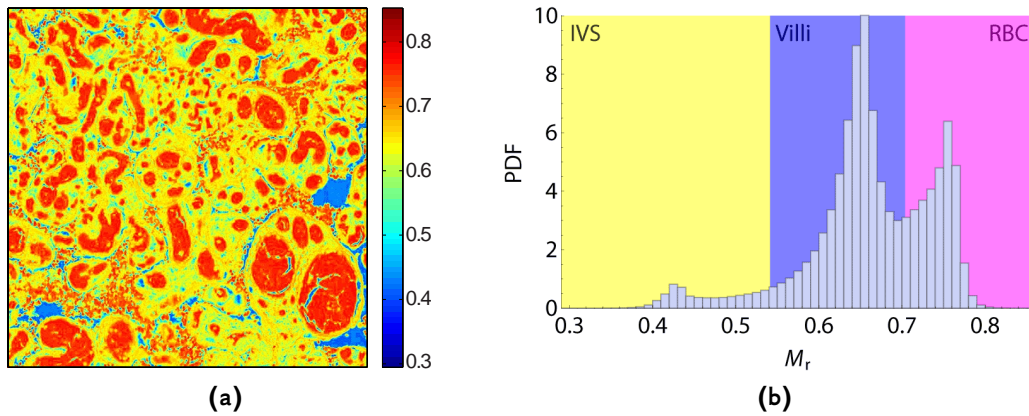


Figure 4.7. Measure M_r of how red is a given pixel: a color map (a) and a histogram of the M_r values distribution (b) plotted for the *dense* placental section. The histogram is divided into three regions (shaded), each corresponding to one of the placental components: IVS (yellow), villi (blue) and RBCs (magenta). The positions of the thresholds are defined as mean values between each two adjacent histogram peaks

pixels in an image, M_r gives a matrix, which can be plotted as a color map, where high values mark pixels most likely to be RBCs (Fig. 4.7a). Analysis of this figure confirms that M_r correctly locates both maternal and fetal RBCs (outside and inside the villi).

To define the shapes of the placental compartments in the section (villi, IVS and RBCs), we now need to determine thresholds in M_r values that would quantify the difference in color seen in Fig. 4.7a. One of the simplest way to do that is to analyze a histogram of the distribution of the values of M_r (Fig. 4.7b). The plotted histogram features three peaks that correspond to the IVS, villous and RBC components (from left to right). This correspondence allows us to define thresholds between the components as the mean values between each two adjacent peaks. The regions into which these thresholds divide the histogram (Fig. 4.7b) provide the initial segmentation of the placental cross-section (Fig. 4.8a).

Analysis of different cross-sections demonstrates that the histogram peaks are always located around the same values (which is explained by the similar coloring of all analyzed sections). However, it may happen that one or more peaks are missing or not well

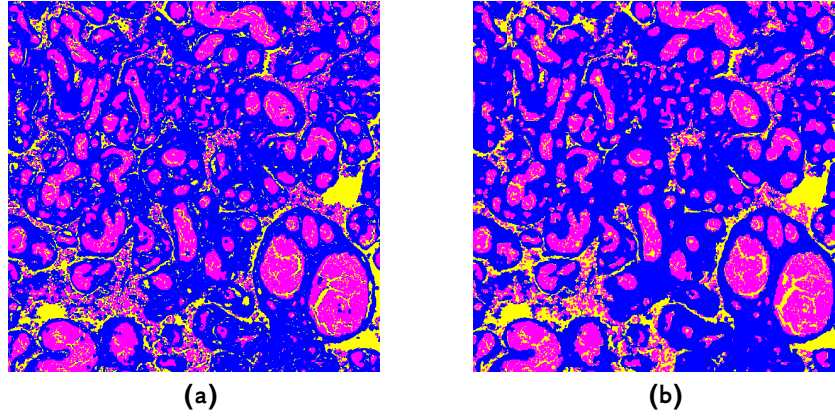


Figure 4.8. (a): The initial segmentation of the *dense* placental cross-section obtained by thresholding the histogram 4.7b. (b): *Dense* image segmentation after small villous and IVS noise has been filtered out (see text). Color code: blue — villi, yellow — IVS, magenta — maternal and fetal RBCs

pronounced due to the absence or little number of pixels corresponding to a specific component. For instance, this behavior can be observed in dense placental regions, when villi and maternal RBCs are so close together that no free IVS is visible. In such situation, we will assign default values to the missing thresholds: $M_r = 0.55$ for the IVS–villi threshold and $M_r = 0.7$ for the villi–RBC threshold.

4.2.3 Refining the segmentation

Filtering out noise

The obtained segmentation achieves a good distinction between the villi, the free IVS and the RBCs. However, we would like the maternal RBCs to be also considered as IVS, and to remove noise present in the segmentation. Also, RBC-free parts of the fetal capillaries (now identified as IVS) should be considered as parts of those capillaries.

One type of noise in Fig. 4.8a are small yellow (IVS) regions inside the blue regions (fetal villi), which correspond to non-intensively colored parts of the villi in the original section (Fig. 4.4d). A distinctive feature of these regions is that they are not in direct contact with either maternal or fetal blood and do not contain RBCs inside. We then replace all yellow regions that correspond to these criteria by the blue color.

Another type of noise is small villous regions, which cannot be associated with fetal villi due to their small size. Indeed, the smallest villi present in the human placenta are the terminal villi with a typical radius of $r \approx 25 \mu\text{m}$. Segmented blue regions that have an area significantly smaller than that of a terminal villus ($\ll \pi r^2 \approx 2000 \mu\text{m}^2$) are RBCs falsely identified as villi, emerging new villi or the results of tangential cuts at villi ends or surfaces. In none of the cases these small blue regions represent fully functional villi that actively participate in the exchange. Therefore, the blue regions, whose area is less than $0.5\pi r^2 \approx 1000 \mu\text{m}^2$, will be replaced by the yellow color.

Finally, we also consider as noise the yellow regions that are in contact with (or contain) magenta regions and that together with all these magenta regions occupy an area that is smaller than a typical area of a red blood cell. By definition, such regions cannot fit an RBC, and hence cannot correspond to a functional part of the IVS. Since

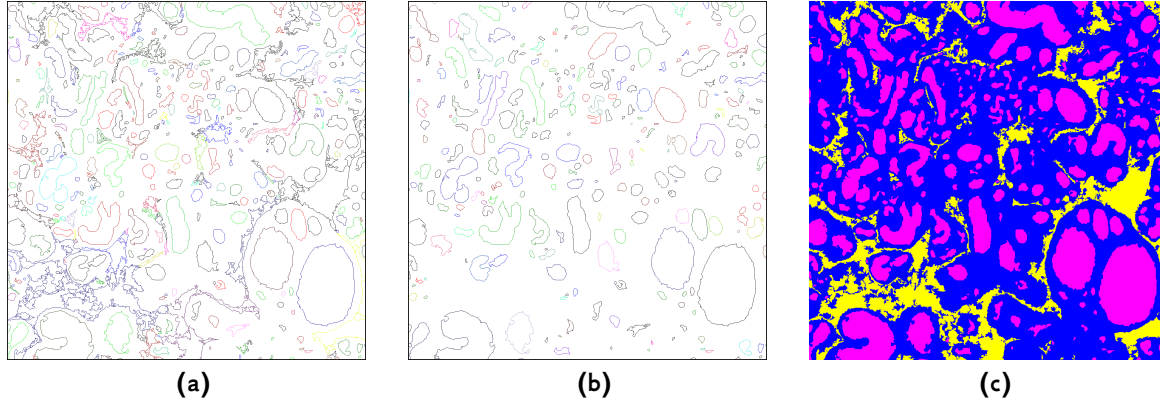


Figure 4.9. (a): Contours of the “complete” IVS regions from Fig. 4.8b. (b): Contours of (a), the perimeter of which for more than 70 % is made up of RBCs. The reference RBCs distribution is taken from the initial segmentation (Fig. 4.8a). (c): The segmentation of the original image after all contours of (b) are set to the RBC color and all other contours of (a) are set to the IVS color. An accurate differentiation between the fetal capillaries and the IVS can be observed. Color code: blue — villi, yellow — IVS, magenta — fetal capillaries

the typical RBC radius is $r \approx 3 \mu\text{m}$, we set the area threshold at $\pi r^2 \approx 28 \mu\text{m}^2$ and convert all yellow and magenta regions with smaller area to the blue color. The segmentation of the *dense* section after these operations is shown in Fig. 4.8b.

Discriminating fetal capillaries from the IVS

Now that we have filtered out the noise, our main concern is to discriminate between the maternal and the fetal RBCs. For this purpose, we take advantage of the following observation that can be made from Figs 4.8a or 4.8b: the perimeter of a fetal capillary is nearly always lined with a continuous layer of RBCs, while the perimeter of a “complete” IVS region (IVS and its RBCs) is normally only partly occupied by the RBCs. To exploit this observation, we will first temporarily remove villous regions from the obtained noise-free picture (Fig. 4.8b) and assign the same color to the IVS and the RBCs. Each region in such picture is either a fetal capillary or a “complete” IVS region. We further extract the contours of each separate region, which are shown in Fig. 4.9a. Relying on Fig. 4.8a, we then calculate the percentage of the pixels of each contour that were identified as RBCs in the initial segmentation. The contours, in which this percentage is small ($\leq 70\%$), will be interpreted as the contours of the IVS and removed. The rest of the contours (Fig. 4.9b) will be considered as the contours of the fetal capillaries. If now we return to the noise-free segmentation picture (Fig. 4.8b) and set the regions of Fig. 4.9b to the RBC color, and all other contours to the IVS color, we obtain a segmentation with rather accurately differentiated fetal capillaries and IVS (Fig. 4.9c).

Smoothing out the contours

Comparing the obtained results (Fig. 4.9c) to the “ideal” manual segmentation of the *dense* section (Fig. 4.4e), one may observe that only one major segmentation problem persists: patchy regions in the IVS, which originally were maternal RBCs, but are now falsely identified as fetal villi. Note that not only the shape of these regions does not

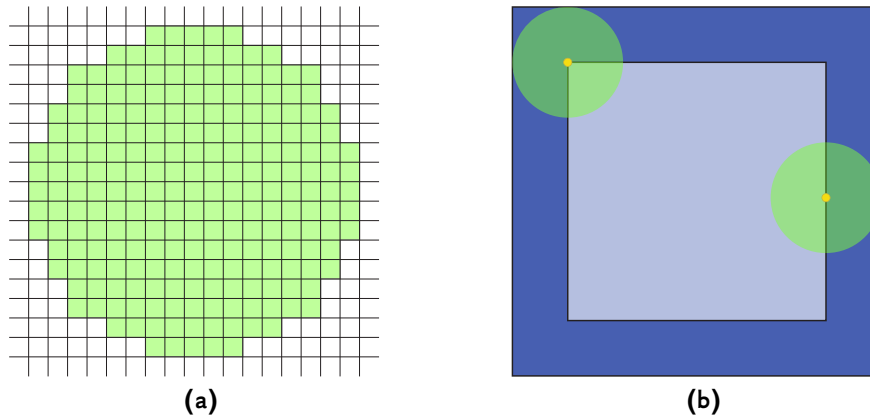


Figure 4.10. (a): A circular structuring element (a probe) of 8 px radius. (b): Illustration of an application of the erosion method to a square. Green circles represent a circular structural element with a center marked by a yellow point. The light blue region shows the result of the erosion, while the dark blue region marks the part of the region discarded during erosion. The result of erosion is defined as the locus of points occupied by the center of the probe at all possible positions of the probe *inside* the original region

correspond to the villi, but also their size is much closer to the characteristic size of an RBC (with a radius of $3\text{--}4\ \mu\text{m}$) than to that of the fetal villi (with the radius of the smallest villi being around $25\ \mu\text{m}$). These regions have escaped the noise filtering by the occupied area described on p. 117, because either they were connected to the “real” villous regions, or were large close-lying agglomerations of RBCs. The main strategy to remove these regions consists in separating them from the “real” villi and smoothing out the boundaries of the “real” villi.

This strategy can be realized by the application of the standard technique of erosion and dilation (Serra, 1982).³ To erode a region, one first chooses a centered structuring element (a probe), e.g. a circular structuring element (Fig. 4.10a). The new eroded region is then defined as the locus of points occupied by the center of the probe at all possible positions of the probe *inside* the original region. An illustration of the erosion performed on a square region with a circular structural element is shown in Fig. 4.10b. The circular shape of the structuring element is a natural choice for an image not composed of straight lines and right corners. At the same time, the size of the structuring element should be chosen based on the characteristic size of the components of the eroded image. Since at this stage our main goal is to remove regions corresponding to agglomerations of RBCs, it is reasonable to take a structuring element with the size of an RBC. Such structuring element will remove separate RBCs and break links between RBC agglomerations and villous regions if these links are single RBC chains. The resolution of all our placental cross-sections being $0.498\ \mu\text{m}/\text{px}$, the RBC radius of around $3\text{--}4\ \mu\text{m}$ yields a structural element with the radius of 8 px (Fig. 4.10a).

The erosion performed in this way will reduce the typical radius of the smallest villi in the picture from $25\ \mu\text{m}$ to $21\ \mu\text{m}$. The objects of the new picture identified as villi, but significantly smaller than that size, are then removed. Those are most probably RBCs agglomerations or cuts of villi at their ends or surfaces. Since such objects are not

³For introduction to standard methods of mathematical morphology and image analysis see Serra (1982), Pratt (1991), Shih (2009).

Table 4.1. The accuracy of the automatic segmentation algorithm estimated by pixel by pixel comparison with the “ideal” segmentation

Image	Total number of pixels	Number of wrongly identified pixels	Percentage of wrongly identified pixels, %
<i>Sparse</i>	2 866 249	23 397	0.82
<i>Dense</i>	1 585 081	42 442	2.68
<i>Low-contrast</i>	1 440 000	200 758	13.94

functional villi, we replace these small objects with the IVS color, namely all objects, whose area is smaller than half of the area of a typical eroded small villus: $\pi(21\mu\text{m})^2/2 \approx 700\mu\text{m}^2$. Finally, we perform the dilation process on all the remaining villous regions. The dilation is the process opposite to the erosion, and the resulting new dilated region is defined as the locus of points covered by the structuring element, while the center of the structuring element occupies all possible positions inside the region. Performing dilation on the eroded villi with the same circular structuring element (having the radius of $4\mu\text{m}$, or 8 px) will nearly completely restore the area of the original villous regions before the erosion. At the same time, small-size spiky parts of their boundaries will not be reproduced, and the boundaries will become smoother, which facilitates the application of morphometrical techniques later on. The image obtained for the *dense* section after the erosion, removal of small “villous” components and dilation is shown in Fig. 4.11e.

4.2.4 Accuracy of the segmentation algorithm

The final segmentation obtained for the three test cross-sections of Fig. 4.4 are shown in Fig. 4.11. As can be seen, the described algorithm gives visually good segmentation results for the *sparse* and *dense* images, but the segmentation is patchy and much less accurate for the *low-contrast* cross-section (due to the reasons discussed in Section 4.2.1 on p. 114). To objectively judge the results, it would be useful to introduce a quantitative measure of segmentation quality. The simplest way is to compare pixel by pixel the obtained segmentations (Figs 4.11d–f) with the “ideal” manual segmentations discussed before (Figs 4.11g–i) and calculate the number of misidentified pixels. Since fetal capillaries were not distinguished during the manual segmentation, for this comparison, we will consider the capillary regions as parts of the corresponding villous regions. The results of the pixel by pixel comparison for the three illustrative images are presented in Table 4.1. One can see that the method is indeed very efficient for the *sparse* and the *dense* cross-section, and performs satisfactory for the *low-contrast* one. However, the error in the *low-contrast* case is likely to be greater if we compare the perimeters and not the areas of the placental compartments, since some villi got divided into several separate regions. Nevertheless, the overall precision of the histomorphometrical results obtained by the automatic segmentation even for low-contrast slides may still be comparable to the precision of those obtained for the same slides by manual point–intersection counting techniques discussed in Section 4.1.3 thanks to considerably greater sample sizes, which can be processed with automatic techniques.

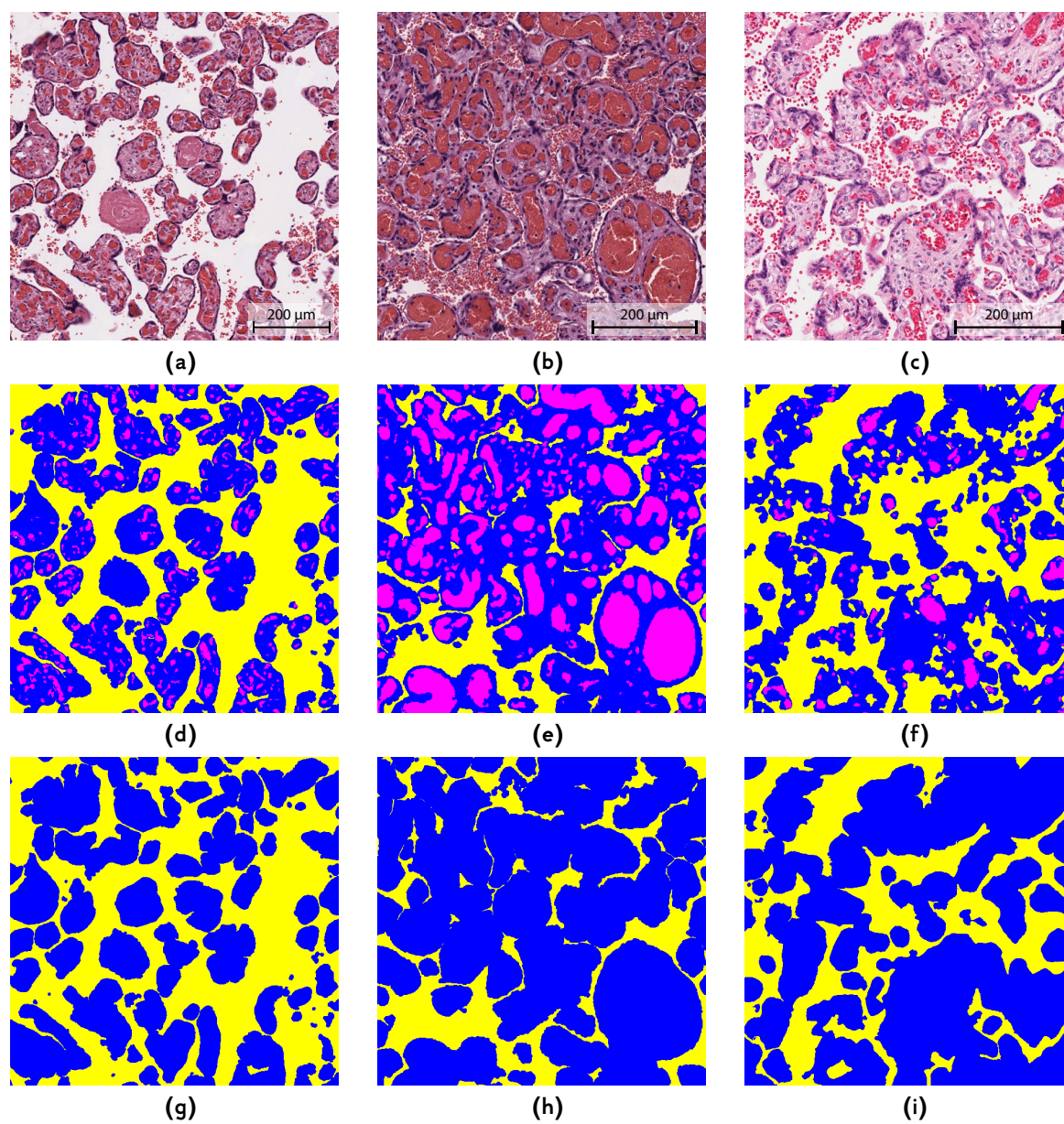


Figure 4.11. Segmentations of the *sparse* (d), *dense* (e) and *low-contrast* (f) placental sections obtained with the presented automatic algorithm. The original images (a–c) and the “ideal” manual segmentations (g–i) are reproduced above and below each image to facilitate comparison. Color code: blue — villi, yellow — IVS, magenta — fetal capillaries

Future work on the segmentation of the cross-sectional components may concentrate on:

- Modification of the segmentation algorithm so that it provides higher segmentation efficiency for low-contrast slides.
- Development of the ways to evaluate the accuracy of the segmentation. For instance, one might compare the fractions of the cross-section occupied by the placental compartments after the initial thresholding and in the final results.
- Development of algorithms of separation of “glued” villi. Note that the “glued” villi remaining in dense or low-contrast slides do not influence the villi density or the total active fetal perimeter (see discussion in Section 3.2.4 on p. 103) measured in this thesis. However, the “glued” villi should be separated if one aims at analysis of distributions of cross-sectional areas and perimeters of *individual* villi.

4.2.5 Histomorphometrical measurements

The second stage of the placental cross-sections analysis consists in performing histomorphometrical measurements on the obtained segmentations. As described earlier, the application of the STPM requires that two parameters be measured: the total villous area and the total villous perimeter. Although it is possible to automatically apply the point-intersection counting techniques of Section 4.1.3 to the obtained segmented placental sections, simpler and substantially more precise methods become available when the placental compartment type is known for each pixel. Thus, the area of each *individual* villus (or villous region) can now be measured by simple counting of the pixels forming the connected region. The question of how to measure the perimeter of each individual villus (or villous region) is more interesting, since several options are available due to the inherent pixelation of each region.

In the present thesis, we will use one of the simplest perimeter estimation methods, namely counting the number of side (not corner) outside neighbors of the boundary pixels of the given region (for details see the caption of Fig. 4.12a). The primary advantage of this measurement method is the simplicity of implementation, since the required number of neighboring pixels can be obtained by performing erosion of the initial region with a circular structuring element of radius 1 px and calculating the difference in area between the new region and the initial one. However, this method is not very accurate and may give an up to a $\sqrt{2}$ error in the perimeter due to an imprecise description of corner regions. If higher precision of the perimeter measurements is required, more sophisticated algorithms should be used. A brief overview of these algorithms is presented in the next two paragraphs to provide the reader with the general idea of the improvement direction.

Mathematical studies investigating different perimeter definitions for pixelated regions have demonstrated that an accurate perimeter estimation requires making some assumptions on the shape of the region (Yang et al., 1994). To measure the perimeters of “blob-like” regions (which are typical in segmented placental cross-sections), one can use a method based on matching pixel patterns (Gray, 1971, Pratt, 1991), 3-bit (Freeman,

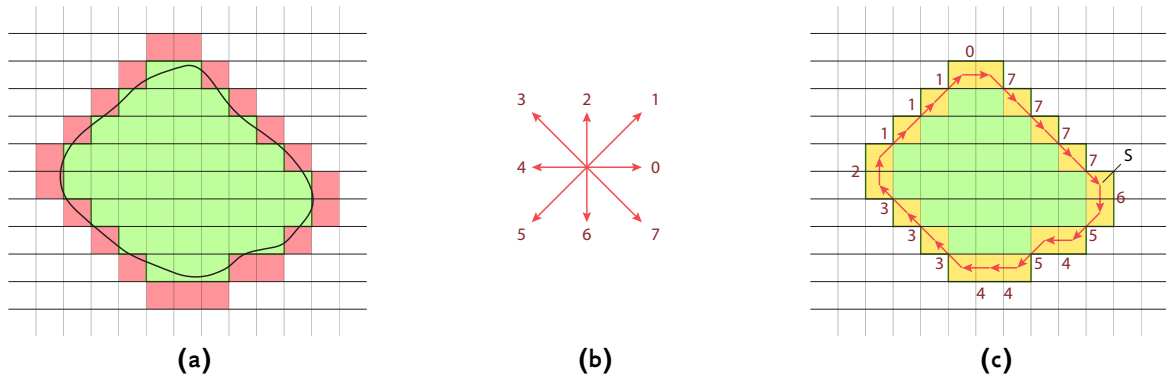


Figure 4.12. (a): Illustration of the perimeter estimation through side neighbor counting used in the present thesis. A thick black line outlines the original continuous region. The shaded green region is the digitized version of the original region after it is projected on a pixel mesh. To estimate the perimeter by the neighbor-counting method, one needs to count all pixels lying outside the pixelated region, which are in side contact with it (shown in red). If the region is partly located at the boundary of the analyzed image, the perimeter of the region is given by the sum of the number of pixels located at the image boundary and the number of pixels in side contact with the region. The perimeter of the example region in this figure is 22 px. Note that using an outside perimeter avoids the problems in definition for 1-pixel-thick region parts, which are encountered with internal perimeter definitions. An alternative and more precise method of perimeter estimation is illustrated in (b) and (c), but is not used for calculations in the present thesis. (b): A chain code of Freeman (1970). Each directed line segment is encoded by a digit from 0 to 7 according to the given scheme. With this code, an arbitrary contour can be digitized, i.e. represented as a sequence of digits. (c): Encoding a region contour with the Freeman's chain code. The same example region as in (a) is used. In the Freeman's method, first the boundary pixels inside the region having side contact with the outside are identified (shaded in yellow). A boundary contour is then constructed by sequentially connecting the centers of the boundary pixels (the red line). Next, this contour is encoded with the chain code of Freeman (b) from the starting point (S). The code for the contour in the picture is 654544333211107777. Once the contour is encoded, the perimeter of the original continuous region can be estimated by the Kulpa's formula (4.2). Since the contour code in the picture contains 6 even digits and 12 odd digits, the perimeter is $3\pi(5 + 3\sqrt{2})/4 \text{ px} \approx 21.8 \text{ px}$. The value provided by this method was proved to be more accurate for blob-like objects than those provided by other methods (Kulpa, 1977). Note however that the difference between this result and our basic neighbor-counting estimation for the example contour (22 px) is only 1%. This perimeter estimation error was obtained for a particular case shown in the figure, but is still significantly low than a typical error one could expect from the segmentation of a low-contrast placental slide (Table 4.1), which explains the use of the simple and less precise perimeter measurement algorithm in this thesis.

1970, Kulpa, 1977, Vossepoel and Smeulders, 1982, Dorst and Smeulders, 1987), 4-bit and generalized chain-coding methods (Saghri and Freeman, 1981), or a mid-crack chain-coding method (Dunkelberger and Mitchell, 1985, Shih and Wong, 1992). A comparison of the efficiency of these methods suggests that Kulpa's modification of the Freeman chain-coding method gives a good perimeter estimation for most blob-like objects met in practice (Kulpa, 1977, Yang et al., 1994).

In this method, the boundary of a region is defined as all inside pixels having at least one outside neighbor among their four side neighbors (boundary pixels are shown in yellow in Fig. 4.12c). The defined boundary is a connected discrete contour if we consider 8-points connectivity between the neighbors. The boundary contour is then encoded with Freeman's chain code describing the line connecting the centers of the boundary pixels by a sequence of numbers, each encoding a certain direction of a line segment (Fig. 4.12b). Kulpa (1977) has then demonstrated that the perimeter of such contour can be calculated as

$$P \equiv \frac{\pi}{8}(1 + \sqrt{2})(n_e + \sqrt{2}n_o), \quad (4.2)$$

Table 4.2. Dependence of the execution time of the developed image analysis code on image size. The growth of execution of time per megapixel of image size is due to the region labeling procedure

Image side, px	1000	2000	3000	4000	5000	6000	7000	8000	9000
Image size, Mpx	1	4	9	16	25	36	49	64	81
Execution time, min	0.12	0.52	1.4	2.6	5.1	8.6	13.0	20.0	40.7
Execution time per megapixel, s/Mpx	7.0	7.8	9.3	9.7	12.3	14.3	16.0	18.8	30.1

where n_e and n_o are the numbers of even and odd numbers in the Freeman's description of the contour, and the factor $\pi/8(1 + \sqrt{2})$ is added to compensate for the staircase-like approximation of the original continuous contour. It was further demonstrated that in practice this algorithm can be implemented directly, without the need to actually encode the contour (Kulpa, 1977).

4.2.6 Code execution time as a function of image size

The computer code implementing all described image analysis algorithms was written in C++. Standard image analysis functions, such as erosion, dilation, region labeling or area computation, were taken from the open source Population image processing library (2012 version) written by Vincent Tariel (<http://www.population-image.fr>). The Population library project was originally started at the Condensed Matter Physics (PMC) laboratory of École Polytechnique as a part of the Ph.D. thesis of Vincent Tariel (Tariel, 2009).

The computer code was compiled with Intel Compiler 14.0.2 and run on a computer cluster consisting of 16 computation nodes, each of which is equipped with 24 Gb of RAM and 2 Intel Xeon E5620 CPUs running at 2.4 GHz with 4 cores each. The computation nodes run under CentOS 5.5, and the distribution of tasks between the computation nodes is performed by a scheduling software TORQUE 2.5.7 running on a separate master node. This computation facility allows to simultaneously run 128 tasks, i.e. to simultaneously process 128 placental images.

The dependence of the code execution time on image size on one processor core of the computation cluster is provided in Table 4.2. One may observe that the execution time per megapixel of image increases with the total number of pixels in the image. This non-linear behavior is mainly due to region labeling operations, which are employed to identify separate regions in the segmented image. This trend suggests that it is more time-efficient to process smaller pictures than larger ones. Moreover, villi density and slide staining may differ from one region to another within the same slide, and choosing smaller pictures allows the algorithm to choose a more appropriate initial segmentation threshold. However, one should not use images that are too small, since in those slides a higher fraction of villi lies on the slide boundary, which introduces errors in histomorphometrical measurements due to the discarded regions outside the slide. With these considerations in mind, in the present thesis, we cut each large placental section into $2500\text{px} \times 2500\text{px}$ images.

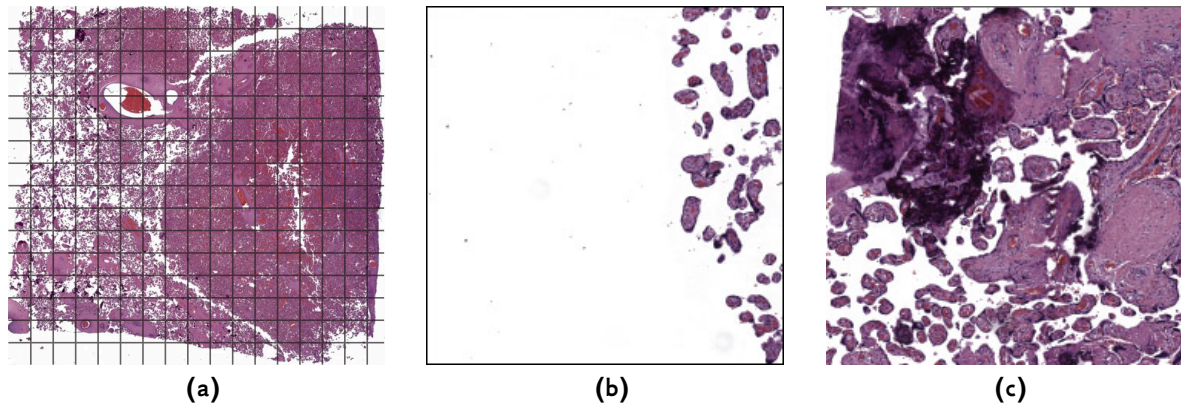


Figure 4.13. Illustration of cutting and selection of placental images. A large placental section (around $2\text{ cm} \times 2\text{ cm}$, or $40\,000\text{ px} \times 40\,000\text{ px}$) is cut into smaller images (around $1.25\text{ mm} \times 1.25\text{ mm}$, or $2500\text{ px} \times 2500\text{ px}$) in a regular fashion starting from the upper left corner (a). Among the cut images, those in which the outside of the placental cross-section occupies more than a half of the image (b) and those which contain staining artifacts (the dark region in (c)) are excluded from the subsequent analysis. All other images are processed. All illustrations are taken from the placenta No. 2780

4.3 Algorithm application to placental cross-sections

4.3.1 Samples description

The developed algorithm was applied to 25 large placental cross-sections (one cross-section per placenta) collected by Dr. Carolyn Salafia (Placental Analytics, LLC, Larchmont, NY) in the hospitals of New York. These sections include 22 placentas from pregnancies diagnosed as healthy and 3 placentas from pregnancies with complications, namely 1 moderate diabetes case, 1 severe diabetes case and 1 pre-eclampsia related intra-uterine growth restriction case (with the delivery at 31 weeks of pregnancy). Each placenta is assigned a unique numeric label which is provided along the results. Each placental section has the physical size of around $2\text{ cm} \times 2\text{ cm}$ and was digitized at a fixed resolution of $0.498\text{ }\mu\text{m/px}$ yielding large images of about $40\,000\text{ px} \times 40\,000\text{ px}$ (160 Mpx). Each image was then cut into smaller fragments of $2500\text{ px} \times 2500\text{ px}$ ($1.25\text{ mm} \times 1.25\text{ mm}$) to optimize the processing time as discussed above (Fig. 4.13a).

All the cut images were then looked through for the presence of staining artifacts or section boundary. Images which visually had more than half of the image area occupied by the white background outside the placental section (Fig. 4.13b) were excluded from further analysis. An example of a staining artifact which may interfere with the segmentation process is shown in Fig. 4.13c. Such images were also excluded. After the automatic segmentation of all images was completed, the images were looked through to visually check the segmentation and to identify cases where it was considerably incorrect. Those were few (3.7 % in total) and were mainly explained by the presence of large stem villi with large vessels poorly filled with RBCs or by regions featuring low contrast between the villous stroma and the IVS (see Fig. 4.4i). The numbers of images at each stage in each placenta are aggregated in Table 4.3.

Table 4.3. The number of images obtained after cutting placental cross-sections, the number of images excluded from analysis before and after segmentation, and the total number of images retained per placenta. Both healthy (H) and pathological placentas are reported. IUGR & PE stands for the pre-eclampsia induced intra-uterine growth restriction case

Placenta label	Healthy/ Pathological	Total number of images	Boundary images and images with artifacts	Incorrectly segmented images	Retained after all stages	Retained after all stages, %
2274	H	270	40	17	213	79
2648	H	308	32	36	220	71
2774	H	306	69	11	226	74
2775	H	297	47	7	243	82
2780	H	306	64	5	237	77
2817	H	228	38	6	184	81
2923	H	204	46	3	155	76
2924	H	224	53	20	151	67
2926	H	255	46	0	209	82
2931	H	306	67	6	233	76
2935	H	272	51	1	220	81
2939	H	208	26	2	180	87
2940	H	238	47	2	189	79
2941	H	307	19	12	276	90
2942	H	270	63	7	200	74
2945	H	425	87	1	337	79
2947	H	214	20	12	182	85
2950	H	352	85	6	261	74
2952	H	234	46	0	188	80
2953	H	315	30	4	281	89
2962	H	336	59	7	270	80
7594-86	H	357	112	14	231	65
4586-02	Sev. diab.	352	195	5	152	43
12302-86	Mod. diab.	353	105	14	234	66
13079-86	IUGR & PE	255	109	18	128	50

4.3.2 Comparison of segmentation results for healthy and pathological placentas with the results obtained with manual histomorphometrical techniques

The results of the histomorphometrical measurements of the villi area and the villi perimeter in the 25 described placentas are reported in Table 4.4. The average values of all characteristics for all healthy and all pathological placentas are shown in Table 4.5. One can see that within the precision of the measurements, no difference between the analyzed healthy and pathological placentas can be observed. This observation should however be regarded with caution since averaging over only three pathological placentas featuring different pathologies cannot be expected to provide a reliable ground for comparison. Analysis of more samples in each pathological category and their comparison to healthy cases is required before any reliable conclusions can be drawn.

However, the statistics obtained for the 22 healthy placentas is larger and can be

Table 4.4. Segmentation results for 22 healthy and 3 pathological placentas obtained with our automatic image analysis. *Notations:* S_{an} — the total analyzed area of the cross-section, φ_{all} — the fraction of S_{an} occupied by all types of villi including their capillaries, φ — the fraction of small villi in the total area of small villi and IVS (small villi density required by the STPM), φ_{IVS} — the fraction of S_{an} occupied by the IVS ($\varphi_{all} + \varphi_{IVS} \equiv 1$), φ_{cap} — the fraction of S_{an} occupied by the fetal capillaries, P_{all} — the total perimeter of all villi in the analyzed cross-sections, $P_{sm.v}$ — the total perimeter of the small villi, ε — the surface density of all villi, r_e — the effective radius of the fetal villi defined by Eq. (3.11), Da — the parameter Da defined by Eq. 3.13. S_{an} , φ_{all} , φ_{cap} and P_{all} were directly measured, while φ_{IVS} , φ , $P_{sm.v}$, ε , r_e and Da were calculated from them. *Calculation details:* Since our segmentation algorithm does not allow to distinguish between small (terminal and mature intermediate) and other villi, we have used the fraction of small villi in the cross-sectional area of all villi equal to $\alpha \equiv 0.665$ and the fraction of small villi in the perimeter of all villi equal to 0.773 (Sen et al., 1979). φ was then calculated by the formula (2.22), and $P_{sm.v} \equiv 0.773P_{all}$. The all-villi surface density ε is the ratio of the all-villi perimeter to their cross-sectional area: $\varepsilon = P_{all}/(\varphi_{all}S_{an})$. According to the definition, the average value of r_e was calculated as $r_e = 2\alpha\varphi_{all}S_{an}/P_{sm.v}$. The average oxygen extraction time in each cross-section was calculated as $\tau_e \equiv Br_e/(2w\kappa)$ and the Damköhler number was calculated as $Da = 2w\kappa L_0/(uBr_e)$, where $w = 2.8 \cdot 10^{-4}$ m/s, $L_0 = 1.6$ cm, $u = 6 \cdot 10^{-4}$ m/s, $B = 94$ (Table 2.2) and κ is expected to be on average 0.35 in the human placenta (see discussion on p. 92)

Placenta label	S_{an} , mm ²	φ_{all}	φ	φ_{IVS}	φ_{cap}	P_{all} , m	$P_{sm.v}$, m	ε , mm ⁻¹	r_e , μ m	τ_e , s	Da
2274	316	0.57	0.47	0.43	0.107	8.8	6.8	49	35	16.8	1.6
2648	336	0.56	0.46	0.44	0.036	9.0	7.0	48	36	17.3	1.5
2774	350	0.65	0.55	0.35	0.073	8.1	6.3	36	48	23.0	1.2
2775	377	0.67	0.57	0.33	0.069	7.6	5.9	30	57	27.3	1.0
2780	367	0.66	0.56	0.34	0.086	8.3	6.4	34	50	24.0	1.1
2817	277	0.64	0.54	0.36	0.025	6.0	4.6	34	51	24.5	1.1
2923	236	0.71	0.62	0.29	0.041	7.4	5.7	44	39	18.7	1.4
2924	233	0.65	0.55	0.35	0.026	7.3	5.6	48	36	17.3	1.6
2926	313	0.55	0.45	0.45	0.023	9.5	7.3	55	31	14.9	1.8
2931	359	0.70	0.61	0.30	0.048	9.2	7.1	37	47	22.5	1.2
2935	334	0.59	0.49	0.41	0.049	7.0	5.4	36	48	23.0	1.1
2939	274	0.63	0.53	0.37	0.011	7.7	6.0	45	39	18.7	1.4
2940	293	0.65	0.55	0.35	0.012	5.8	4.5	30	56	26.9	1.0
2941	428	0.56	0.46	0.44	0.025	12.5	9.7	52	33	15.8	1.7
2942	305	0.69	0.60	0.31	0.016	7.7	6.0	37	47	22.5	1.2
2945	514	0.56	0.46	0.44	0.007	11.3	8.7	39	44	21.1	1.3
2947	280	0.63	0.53	0.37	0.008	7.0	5.4	40	43	20.6	1.3
2950	402	0.61	0.51	0.39	0.013	8.6	6.6	35	49	23.5	1.1
2952	288	0.55	0.45	0.45	0.008	8.1	6.3	51	34	16.3	1.7
2953	417	0.69	0.60	0.31	0.011	8.9	6.9	31	56	26.9	1.0
2962	403	0.71	0.62	0.29	0.023	9.6	7.4	34	51	24.5	1.1
7594-86	342	0.57	0.47	0.43	0.042	9.2	7.1	47	36	17.3	1.5
4586-02	243	0.64	0.54	0.36	0.047	5.3	4.1	34	50	24.0	1.1
12302-86	358	0.60	0.50	0.40	0.025	10.0	7.7	47	37	17.7	1.5
13079-86	198	0.52	0.42	0.48	0.070	4.5	3.5	44	39	18.7	1.4

Table 4.5. Mean values of the parameters from the segmentation statistics presented in Table 4.4. Within the precision of measurements, no difference can be observed between the analyzed healthy and pathological cases. The fourth column features values calculated on average from the previously published data on healthy placentas (Aherne and Dunnill, 1966, Mayhew et al., 1993a, Lee and Mayhew, 1995, Mayhew and Jairam, 2000, Nelson et al., 2009, see also Tables 2.3 and 2.5)

	Healthy	Pathological	Literature data
$S_{\text{an}}, \text{mm}^2$	330 ± 70	270 ± 80	
φ_{all}	0.63 ± 0.05	0.59 ± 0.06	0.49 ± 0.08
φ	0.53 ± 0.06	0.49 ± 0.06	0.46 ± 0.06
φ_{IVS}	0.37 ± 0.05	0.41 ± 0.06	
φ_{cap}	0.04 ± 0.03	0.05 ± 0.02	
P_{all}, m	8.3 ± 1.6	6.6 ± 3.0	
$P_{\text{sm.v}}, \text{m}$	6.4 ± 1.3	5.1 ± 2.3	
$\varepsilon, \text{mm}^{-1}$	40 ± 8	41 ± 7	44 ± 6
$r_e, \mu\text{m}$	44 ± 8	42 ± 4	41 ± 3
τ_e, s	21 ± 4	20 ± 2	19.7 ± 1.4
Da	1.3 ± 0.2	1.3 ± 0.2	1.3 ± 0.1

compared to the previously published histomorphometrical data. Since the placentas differ in size, the comparison of the characteristics is meaningful only for those of them which are not supposed to scale with the size of the placenta, namely, the villi density, the small villi density, the all-villi surface density, the effective villi radius (equal to twice the inverse small villi surface density: $r_e \equiv 2/\varepsilon_{\text{sm.v}}$) and the Damköhler number Da. The values of these characteristics averaged across the previous studies cited in Tables 2.3 and 2.5 are reproduced in the fourth column of Table 4.5. Comparison of our results to the published data demonstrates that within the precision of the measurements, all mentioned characteristics (except for the all-villi density φ_{all}) agree well between the studies. The difference in φ_{all} is explained by the fact that the previous studies calculated the all-villi volume fraction in the total volume of the placenta that includes the basal and the chorionic plates, while we exclude these regions from the analysis. The traditional way of calculation should effectively diminish the presence of villi in the placenta resulting in smaller φ_{all} values than in our study, which is indeed observed. This explanation is further justified by the fact that the calculation of φ (which does not include placental membranes) gives values which well agree between the studies.

4.3.3 Efficiency diagrams

The histomorphometrical results obtained for each analyzed placenta can now be plotted on the efficiency diagrams introduced in the previous chapter (Fig. 4.14). From the *villi density efficiency* diagram (Fig 4.14a), it can be seen that the villi density of a typical human placenta is very efficient for the given effective villi radius. Indeed, the villi density is such that the placenta extracts more than 90 % of all oxygen that it could extract with the observed geometry of the villi and with all other parameters fixed. However, the *overall geometry efficiency* diagram 4.14b demonstrates that the extraction could be even more efficient if the villi were smaller. Precisely, the observed villi radius allows the placenta to extract only around 30–40 % of the maximal oxygen flow that could enter

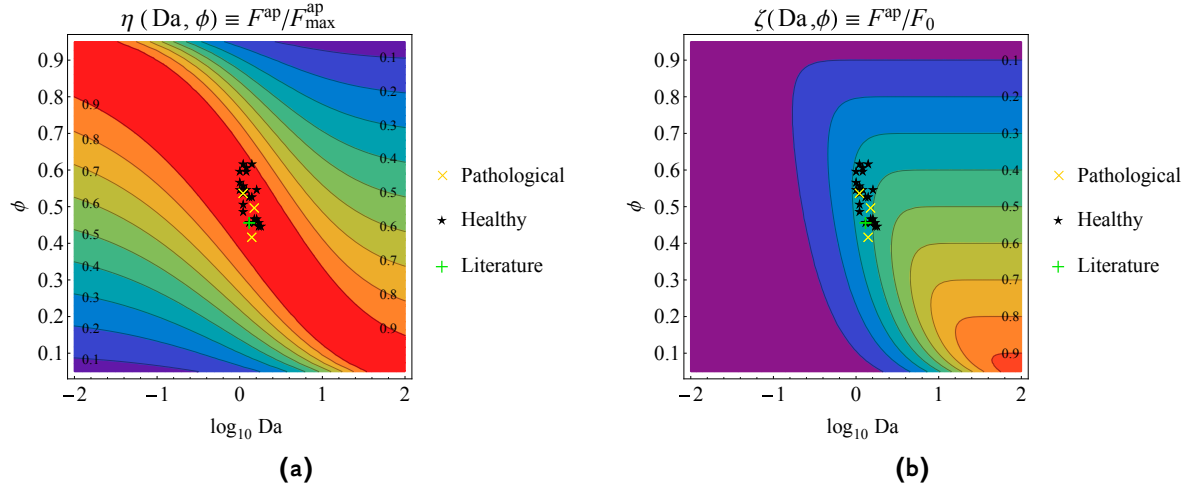


Figure 4.14. The efficiency diagrams introduced in the previous chapter (Fig. 3.3) with the histomorphometrical data obtained with the automatic segmentation method for 22 healthy and 3 pathological placentas: the villi density efficiency (a) and the overall geometry efficiency (b)

a stream-tube free of villi. However, as discussed in Chapter 3, this apparent inefficiency may be explained by the fact that the developed theory does not take into account the internal structure of the villi (e.g., fetal capillaries), which presents a biological restriction for diminishing the size of the villi.

A remark should be made here about the calculation of the Damköhler number $Da \equiv 2wkL_0/(uBr_e)$. In the calculations performed in this chapter, we have assumed that all the parameters used to compute Da remain constant except for the effective villi radius. However, as discussed in Section 4.1.1, this assumption is most probably false for the maternal blood flow velocity u and is likely to not always apply to the placental membrane permeability w . In the real situation, the maternal blood flow velocity would depend on the villi density, as well as on the difference in the hydrostatic blood pressure between the spiral arteries and the decidual veins that drives the maternal blood through the placenta. Unfortunately, the available experimental data is insufficient to introduce these factors into our calculations. To make the model predictions more accurate, the maternal blood velocity should be measured non-invasively *in vivo* or in artificial placental perfusion setups, or a completely resolved 3D placental structure should be obtained *in vivo* or *post-partum*, so that the maternal blood flow patterns can be simulated. Note that the changes in the placental structure during the delivery and the fixation of the slides may have also to some extent influenced the efficiency predictions.

Variations in the placental membrane permeability are most likely to be caused by variations in the thickness of the fetal endothelial and epithelial layers. This thickness can be estimated from the same placental slides either by traditional manual methods or by modifying the automatic segmentation algorithm. Although using the automatic algorithm may provide higher precision estimation, performing the modifications allowing to segment these boundary layers would require significant effort. This is mainly due to the discrete character and the low contrast of the villous trophoblast boundary layer and the fetal endothelial layer (see zoomed regions of placental sections in Figs 4.4c,f,i). Variations of the villi density efficiency η , overall geometry efficiency ζ and placental membrane

permeability inside a single placental villus and inside the placental disk are further discussed in Section D.1.1 of Appendix D on p. 150).

4.4 Concluding remarks

In this chapter we have described an automatic image analysis algorithm which relies on standard image analysis techniques, but automatically chooses the necessary segmentation parameters. The main advantage of our method is that the main part of the segmentation process is carried out automatically, which allows to analyze one large human placental cross-section ($2\text{ cm} \times 2\text{ cm}$) in less than an hour. The amount of information collected during such segmentation lies far beyond the capacities of the traditional point-intersection counting techniques. For comparison, Laga et al. (1973) have analyzed at most 2500 events (points) per placenta with the point-intersection counting method (and other studies normally limited themselves to much smaller number of events), while we have actually determined the exact positions, areas and perimeters of about 17 000 villous regions per placenta and fetal capillaries in each of them. Therefore, the proposed method not only provides much greater accuracy for the traditionally measured characteristics averaged over the whole placenta and allows to study their regional variations, but also allows to quantitatively assess the distributions of sizes, areas and perimeters of the villous regions, IVS and fetal capillaries inside the given placenta. Further studies may focus on using this segmentation algorithm for obtaining and understanding the shape of such distributions, which may bring about new insights into the large-scale structural organization of the human placenta.

For validation, the developed method was applied to 22 healthy human placentas. The results of the performed histological measurements were demonstrated to correspond to the previously published results. We have also analyzed 3 pathological placentas (1 moderate diabetes, 1 severe diabetes and 1 pre-eclamptic with IUGR case), but the results were inconclusive due to the low number of samples. Further studies on a large number of samples of each main type of placental pathologies are required. Such studies are expected to confirm previously observed quantitative structural differences in the pathological placentas (see Table 1.1).

To analyze the efficiency of oxygen transfer in each placenta, we have plotted the obtained histomorphometrical results on the efficiency diagrams provided by the earlier developed STPM. The diagrams demonstrated that the villi density of a healthy human placenta lies within 10% of the expected maximum if all other parameters are fixed. However, the *overall geometry efficiency* including other geometrical parameters (namely, the villi size and the stream-tube length), was found to be only 30–40%. The possible explanations of this low value are the existence of the internal structure of the villi responsible for the transport of the absorbed oxygen to the fetus, or biological adaptation, for instance, to provide increased robustness to the mother-fetus exchange. Insufficient experimental data for pathological cases has not allowed us to calculate the degree to which the placental oxygen exchange function is altered in pathological cases.

The proposed method has several drawbacks. First, it significantly depends on the correct staining of the analyzed image and image acquisition parameters, and its efficiency

may significantly decrease if the concentration of the H&E stain is varied, if it is not distributed uniformly across the section or if another stain is used. Second, our algorithm cannot in its present form separate “glued” villi often seen in the dense regions of the placental cross-sections. Although the parts of the villi that are not in contact with the IVS *in vivo* do not participate in the exchange and hence do not alter the predictions of our model, such “glued” villi can alter the distribution of individual villi sizes and perimeters. Whether these “glued” villi actually lie close to each other *in vivo* also remains an open question. Finally, the accuracy of the oxygen exchange efficiency predictions is decreased by the absence of the measurements of the linear maternal blood velocity in the IVS and of the placental membrane permeability.

Chapter 5

Conclusions and Further Development

5.1 Results summary

MORE than six decades of placenta modeling have much contributed to our understanding of the organ function. Modeling respiratory gas exchange has evolved from representing the placenta as a pair of “capillaries” conducting all fetal and maternal placental blood flows, to describing whole placentones filled with an effective porous medium. In this thesis, a new step has been made towards establishing the relation between the structure and function of the human placenta.

None of the previous models provided a mathematical description of both diffusion and convection of oxygen (or another substance) in a 3D model of the human placenta, so we have started our investigation by constructing a simplified 2D+1D model of the placental structure (Chapter 2). The maternal blood flow of the human placenta can be subdivided into stream tubes of maternal blood. Each such stream tube is curved, aligned along the maternal blood flow and is crossed at random angles and positions by fetal villi. In the absence of high-resolution 3D data, as a first approximation, we considered one such stream-tube unfolded, with oxygen-absorbing fetal villi represented as small parallel tubes inside the stream tube. Other assumptions that were made (Section 2.1.1) are either physical assumptions (such as the use of the slip boundary conditions for the maternal blood flow at the villi boundaries, the efficient fetal circulation, or the linearization of the oxygen-hemoglobin dissociation curve), or purely technical (such as the perfect sink boundary condition for oxygen uptake at the villi boundaries or the circular shape of the stream-tube). Such formulation of the problem was surely an engineering simplification of the real placental geometry, but allowed us to focus on an optimal cross-sectional geometry that would provide the maximal oxygen uptake.

Investigating the model, we have first numerically solved the oxygen convection-diffusion equation in geometries with various densities of circular villi (Chapter 2). For this purpose we estimated the standard dimensionless hydrodynamic numbers characterizing the maternal blood flow and oxygen absorption, as well as other placenta-specific model parameters (Section 2.3). Among the less known placenta parameters, we identified:

- linear maternal blood velocity in the IVS (in m/s, since knowing the flow in ml/min is not enough),

- local permeability of the placental membrane,
- stream-tube length.

The numerical simulations allowed estimation of the oxygen uptake of a stream tube with an arbitrary villi density in the expected physiological range of maternal blood flow velocities and stream-tube lengths. It was also demonstrated that this model exhibits an optimal villi density that provides the maximal oxygen uptake. This optimality was explained as a trade-off between the incoming oxygen flow and the absorbing villous surface, which differed from previously published hypotheses (Chernyavsky et al., 2010). The predicted optimal villi density values agreed with the experimental data (Table 2.5), which suggests that the selective pressure during the evolution of the placenta structure may be related to oxygen and carbon dioxide transfer before other factors. The results of this chapter have been published in Serov et al. (2015a).

The next step in the analysis of the role of the geometry in the placental oxygen transport consisted in relaxing the assumption of circular villi and switching to villi of arbitrary shape (like those observed in histological sections). Making this step required identification of the main geometrical parameters influencing oxygen uptake (Section 3.1.4) and the development of an approximate analytical solution as a function of these geometrical parameters (Chapter 3), since numerical calculations cannot provide a general solution for arbitrary villi shapes. The development of the approximate analytical uptake theory was possible due to the fact that:

- the fetal oxygen uptake linearly depends on stream-tube length at small stream-tube lengths,
- oxygen uptake at the infinite stream-tube length is equal to the incoming oxygen flow,
- the fetal oxygen uptake is a smooth monotonous function of the stream-tube length
- most importantly, the main part of the influence of a rather uniform geometry on the oxygen uptake can be expressed through only two geometrical parameters of the cross-section: the villi density and the effective villi radius.

The developed approximate analytical solution is valid for uniform random distribution of fetal villi of arbitrary shapes. Its application to non-uniform villi distributions can be achieved through the analysis of the dependence of the parameter κ on the stream-tube cross-sectional geometry for each type of the non-uniform distributions. However, this extension of the analytical approach was not considered in the present work, since fetal villi seem to be rather uniformly distributed on a local scale (of about a hundred of villi, see Figs 4.4, and 4.13a) and since biological interplacental structural variations (e.g., compare ϕ for different healthy placentas in Table 4.4) may have greater impact on the results than the non-uniformity of the villi distribution inside each individual placenta.

The development of the analytical approach generalized the results obtained by the numerical simulations. Approximate analytical formulas were obtained for the optimal villi density and for the corresponding maximal fetal oxygen uptake. The fetal oxygen uptake

of an arbitrary non-optimal geometry was also calculated, and it was found that in a first approximation only two geometrical parameters are required for its calculation: the villi density ϕ and the effective villi radius r_e . Moreover, all model parameters, geometrical and physiological, were demonstrated to enter the final expressions in the form of only two parameter combinations (F_0 and Da).

The obtained parameter combinations were demonstrated to have a clear physical meaning. The first parameter F_0 can be interpreted as the oxygen inflow into the stream tube if no villi obstructed the flow. The second parameter $Da \equiv \tau_{tr}/\tau_e$ is the Damköhler number for oxygen uptake in the human placenta. It is defined as the ratio of the rates of two processes: the rate of oxygen extraction in the stream-tube cross-section ($1/\tau_e$) and the rate of the maternal blood flow through the placenta ($1/\tau_{tr}$). The Damköhler number is then a quantitative measure of competition between the two processes, and the most efficient oxygen transport is achieved when Da is of the order of 1.

The theory helped to analyze the fictitious case of blood containing no hemoglobin, like in artificial placenta perfusion experiments. It was demonstrated that artificial perfusion experiments with no-hemoglobin blood tend to underestimate the *in vivo* oxygen uptake by two orders of magnitude. A method of recalculation of the results of artificial perfusion experiments to account for oxygen-hemoglobin dissociation was proposed.

The capacity of the theory to provide an oxygen uptake estimation for an arbitrary geometry and the existence of an optimal geometry for the given set of non-geometrical model parameters have allowed us to introduce a measure of optimality of any geometry, which we call the *overall geometry efficiency* (ζ). We defined it as the fraction of the incoming oxygen flow if no villi obstructed the stream-tube cross-section (F_0) that is absorbed by the given non-optimal geometry. Plotted as a function of the villi density and the effective villi radius (or more precisely, the parameter Da), this characteristic provides an efficiency diagram. The analysis of the diagram yields the conclusion that the highest oxygen exchange efficiency is achieved if the cross-sectional area of the villi tends to zero, while their cross-sectional perimeter stays finite. Naturally, such geometry would give a high oxygen inflow into the stream tube, since fetal villi do not obstruct the flow, and a high oxygen uptake due to a large exchange surface. However, due to biological restrictions, this ideal case cannot be attained, and oxygen exchange efficiency of the human placenta will be much less than 100 % in this scale. For the 22 analyzed human placentas, ζ was found to lie around 30–40 %.

Since the villi radius cannot be made smaller than a certain value, it is convenient to introduce a *villi density efficiency* (η) characterizing how close the villi density for the given fixed villi radius is to the optimal one. Defined as the ratio of the fetal oxygen uptake for the given villi density and for the optimal one, the villi density efficiency can also be plotted as a diagram in ϕ and r_e (or Damköhler number). Our calculations have demonstrated that the villi density of a healthy human placenta lies within 10 % of the expected maximum if all other parameters are fixed. These results have been published in Serov et al. (2015b).

The plotted efficiency diagrams open a way to convert the proposed stream tube placenta model into a diagnostic tool for the human placenta. Indeed, by measuring

the model parameters in a given human placenta and putting the obtained points on the two diagrams, one can compare the performance of different placentas. However, the available point-intersection counting techniques of analysis of histological placental slides require significant time and human effort to obtain the histomorphometrical data required by the model. To correct for the lack of an efficient histological analysis method, we have proposed a computer algorithm (Chapter 4), which is based on standard image analysis techniques, but automatically chooses the necessary parameters to perform image segmentation and to yield the required histomorphometrical data. The obtained results were shown to correspond to the previously published ones obtained by the traditional methods. However, the proposed algorithm considerably decreases the time required to obtain these data, does not require human attention for the main part of the process and significantly increases the amount and hence the precision of the obtained results.

The automatic method was further applied to 22 healthy and 3 pathological placentas collected by Dr. Carolyn Salafia in the hospitals of New York (Section 4.3). Plotting the measured values on the efficiency diagrams revealed that the villi density efficiency of a healthy human placenta lies within 10 % of the predicted maximal value. The overall geometry efficiency of the healthy placenta was found to be rather low (around 30–40 %), which is probably due to the physiological restrictions on the minimal size of a villus. Unfortunately, the low number of analyzed pathological cross-sections (also featuring different pathologies) has not allowed us to observe the difference in the exchange efficiency between the two categories. However, from general observations on pathological cross-sections (coming, for instance, from pre-eclamptic or diabetic placentas, see Fig. 1.15), one may expect that the average villi density of the effective villi radius may be significantly different under these conditions than in healthy samples. This would put these placentas into the regions of lower efficiency in the obtained efficiency diagrams and suggest an explanation for the higher risk of adverse pregnancy outcome or intra-uterine growth restriction (IUGR) observed in these cases. Further studies are required to validate these speculations.

On the whole, the present study is a new step in the investigation of the structure–function relation in the human placenta. One of our main foci was to show how the results of a theoretical model can be put into practice and to create a possible base for a new tool of *post-partum* evaluation of the placental oxygen exchange efficiency. Once sufficient histomorphometrical results are collected for pathological placentas, the developed model could be potentially used in the routine medical diagnostics.

5.2 Further development

5.2.1 Development of the model

Further development of the model should focus on several principal directions:

1. The effect of the non-slip boundary conditions (BC) on the model predictions should be evaluated. As discussed in Section 2.4.4 on p. 84, *a priori*, there is no reason to prefer the slip BC and the flat velocity profile to the non-slip BC and the developed velocity profile, since both can be equally far from the real non-developed

profile. In the absence of experimental studies on the non-developed *in vivo* velocity profile or a high-resolution structure of the IVS, it may be interesting to perform the calculations in the same geometrical configuration of the 2D+1D stream tube placenta model, but with the non-slip BC (and hence non-uniform velocity), and to evaluate the difference in oxygen uptake. The articles of Singh (1958), Lundberg et al. (1963), Papoutsakis et al. (1980), Jones (1988, 2009) may provide a good starting point for research in this direction.

2. One may improve the representation of the placental geometrical structure, for example, by introducing branching of villi and variations in villi sizes, shapes or co-orientations (see, for instance, Gordon et al., 2007b).
3. Future studies can try to simultaneously account for both maternal and fetal circulations by combining the developed STPM with fetal transport models (e.g., Gordon et al., 2007b, Gill et al., 2011). This approach may be able to predict the minimal villi size, which still allows to efficiently transport the absorbed oxygen to the fetus. The STPM alone cannot provide such estimations.
4. Investigation of the screening concept understood as a competition for the solute between different villi or fetal capillaries (see discussion on p. 3.2.4) is another interesting direction. This effect, which is more likely to occur in dense configurations of villi or fetal capillaries (see Fig. 3.7 and Gill et al., 2011), may bring new insights into the robustness of placental function and into the principles of its structural organization.
5. Combination of our STPM (focusing on the geometrical structure of the organ) with models of exchange of other substances (focusing on biochemical reactions, see, for instance, Sengers et al., 2010) presents an interesting perspective.
6. The proposed image analysis algorithm should be applied to a larger number of both healthy and pathological placental samples to validate the results presented in this thesis. Besides the average villi density and the effective villi radius that we have discussed, it can also provide detailed distributions of the areas, perimeters and shapes of villous, IVS and capillary regions inside a given sample. To our knowledge, such data have never been analyzed on a large scale (e.g., featuring more than a thousand villi) and have never been compared within or between placentas.

5.2.2 Development of the field

The placenta models based on histological placental slides (like the one described in this thesis) show great potential in describing and predicting solute uptake thanks to a clearly defined uptake surface. However these models are not the only way to describe the human placenta. Another type of models, porous-medium models, have been shown valuable for the description of the large-scale maternal blood flow pattern in the IVS of the human placenta (Erian et al., 1977, Chernyavsky et al., 2010). These models can now be further improved:

- to account for regional variations of the porosity to imitate villi density variations observed in histological placenta sections and to take histological sections or micro-CT data as input,
- to study the influence of lateral venous outlets in the placental septa at the sides of a placentone on the blood circulation and oxygen uptake of the placentone,
- or to analyze the shear stress exerted on the villi by the maternal blood flow.

Although we have advanced in understanding the placental function, our knowledge on the placental mass transport still remains very incomplete. The overall development of the field is hindered by the lack of experimental data that are critical for model development and validation. The main challenges in the field include:

- A high-resolution 3D geometrical structure of the placenta is yet unavailable, especially in dense exchange regions. Meanwhile, placenta models can be based on high-resolution 2D histological placental cross-sections and low-resolution 3D structures from *ex vivo* MRI angiography or micro-CT. An interesting approach may be to obtain serial sections of the same placenta with a small step (e.g., 10–50 μm) and then to reconstruct the 3D structure of the placenta from these data. Such reconstruction may however require significant efforts.
- High-resolution experimental determination of the *in vivo* placental blood flow has not yet been performed. Characteristic linear velocities of the blood flow in the IVS of the human placenta are not known either, although they are indispensable for modeling diffusion-convection equations in non-porous-medium models.
- Oxygen and carbon dioxide concentrations are not known in the IVS of the human placenta and are not available on a regular basis even in the umbilical and uterine arteries of the human placenta, whereas they are crucial for the verification and validation of the placental exchange models. The same is true for other substances (nutrients, glucose, amino acids, etc.). For oxygen, some advances may be expected with the development of BOLD MRI techniques.
- Although the histomorphometrical data obtained from the analysis of placental cross-sections has been extensively used, there is no generally accepted opinion in the scientific community on the degree, to which the obtained formaldehyde-fixed histological sections represent the *in vivo* placental structure. The changes to the placental structure during fixation and the methodology of how to correct for the observed difference are yet to be established.

To conclude, numerous approaches — experimental, computational and theoretical — have been proposed for the investigation of the human placenta. Scientists have encountered gaps between these methods, when, for instance, the results of placenta models could not be directly validated in the existing experiments, or, on the opposite, experimentally observed phenomena did not yet have a convincing theoretical rationale. We believe that the primary way to the comprehensive understanding of the placenta and

to the elimination of these gaps lies through collaboration and interaction between the teams using different approaches, when theoretical groups will develop descriptions of the observed phenomena, while experimental teams will attempt to take into account the requirements of the theory. We hope that the effort to connect the experiment and the theory undertaken in this thesis will further stimulate the development of this rapidly growing field and facilitate the exchange between modelers, physiologists, placenta pathologists and obstetricians.

Appendices

Appendix A

Hormones secreted by the placenta

The placenta secretes endocrine, paracrine and autocrine factors, the synthesis and the function of which are briefly reviewed below.

- *Progesterone* is produced in the placenta and is released into both fetal and maternal circulations. It inhibits uterine contractions and suppresses estrus and release of luteinizing hormone from the pituitary gland (Gude et al., 2004).
- *Estrogens* produced in the placenta (including estrone, estradiol and estriol) act as specialized growth hormones for mother's reproductive organs, including breasts, uterus, cervix and vagina (Page, 1993). Estrogens are conjugated (e.g., with sulphate or glucuronide) in the fetal circulation to protect the fetus from high levels of free estrogens (Gude et al., 2004).
- *Human chorionic gonadotrophin* is produced by placental trophoblasts and is predominantly secreted into the maternal circulation. It is known to stimulate (together with estradiol and glucocorticoids) cytotrophoblast cell fusion and functional differentiation of villous trophoblast (Malassiné and Cronier, 2002). It may also help to prolong the life of the corpus luteum in the ovaries in early pregnancy (Gude et al., 2004).
- *Human placental lactogen* is released into both maternal and fetal circulation and is reported to modulate embryonic development, to regulate intermediary metabolism and to stimulate the production of insulin-like growth factors, insulin, adrenocortical hormones and pulmonary surfactant (Handwerger and Freemark, 2000). It may also be involved in angiogenesis (Corbacho et al., 2002).
- *Placental growth hormone* is secreted into the maternal circulation and is reported to influence maternal adjustments to pregnancy, maternal insulin-like growth factor I (IGF-I) levels, and placental development via an autocrine or paracrine mechanism (Lacroix et al., 2002, Gude et al., 2004). It is also known to stimulate (together with the human placental lactogen) maternal IGF production and modulate intermediary metabolism, providing the fetus with higher levels of glucose and amino acids (Handwerger and Freemark, 2000).

- Small quantities of *chorionic thyrotropin* and *corticotropin* released by the placenta into the maternal circulation may help modulate the maternal metabolism (Gude et al., 2004).
- *Cytokines, chemokines and eicosanoids* may be involved in parturition (Keelan et al., 2003) and in control of blood flow through the placenta (Gude et al., 2004).
- Numerous *autacoids*, including *endothelins* (Grabau et al., 1997), *adrenomedullin* (Al-Ghafa et al., 2003) and *nitric oxide* (Gude et al., 1994), produced by the placenta are also believed to be involved in the control of blood flow through the placenta (Gude et al., 1998).
- Large amounts of *acetylcholine* produced by the placenta are believed to influence cell proliferation and differentiation, organization of the cytoskeleton, as well as cell–cell interaction, cell migration and immune functions (Wessler et al., 2003, King et al., 1991, Gude et al., 2004).

Appendix B

Typical parameters used in placental mass-transport modeling

The parameters commonly used in mass-transport placenta models are presented in Table B.1.

Table B.1. A summary of the parameters commonly used in mass-transport placenta models (including those used in the present thesis). The parameters are described following Faber (1969) or other sources (marked in the corresponding cells). Relation to similar parameters not included into the table is shown where possible. Indices m and f are used to distinguish between the maternal and the fetal circulations, while indices a and v are used to distinguish between the arterial and venous blood

Symbol & Unit	Definition & Description
Basic geometrical variables	
L , m	Characteristic length of the modeled exchange unit
S , m ²	Area of the exchange surface between the maternal and the fetal blood
V_{tot} , m ³	Total volume of the placenta
V_{vil} , m ³	Total volume of the fetal villi in the placenta
V_{IVS} , m ³	Total volume of the intervillous space in the placenta
Derived geometrical variables	
V_{oth} , m ³	$V_{\text{oth}} = V_{\text{tot}} - V_{\text{vil}} - V_{\text{IVS}}$ Total volume occupied by all other placental compartments
φ	$\varphi = V_{\text{vil}} / (V_{\text{vil}} + V_{\text{IVS}})$ Villi density in the placenta. In the present thesis, only small villi (terminal and mature intermediate) are included in the calculation of φ . A similar parameter was called a <i>volume fraction of villous material</i> by Chernyavsky et al. (2010). $(1 - \varphi)$ is similar to the <i>voidage of the placental volume</i> discussed by Schmid-Schönbein (1988)

Symbol & Unit	Description & Description
$\varepsilon, \text{ m}^{-1}$	$\varepsilon = S/V_{\text{vil}}$ Surface-to-volume ratio for the fetal villi. A reciprocal parameter $2/\varepsilon$ was called an effective villi radius (Section 3.1.4), and a similar parameter V_{IVS}/S was called an <i>equivalent channel diameter</i> by Schmid-Schönbein (1988)
Basic physiological variables	
$c_{\text{pl}}, \text{ mol/m}^3$	Concentration of a solute dissolved in the blood plasma
$\bar{c}_{\text{pl}}, \text{ mol/m}^3$	Average concentration of the solute in the blood plasma
$n, \text{ mol/m}^3$	<i>Content</i> of the solute is the total amount of solute contained in a unit volume of blood including solute dissolved in the blood plasma and bound to blood proteins (such as hemoglobin)
$p, \text{ mmHg}$	<i>Partial pressure</i> is often used instead of the concentration or content to describe gas exchange
$Q, \text{ m}^3/\text{s}$	Volumetric blood flow rate
$u, \text{ m/s}$	Linear velocity of the blood flow
$w, \text{ m/s}$	Solute-dependent <i>membrane permeability</i> is the proportionality constant between the rate of solute transfer per unit of membrane surface (in $\text{mol}/(\text{m}^2\text{s})$) and the concentration difference (in mol/m^3) on both sides of the membrane
$\alpha,$ $\text{ml O}_2/(\text{ml Bl} \cdot \text{mmHg})$	<i>Oxygen solubility in blood plasma</i> is the change in the amount of the dissolved oxygen per unit of oxygen partial pressure change
$\alpha',$ $\text{ml O}_2/(\text{ml Bl} \cdot \text{mmHg})$	<i>Effective oxygen solubility</i> is the sum of the oxygen solubility in the blood plasma α and the change in the amount of bound oxygen per unit of partial pressure change (Bartels and Moll, 1964, Opitz and Thews, 1952). If the oxygen dissociation curve is linearized, the second contribution can be made independent of p . Such linearization procedure was proposed in Section 2.2.4 of the present thesis in terms of the coefficient $B = \alpha'/\alpha$ and by Heilmann et al. (1979). A piece-wise linearization of the dissociation curve was used by Costa et al. (1992)
$D, \text{ m}^2/\text{s}$	<i>Diffusivity</i> of solute in blood
$\tau_e, \text{ s}$	<i>Characteristic time of solute exchange</i> between the maternal and the fetal blood
Derived physiological parameters	
f	$f = n/c$ Ratio of the content and the concentration of the solute
$\tau_{\text{tr}}, \text{ s}$	$\tau_{\text{tr}} = L/u$ <i>Transit time</i> of the maternal blood through the placenta

Symbol & Unit	Description & Description
Q_{tr} , mol/s	$Q_{tr} = Q_m f_m (c_{ma} - c_{mv}) = Q_f F_f (c_{fv} - c_{fa})$ Total rate of solute transfer between the maternal and the fetal circulations
P , m ³ /s	$P = Q_{tr} / (\bar{c}_m - \bar{c}_f)$ <i>Placental permeability</i> is the total rate of solute transfer between the circulations per unit of mean concentration difference between the exchanging blood flows
D_p , ml/(mmHg · min)	$D_p = Q_{tr} / (\bar{p}_m - \bar{p}_f) \cdot 22.4 \text{ l/mol}$ <i>Placental diffusing capacity</i> is often used instead of the placental permeability for respiratory gases. In analogy to the placental permeability, it is defined as the total rate of solute transfer between the circulations (but in ml gas/min) per unit of mean partial pressure difference of the gas in the exchanging flows. The index p is traditionally added to distinguish the placental diffusing capacity from that of lungs
T_m ,	$T_m = (c_{ma} - c_{mv}) / (c_{ma} - c_{fa})$ <i>Maternal transport fraction</i> is the dimensionless concentration change in the exchange unit, also known as the <i>transfer index</i> or the <i>placental effectiveness</i> (Battaglia and Meschia, 1986). Higher T_m values correspond to a more efficient exchanger. Similar parameters were used under different names by Bartels and Moll (1964), Faber (1995), Power et al. (1972a), Rankin (1972)
T_f ,	$T_f = (c_{fv} - c_{fa}) / (c_{ma} - c_{fa})$ <i>Fetal transport fraction</i> is defined in analogy to the maternal transport fraction. Higher T_f values correspond to a more efficient exchanger.
d ,	$d = P / (Q_m f_m)$ <i>Permeability variable</i> (not to be confused with the membrane or placental permeabilities) is a dimensionless permeability of the placental membrane. The permeability variable can be alternatively defined as $d = P / \sqrt{Q_m f_m Q_f f_f}$, so as not to prefer the maternal circulation to the fetal one (Faber, 1995)
R ,	$R = Q_f f_f / (Q_m f_m)$ <i>Flow ratio</i> . In case of oxygen, it is also sometimes also called the <i>hemoglobin flow ratio</i> to distinguish it from Q_f / Q_m (Power et al., 1972a)

Symbol & Unit	Description & Description
$C, \text{ m}^3/\text{s}$	$C = Q_{\text{tr}}/(c_{\text{ma}} - c_{\text{fa}})$ <i>Placental clearance</i> is the ratio of the solute transfer rate and the materno-fetal arterial concentrations difference (Meschia et al., 1967a). The placenta clearance is related to the transport fractions T : $C = Q_{\text{mf}}T_m = Q_{\text{ff}}T_f$
$T_{\text{cm}},$ $\text{ml O}_2/(\text{mmHg} \cdot \text{s})$	$T_{\text{cm}} = \alpha'Q_m$ <i>Transport capacity of the maternal blood</i> is the change in the amount of oxygen brought to the placenta by the maternal blood per unit of change of the oxygen partial pressure in the maternal blood (Bartels and Moll, 1964). It can be shown to be related to the parameter F_0 discussed in the thesis: $T_{\text{cm}} = F_0\alpha(1 - \phi)/c_{\text{ma}}$
$T_{\text{cf}},$ $\text{ml O}_2/(\text{mmHg} \cdot \text{s})$	$T_{\text{cf}} = \alpha'Q_f$ <i>Transport capacity of the fetal blood</i> is defined in analogy to that of the maternal blood
Da	$\text{Da} \equiv \tau_{\text{tr}}/\tau_e = Q_{\text{tr}}/(Q_m c_{\text{ma}} f_m)$ The <i>Damköhler number</i> is a standard parameter of chemical engineering defined as the ratio of the rate of a chemical reaction and the rate of mass transport. For its application to the placenta, see Section 2.1.2 on p. 64. If the fetal arterial blood is assumed to contain no solute ($c_{\text{fa}} = 0$) and maternal and fetal blood flows are the same ($Q_m = Q_f$), Da is equal to T_m . Note that the permeability variable d is equal to Da divided by the mean solute concentration difference between the maternal and fetal circulations. A parameter similar to the Damköhler number, a <i>coefficient of oxygen utilization</i> $((p_{\text{ma}} - p_{\text{mv}})/p_{\text{ma}})$ was introduced by Barron (1951). Compared to Da, it uses oxygen partial pressures instead of concentrations and assumes equal maternal and fetal blood flow rates
Pe	$\text{Pe} = Lu/D$ The <i>Péclet number</i> is defined as the ratio of the rates of convective and diffusive transport in a given direction (Incropera and Dewitt, 2001). For its application to the placenta, see Section 2.1.2 on p. 63

Appendix C

Error estimation

The uncertainties in the measurements of the parameters of the model can be used to estimate the error in the predictions of the optimal villi density φ_{opt} and the maximal oxygen uptake F_0 . It is known that if a variable f depends on several independent variables x_i with known standard deviations δx_i , its standard deviation δf has the following form (Taylor, 1996):

$$(\delta f)^2 = \sum_i \left(\frac{\partial f}{\partial x_i} \delta x_i \right)^2.$$

This formula can be applied to estimate the standard deviations of φ_{opt} and F_0 due to the uncertainties in the measurements of the parameters of the model, for which error estimations are known (B, D, r, R, w, c_0). Variations of the parameters $c_{\text{max}}, \beta_{60}, k_{\text{hn}}$ are included in the variation of B . For the parameters u and L no error estimations is available. The variations $\delta \varphi_0$ and δF_{max} are then:

$$\begin{aligned} (\delta \varphi_{\text{opt}})^2 &= \left(\frac{\partial \varphi_{\text{opt}}}{\partial B} \delta B \right)^2 + \left(\frac{\partial \varphi_{\text{opt}}}{\partial D} \delta D \right)^2 + \left(\frac{\partial \varphi_{\text{opt}}}{\partial r} \delta r \right)^2 + \left(\frac{\partial \varphi_{\text{opt}}}{\partial R} \delta R \right)^2 + \left(\frac{\partial \varphi_{\text{opt}}}{\partial w} \delta w \right)^2 \\ &\quad + \left(\frac{\partial \varphi_{\text{opt}}}{\partial c_0} \delta c_0 \right)^2, \\ (\delta F_0)^2 &= \left(\frac{\partial F_0}{\partial B} \delta B \right)^2 + \left(\frac{\partial F_0}{\partial D} \delta D \right)^2 + \left(\frac{\partial F_0}{\partial r} \delta r \right)^2 + \left(\frac{\partial F_0}{\partial R} \delta R \right)^2 + \left(\frac{\partial F_0}{\partial w} \delta w \right)^2 \\ &\quad + \left(\frac{\partial F_0}{\partial c_0} \delta c_0 \right)^2. \end{aligned}$$

Since the analytical formulas for the dependence of φ_{opt} and F_0 on the parameters of the model were not available, the partial derivatives appearing in the variations $\delta \varphi_0$ and δF_{max} were calculated numerically. For each variable independently, small deviations were assumed and estimations for the partial derivatives were obtained:

- for φ_{opt} : $\frac{\partial \varphi_{\text{opt}}}{\partial B} = -1.6 \cdot 10^{-3}$, $\frac{\partial \varphi_{\text{opt}}}{\partial D} \approx 0 \text{ s/m}^2$, $\frac{\partial \varphi_{\text{opt}}}{\partial r} = -3800 \text{ m}^{-1}$, $\frac{\partial \varphi_{\text{opt}}}{\partial R} \approx 0 \text{ m}^{-1}$, $\frac{\partial \varphi_{\text{opt}}}{\partial w} = 550 \text{ s/m}$, $\frac{\partial \varphi_{\text{opt}}}{\partial c_0} \approx 0 \text{ m}^3/\text{mol}$;
- for F_0 : $\frac{\partial F_0}{\partial B} = 6.8 \cdot 10^{-9} \text{ mol/s}$, $\frac{\partial F_0}{\partial D} \approx 0 \text{ mol/m}^2$, $\frac{\partial F_0}{\partial r} = -1.2 \cdot 10^{-2} \text{ mol}/(\text{m} \cdot \text{s})$, $\frac{\partial F_0}{\partial R} = 1.4 \cdot 10^{-4} \text{ mol}/(\text{m} \cdot \text{s})$, $\frac{\partial F_0}{\partial w} = 1.7 \cdot 10^{-3} \text{ mol/m}$, $\frac{\partial F_0}{\partial c_0} = 1.7 \cdot 10^{-5} \text{ m}^3/\text{s}$.

Note that at the numerical precision, φ_{opt} and F_0 appear to be independent of the

diffusivity D of oxygen. Such behavior cannot be universal for all values of the parameters (since $D = 0$, for example, would obviously give no oxygen uptake), but seems to be approximately valid for the normal placenta parameters (Table 2.2). Substituting the standard deviation of the parameters: $\delta B = 2$, $\delta r = 3 \cdot 10^{-6} \text{ m}$, $\delta R = 4 \cdot 10^{-3} \text{ m}$, $\delta w = 1.1 \cdot 10^{-4} \text{ m/s}$, $\delta c_0 = 2 \cdot 10^{-3} \text{ mol/m}^3$ (Table 2.2), we obtain $\delta \phi_0 = 0.06$ and $\delta F_{\max} = 6 \cdot 10^{-7} \text{ mol/s}$.

Appendix D

Typical problems of histomorphometrical placental studies

This appendix briefly reviews three main problems encountered during preparation, analysis and interpretation of histological placental cross-sections:

- Inhomogeneity of the fetal villous tree,
- Immersion fixation vs. perfusion fixation of placental samples,
- Influence of the fixative on histomorphometrical measurements.

D.1 Inhomogeneity of the fetal villous tree

The following sections briefly review the experimental data collected on the intraplacentone (intralobular) and intraplacental variations of the placental structure.

D.1.1 Intraplacentone structural variations

Villi density φ and the effective villi radius r_e

Experimental studies report that regional differences in the villous tree structure of the human placenta become apparent only at the end of the second trimester, while the villous tree is largely homogeneous before that period (Benirschke et al., 2006). However, most placentas are subjected to a histological analysis in the third trimester of pregnancy and thus feature an inhomogeneous structure. An analysis of only one region of a placentone may therefore not provide representative information about the whole placentone. Pioneering studies of intraplacentone (intralobular) variations of the placental structure have been performed by Bacon et al. (1986), Critchley and Burton (1987).

In the study of Bacon et al. (1986), the placentas were fixed by perfusion and individual placentones were isolated according to grooves visible in the basal plate. Each analyzed placentone was then subdivided into 3 zones in the horizontal plane and 3 plates in the vertical plane, giving in total 9 different areas (see Fig. D.1). Area fractions of small villi (terminal and mature intermediate) and of the intervillous space were measured in the cross-sections, and the obtained data is summarized in Table D.1. These data allow

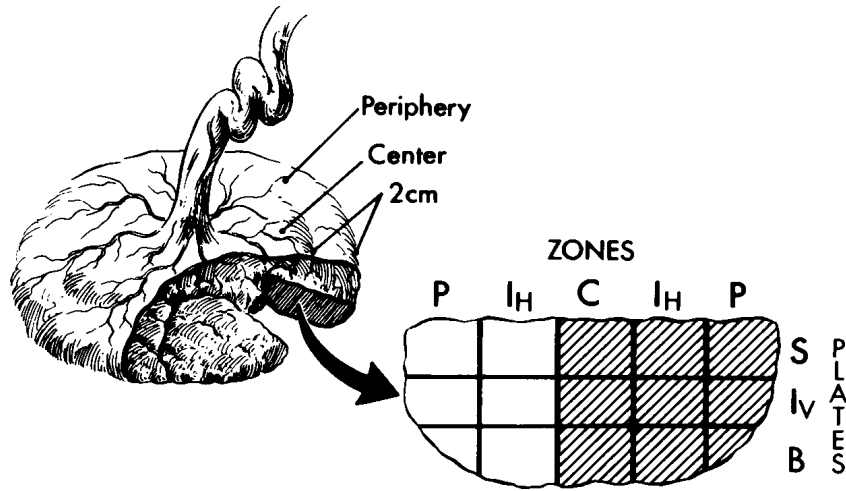


Figure D.1. Scheme of the areas of a placenta (periphery, center) and of a placentone (9 regions) sampled by Bacon et al. (1986). Notations: C — central, I_H — intermediate and P — peripheral in the horizontal plane; S — subchorial, I_V — intermediate and B — parabasal plates in the vertical plane. Reproduced from Bacon et al. (1986)

one to calculate the villi density ϕ in each placentone region, the spatial distribution of which is shown in Fig. D.2a. One can observe that ϕ can vary from 0.44 to 0.65 (i.e. by around 50%) between the sampled regions. Such variation is comparable to the structural difference of about 50% between healthy and diabetic pregnancies reported by Mayhew and Jairam (2000). It is therefore clear that the sites of histomorphometrical analysis have to be correctly chosen and specified along the reported data for one to be able to confidently discriminate between intraplacental and interplacental variations.

Bacon et al. (1986) have also estimated surface densities (the total perimeter of the component divided by the total area of the analyzed placental cross-section) of small fetal villi and of fetal capillaries. The results of these measurements allow to assess variations of the effective villi radius (r_e , see Eq. (3.11) on p. 93). The original data and the calculated values of r_e can be found in Table D.1. Spatial distribution of r_e in a placentone is shown in Fig. D.2b. One can see that this distribution is much more uniform than that of ϕ , with slightly larger r_e at the periphery of the placentone than in its center.

The calculated ϕ and r_e for the different regions of the placentone allow one to estimate the Damköhler number Da , the villi density efficiency η and the overall geometry efficiency ζ , as discussed in Chapters 3 and 4. Since other model parameters were not measured by Bacon et al. (1986), we assign them the following values: the average maternal blood flow velocity $u \approx 6 \cdot 10^4$ m/s, the permeability of the materno-fetal membrane $w \approx 2.8 \cdot 10^{-4}$ m/s, the stream-tube length $L_0 \approx 1.6$ cm, the oxygen-hemoglobin dissociation constant $B \approx 94$ (Table 2.2 on p. 71), and the parameter $\kappa \approx 0.35$ (see Sect. 3.2.2 on p. 99). The spatial variation of the efficiencies η and ζ is shown in Fig. D.2c, d. One can see that the villi density is very close to its optimal values in the top central and top peripheral regions of the placentone (Fig. D.2c). Near the basal plate the villi density efficiency is lower, especially at the periphery of the placentone. The overall geometry efficiency ζ appears to be rather uniform near the center of the placentone (zones C and I_H ; plates B , I_V , S), with slightly lower values achieved at the

periphery of the placentone near the basal plate. Intraplacentone variations of η and ζ suggest that different parts of the placentone may fulfill different functions with central parts more adapted to oxygen uptake. Note however that these are only approximate estimations based on the uniform maternal blood velocity u in the placentone. In the real distribution of u , one would expect much higher values in the central cavity, and thus decreased exchange efficiency. It is likely that in such situation the peripheral regions will show greater contribution to oxygen uptake. Trophoblast layer thickness may also vary between the regions (and hence w), which can also modify the obtained quantitative conclusions. Further studies will have to clarify these questions. Although these results may not be quantitatively correct, they emphasize the importance of specification of the location of the analyzed placentone region along with histological data. Applied to histological studies of pathological placentas, such approach could diminish variations of the results within each pathological group and clearer demonstrate the difference from the control group.

Trophoblast layer thickness

Intraplacentone variations of the trophoblast layer thickness have been studied by [Critchley and Burton \(1987\)](#). The trophoblast layer is a boundary layer that covers fetal villi, and it is the only fetal tissue in direct contact with the maternal blood. The trophoblast layer consists of an outer continuous layer called syncytiotrophoblast (or syncytium), a discontinuous layer of cytotrophoblast (or Langhans' cells) below it and the trophoblastic basement membrane (separating cytotrophoblast from the villous stroma, see Fig. D.3).

Table D.1. Intraplacentone variations of area fractions of the placental components as reported by [Bacon et al. \(1986\)](#). The value of villi density was calculated for each area by the following formula: $\phi \equiv S_{\text{sm.v}}/(S_{\text{sm.v}} + S_{\text{IVS}})$. Notations: $S_{\text{sm.v}}$ — small villi volume, S_{tot} — total volume of the placenta, S_{IVS} — volume of the IVS. Absolute standard deviations of $S_{\text{sm.v}}/S_{\text{tot}}$ and $S_{\text{IVS}}/S_{\text{tot}}$ were reported to lie below 4 %. This value yielded a standard deviation for ϕ less than 0.014 for all areas. Significant variations of villi density can be observed between the sampled areas. The presence of the central cavity can be seen from lower values of ϕ in the center than at the periphery of the placentone for all plates. The small villi surface density was defined as $P_{\text{sm.v}}/S_{\text{tot}}$, where $P_{\text{sm.v}}$ is the total perimeter of the small villi (terminal and mature intermediate) in the analyzed cross-section. The standard deviation of $P_{\text{sm.v}}/S_{\text{tot}}$ was reported to be not greater than 2.6 mm^{-1} for each region. The effective villi radius (r_e , see Eq. (3.11)) was calculated from these data by the following formula: $r_e \equiv 2S_{\text{sm.v}}/P_{\text{sm.v}} = 2(S_{\text{sm.v}}/S_{\text{tot}})/(P_{\text{sm.v}}/S_{\text{tot}})$. Standard deviations of the effective radius (δr_e) were assessed in each case. The Damköhler number Da was calculated according to Eq. (3.13) as $Da \equiv 2wkL_0/(uBr_e)$. The parameters entering this equation are discussed in the main text. The villi density efficiency η and the overall geometry efficiency ζ were estimated according to Eqs (3.12) and (3.21)

Vertical stratification plates	Subchorial (S)			Intermediate (I_V)			Parabasal (B)		
Horizontal stratification zones	C	I_H	P	C	I_H	P	C	I_H	P
$S_{\text{sm.v}}/S_{\text{tot}}$, %	18	30	25	42	44	52	40	39	46
$S_{\text{IVS}}/S_{\text{tot}}$, %	23	23	27	40	32	31	31	32	25
$P_{\text{sm.v}}/S_{\text{tot}}$, mm^{-1}	11.8	18.2	14.1	25.3	28.9	30.6	25.5	24.0	26.8
ϕ	0.44	0.57	0.48	0.51	0.58	0.62	0.57	0.55	0.65
r_e , μm	31	33	36	33	30	34	31	33	34
δr_e , μm	± 14	± 9	± 12	± 7	± 6	± 6	± 6	± 7	± 6
Da	1.82	1.69	1.57	1.67	1.83	1.64	1.77	1.71	1.62
η , %	100	95	100	100	93	89	95	97	84
ζ , %	43	38	40	40	39	35	39	39	33

Molecules have to cross the trophoblast layer to get from the maternal bloodstream into the fetal circulation, so thinner layers accelerate the exchange of passively transported substances. Parts of the trophoblast layer, which are thinner and which lie close to fetal capillaries are called vasculosyncytial membranes and are believed to be the main sites of oxygen exchange due to a significantly reduced diffusion path for the crossing molecules (see Fig. D.3). The assumption of a uniform oxygen concentration at the villous boundary or of a uniform permeability of the trophoblast layer may therefore be not valid in the presence of vasculosyncytial membranes (compare to Gill et al., 2011). An accurate model of intravillous transport could feature uniform substance concentration outside a villus and take into account the variable trophoblast layer thickness. This is especially important since the trophoblast layer is considered to make the highest contribution to the total diffusive resistance of the oxygen diffusing path between the mother and the fetus (see Mayhew et al., 1984, 1986).

Three mechanisms are responsible for the formation of vasculosyncytial membranes from a uniform trophoblast layer (Critchley and Burton, 1987):

- Increased fetal vasodilation, for example in response to hypoxia, can result in tension within the trophoblast layer and thinning of the barrier.
- Alternatively, fetal capillaries may remain constant in diameter but indent further

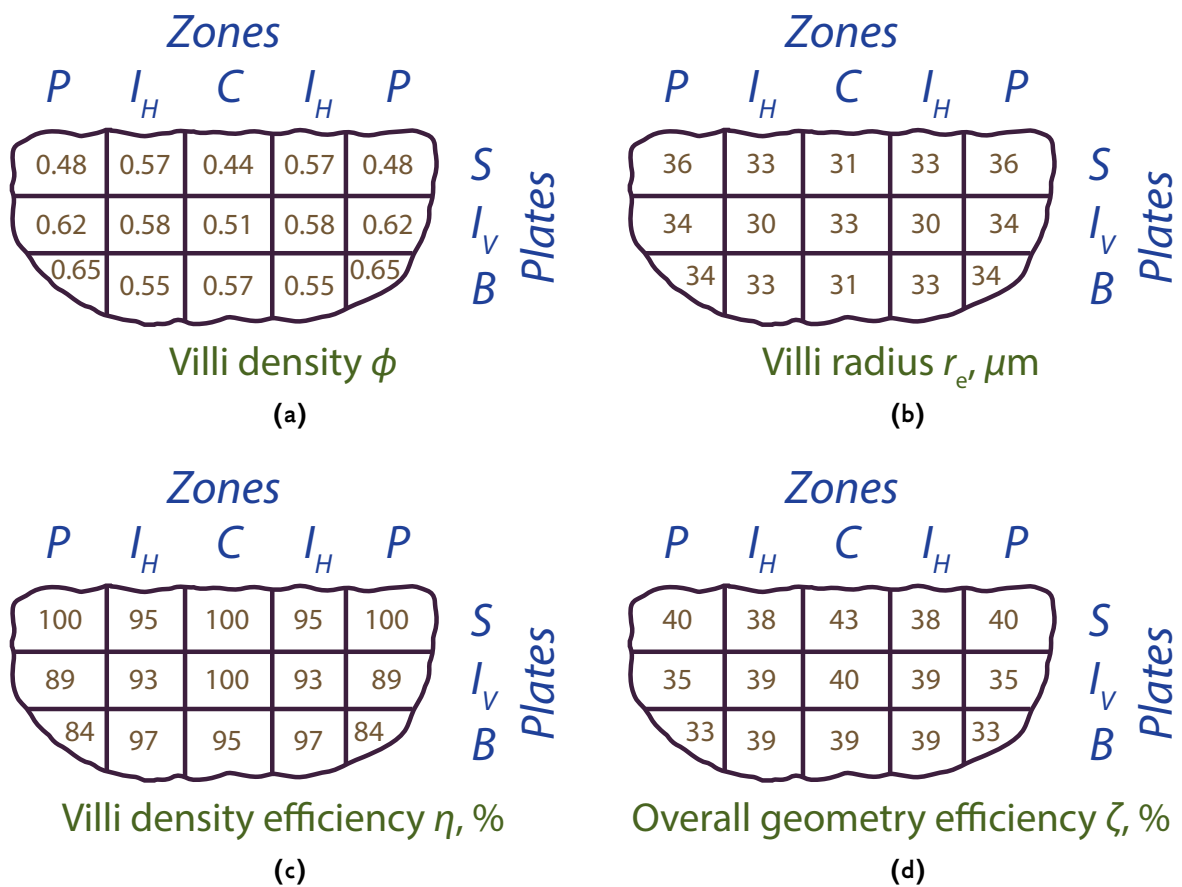


Figure D.2. Symmetrical schematic illustration of intraplacental variations of the villi density ϕ (a), the effective villi radius r_e (b), villi density efficiency η (c) and overall geometry efficiency ζ (d) based on data from Table D.1

into the trophoblast. This effect has been observed in high-altitude pregnancies, where oxygen content of the inhaled air is lower (Jackson et al., 1986).

- Lastly, the syncytioplasm may stream away from the region of a developing vasculosyncytial membrane, accumulating at other points on the villous surface and creating syncytial knots (Tominaga and Page, 1966). Such redistribution can be induced by cytoskeletal elements present within the syncytium (Ockleford et al., 1981).

These mechanisms demonstrate that the trophoblast layer thickness is not constant. Multiple studies have reported modifications of the trophoblast layer thickness under different pathological conditions, which may suggest adaptation of the exchange properties of the organ (see Fox, 1964, Piotrowicz et al., 1969, Beischer et al., 1970, Fox, 1970, Heinrich et al., 1976, Kaufmann et al., 1977, Voigt et al., 1978, Hammersen, 1980, Sala et al., 1984, Burton et al., 1987, Kosanke et al., 1998). Bacon et al. (1984) reported a reduction of the arithmetic mean trophoblast layer thickness in guinea-pigs under long-term hypoxia in a 12% oxygen environment. Jackson et al. (1985) have also demonstrated a decrease in the harmonic mean thickness of the trophoblast layer in placentas of women living at the altitude of 3600 m (with lower oxygen content of the air) compared to the placentas of a control group living at 400 m. It has been reported that the layer thickness is the greatest near the openings of the spiral arteries, in the region of the highest p_{O_2} (Wigglesworth, 1969, Jackson et al., 1985, Mayhew et al., 1986). Conversely, the thinnest layer was observed at the periphery of the placentone, near the venous outlets. These results can be interpreted as that the fetal villi are protected from large oxygen tensions near the center of the lobule, but at the periphery of the placentone the permeability of their membranes is increased to adapt to lower oxygen tensions.

Critchley and Burton (1987) have analyzed intraplacentone variations of the trophoblast thickness layer in ten healthy placentas fixed by perfusion. Each placentone (1 placentone per placenta) was divided into smaller regions: *C* — central and *P* — peripheral in the horizontal plane; *S* — subchorial, *I_V* — intermediate and *B* — parabasal plates in the vertical plane, altogether giving 6 different regions (note that less regions have been distinguished compared to 9 regions of Bacon et al. (1986)). The results of the measurements of the mean arithmetic trophoblast thickness (h_a) and the mean harmonic trophoblast thickness (h_h) in each region are reported in Table D.2. Spatial distributions of h_a and h_h are schematically shown in Figs D.4a,b. It can be observed that both h_a and h_h exhibit the lowest values (and hence the highest permeability of the trophoblast layer) in the intermediate vertical plate, while the highest values (and the lowest permeability) are achieved in the parabasal plate.

These values can be used for assessment of the influence of the trophoblast layer thickness on the permeability of the materno-fetal barrier w and therefore on the villi density efficiency η and overall geometry efficiency ζ . In the following, we assume that it is the harmonic mean trophoblast layer thickness h_h and not the arithmetic mean trophoblast layer thickness h_a that determines the permeability of the trophoblast layer. The harmonic mean thickness is considered to be of greater importance since it gives better account for

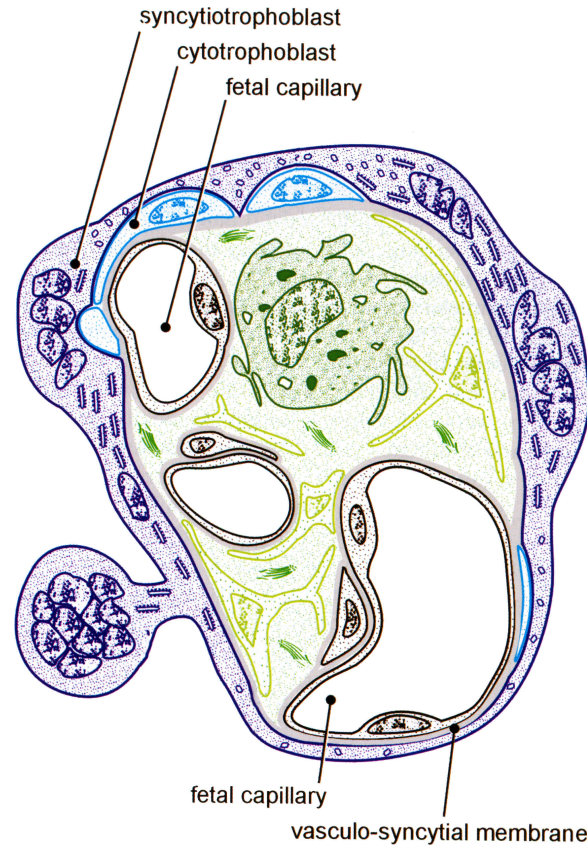


Figure D.3. Trophoblast layer of a terminal fetal villus in the human placenta and location of vasculosyncytial membranes. Simplified from Benirschke et al. (2006)

Table D.2. Intraplacentone variations of the mean arithmetic (h_a) and mean harmonic (h_h) thicknesses of the villous trophoblast layer as measured by Critchley and Burton (1987). Standard deviations (δh_a , δh_h) are provided along the original values. Feto-maternal barrier permeability w was estimated for each region taking into account that $w \sim 1/h_h$ and under the assumption that $h_h = 3.45 \mu\text{m}$ corresponds to $w = 2.8 \cdot 10^{-4} \text{ m/s}$. The Damköhler number $\text{Da} \equiv 2w\kappa L_0/(uBr_e)$ was then calculated according to Eq. (3.13) based on r_e values from Table D.1. The villi density efficiency η and the overall geometry efficiency ζ were estimated according to Eqs (3.12) and (3.21) and based on the values of ϕ reported in Table D.1 for central (C) and peripheral (P) placentone zones

Vertical stratification plates	Subchorial (S)		Intermediate (I_V)		Parabasal (B)	
Horizontal stratification zones	C	P	C	P	C	P
h_a , μm	4.17	4.15	4.07	3.76	4.59	4.36
δh_a , μm	± 0.68	± 0.83	± 0.69	± 0.55	± 0.69	± 0.63
h_h , μm	3.14	2.94	2.97	2.65	3.45	3.22
δh_h , μm	± 0.55	± 0.58	± 0.48	± 0.44	± 0.63	± 0.59
w , 10^{-4} m/s	3.1	3.3	3.3	3.6	2.8	3.0
Da	2.00	1.84	1.95	2.13	1.77	1.74
η , %	100	100	99	83	95	82
ζ , %	44	42	43	37	39	34

thin regions, and those are believed to act like low resistance oxygen pathways connected in parallel to high resistance ones (see discussion in Mayhew et al., 1986). To better understand this argumentation, one can consider To assess intraplacentone variations of the permeability w we:

- use the fact that w is inversely proportional to the thickness of the layer: $w \sim 1/h_h$ (due to purely diffusive 1D transport);
- assume that the average value $w \approx 2.8 \cdot 10^{-4} \text{ m/s}$ (Table 2.2) corresponds to the highest value $h_h = 3.45 \mu\text{m}$ measured by Critchley and Burton (1987).

The obtained values of w are reported in Table D.2. Combination of w and r_e in the central (C) and peripheral (P) regions from Table D.1 allows one to estimate intraplacentone variations of the Damköhler number according to Eq. (3.13): $Da \equiv 2wkL_0/(uBr_e)$ (for the values of other parameters see the discussion above). The obtained Da values can now be combined with ϕ from the study of Bacon et al. (1986) (Table D.1) to yield variations of the villi density efficiency η and overall geometry efficiency ζ that take into account variations of the trophoblast barrier thickness (Figs D.4c,d). It can be seen that η has not significantly changed as compared to the estimations with no account for trophoblast thickness variations (Fig. D.2c). The villi density is still close to the optimal

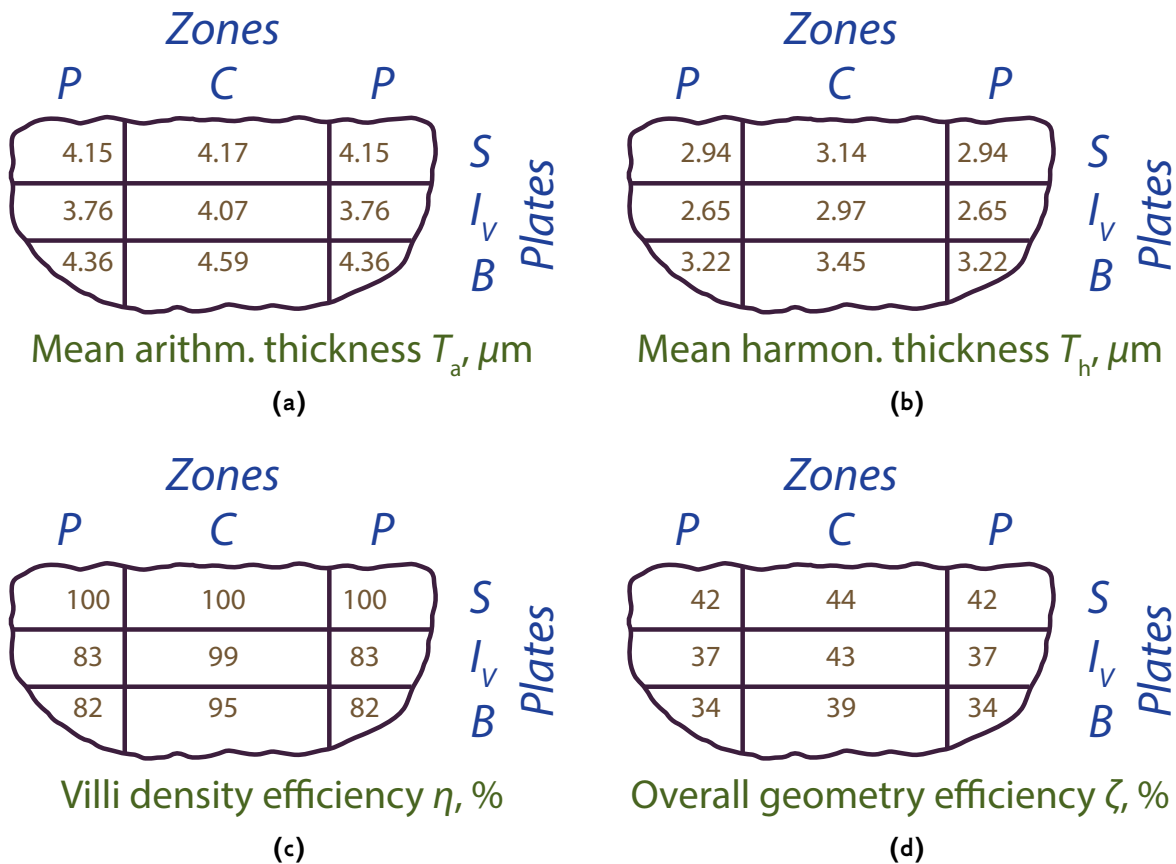


Figure D.4. Symmetrical schematic illustration of intraplacentone variations of the mean arithmetic thickness of the trophoblast barrier h_a (a), the mean harmonic thickness of the trophoblast barrier h_h (b), villi density efficiency η (c) and overall geometry efficiency ζ (d) based on data from Table D.2. The results presented for η and ζ take into account variations of the trophoblast barrier thickness, but do not demonstrate much difference compared to estimations made with a uniform trophoblast barrier thickness (Figs D.2c,d)

Table D.3. Intraplacentone variations of histomorphometrical data as reported by Bacon et al. (1986). The area fraction of the small villi ($S_{sm.v}/S_{tot}$) and of the intervillous space (S_{IVS}/S_{tot}) has been measured near the center of the placental disk and at its periphery. Villi density in each region was then calculated as $\varphi \equiv S_{sm.v}/(S_{sm.v} + S_{IVS})$ (see discussion in Section 2.4.3 on p. 82). The villi density appears to be higher near the center of the placental disk than at its periphery

	Center	Periphery
$S_{sm.v}/S_{tot}$, %	40.2 ± 3.7	34.5 ± 2.9
S_{IVS}/S_{tot} , %	26.7 ± 2.6	31.9 ± 3.0
φ	0.60 ± 0.03	0.52 ± 0.03

one in the center of the placentone and near the chorionic plate and less efficient at the periphery of the placentone. The distribution of the overall geometry efficiency ζ also reproduces the one obtained without taking trophoblast thickness variations into account. One may therefore speculate that biological intraplacentone variations of h_h do not yield significant variations of oxygen exchange efficiency between different placentone regions. Note that these estimations were obtained under the assumption that the maternal blood velocity is uniform in the placentone. This assumption is likely be far from the situation *in vivo*, and the performed estimations should be reconsidered once more accurate maternal blood velocity distribution inside a placentone is obtained.

D.1.2 Intraplacentone structural variations

Placentones from different regions of the placenta may also show different degrees of maturation, yielding that even a careful study of several sections from a given placentone can lead to wrong interpretations (Benirschke et al., 2006, p. 164). The same problem is raised by Burton (1987): "Strict attention must be paid to the sampling regimen if meaningful results are to be obtained. Sadly this has not always been taken into consideration in the past, and so many of the published claims must be qualified accordingly". An extensive discussion of representative placenta sampling can be found in Mayhew (2006b, 2008).

To quantify regional structural differences in the placenta as a whole, Bacon et al. (1986) have compared fractions of small villi ($S_{sm.v}/S_{tot}$) and of the intervillous space (S_{IVS}/S_{tot}) near the center of the placental disk and at its periphery (see Fig. D.1 and Table D.3). One can observe that the villi density in the center of the placental disk (0.60) is on average higher than at its periphery (0.52). Therefore to allow for accurate interpretation of the histological data, the region of sampling has to be specified along the reported data. It is interesting to mention that variations in the placental morphology have been correlated to alterations in Doppler velocimetries of the uterine and the umbilical arteries before delivery (Madazli et al., 2003).

D.2 Immersion fixation vs. perfusion fixation of placental samples

The umbilical cord can be clamped within one minute after delivery, so that fetal blood loss after birth can be avoided (Bouw et al., 1976). However, it has been demonstrated that *placental transfusion* starts much earlier, with the beginning of labour (Sisson, 1978).

This phenomenon consists in the compression of the placenta (a highly vascular organ) during delivery by uterine contractions expelling both the baby and the placenta. The compressive forces result in a considerable shift of blood from the placental fetal vasculature to the baby. Following this shift, the placental fetal vascular system collapses under the hydrostatic pressure of the maternal blood, and histological placental cross-sections prepared in a standard way (by immersion into a fixative) may not correctly represent the *in vivo* situation. The maternal blood also leaks through the orifices of the maternal veins in the basal plate during and after delivery, under the force of the maternal hydrostatic blood pressure, which is higher than the atmospheric pressure. The placental transfusion and the collapse of the fetal capillaries lead to additional shrinkage of the IVS and to even greater loss of the maternal blood.

The effect of placental transfusion on the histomorphometry of the fetal villous tree has been quantitatively assessed by [Burton et al. \(1987\)](#). Ten placentas were analyzed, 5 of which were obtained by vaginal delivery (VD) and 5 by Caesarian section (CD). For each placenta two groups of five samples were prepared. Samples of the first group were fixed in a traditional way, by immersion into a fixative (IF); the second group was perfused with the same fixative (PF). The authors used a double perfusion system of their own invention to apply physiological pressures to the placenta from the fetal and the maternal side and try to recreate the antenatal state of the villous tree. Two types of comparison were performed: VD vs. CD samples and IF vs. PF samples. Note that before the histomorphometrical analysis all samples were dehydrated with acetone, which may have influenced the obtained results.

The following results were obtained:

- The mean villous radius was similar in both PF ($32 \pm 1.5 \mu\text{m}$) and IF samples ($29 \pm 1.5 \mu\text{m}$), suggesting that the total volume of the villi does not significantly depend on the fixation technique.
- The volume fractions of fetal capillaries in the villi in IF samples, PF samples and *in situ* biopsy (ISB) samples were however different. It was observed that the PF value (38.4 %) is close to earlier measured ISB values (35.1–45.2 %) ([Sen et al., 1979](#), [Voigt et al., 1978](#)), suggesting that PF samples give results close to the *in vivo* structure. At the same time, the IF values (13.7–26.2 %) obtained by standard techniques ([Laga et al., 1973](#), [Teasdale, 1978](#), [van der Velde et al., 1983](#), [Burton et al., 1987](#)) were much farther from the *in vivo* situation. The IF technique also gave larger relative errors compared to the PF and ISB techniques. Using the latter two may therefore reduce intraplacental results variations and facilitate the analysis of interplacental structural differences.
- Greater collapse (lower volume) of fetal capillaries was also observed in CD samples than in VD samples. The degree of collapse of the fetal capillaries was estimated by calculating the average difference of the capillary area in the IF and PF samples and dividing it by the average capillary area in PF samples. It was found that the capillary collapse amounted to 23 % in CD and 42 % in VD. It was thus confirmed

that the placenta is much more subject to compression during VD than during CD, as expected.

- The mean number of capillaries per villus was slightly higher in the IF samples (4.86 ± 0.58) than in the PF samples (4.20 ± 0.39), which was interpreted as that partial collapse of fetal capillaries during IF generated several visible capillary profiles instead of one visible in PF samples.
- The arithmetic mean thickness (h_a) and the harmonic mean thickness (h_h) of the materno-fetal barrier (the vasculosyncytial membrane) were assessed for each sample. It was found that on average both variables were significantly lower in PF samples (h_a : $4.84 \pm 0.50 \mu\text{m}$, h_h : $3.63 \pm 0.42 \mu\text{m}$) than in IF samples (h_a : $6.03 \pm 0.64 \mu\text{m}$, h_h : $4.87 \pm 0.66 \mu\text{m}$), which is probably explained by the partial collapse of the fetal vessels and extension of the villous stroma during IF.

The effects of double perfusion on histomorphometrical data were also investigated by Bacon et al. (1986), Karimu and Burton (1994).

D.3 Influence of the fixative on histomorphometrical measurements

Another study investigated the effects of the fixative on the obtained histomorphometrical measurements (Barker et al., 1988). For this purpose:

- the maternal blood volume (MBV) and the fetal blood volume (FBV) of 6 placentas were estimated by both standard histomorphometrical (HM) and hemoglobin content (HBC) techniques;
- a linear size of the same villi was also measured before and after fixation.

The following results were obtained:

- The hemoglobin content technique demonstrates that the MBV amounts to $11.0 \pm 1.5\%$ of the placental volume, while the remaining $89.0 \pm 1.5\%$ of the volume corresponds to fetal tissues. $9.0 \pm 0.6\%$ in these 89% correspond to the FBV. However, when the placenta is put into a fixative, its overall volume stays the same, but the HM technique demonstrates that the percentage of volume of the villous tissues reduces from 89% to $64.7 \pm 1.5\%$, while the MBV increases from 11.0% to $35.3 \pm 1.5\%$. The HM results were thus shown to be significantly different from the histological placental structure expected *in vivo*. It was also demonstrated that the shrinkage of the tissues is reversible if the salinity of the fixative solution is changed, which suggests that the observed changes are due to osmotic forces.
- The measurements of the FBV by both HM ($11.0 \pm 0.7\%$) and HBC ($9.0 \pm 0.6\%$) techniques indicate that the shrinkage mainly occurs in non-vascular villous tissue, and the FBV does not change much. Presumably, during fixation the water from interstitial and intracellular spaces is transferred to the intervillous space (MBV), which explains the observed changes in component proportions.

- Independently measured linear shrinkage of the villi was reported to be 0.89 ± 0.02 , which can be recalculated into the volume shrinkage of $0.89^3 \approx 0.70$ and which corresponds to the previous conclusions.

The tissue shrinkage due to fixation and to the cease of blood circulation have thus to be taken into account if accurate estimations of the *in vivo* morphology are required. Some groups tried to introduce corrections coefficients to compensate for the tissue shrinkage (Lee and Mayhew, 1995), but the method has not been re-used by other groups.

Appendix E

Comparison of oxygen exchange efficiency at low and high altitudes

Pregnancies at high altitude impose greater burden on the placenta due to a lower oxygen content of the inhaled air. It has been observed that placentas of such pregnancies feature larger intervillous space, but lower villous volume, surface area and average length (Jackson et al., 1985, 1987a,b, 1988a,b, Mayhew et al., 1990, Lee and Mayhew, 1995). After the development of the analytical theory of placental oxygen exchange and introduction of the villi density efficiency η and the overall geometry efficiency ζ (Chapter 3), it seems interesting to compare oxygen exchange efficiency of low altitude and high altitude placentas. The following calculations will be based on histomorphometrical data of Lee

Table E.1. Histomorphometrical data from 24 low-altitude and 45 high-altitude placentas obtained by Lee and Mayhew (1995): total placental volume (V_{tot}), total villous volume (V_{vil}), intervillous space volume (V_{IVS}), total villous surface area (S_{vil}). Small villi volume $V_{\text{sm.v}}$ was calculated from V_{vil} under the assumption that small villi account for 66.5 % of the total villi volume (Sen et al., 1979). Small villi surface area $S_{\text{sm.v}}$ was calculated from S_{vil} under the assumption that small villi account for 77.3 % of the total villi surface area (Sen et al., 1979). The villi density ϕ was estimated as $\phi \equiv V_{\text{sm.v}}/(V_{\text{sm.v}} + V_{\text{IVS}})$ (see Section 2.4.3 on p. 82) and the effective villi radius was calculated as $r_e \equiv 2V_{\text{sm.v}}/S_{\text{sm.v}}$ (see discussion in Section 3.1.4 on p. 93). The Damköhler number Da was calculated according to Eq. (3.13) as $Da \equiv 2wkL_0/(uBr_e)$, where the average maternal blood flow velocity $u \approx 6 \cdot 10^4$ m/s, the permeability of the materno-fetal membrane $w \approx 2.8 \cdot 10^{-4}$ m/s, the stream-tube length $L_0 \approx 1.6$ cm, the oxygen-hemoglobin dissociation constant $B \approx 94$ (Table 2.2 on p. 71), and the parameter $\kappa \approx 0.35$ (see Sect. 3.2.2 on p. 99). The villi density efficiency η and the overall geometry efficiency ζ were then estimated according to Eqs (3.12) and (3.21)

	Low altitude	High altitude
$V_{\text{tot}}, \text{ cm}^3$	433±19	448±12
$V_{\text{vil}}, \text{ cm}^3$	158±11	120.0±4.5
$V_{\text{IVS}}, \text{ cm}^3$	177±12	249±8
$S_{\text{vil}}, \text{ m}^2$	6.8	5.6
$V_{\text{sm.v}}, \text{ cm}^3$	105.1±7.3	79.8±3.0
$S_{\text{sm.v}}, \text{ m}^2$	5.3	4.3
ϕ	0.37	0.24
$r_e, \mu\text{m}$	40	37
Da	1.4	1.5
$\eta, \%$	96	76
$\zeta, \%$	35	29

and Mayhew (1995). The authors have measured total placental volumes, volumes of the villi and of the intervillous space, as well as surface areas of the villi in 24 low-altitude and 45 high-altitude placentas (see Table E.1). These data allow one to estimate the volume of the small villi, their villi density φ , surface area of the small villi and their effective radius r_e (Table E.1). After that, the villi density efficiency η and the overall geometry efficiency ζ can be calculated (Table E.1). It can be seen that the villi density at high-altitude is significantly lower than at low altitude. The authors interpret this observation as that high-altitude placentas have adapted to lower oxygen content by increasing the IVS, and hence the amount of the maternal blood in the placenta. The calculations of the placental exchange efficiencies η and ζ demonstrate a significant decrease in both quantities. This conclusion might be interpreted as that the structure of high-altitude placentas is less adapted to oxygen exchange than that of low-altitude placentas. However, it does not seem logical that the selective evolutionary pressure in altered environment would lead to a decreased exchange efficiency. It is more probable that not only the volumes of the placental compartments and their surface areas have changed, but also other geometrical and physiological parameters, such as the velocity u of the maternal blood flow or the permeability of the feto-maternal barrier w , the variations of which have not been analyzed by Lee and Mayhew (1995). If the permeability of the barrier were increased (for instance, due to a decreased trophoblast layer thickness) or the velocity of the maternal blood were higher, the high-altitude placentas may provide the exchange efficiency comparable to that of low-altitude placentas. These parameters may have "less optimal" values at the low altitude to protect the fetus from high oxygen concentrations. Further experimental studies are thus required with special focus on these parameters.

Bibliography

- Abramowicz, J. S. and Sheiner, E., 2007. In utero imaging of the placenta: importance for diseases of pregnancy. *Placenta*, 28 Suppl A:S14–22. <http://dx.doi.org/10.1016/j.placenta.2007.02.004>. URL: <<http://www.ncbi.nlm.nih.gov/pubmed/17383721>>.
- Acharya, G. and Sitras, V., 2009. Oxygen uptake of the human fetus at term. *Acta Obstet. Gynecol. Scand.*, 88(1):104–9. <http://dx.doi.org/10.1080/00016340802460339>. URL: <<http://www.ncbi.nlm.nih.gov/pubmed/18991146>>.
- Acharya, G., Wilsgaard, T., Rosvold Berntsen, G. K., Maltau, J. M., and Kiserud, T., 2005. Reference ranges for umbilical vein blood flow in the second half of pregnancy based on longitudinal data. *Prenat. Diagn.*, 25(2):99–111. <http://dx.doi.org/10.1002/pd.1091>. URL: <<http://www.ncbi.nlm.nih.gov/pubmed/15712315>>.
- Aherne, W. and Dunnill, M. S., 1966. Quantitative aspects of placental structure. *J. Pathol. Bacteriol.*, 91(1):123–39. <http://dx.doi.org/10.1002/path.1700910117>. URL: <<http://www.ncbi.nlm.nih.gov/pubmed/5941387>>.
- Aifantis, E. C., 1978. Towards a rational modeling for the human placenta. *Math. Biosci.*, 40(3-4): 281–301. [http://dx.doi.org/10.1016/0025-5564\(78\)90090-1](http://dx.doi.org/10.1016/0025-5564(78)90090-1).
- Al-Ghaffra, A., Gude, N. M., Brennecke, S. P., and King, R. G., 2003. Labour-associated changes in adrenomedullin content in human placenta and fetal membranes. *Clin. Sci. (Lond.)*, 105(4):419–23. <http://dx.doi.org/10.1042/CS20030027>. URL: <<http://www.ncbi.nlm.nih.gov/pubmed/12769815>>.
- Ala-Kokko, T. I. I., Myllynen, P., Vahakangas, K., and Vähäkangas, K., 2000. Ex vivo perfusion of the human placental cotyledon: implications for anesthetic pharmacology. *Int. J. Obstet. Anesth.*, 9(1):26–38. <http://dx.doi.org/10.1054/ijoa.1999.0312>.
- Alastruey, J., Sherwin, S. J., Parker, K. H., and Rubens, D. D., 2009. Placental transfusion insult in the predisposition for SIDS: a mathematical study. *Early Hum. Dev.*, 85(7):455–9. <http://dx.doi.org/10.1016/j.earlhumdev.2009.04.001>. URL: <<http://www.ncbi.nlm.nih.gov/pubmed/19446412>>.
- Alison, M., Chalouhi, G. E., Autret, G., Balvay, D., Thiam, R., Salomon, L. J., Cuenod, C. A., Clement, O., and Siauve, N., 2013. Use of intravoxel incoherent motion MR imaging to assess placental perfusion in a murine model of placental insufficiency. *Invest. Radiol.*, 48(1):17–23. <http://dx.doi.org/10.1097/RLI.0b013e318271a5f8>. URL: <<http://www.ncbi.nlm.nih.gov/pubmed/23192161>>.
- Almasry, S. M. and Elfayomy, A. K., 2012. Morphometric analysis of terminal villi and gross morphological changes in the placentae of term idiopathic intrauterine growth restriction. *Tissue Cell*, 44(4):214–9. <http://dx.doi.org/10.1016/j.tice.2012.03.006>. URL: <<http://www.ncbi.nlm.nih.gov/pubmed/22541804>>.
- Assali, N. S., Douglass, R. A., Baird, W. W., Nicholson, D. B., and Suyemoto, R., 1953. Measurement of uterine blood flow and uterine metabolism. IV. Results in normal pregnancy. *Am. J. Obstet. Gynecol.*, 66(2):248–53. URL: <<http://www.ncbi.nlm.nih.gov/pubmed/13065329>>.
- Avni, R., Raz, T., Biton, I. E., Kalchenko, V., Garbow, J. R., and Neeman, M., 2012. Unique in utero identification of fetuses in multifetal mouse pregnancies by placental bidirectional arterial spin labeling MRI. *Magn. Reson. Med.*, 68(2):560–70. <http://dx.doi.org/10.1002/mrm.23246>. URL: <<http://www.ncbi.nlm.nih.gov/pubmed/22162003>>.
- Bacon, B. J., Gilbert, R. D., Kaufmann, P., Smith, A. D., Trevino, F. T., and Longo, L. D., 1984. Placental anatomy and diffusing capacity in guinea pigs following long-term maternal hypoxia. *Placenta*, 5(6): 475–87. URL: <<http://www.ncbi.nlm.nih.gov/pubmed/6527981>>.
- Bacon, B. J., Gilbert, R. D., and Longo, L. D., 1986. Regional anatomy of the term human placenta. *Placenta*, 7(3):233–41. [http://dx.doi.org/10.1016/S0143-4004\(86\)80161-8](http://dx.doi.org/10.1016/S0143-4004(86)80161-8). URL: <<http://www.ncbi.nlm.nih.gov/pubmed/3014340>>.

- <http://www.ncbi.nlm.nih.gov/pubmed/3737577>>.
- Baergen, R. N., 2007. The placenta as witness. *Clin. Perinatol.*, 34(3):393–407. <http://dx.doi.org/10.1016/j.clp.2007.03.013>. URL: <<http://www.ncbi.nlm.nih.gov/pubmed/17765490>>.
- Bakardjiev, A. I., Theriot, J. A., and Portnoy, D. A., 2006. Listeria monocytogenes traffics from maternal organs to the placenta and back. *PLoS Pathog.*, 2(6):e66. <http://dx.doi.org/10.1371/journal.ppat.0020066>. URL: <<http://www.ncbi.nlm.nih.gov/pubmed/16846254>>.
- Barker, D. J. P., 1994. *Mothers, Babies and Disease in Later Life*. BMJ Publishing group, London.
- Barker, D. J. P., 1995. Fetal origins of coronary heart disease. *Br. Med. J.*, 311(6998):171–4. <http://dx.doi.org/10.1136/bmj.311.6998.171>. URL: <<http://www.ncbi.nlm.nih.gov/pubmed/7613432>>.
- Barker, G., Cunliffe, N., Bardsley, W. G., D'Souza, S. W., Donnai, P., and Boyd, R. D., 1988. Fetal and maternal blood volumes in shed human placentae: discrepant results comparing morphometry to haemoglobin content. *Placenta*, 9(3):289–96. [http://dx.doi.org/10.1016/0143-4004\(88\)90036-7](http://dx.doi.org/10.1016/0143-4004(88)90036-7). URL: <<http://www.ncbi.nlm.nih.gov/pubmed/3050971>>.
- Barron, D. H., 1951. Some aspects of the transfer of oxygen across the syndesmochorial placenta of the sheep. *Yale J. Biol. Med.*, 24(3):169–90. URL: <<http://www.ncbi.nlm.nih.gov/pubmed/14901887>>.
- Barta, E. and Drugan, A., 2010. Glucose transport from mother to fetus - a theoretical study. *J. Theor. Biol.*, 263(3):295–302. <http://dx.doi.org/10.1016/j.jtbi.2009.12.010>. URL: <<http://www.ncbi.nlm.nih.gov/pubmed/20006624>>.
- Bartels, H. and Moll, W., 1964. Passage of inert substances and oxygen in the human placenta. *Pflüg. Arch. Gesamte Physiol. Mensch. Tiere*, 280:165–77. <http://dx.doi.org/10.1007/BF00363755>. URL: <<http://www.ncbi.nlm.nih.gov/pubmed/14253711>>.
- Bartels, H., Moll, W., and Metcalfe, J., 1962. Physiology of gas exchange in the human placenta. *Am. J. Obstet. Gynecol.*, 84:1714–30. URL: <<http://www.ncbi.nlm.nih.gov/pubmed/13969669>>.
- Battaglia, F. C. and Meschia, G., 1986. *An Introduction to Fetal Physiology*. Academic Press, Inc., London.
- Baumann, M. U., Deborde, S., and Illsley, N. P., 2002. Placental glucose transfer and fetal growth. *Endocrine*, 19(1):13–22. <http://dx.doi.org/10.1385/ENDO:19:1:13>. URL: <<http://www.ncbi.nlm.nih.gov/pubmed/12583599>>.
- Beck, T., 1991. Placental morphometry using a computer assisted measuring programme: reference values for normal pregnancies at term. *Arch. Gynecol. Obstet.*, 249(3):135–47. <http://dx.doi.org/10.1007/BF02391580>. URL: <<http://www.ncbi.nlm.nih.gov/pubmed/1772266>>.
- Beischer, N. A., Sivasamboo, R., Vohra, S., Silpisornkosal, S., and Reid, S., 1970. Placental hypertrophy in severe pregnancy anaemia. *J. Obstet. Gynaecol. Br. Commonw.*, 77(5):398–409. URL: <<http://www.ncbi.nlm.nih.gov/pubmed/5427603>>.
- Bejan, A., 1984. *Convection Heat Transfer*. John Wiley & Sons, New York.
- Benes, N. and Verweij, H., 1999. Comparison of Macro- and Microscopic Theories Describing Multicomponent Mass Transport in Microporous Media. *Langmuir*, 15(23):8292–8299. <http://dx.doi.org/10.1021/la9905012>.
- Benirschke, K., Kaufmann, P., and Baergen, R. N., 2006. *Pathology of the Human Placenta*. Springer, NY, 5th edition.
- Bonel, H. M., Stolz, B., Diedrichsen, L., Frei, K., Saar, B., Tutschek, B., Raio, L., Surbek, D., Srivastav, S., Nelle, M., Slotboom, J., and Wiest, R., 2010. Diffusion-weighted MR imaging of the placenta in fetuses with placental insufficiency. *Radiology*, 257(3):810–9. <http://dx.doi.org/10.1148/radiol.10092283>. URL: <<http://www.ncbi.nlm.nih.gov/pubmed/21084415>>.
- Borbely, A. U., Sandri, S., Fernandes, I. R., Prado, K. M., Cardoso, E. C., Correa-Silva, S., Albuquerque, R., Knöfler, M., Beltrão Braga, P., Campa, A., and Bevilacqua, E., 2014. The term basal plate of the human placenta as a source of functional extravillous trophoblast cells. *Reprod. Biol. Endocrinol.*, 12:7. <http://dx.doi.org/10.1186/1477-7827-12-7>. URL: <<http://www.ncbi.nlm.nih.gov/pubmed/24467708>>.
- Borell, U., Fernstrom, I., and Westman, A., 1958. Eine arteriographische Studie des Plazentarkreislaufs [Arteriographic study of placental circulation]. *Geburtshilfe Frauenheilkd.*, 18:1–9.
- Bouw, G. M., Stolte, L. A. M., Baak, J. P. A., and Oort, J., 1976. Quantitative morphology of the placenta I. Standardization of sampling. *Eur. J. Obstet. Gynecol. Reprod. Biol.*, 6(6):325–331. [http://dx.doi.org/10.1016/0028-2243\(76\)90050-2](http://dx.doi.org/10.1016/0028-2243(76)90050-2).
- Boyd, J. D. and Hamilton, W. J., 1970. *The human placenta*. W. Heffer&Sons Ltd, Cambridge.
- Boyd, P. A., 1984. Quantitative structure of the normal human placenta from 10 weeks of gestation

- to term. *Early Hum. Dev.*, 9(4):297–307. [http://dx.doi.org/10.1016/0378-3782\(84\)90074-4](http://dx.doi.org/10.1016/0378-3782(84)90074-4). URL: <http://www.ncbi.nlm.nih.gov/pubmed/6745150>.
- Boyd, P. A. and Scott, A., 1985. Quantitative structural studies on human placentas associated with pre-eclampsia, essential hypertension and intrauterine growth retardation. *Br. J. Obstet. Gynaecol.*, 92(7):714–21. <http://dx.doi.org/10.1111/j.1471-0528.1985.tb01454.x>. URL: <http://www.ncbi.nlm.nih.gov/pubmed/4016032>.
- Boyd, P. A., Scott, A., and Keeling, J. W., 1986. Quantitative structural studies on placentas from pregnancies complicated by diabetes mellitus. *Br. J. Obstet. Gynaecol.*, 93(1):31–5. <http://dx.doi.org/10.1111/j.1471-0528.1986.tb07809.x>. URL: <http://www.ncbi.nlm.nih.gov/pubmed/3942705>.
- Browne, J. C. M. and Veall, N., 1953. The maternal placental blood flow in normotensive and hypertensive women. *J. Obstet. Gynaecol. Br. Emp.*, 60(2):141–7. <http://dx.doi.org/10.1111/j.1471-0528.1953.tb07668.x>. URL: <http://www.ncbi.nlm.nih.gov/pubmed/13053276>.
- Bulla, R., Bossi, F., Radillo, O., de Seta, F., and Tedesco, F., 2003. Placental trophoblast and endothelial cells as target of maternal immune response. *Autoimmunity*, 36(1):11–8. <http://dx.doi.org/10.1080/0891693031000067331>. URL: <http://www.ncbi.nlm.nih.gov/pubmed/12765466>.
- Burchell, R. C., 1967. Arterial blood flow into the human intervillous space. *Am. J. Obstet. Gynecol.*, 98(3):303–11. URL: <http://www.ncbi.nlm.nih.gov/pubmed/5621448>.
- Burton, G. J., 1987. The fine structure of the human placental villus as revealed by scanning electron microscopy. *Scanning Microsc.*, 1(4):1811–28. URL: <http://www.ncbi.nlm.nih.gov/pubmed/3324327>.
- Burton, G. J. and Palmer, M. E., 1988. Eradicating fetomaternal fluid shift during perfusion fixation of the human placenta. *Placenta*, 9(3):327–32. [http://dx.doi.org/10.1016/0143-4004\(88\)90040-9](http://dx.doi.org/10.1016/0143-4004(88)90040-9). URL: <http://www.ncbi.nlm.nih.gov/pubmed/3050973>.
- Burton, G. J., Ingram, S., and Palmer, M., 1987. The influence of mode of fixation on morphometrical data derived from terminal villi in the human placenta at term: a comparison of immersion and perfusion fixation. *Placenta*, 8(1):37–51. [http://dx.doi.org/10.1016/0143-4004\(87\)90038-5](http://dx.doi.org/10.1016/0143-4004(87)90038-5). URL: <http://www.ncbi.nlm.nih.gov/pubmed/3295856>.
- Burton, G. J., Watson, A. L., Hempstock, J., Skepper, J. N., and Jauniaux, E., 2002. Uterine glands provide histiotrophic nutrition for the human fetus during the first trimester of pregnancy. *J. Clin. Endocrinol. Metab.*, 87(6):2954–9. <http://dx.doi.org/10.1210/jcem.87.6.8563>. URL: <http://www.ncbi.nlm.nih.gov/pubmed/12050279>.
- Burton, G. J., Woods, A. W., Jauniaux, E., and Kingdom, J. C. P., 2009. Rheological and physiological consequences of conversion of the maternal spiral arteries for uteroplacental blood flow during human pregnancy. *Placenta*, 30(6):473–82. <http://dx.doi.org/10.1016/j.placenta.2009.02.009>. URL: <http://www.ncbi.nlm.nih.gov/pubmed/19375795>.
- Butler, L. A., Longo, L. D., and Power, G. G., 1976. Placental blood flows and oxygen transfer during uterine contractions: A mathematical model. *J. Theor. Biol.*, 61(1):81–95. [http://dx.doi.org/10.1016/0022-5193\(76\)90106-5](http://dx.doi.org/10.1016/0022-5193(76)90106-5). URL: <http://www.ncbi.nlm.nih.gov/pubmed/979298>.
- Carter, A. M. Placental circulation. In Steven, D. H., editor, *Comp. Placentation. Essays Struct. Funct.*, pages 108–56. Academic Press, New York, 1975.
- Carter, A. M., 1989. Factors affecting gas transfer across the placenta and the oxygen supply to the fetus. *J. Dev. Physiol.*, 12(6):305–22. URL: <http://www.ncbi.nlm.nih.gov/pubmed/2701106>.
- Challier, J.-C. and Uzan, S., 2003. Le placenta humain et ses pathologies: l'oxygène en question. *Med. Sci. (Paris)*, 19(11):1111–20. <http://dx.doi.org/10.1051/medsci/200319111111>. URL: <http://www.ncbi.nlm.nih.gov/pubmed/14648482>.
- Chernyavsky, I. L. *A Multiscale Analysis of Flow and Transport in the Human Placenta*. Ph.D. Thesis, University of Nottingham, 2011. URL: <http://eprints.nottingham.ac.uk/id/eprint/13678>.
- Chernyavsky, I. L., Jensen, O. E., and Leach, L., 2010. A mathematical model of intervillous blood flow in the human placenta. *Placenta*, 31(1):44–52. <http://dx.doi.org/10.1016/j.placenta.2009.11.003>. URL: <http://www.ncbi.nlm.nih.gov/pubmed/19945160>.
- Chernyavsky, I. L., Leach, L., Dryden, I. L., and Jensen, O. E., 2011. Transport in the placenta: homogenizing haemodynamics in a disordered medium. *Philos. Trans. A. Math. Phys. Eng. Sci.*, 369(1954):4162–82. <http://dx.doi.org/10.1098/rsta.2011.0170>. URL: <http://www.ncbi.nlm.nih.gov/pubmed/21969671>.
- Corbacho, A. M., Martínez De La Escalera, G., and Clapp, C., 2002. Roles of prolactin and related

- members of the prolactin/growth hormone/placental lactogen family in angiogenesis. *J. Endocrinol.*, 173 (2):219–38. URL: <<http://www.ncbi.nlm.nih.gov/pubmed/12010630>>.
- Costa, A., Costantino, M. L., and Fumero, R., 1992. Oxygen exchange mechanisms in the human placenta: mathematical modelling and simulation. *J. Biomed. Eng.*, 14(5):385–9. [http://dx.doi.org/10.1016/0141-5425\(92\)90083-W](http://dx.doi.org/10.1016/0141-5425(92)90083-W). URL: <<http://www.ncbi.nlm.nih.gov/pubmed/1405555>>.
- Cotter, S. L., Klika, V., Kimpton, L., Collins, S., and Heazell, A. E. P., 2014. A stochastic model for early placental development. *J. R. Soc. Interface*, 11(97):20140149. <http://dx.doi.org/10.1098/rsif.2014.0149>. URL: <<http://www.ncbi.nlm.nih.gov/pubmed/24850904>>.
- Critchley, G. R. and Burton, G. J., 1987. Intralobular variations in barrier thickness in the mature human placenta. *Placenta*, 8(2):185–94. URL: <<http://www.ncbi.nlm.nih.gov/pubmed/3615377>>.
- Demené, C., Pernot, M., Biran, V., Alison, M., Fink, M., Baud, O., and Tanter, M., 2014. Ultrafast Doppler reveals the mapping of cerebral vascular resistivity in neonates. *J. Cereb. Blood Flow Metab.*, 34(6):1009–17. <http://dx.doi.org/10.1038/jcbfm.2014.49>. URL: <<http://www.ncbi.nlm.nih.gov/pubmed/24667916>>.
- Deng, H.-F., 1989. Generalized Fick Law, Its Microscopic Derivation, and Dispersive Diffusion. *Phys. status solidi*, 156(1):K11–K16. <http://dx.doi.org/10.1002/pssb.2221560142>.
- Desforges, M. and Sibley, C. P., 2010. Placental nutrient supply and fetal growth. *Int. J. Dev. Biol.*, 54(2-3):377–90. <http://dx.doi.org/10.1387/ijdb.082765md>. URL: <<http://www.ncbi.nlm.nih.gov/pubmed/19876836>>.
- Detmar, J., Rennie, M. Y., Whiteley, K. J., Qu, D., Taniuchi, Y., Shang, X., Casper, R. F., Adamson, S. L., Sled, J. G., and Jurisicova, A., 2008. Fetal growth restriction triggered by polycyclic aromatic hydrocarbons is associated with altered placental vasculature and AhR-dependent changes in cell death. *Am. J. Physiol. Endocrinol. Metab.*, 295(2):E519–30. <http://dx.doi.org/10.1152/ajpendo.90436.2008>. URL: <<http://www.ncbi.nlm.nih.gov/pubmed/18559983>>.
- Dijkhuizen, P., Buursma, A., Fongers, T. M., Gerding, A. M., Oeseburg, B., and Zijlstra, W. G., 1977. The oxygen binding capacity of human haemoglobin. Hüfner's factor redetermined. *Pflugers Arch.*, 369 (3):223–31. <http://dx.doi.org/10.1007/BF00582188>. URL: <<http://www.ncbi.nlm.nih.gov/pubmed/561369>>.
- Dormandy, J. A., 1970. Clinical significance of blood viscosity. *Ann. R. Coll. Surg. Engl.*, 47(4):211–28. URL: <<http://www.ncbi.nlm.nih.gov/pubmed/5475693>>.
- Dorst, L. and Smeulders, A. W., 1987. Length estimators for digitized contours. *Comput. Vision, Graph. Image Process.*, 39(3):393. [http://dx.doi.org/10.1016/S0734-189X\(87\)80194-9](http://dx.doi.org/10.1016/S0734-189X(87)80194-9).
- Dubova, E. A., Pavlov, K. A., Yesayan, R. M., Nagovitsyna, M. N., Tkacheva, O. N., Shestakova, M. V., and Shchegolev, A. I., 2011. Morphometric characteristics of placental villi in pregnant women with diabetes. *Bull. Exp. Biol. Med.*, 151(5):650–4. <http://dx.doi.org/10.1007/s10517-011-1406-9>. URL: <<http://www.ncbi.nlm.nih.gov/pubmed/22462069>>.
- Dunkelberger, K. A. and Mitchell, O. R. Contour tracking for precision measurement. In *Proc. IEEE Int. Conf. Robot. Autom.*, pages 22–7, St. Louis, 1985.
- Dymling, S. O., Persson, H. W., and Hertz, C. H., 1991. Measurement of blood perfusion in tissue using doppler ultrasound. *Ultrasound Med. Biol.*, 17(5):433–44. [http://dx.doi.org/10.1016/0301-5629\(91\)90179-Z](http://dx.doi.org/10.1016/0301-5629(91)90179-Z). URL: <<http://www.ncbi.nlm.nih.gov/pubmed/1835810>>.
- Egbor, M., Ansari, T., Morris, N., Green, C. J., and Sibbons, P. D., 2006. Pre-eclampsia and fetal growth restriction: how morphometrically different is the placenta? *Placenta*, 27(6-7):727–34. <http://dx.doi.org/10.1016/j.placenta.2005.06.002>. URL: <<http://www.ncbi.nlm.nih.gov/pubmed/16125226>>.
- Erian, F. F., Corrsin, S., and Davis, S. H., 1977. Maternal, placental blood flow: a model with velocity-dependent permeability. *J. Biomech.*, 10(11/12):807–14. [http://dx.doi.org/10.1016/0021-9290\(77\)90095-1](http://dx.doi.org/10.1016/0021-9290(77)90095-1). URL: <<http://www.ncbi.nlm.nih.gov/pubmed/606727>>.
- Eriksson, J. G., Kajantie, E., Osmond, C., Thornburg, K., and Barker, D. J. P., 2010. Boys live dangerously in the womb. *Am. J. Hum. Biol.*, 22(3):330–5. <http://dx.doi.org/10.1002/ajhb.20995>. URL: <<http://www.ncbi.nlm.nih.gov/pubmed/19844898>>.
- Faber, J. J., 1969. Application of the theory of heat exchangers to the transfer of inert materials in placentas. *Circ. Res.*, 24(2):221–34. <http://dx.doi.org/10.1161/01.RES.24.2.221>. URL: <<http://www.ncbi.nlm.nih.gov/pubmed/5764583>>.
- Faber, J. J., 1977. Steady-state methods for the study of placental exchange. *Fed. Proc.*, 36(12):2640–6.

- URL: <<http://www.ncbi.nlm.nih.gov/pubmed/410666>>.
- Faber, J. J., 1995. Review of flow limited transfer in the placenta. *Int. J. Obstet. Anesth.*, 4(4):230–7. [http://dx.doi.org/10.1016/0959-289X\(95\)82916-X](http://dx.doi.org/10.1016/0959-289X(95)82916-X). URL: <<http://www.ncbi.nlm.nih.gov/pubmed/15637016>>.
- Faber, J. J. and Anderson, D. F., 1990. Model study of placental water transfer and causes of fetal water disease in sheep. *Am. J. Physiol.*, 258(5 Pt 2):R1257–70. URL: <<http://www.ncbi.nlm.nih.gov/pubmed/2186642>>.
- Faber, J. J. and Hart, F. M., 1966. The rabbit placenta as an organ of diffusional exchange. Comparison with other species by dimensional analysis. *Circ. Res.*, 19(4):816–33. <http://dx.doi.org/10.1161/01.RES.19.4.816>. URL: <<http://www.ncbi.nlm.nih.gov/pubmed/4958385>>.
- Faber, J. J., Thornburg, K. L., and Binder, N. D., 1992. Physiology of placental transfer in mammals. *Integr. Comp. Biol.*, 32(2):343–54. <http://dx.doi.org/10.1093/icb/32.2.343>.
- Felici, M., Filoche, M., Straus, C., Similowski, T., and Sapoval, B., 2005. Diffusional screening in real 3D human acini - a theoretical study. *Respir. Physiol. Neurobiol.*, 145(2-3):279–93. <http://dx.doi.org/10.1016/j.res.2004.10.012>. URL: <<http://www.ncbi.nlm.nih.gov/pubmed/15705542>>.
- Filoche, M., Serov, A. S., Salafia, C. M., and Grebenkov, D. S., 2015. The role of morphology in mathematical models of placental gas exchange. *J. Appl. Physiol.*, (submitted).
- Fogler, H. S., 2005. *Elements of chemical reaction engineering*. Prentice Hall, Upper Saddle River, NJ, 4th edition.
- Foucquier, A., Filoche, M., Moreira, A. A., Andrade, J. S., Arbia, G., and Sapoval, B., 2013. A first principles calculation of the oxygen uptake in the human pulmonary acinus at maximal exercise. *Respir. Physiol. Neurobiol.*, 185(3):625–38. <http://dx.doi.org/10.1016/j.res.2012.10.013>. URL: <<http://www.ncbi.nlm.nih.gov/pubmed/23201099>>.
- Fox, H., 1964. The pattern of villous variability in the normal placenta. *J. Obstet. Gynaecol. Br. Commonw.*, 71:749–58. URL: <<http://www.ncbi.nlm.nih.gov/pubmed/14212203>>.
- Fox, H., 1970. Effect of hypoxia on trophoblast in organ culture. A morphologic and autoradiographic study. *Am. J. Obstet. Gynecol.*, 107(7):1058–64. URL: <<http://www.ncbi.nlm.nih.gov/pubmed/5429972>>.
- Franke, V. E., Parker, K. H., Wee, L. Y., Fisk, N. M., and Sherwin, S. J., 2003. Time domain computational modelling of 1D arterial networks in monochorionic placentas. *ESAIM Math. Model. Numer. Anal.*, 37(4):557–80. <http://dx.doi.org/10.1051/m2an:2003047>.
- Franken, H., 1954. Beitrag zur Veranschaulichung von Struktur und Funktion der Plazenta. *Zentralbl. Gynakol.*, 76:729–45.
- Freeman, H. Boundary encoding and processing. In Lipkin, B. S. and Rosenfeld, A., editors, *Pict. Process. Psychopictorics*, pages 241–66. Academic Press, Orlando, FL, 1970.
- Freese, U. E., 1968. The uteroplacental vascular relationship in the human. *Am. J. Obstet. Gynecol.*, 101(1):8–11. <http://dx.doi.org/10.5555/uri:pii:0002937868904766>. URL: <<http://www.ncbi.nlm.nih.gov/pubmed/4967092>>.
- Freese, U. E. Vascular relations of placental exchange areas in primates and man. In Longo, L. D. and Bartels, H., editors, *Respiratory Gas Exchange and Blood Flow in the Placenta*, pages 31–63, Bethesda, Maryland, 1972. Nat. Inst. Child Health Hum. Dev.
- Freese, U. E., Ranniger, K., and Kaplan, H., 1966. The fetal-maternal circulation of the placenta. II. An X-ray cinematographic study of pregnant rhesus monkeys. *Am. J. Obstet. Gynecol.*, 94(3):361–6. URL: <<http://www.ncbi.nlm.nih.gov/pubmed/4955544>>.
- Gill, J. S., Salafia, C. M., Grebenkov, D. S., and Vvedensky, D. D., 2011. Modeling oxygen transport in human placental terminal villi. *J. Theor. Biol.*, 291:33–41. <http://dx.doi.org/10.1016/j.jtbi.2011.09.008>. URL: <<http://www.ncbi.nlm.nih.gov/pubmed/21959313>>.
- Gordon, Z., Elad, D., Almog, R., Hazan, Y., Jaffa, A. J., and Eytan, O., 2007a. Anthropometry of fetal vasculature in the chorionic plate. *J. Anat.*, 211(6):698–706. <http://dx.doi.org/10.1111/j.1469-7580.2007.00819.x>. URL: <<http://www.ncbi.nlm.nih.gov/pubmed/17973911>>.
- Gordon, Z., Eytan, O., Jaffa, A. J., and Elad, D., 2007b. Fetal blood flow in branching models of the chorionic arterial vasculature. *Ann. N. Y. Acad. Sci.*, 1101:250–65. <http://dx.doi.org/10.1196/annals.1389.037>. URL: <<http://www.ncbi.nlm.nih.gov/pubmed/17416927>>.
- Gordon, Z., Eytan, O., Jaffa, A. J., and Elad, D., 2007c. Hemodynamic analysis of Hyrtl anastomosis in human placenta. *Am. J. Physiol. Regul. Integr. Comp. Physiol.*, 292(2):R977–82. <http://dx.doi.org/>

- 10.1152/ajpregu.00410.2006. URL: <<http://www.ncbi.nlm.nih.gov/pubmed/17038439>>.
- Goubalan, S. R. T. J. *Méthodes numériques de segmentation en imagerie biologique*. M. Sc. Thesis, École Polytechnique, 2013.
- Grabau, B. J., Gude, N. M., King, R. G., Riley, S. C., and Brennecke, S. P., 1997. Endothelins-1, 2 and 3 are released in vitro from the human bilaterally perfused placenta. *J. Perinat. Med.*, 25(1):11–6. URL: <<http://www.ncbi.nlm.nih.gov/pubmed/9085198>>.
- Gray, H., 1918. *Anatomy of the Human Body*. Lea & Febiger, Philadelphia, 20th edition.
- Gray, S., 1971. Local Properties of Binary Images in Two Dimensions. *IEEE Trans. Comput.*, C-20(5): 551–61. <http://dx.doi.org/10.1109/T-C.1971.223289>.
- Groome, L. J., 1991. A theoretical analysis of the effect of placental metabolism on fetal oxygenation under conditions of limited oxygen availability. *Biosystems.*, 26(1):45–56. [http://dx.doi.org/10.1016/0303-2647\(91\)90036-K](http://dx.doi.org/10.1016/0303-2647(91)90036-K). URL: <<http://www.ncbi.nlm.nih.gov/pubmed/1760534>>.
- Grosser, O., 1909. *Vergleichende Anatomie und Entwicklungsgeschichte der Eihaut und der Plazenta mit besonderer Berücksichtigung der Menschen*. W. Braumüller, Vienna.
- Grosser, O., 1927. *Frühentwicklung, Eihautbildung und Placentation des Menschen und der Säugetiere*. J.F. Bergmann, München.
- Gude, N. M., Di Iulio, J., Brennecke, S. P., and King, R. G., 1994. Human placental villous nitric oxide synthase activity. *Pharmacol. Commun.*, 4:163–71.
- Gude, N. M., King, R. G., and Brennecke, S. P., 1998. Autocoid interactions in the regulation of blood flow in the human placenta. *Clin. Exp. Pharmacol. Physiol.*, 25(9):706–11. <http://dx.doi.org/10.1111/j.1440-1681.1998.tb02280.x>. URL: <<http://www.ncbi.nlm.nih.gov/pubmed/9750960>>.
- Gude, N. M., Roberts, C. T., Kalionis, B., and King, R. G., 2004. Growth and function of the normal human placenta. *Thromb. Res.*, 114(5-6):397–407. <http://dx.doi.org/10.1016/j.thromres.2004.06.038>. URL: <<http://www.ncbi.nlm.nih.gov/pubmed/15507270>>.
- Guettouche, A., Challier, J. C., Ito, Y., Papapanayotou, C., Cherruault, Y., and Azancot-Benisty, A., 1992. Mathematical modeling of the human fetal arterial blood circulation. *Int. J. Biomed. Comput.*, 31(2): 127–39. [http://dx.doi.org/10.1016/0020-7101\(92\)90068-4](http://dx.doi.org/10.1016/0020-7101(92)90068-4). URL: <<http://www.ncbi.nlm.nih.gov/pubmed/1517000>>.
- Guilbeau, E. J. and Reneau, D. D., 1973. Mathematical analysis of combined placental-fetal oxygen transport. *Adv. Exp. Med. Biol.*, 37:1007–16. http://dx.doi.org/10.1007/978-1-4684-5089-7_43. URL: <<http://www.ncbi.nlm.nih.gov/pubmed/4766476>>.
- Guilbeau, E. J., Reneau, D. D., and Knisely, M. H. The effects of placental oxygen consumption and the contractions of labor on fetal oxygen supply. A steady and unsteady state mathematical simulation. In Longo, L. D. and Bartels, H., editors, *Respiratory Gas Exchange and Blood Flow in the Placenta*, pages 297–344, Bethesda, MD, 1972. Nat. Inst. Child Health Hum. Dev.
- Guilbeau, E. J., Reneau, D. D., and Knisely, M. H. A detailed quantitative analysis of O₂ transport in the human placenta during steady- and unsteady-state conditions. In Reneau, D. D., editor, *Chem. Eng. Med.*, volume 118 of *Advances in Chemistry*, chapter 7, pages 130–71. American chemical society, Washington, 1973. <http://dx.doi.org/10.1021/ba-1973-0118>.
- Guiot, C., Piantà, P. G., and Todros, T., 1992. Modelling the feto-placental circulation: 1. A distributed network predicting umbilical haemodynamics throughout pregnancy. *Ultrasound Med. Biol.*, 18(6-7): 535–44. [http://dx.doi.org/10.1016/0301-5629\(92\)90068-L](http://dx.doi.org/10.1016/0301-5629(92)90068-L). URL: <<http://www.ncbi.nlm.nih.gov/pubmed/1413265>>.
- Gundersen, H. J. G. and Jensen, E. B. V., 1987. The efficiency of systematic sampling in stereology and its prediction. *J. Microsc.*, 147(3):229–63. <http://dx.doi.org/10.1111/j.1365-2818.1987.tb02837.x>. URL: <<http://www.ncbi.nlm.nih.gov/pubmed/3430576>>.
- Gundersen, H. J. G., Jensen, E. B. V., Kiêu, K., and Nielsen, J., 1999. The efficiency of systematic sampling in stereology - Reconsidered. *J. Microsc.*, 193(3):199–211. <http://dx.doi.org/10.1046/j.1365-2818.1999.00457.x>. URL: <<http://www.ncbi.nlm.nih.gov/pubmed/10348656>>.
- Hafez, S. A., Borowicz, P., Reynolds, L. P., and Redmer, D. A., 2010. Maternal and fetal microvasculature in sheep placenta at several stages of gestation. *J. Anat.*, 216(3):292–300. <http://dx.doi.org/10.1111/j.1469-7580.2009.01184.x>. URL: <<http://www.ncbi.nlm.nih.gov/pubmed/20070427>>.
- Hafner, E., Metzenbauer, M., Stümpflen, I., and Waldhör, T., 2013. Measurement of placental bed vascularization in the first trimester, using 3D-power-Doppler, for the detection of pregnancies at-risk for

- fetal and maternal complications. *Placenta*, 34(10):892–8. <http://dx.doi.org/10.1016/j.placenta.2013.06.303>. URL: <<http://www.ncbi.nlm.nih.gov/pubmed/23890468>>.
- Haggarty, P., 2002. Placental regulation of fatty acid delivery and its effect on fetal growth—a review. *Placenta*, 23 Suppl A:S28–38. <http://dx.doi.org/10.1053/plac.2002.0791>. URL: <<http://www.ncbi.nlm.nih.gov/pubmed/11978057>>.
- Haller, U., 1968. Beitrag zur Morphologie der Utero-Placentargefäße. *Arch. Gynakol.*, 205:185–202.
- Hammersen, F. Endothelial contractility — does it exist? In Altura, B. M., editor, *Adv. Microcirc.*, volume 9, pages 95–134. Karger, Basel, 1980.
- Handwerker, S. and Freemark, M., 2000. The roles of placental growth hormone and placental lactogen in the regulation of human fetal growth and development. *J. Pediatr. Endocrinol. Metab.*, 13(4):343–56. <http://dx.doi.org/10.1515/JPEM.2000.13.4.343>. URL: <<http://www.ncbi.nlm.nih.gov/pubmed/10776988>>.
- Hausen, H., 1950. *Wärmeübertragung im Gegenstrom, Gleichstrom und Kreuzstrom*. Springer, Berlin, Göttingen, Heidelberg. <http://dx.doi.org/10.1007/978-3-642-88686-7>.
- Heilmann, L., Grebner, H., Mattheck, C., and Ludwig, H., 1979. Mathematical, clinical, and laboratory study of hemodynamic changes in the placental circulation. *Arch. Gynecol.*, 227(4):303–13. <http://dx.doi.org/10.1007/BF02109919>. URL: <<http://www.ncbi.nlm.nih.gov/pubmed/518133>>.
- Heinrich, D., Metz, J., Raviola, E., and Forssmann, W. G., 1976. Ultrastructure of perfusion-fixed fetal capillaries in the human placenta. *Cell Tissue Res.*, 172(2):157–69. URL: <<http://www.ncbi.nlm.nih.gov/pubmed/991209>>.
- Herbst, R. and Multier-Lajous, A.-M. Scanning electron microscopic visualization of the placental exchange area. In Longo, L. D. and Bartels, H., editors, *Respiratory Gas Exchange and Blood Flow in the Placenta*, pages 23–30, Bethesda, Maryland, 1972. Nat. Inst. Child Health Hum. Dev.
- Higgins, M., Felle, P., Mooney, E. E., Bannigan, J., and McAuliffe, F. M., 2011. Stereology of the placenta in type 1 and type 2 diabetes. *Placenta*, 32(8):564–9. <http://dx.doi.org/10.1016/j.placenta.2011.04.015>. URL: <<http://www.ncbi.nlm.nih.gov/pubmed/21621839>>.
- Hill, E. P., Power, G. G., and Longo, L. D., 1972. A mathematical model of placental O₂ transfer with consideration of hemoglobin reaction rates. *Am. J. Physiol.*, 222(3):721–9. URL: <<http://www.ncbi.nlm.nih.gov/pubmed/5022686>>.
- Hill, E. P., Power, G. G., and Longo, L. D., 1973. A mathematical model of carbon dioxide transfer in the placenta and its interaction with oxygen. *Am. J. Physiol.*, 224(2):283–99. URL: <<http://www.ncbi.nlm.nih.gov/pubmed/4686484>>.
- Hill, E. P., Hill, J. R., Power, G. G., and Longo, L. D., 1977. Carbon monoxide exchanges between the human fetus and mother: a mathematical model. *Am. J. Physiol.*, 232(3):H311–23. URL: <<http://www.ncbi.nlm.nih.gov/pubmed/842687>>.
- Howard, C. V. and Reed, M. G., 2005. *Unbiased stereology. Three-dimensional measurement in microscopy*. Garland Science/Bios Scientific, Abingdon.
- Huen, I., Morris, D. M., Wright, C., Parker, G. J. M., Sibley, C. P., Johnstone, E. D., and Naish, J. H., 2013. R₁ and R₂* changes in the human placenta in response to maternal oxygen challenge. *Magn. Reson. Med.*, 70(5):1427–33. <http://dx.doi.org/10.1002/mrm.24581>. URL: <<http://www.ncbi.nlm.nih.gov/pubmed/23280967>>.
- Huppertz, B., Burton, G. J., Cross, J. C., and Kingdom, J. C. P., 2006. Placental morphology: from molecule to mother — a dedication to Peter Kaufmann — a review. *Placenta*, 27 Suppl A:S3–8. <http://dx.doi.org/10.1016/j.placenta.2006.01.007>. URL: <<http://www.ncbi.nlm.nih.gov/pubmed/16542720>>.
- Hutcheon, J. A., McNamara, H., Platt, R. W., Benjamin, A., and Kramer, M. S., 2012. Placental weight for gestational age and adverse perinatal outcomes. *Obstet. Gynecol.*, 119(6):1251–8. <http://dx.doi.org/10.1097/AOG.0b013e318253d3df>. URL: <<http://www.ncbi.nlm.nih.gov/pubmed/22617591>>.
- Illsley, N. P., Fox, H., Van der Veen, F., Chawner, L., and Penfold, P., 1985. Human placental ultrastructure after in vitro dual perfusion. *Placenta*, 6(1):23–32. [http://dx.doi.org/10.1016/S0143-4004\(85\)80029-1](http://dx.doi.org/10.1016/S0143-4004(85)80029-1). URL: <<http://www.ncbi.nlm.nih.gov/pubmed/3991473>>.
- Incropera, F. P. and Dewitt, D. P., 2001. *Fundamentals of Heat and Mass Transfer*. John Wiley & Sons, Chicago, IL, 5-th edition.
- Jackson, M. R., Joy, C. F., Mayhew, T. M., and Haas, J. D., 1985. Stereological studies on the true thickness of the villous membrane in human term placentae: a study of placentae from high-altitude pregnancies.

- Placenta*, 6(3):249–58. URL: <<http://www.ncbi.nlm.nih.gov/pubmed/4022953>>.
- Jackson, M. R., Mayhew, T. M., and Haas, J. D., 1986. The human placenta at high altitude in Bolivia. III. Quantitative evidence for peripheralisation of fetal capillaries within villi. *J. Anat.*, 149:214–5. URL: <<http://www.ncbi.nlm.nih.gov/pubmed/17103595>>.
- Jackson, M. R., Mayhew, T. M., and Haas, J. D., 1987a. Morphometric studies on villi in human term placenta and the effects of altitude, ethnic grouping and sex of newborn. *Placenta*, 8(5):487–95. [http://dx.doi.org/10.1016/S0143-4004\(85\)80029-1](http://dx.doi.org/10.1016/S0143-4004(85)80029-1). URL: <<http://www.ncbi.nlm.nih.gov/pubmed/3422920>>.
- Jackson, M. R., Mayhew, T. M., and Haas, J. D., 1987b. The volumetric composition of human term placenta: altitudinal, ethnic and sex differences in Bolivia. *J. Anat.*, 152:173–87. URL: <<http://www.ncbi.nlm.nih.gov/pubmed/3654368>>.
- Jackson, M. R., Mayhew, T. M., and Haas, J. D., 1988a. On the factors which contribute to thinning of the villous membrane in human placenta at high altitude. II. An increase in the degree of peripheralization of fetal capillaries. *Placenta*, 9(1):9–18. [http://dx.doi.org/10.1016/0143-4004\(88\)90068-9](http://dx.doi.org/10.1016/0143-4004(88)90068-9). URL: <<http://www.ncbi.nlm.nih.gov/pubmed/3362794>>.
- Jackson, M. R., Mayhew, T. M., and Haas, J. D., 1988b. On the factors which contribute to thinning of the villous membrane in human placenta at high altitude. I. Thinning and regional variation in thickness of trophoblast. *Placenta*, 9(1):1–8. [http://dx.doi.org/10.1016/0143-4004\(88\)90067-7](http://dx.doi.org/10.1016/0143-4004(88)90067-7). URL: <<http://www.ncbi.nlm.nih.gov/pubmed/3362790>>.
- Jauniaux, E. and Burton, G. J., 2006. Villous histomorphometry and placental bed biopsy investigation in Type I diabetic pregnancies. *Placenta*, 27(4-5):468–74. <http://dx.doi.org/10.1016/j.placenta.2005.04.010>. URL: <<http://www.ncbi.nlm.nih.gov/pubmed/16009423>>.
- Jauniaux, E., Jurkovic, D., and Campbell, S., 1995. Current topic: in vivo investigation of the placental circulations by Doppler echography. *Placenta*, 16(4):323–31. [http://dx.doi.org/10.1016/0143-4004\(95\)90089-6](http://dx.doi.org/10.1016/0143-4004(95)90089-6). URL: <<http://www.ncbi.nlm.nih.gov/pubmed/7567794>>.
- Jauniaux, E., Watson, A. L., Hempstock, J., Bao, Y.-P., Skepper, J. N., and Burton, G. J., 2000. Onset of maternal arterial blood flow and placental oxidative stress. *Am. J. Pathol.*, 157(6):2111–22. [http://dx.doi.org/10.1016/S0002-9440\(10\)64849-3](http://dx.doi.org/10.1016/S0002-9440(10)64849-3). URL: <<http://www.ncbi.nlm.nih.gov/pubmed/11106583>>.
- Jirkovská, M., 2013. Spatial arrangement of the microvascular bed in the human placenta. *Androl. Gynecol. Curr. Res.*, 01(04). <http://dx.doi.org/10.4172/2327-4360.1000110>.
- Jirkovská, M., Šmidová, J., and Frýda, T., 1994. Morphometric analysis of the vascularization of the terminal villi in normal and diabetic placenta. *Acta Stereol.*, 13(1):43–7. URL: <<http://popups.ulg.ac.be/0351-580X/index.php?id=982>>.
- Jirkovská, M., Kubínová, L., Janáček, J., Moravcová, M., Krejčí, V., and Karen, P., 2002. Topological Properties and Spatial Organization of Villous Capillaries in Normal and Diabetic Placentas. *J. Vasc. Res.*, 39(3):268–78. <http://dx.doi.org/10.1159/000063692>. URL: <<http://www.ncbi.nlm.nih.gov/pubmed/12097825>>.
- Jirkovská, M., Kubínová, L., Janáček, J., and Kaláb, J., 2007. 3-D study of vessels in peripheral placental villi. *Image Anal. Stereol.*, 26(3):165–8. <http://dx.doi.org/10.5566/ias.v26.p165-168>.
- Jirkovská, M., Janáček, J., Kaláb, J., and Kubínová, L., 2008. Three-dimensional arrangement of the capillary bed and its relationship to microrheology in the terminal villi of normal term placenta. *Placenta*, 29(10):892–7. <http://dx.doi.org/10.1016/j.placenta.2008.07.004>. URL: <<http://www.ncbi.nlm.nih.gov/pubmed/18768220>>.
- Jirkovská, M., Kučera, T., Kaláb, J., Jadrníček, M., Niedobová, V., Janáček, J., Kubínová, L., Moravcová, M., Zížka, Z., and Krejčí, V., 2012. The branching pattern of villous capillaries and structural changes of placental terminal villi in type I diabetes mellitus. *Placenta*, 33(5):343–51. <http://dx.doi.org/10.1016/j.placenta.2012.01.014>. URL: <<http://www.ncbi.nlm.nih.gov/pubmed/22317894>>.
- Jones, A., 1988. Eigenvalues and eigenfunctions for general graetz problems. *Appl. Math. Lett.*, 1(3):229–233. [http://dx.doi.org/10.1016/0893-9659\(88\)90082-1](http://dx.doi.org/10.1016/0893-9659(88)90082-1).
- Jones, A., 2009. Quadratic eigenvalue problems. *Bull. Aust. Math. Soc.*, 37(02):273. <http://dx.doi.org/10.1017/S0004972700026824>.
- Jones, N. W., Hutchinson, E. S., Brownbill, P., Crocker, I. P., Eccles, D., Bugg, G. J., and Raine-Fenning, N. J., 2009. In vitro dual perfusion of human placental lobules as a flow phantom to investigate the relationship between fetoplacental flow and quantitative 3D power doppler angiography. *Placenta*, 30(2):130–5. <http://dx.doi.org/10.1016/j.placenta.2008.11.002>. URL: <<http://www.ncbi.nlm.nih.gov/pubmed/>

- 19059643>.
- Joos, G. and Freeman, I. M., 1951. *Theoretical Physics*. Hafner Publishing, NY, 2nd edition.
- Kaplan, A. D., Jaffa, A. J., Timor, I. E., and Elad, D., 2010. Hemodynamic analysis of arterial blood flow in the coiled umbilical cord. *Reprod. Sci.*, 17(3):258–68. <http://dx.doi.org/10.1177/1933719109351596>. URL: <<http://www.ncbi.nlm.nih.gov/pubmed/20023275>>.
- Karimu, A. L. and Burton, G. J., 1993. Star volume estimates of the intervillous clefts in the human placenta: how changes in umbilical arterial pressure might influence the maternal placental circulation. *J. Dev. Physiol.*, 19(3):137–42. URL: <<http://www.ncbi.nlm.nih.gov/pubmed/8089439>>.
- Karimu, A. L. and Burton, G. J., 1994. The effects of maternal vascular pressure on the dimensions of the placental capillaries. *Br. J. Obstet. Gynaecol.*, 101(1):57–63. URL: <<http://www.ncbi.nlm.nih.gov/pubmed/8297870>>.
- Kaufmann, P., 1985a. Influence of ischemia and artificial perfusion on placental ultrastructure and morphometry. *Contrib. Gynecol. Obstet.*, 13:18–26. URL: <<http://www.ncbi.nlm.nih.gov/pubmed/3995979>>.
- Kaufmann, P., 1985b. Basic morphology of the fetal and maternal circuits in the human placenta. *Contrib. Gynecol. Obstet.*, 13:5–17. URL: <<http://www.ncbi.nlm.nih.gov/pubmed/3995983>>.
- Kaufmann, P. and Scheffen, I. Placental development. In Polin, P. and Fox, W., editors, *Neonatal Fetal Med. Pathophysiol. Vol. 1*, pages 47–55. Saunders, Orlando, 1992.
- Kaufmann, P., Gentzen, D. M., and Davidoff, M., 1977. [The ultrastructure of Langhans cells in pathologic human placentas (author's transl)]. *Arch. Gynakol.*, 222(4):319–32. URL: <<http://www.ncbi.nlm.nih.gov/pubmed/407885>>.
- Kaufmann, P., Sen, D. K., and Schweikhart, G., 1979. Classification of Human Placental Villi I. Histology. *Cell Tissue Res.*, 200(3):409–23. <http://dx.doi.org/10.1007/BF00234852>. URL: <<http://www.ncbi.nlm.nih.gov/pubmed/487407>>.
- Keelan, J. A., Blumenstein, M., Helliwell, R. J. A., Sato, T. A., Marvin, K. W., and Mitchell, M. D., 2003. Cytokines, prostaglandins and parturition—a review. *Placenta*, 24 Suppl A:S33–46. URL: <<http://www.ncbi.nlm.nih.gov/pubmed/12842412>>.
- King, B. F., 1992. Comparative studies of structure and function in mammalian placentas with special reference to maternal-fetal transfer of iron. *Integr. Comp. Biol.*, 32(2):331–42. <http://dx.doi.org/10.1093/icb/32.2.331>.
- King, R. G., Gude, N. M., Krishna, B. R., Chen, S., Brennecke, S. P., Boura, A. L., and Rook, T. J., 1991. Human placental acetylcholine. *Reprod. Fertil. Dev.*, 3(4):405–11. URL: <<http://www.ncbi.nlm.nih.gov/pubmed/1957029>>.
- Kirschbaum, T. H. and Shapiro, N. Z., 1969. A mathematical model of placental oxygen transfer. *J. Theor. Biol.*, 25(3):380–402. [http://dx.doi.org/10.1016/S0022-5193\(69\)80028-7](http://dx.doi.org/10.1016/S0022-5193(69)80028-7). URL: <<http://www.ncbi.nlm.nih.gov/pubmed/5394213>>.
- Kjelstrup, S. and Bedeaux, D., 2008. *Non-Equilibrium Thermodynamics Of Heterogeneous Systems (Series On Advances In Statistical Mechanics)*. World Scientific Publishing Co. Pte. Ltd., Singapore.
- Klein, G. Makroskopisches Verhalten der UteroPlacentargefäße. In Hofmeier, M., editor, *Die Menschl. Placenta. Beitrage zur Norm. und Pathol. Anat. derselben*, pages 72–87. Bergmann, Wiesbaden, 1890.
- Kleiner-Assaf, A., Jaffa, A. J., and Elad, D., 1999. Hemodynamic model for analysis of Doppler ultrasound indexes of umbilical blood flow. *Am. J. Physiol.*, 276(6 Pt 2):H2204–14. URL: <<http://www.ncbi.nlm.nih.gov/pubmed/10362705>>.
- Koide, T., 2005. Microscopic derivation of causal diffusion equation using the projection operator method. *Phys. Rev. E*, 72(2):026135. <http://dx.doi.org/10.1103/PhysRevE.72.026135>.
- Konje, J. C., Huppertz, B., Bell, S. C., Taylor, D. J., and Kaufmann, P., 2003. 3-Dimensional Colour Power Angiography for Staging Human Placental Development. *Lancet*, 362(9391):1199–201. [http://dx.doi.org/10.1016/S0140-6736\(03\)14514-X](http://dx.doi.org/10.1016/S0140-6736(03)14514-X). URL: <<http://www.ncbi.nlm.nih.gov/pubmed/14568743>>.
- Korteweg, F. J., Erwich, J. J. H. M., Holm, J. P., Ravisé, J. M., van der Meer, J., Veeger, N. J. G. M., and Timmer, A., 2009. Diverse placental pathologies as the main causes of fetal death. *Obstet. Gynecol.*, 114(4):809–17. <http://dx.doi.org/10.1097/A0G.0b013e3181b72ebe>. URL: <<http://www.ncbi.nlm.nih.gov/pubmed/19888039>>.
- Kosanke, G., Kadyrov, M., Korr, H., and Kaufmann, P., 1998. Maternal anemia results in increased proliferation in human placental villi. *Placenta*, 19(S1):339–57. [http://dx.doi.org/10.1016/S0143-4004\(98\)80024-6](http://dx.doi.org/10.1016/S0143-4004(98)80024-6).

- Kramer, E. M. and Myers, D. R., 2013. Osmosis is not driven by water dilution. *Trends Plant Sci.*, 18: 195–7. <http://dx.doi.org/10.1016/j.tplants.2012.12.001>.
- Kulpa, Z., 1977. Area and perimeter measurement of blobs in discrete binary pictures. *Comput. Graph. Image Process.*, 6(5):434–51. [http://dx.doi.org/10.1016/S0146-664X\(77\)80021-X](http://dx.doi.org/10.1016/S0146-664X(77)80021-X).
- Lacroix, M. C., Guibourdenche, J., Frendo, J. L., Muller, F., and Evain-Brion, D., 2002. Human placental growth hormone—a review. *Placenta*, 23 Suppl A:S87–94. <http://dx.doi.org/10.1053/plac.2002.0811>. URL: <<http://www.ncbi.nlm.nih.gov/pubmed/11978064>>.
- Laga, E. M., Driscoll, S. G., and Munro, H. N., 1972. Comparison of placentas from two socioeconomic groups. I. Morphometry. *Pediatrics*, 50(1):24–32. URL: <<http://www.ncbi.nlm.nih.gov/pubmed/5038106>>.
- Laga, E. M., Driscoll, S. G., and Munro, H. N., 1973. Quantitative studies of human placenta. I. Morphometry. *Biol. Neonate*, 23(3):231–59. <http://dx.doi.org/10.1159/000240605>. URL: <<http://www.ncbi.nlm.nih.gov/pubmed/4773529>>.
- Laga, E. M., Driscoll, S. G., and Munro, H. N. Human Placental Structure: Relationship to Fetal Nutrition. In Josimovich, J. B., Reynolds, M., and Cobo, E., editors, *Probl. Hum. Reprod. vol. 2, Lactog. Horm. Fetal Nutr. Lact.*, pages 143–81. John Wiley, London, 1974.
- Lampert, H., 1954. The transport of oxygen in the sheep's placenta: the diffusion constant of the placenta. *Yale J. Biol. Med.*, 27(1):26–34. URL: <<http://www.ncbi.nlm.nih.gov/pubmed/13196399>>.
- Langheinrich, A. C., Wienhard, J., Vormann, S., Hau, B., Bohle, R. M., and Zygmunt, M., 2004. Analysis of the fetal placental vascular tree by X-ray micro-computed tomography. *Placenta*, 25(1):95–100. <http://dx.doi.org/10.1016/j.placenta.2003.08.010>. URL: <<http://www.ncbi.nlm.nih.gov/pubmed/15013644>>.
- Langheinrich, A. C., Vorman, S., Seidenstücker, J., Kampschulte, M., Bohle, R. M., Wienhard, J., and Zygmunt, M., 2008. Quantitative 3D micro-CT imaging of the human feto-placental vasculature in intrauterine growth restriction. *Placenta*, 29(11):937–41. <http://dx.doi.org/10.1016/j.placenta.2008.08.017>. URL: <<http://www.ncbi.nlm.nih.gov/pubmed/18851884>>.
- Lardner, T. J., 1975. A model for placental oxygen exchange. *J. Biomech.*, 8(2):131–4. [http://dx.doi.org/10.1016/0021-9290\(75\)90093-7](http://dx.doi.org/10.1016/0021-9290(75)90093-7). URL: <<http://www.ncbi.nlm.nih.gov/pubmed/1150679>>.
- Law, R. and Bukwirwa, H., 1999. The physiology of oxygen delivery. *Updat. Anaesth.*, 10:8–14. <http://dx.doi.org/10.1111/j.1741-6892.2004.00434.x>. URL: <<http://www.ncbi.nlm.nih.gov/pubmed/16214521>>.
- Lebowitz, J. L. and Spohn, H., 1982. Microscopic basis for Fick's law for self-diffusion. *J. Stat. Phys.*, 28(3):539–556. <http://dx.doi.org/10.1007/BF01008323>.
- Lee, R. and Mayhew, T. M., 1995. Star volumes of villi and intervillous pores in placentae from low and high altitude pregnancies. *J. Anat.*, 186((Pt 2)):349–55. URL: <<http://www.ncbi.nlm.nih.gov/pubmed/7649834>>.
- Leiser, R. and Kohler, T., 1983. The blood vessels of the cat girdle placenta. Observations on corrosion casts, scanning electron microscopical and histological studies. I. Maternal vasculature. *Anat. Embryol. (Berl.)*, 167(1):85–93. <http://dx.doi.org/10.1007/BF00304602>. URL: <<http://www.ncbi.nlm.nih.gov/pubmed/6349423>>.
- Leiser, R. and Kohler, T., 1984. The blood vessels of the cat girdle placenta. Observations on corrosion casts, scanning electron microscopical and histological studies. II. Fetal vasculature. *Anat. Embryol. (Berl.)*, 170(2):209–16. <http://dx.doi.org/10.1007/BF00319006>. URL: <<http://www.ncbi.nlm.nih.gov/pubmed/6517355>>.
- Leiser, R., Krebs, C., Ebert, B., and Dantzer, V., 1997. Placental vascular corrosion cast studies: a comparison between ruminants and humans. *Microsc. Res. Tech.*, 38(1-2):76–87. [http://dx.doi.org/10.1002/\(SICI\)1097-0029\(19970701/15\)38:1/2<76::AID-JEMT9>3.0.CO;2-S](http://dx.doi.org/10.1002/(SICI)1097-0029(19970701/15)38:1/2<76::AID-JEMT9>3.0.CO;2-S). URL: <<http://www.ncbi.nlm.nih.gov/pubmed/9260839>>.
- Lewis, R. M., Brooks, S., Crocker, I. P., Glazier, J., Hanson, M. A., Johnstone, E. D., Panitchob, N., Please, C. P., Sibley, C. P., Widdows, K. L., and Sengers, B. G., 2013. Review: Modelling placental amino acid transfer – from transporters to placental function. *Placenta*, 34 Suppl:S46–51. <http://dx.doi.org/10.1016/j.placenta.2012.10.010>. URL: <<http://www.ncbi.nlm.nih.gov/pubmed/23187090>>.
- Linduska, N., Dekan, S., Messerschmidt, A., Kasprian, G., Brugger, P. C., Chalubinski, K., Weber, M., and Prayer, D., 2009. Placental pathologies in fetal MRI with pathohistological correlation. *Placenta*, 30(6):

- 555–9. <http://dx.doi.org/10.1016/j.placenta.2009.03.010>. URL: <<http://www.ncbi.nlm.nih.gov/pubmed/19394080>>.
- Longo, L. D. Respiratory gas exchange. In Fishman, A. P., Farhi, L. E., Tenney, S. M., and Geiger, S. R., editors, *Handb. Physiol. Sect. 3 Respir. Syst. Vol. IV, Gas Exch.*, pages 351–401. American Physiological Society, Bethesda, MD, 1987.
- Longo, L. D. and Bartels, H. Table of Contents. In Longo, L. D. and Bartels, H., editors, *Respiratory Gas Exchange and Blood Flow in the Placenta*, Bethesda, MD, 1972. Nat. Inst. Child Health Hum. Dev.
- Longo, L. D. and Power, G. G., 1969. Analyses of PO₂ and PCO₂ differences between maternal and fetal blood in the placenta. *J. Appl. Physiol.*, 26(1):48–55. URL: <<http://www.ncbi.nlm.nih.gov/pubmed/5765204>>.
- Longo, L. D., Power, G. G., and Forster, R. E., 1969. II. Placental diffusing capacity for carbon monoxide at varying partial pressures of oxygen. *J. Appl. Physiol.*, 26(3):360–70. URL: <<http://www.ncbi.nlm.nih.gov/pubmed/5773178>>.
- Longo, L. D., Hill, E. P., and Power, G. G., 1972a. Theoretical analysis of factors affecting placental O₂ transfer. *Am. J. Physiol.*, 222(3):730–9. URL: <<http://www.ncbi.nlm.nih.gov/pubmed/5022687>>.
- Longo, L. D., Hill, E. P., and Power, G. G. Factors affecting placental oxygen transfer. In Longo, L. D. and Bartels, H., editors, *Respiratory Gas Exchange and Blood Flow in the Placenta*, pages 345–93, Bethesda, Maryland, 1972b. Nat. Inst. Child Health Hum. Dev.
- Longo, L. D., Hill, E. P., and Power, G. G. Factors affecting placental oxygen transfer. In Reneau, D. D., editor, *Chem. Eng. Med.*, chapter 6, pages 88–129. American chemical society, Washington, 1973. <http://dx.doi.org/10.1021/ba-1973-0118.ch006>.
- Luckhardt, M., Leiser, R., Kingdom, J., Malek, A., Sager, R., Kaisig, C., and Schneider, H., 1996. Effect of physiologic perfusion-fixation on the morphometrically evaluated dimensions of the term placental cotyledon. *J. Soc. Gynecol. Investig.*, 3(4):166–71. [http://dx.doi.org/10.1016/1071-5576\(96\)00023-8](http://dx.doi.org/10.1016/1071-5576(96)00023-8). URL: <<http://www.ncbi.nlm.nih.gov/pubmed/8796826>>.
- Lundberg, R. E., Reynolds, W. C., and Kays, W. M. Heat Transfer with Laminar Flow in Concentric Annuli with Constant and Variable Wall Temperature and Heat Flux. NASA Technical Note D-1972, 1963. URL: <<http://ntrs.nasa.gov/archive/nasa/casi.ntrs.nasa.gov/19630010444.pdf>>.
- Mac Gabhann, F. and Popel, A. S., 2004. Model of competitive binding of vascular endothelial growth factor and placental growth factor to VEGF receptors on endothelial cells. *Am. J. Physiol. Heart Circ. Physiol.*, 286(1):H153–64. <http://dx.doi.org/10.1152/ajpheart.00254.2003>. URL: <<http://www.ncbi.nlm.nih.gov/pubmed/12714333>>.
- MacDorma, M. F., Kirmeyer, S. E., and Wilson, E. C., 2012. Fetal and Perinatal Mortality, US, 2006. *Natl. Vital Stat. Rep.*, 60(8).
- Madazli, R., Somunkiran, A., Calay, Z., Ilvan, S., and Aksu, M. F., 2003. Histomorphology of the placenta and the placental bed of growth restricted fetuses and correlation with the Doppler velocimetry of the uterine and umbilical arteries. *Placenta*, 24(5):510–6. <http://dx.doi.org/10.1053/plac.2002.0945>. URL: <<http://www.ncbi.nlm.nih.gov/pubmed/12744927>>.
- Malassiné, A. and Cronier, L., 2002. Hormones and human trophoblast differentiation: a review. *Endocrine*, 19(1):3–11. <http://dx.doi.org/10.1385/ENDO:19:1:3>. URL: <<http://www.ncbi.nlm.nih.gov/pubmed/12583598>>.
- Maly, A., Goshen, G., Sela, J., Pinelis, A., Stark, M., and Maly, B., 2005. Histomorphometric study of placental villi vascular volume in toxemia and diabetes. *Hum. Pathol.*, 36(10):1074–9. <http://dx.doi.org/10.1016/j.humpath.2005.07.021>. URL: <<http://www.ncbi.nlm.nih.gov/pubmed/16226106>>.
- Manganaro, L., Fierro, F., Tomei, A., La Barbera, L., Savelli, S., Sollazzo, P., Sergi, M. E., Vinci, V., Ballesio, L., and Marini, M., 2010. MRI and DWI: feasibility of DWI and ADC maps in the evaluation of placental changes during gestation. *Prenat. Diagn.*, 30(12-13):1178–84. <http://dx.doi.org/10.1002/pd.2641>. URL: <<http://www.ncbi.nlm.nih.gov/pubmed/21064115>>.
- Marin, J. J. G., Macias, R. I. R., and Serrano, M. A., 2003. The hepatobiliary-like excretory function of the placenta. A review. *Placenta*, 24(5):431–8. <http://dx.doi.org/10.1053/plac.2002.0951>. URL: <<http://www.ncbi.nlm.nih.gov/pubmed/12774824>>.
- Masselli, G. and Gualdi, G., 2013. MR imaging of the placenta: what a radiologist should know. *Abdom. Imaging*, 38(3):573–87. <http://dx.doi.org/10.1007/s00261-012-9929-8>. URL: <<http://www.ncbi.nlm.nih.gov/pubmed/22797659>>.

- Mayhew, T. M., 1996. Patterns of villous and intervillous space growth in human placentas from normal and abnormal pregnancies. *Eur. J. Obstet. Gynecol. Reprod. Biol.*, 68(1-2):75–82. [http://dx.doi.org/10.1016/0301-2115\(96\)02486-4](http://dx.doi.org/10.1016/0301-2115(96)02486-4). URL: <<http://www.ncbi.nlm.nih.gov/pubmed/8886685>>.
- Mayhew, T. M., 2002. Enhanced fetoplacental angiogenesis in pre-gestational diabetes mellitus: the extra growth is exclusively longitudinal and not accompanied by microvascular remodelling. *Diabetologia*, 45(10):1434–9. <http://dx.doi.org/10.1007/s00125-002-0927-1>. URL: <<http://www.ncbi.nlm.nih.gov/pubmed/12378385>>.
- Mayhew, T. M., 2006a. Allometric studies on growth and development of the human placenta: growth of tissue compartments and diffusive conductances in relation to placental volume and fetal mass. *J. Anat.*, 208(6):785–94. <http://dx.doi.org/10.1111/j.1469-7580.2006.00566.x>. URL: <<http://www.ncbi.nlm.nih.gov/pubmed/16761978>>.
- Mayhew, T. M., 2006b. Stereology and the placenta: Where's the point? – A review. *Placenta*, 27 Suppl A:S17–25. <http://dx.doi.org/10.1016/j.placenta.2005.11.006>. URL: <<http://www.ncbi.nlm.nih.gov/pubmed/16406003>>.
- Mayhew, T. M., 2008. Taking tissue samples from the placenta: an illustration of principles and strategies. *Placenta*, 29(1):1–14. <http://dx.doi.org/10.1016/j.placenta.2007.05.010>. URL: <<http://www.ncbi.nlm.nih.gov/pubmed/17658596>>.
- Mayhew, T. M., 2009. A stereological perspective on placental morphology in normal and complicated pregnancies. *J. Anat.*, 215(1):77–90. <http://dx.doi.org/10.1111/j.1469-7580.2008.00994.x>. URL: <<http://www.ncbi.nlm.nih.gov/pubmed/19141109>>.
- Mayhew, T. M. and Burton, G. J., 1988. Methodological problems in placental morphometry: apologia for the use of stereology based on sound sampling practice. *Placenta*, 9(6):565–81. [http://dx.doi.org/10.1016/0143-4004\(88\)90001-X](http://dx.doi.org/10.1016/0143-4004(88)90001-X). URL: <<http://www.ncbi.nlm.nih.gov/pubmed/3070535>>.
- Mayhew, T. M. and Burton, G. J., 1997. Stereology and its impact on our understanding of human placental functional morphology. *Microsc. Res. Tech.*, 38(1-2):195–205. [http://dx.doi.org/10.1002/\(SICI\)1097-0029\(19970701/15\)38:1/2<195::AID-JEMT20>3.0.CO;2-J](http://dx.doi.org/10.1002/(SICI)1097-0029(19970701/15)38:1/2<195::AID-JEMT20>3.0.CO;2-J). URL: <<http://www.ncbi.nlm.nih.gov/pubmed/9260850>>.
- Mayhew, T. M. and Jairam, I. C., 2000. Stereological comparison of 3D spatial relationships involving villi and intervillous pores in human placentas from control and diabetic pregnancies. *J. Anat.*, 197((Pt 2)):263–74. <http://dx.doi.org/10.1046/j.1469-7580.2000.19720263.x>. URL: <<http://www.ncbi.nlm.nih.gov/pubmed/11005718>>.
- Mayhew, T. M. and Sisley, I., 1998. Quantitative studies on the villi, trophoblast and intervillous pores of placentae from women with well-controlled diabetes mellitus. *Placenta*, 19(5-6):371–7. [http://dx.doi.org/10.1016/S0143-4004\(98\)90076-5](http://dx.doi.org/10.1016/S0143-4004(98)90076-5). URL: <<http://www.ncbi.nlm.nih.gov/pubmed/9699957>>.
- Mayhew, T. M. and Wadrop, E., 1994. Placental morphogenesis and the star volumes of villous trees and intervillous pores. *Placenta*, 15(2):209–17. [http://dx.doi.org/10.1016/S0143-4004\(05\)80457-6](http://dx.doi.org/10.1016/S0143-4004(05)80457-6). URL: <<http://www.ncbi.nlm.nih.gov/pubmed/8008735>>.
- Mayhew, T. M., Joy, C. F., and Haas, J. D., 1984. Structure-function correlation in the human placenta: the morphometric diffusing capacity for oxygen at full term. *J. Anat.*, 139(Pt 4):691–708. URL: <<http://www.ncbi.nlm.nih.gov/pubmed/6526720>>.
- Mayhew, T. M., Jackson, M. R., and Haas, J. D., 1986. Microscopical morphology of the human placenta and its effects on oxygen diffusion: a morphometric model. *Placenta*, 7(2):121–31. [http://dx.doi.org/10.1016/S0143-4004\(86\)80003-0](http://dx.doi.org/10.1016/S0143-4004(86)80003-0). URL: <<http://www.ncbi.nlm.nih.gov/pubmed/3725744>>.
- Mayhew, T. M., Jackson, M. R., and Haas, J. D., 1990. Oxygen diffusive conductances of human placentae from term pregnancies at low and high altitudes. *Placenta*, 11(6):493–503. [http://dx.doi.org/10.1016/S0143-4004\(05\)80195-X](http://dx.doi.org/10.1016/S0143-4004(05)80195-X). URL: <<http://www.ncbi.nlm.nih.gov/pubmed/2290801>>.
- Mayhew, T. M., Sørensen, F. B., Klebe, J. G., and Jackson, M. R., 1993a. Oxygen diffusive conductance in placentae from control and diabetic women. *Diabetologia*, 36(10):955–60. <http://dx.doi.org/10.1007/BF02374479>. URL: <<http://www.ncbi.nlm.nih.gov/pubmed/8243876>>.
- Mayhew, T. M., Sørensen, F. B., Klebe, J. G., and Jackson, M. R., 1993b. The effects of mode of delivery and sex of newborn on placental morphology in control and diabetic pregnancies. *J. Anat.*, 183((Pt 3)):545–52. URL: <<http://www.ncbi.nlm.nih.gov/pubmed/8300431>>.
- Mayhew, T. M., Sørensen, F. B., Klebe, J. G., and Jackson, M. R., 1994. Growth and maturation of villi in placentae from well-controlled diabetic women. *Placenta*, 15(1):57–65. <http://dx.doi.org/10.1016/>

- S0143-4004(05)80236-X. URL: <<http://www.ncbi.nlm.nih.gov/pubmed/8208670>>.
- Mayhew, T. M., Ohadike, C., Baker, P. N., Crocker, I. P., Mitchell, C., and Ong, S. S., 2003. Stereological investigation of placental morphology in pregnancies complicated by pre-eclampsia with and without intrauterine growth restriction. *Placenta*, 24(2-3):219–26. <http://dx.doi.org/10.1053/plac.2002.0900>. URL: <<http://www.ncbi.nlm.nih.gov/pubmed/12566249>>.
- Mayhew, T. M., Charnock-Jones, D. S., and Kaufmann, P., 2004a. Aspects of human fetoplacental vasculogenesis and angiogenesis. III. Changes in complicated pregnancies. *Placenta*, 25(2-3):127–39. <http://dx.doi.org/10.1016/j.placenta.2003.10.010>. URL: <<http://www.ncbi.nlm.nih.gov/pubmed/14972445>>.
- Mayhew, T. M., Wijesekara, J., Baker, P. N., and Ong, S. S., 2004b. Morphometric evidence that villous development and fetoplacental angiogenesis are compromised by intrauterine growth restriction but not by pre-eclampsia. *Placenta*, 25(10):829–33. <http://dx.doi.org/10.1016/j.placenta.2004.04.011>. URL: <<http://www.ncbi.nlm.nih.gov/pubmed/15451198>>.
- Ménigault, E., Berson, M., Vieyres, P., Lepoivre, B., Pourcelot, D., and Pourcelot, L., 1998. Feto-maternal circulation: mathematical model and comparison with Doppler measurements. *Eur. J. Ultrasound*, 7(2): 129–43. [http://dx.doi.org/10.1016/S0929-8266\(98\)00018-4](http://dx.doi.org/10.1016/S0929-8266(98)00018-4). URL: <<http://www.ncbi.nlm.nih.gov/pubmed/9614282>>.
- Meschia, G., Battaglia, F. C., and Bruns, P. D., 1967a. Theoretical and experimental study of transplacental diffusion. *J. Appl. Physiol.*, 22(6):1171–8. URL: <<http://www.ncbi.nlm.nih.gov/pubmed/6027067>>.
- Meschia, G., Cotter, J. R., Makowski, E. L., and Barron, D. H., 1967b. Simultaneous measurement of uterine and umbilical blood flows and oxygen uptakes. *Q. J. Exp. Physiol. Cogn. Med. Sci.*, 52(1):1–18. <http://dx.doi.org/10.1113/expphysiol.1967.sp001877>.
- Metcalfe, J., Romney, S. L., Ramsey, L. H., Reid, D. E., and Burwell, C. S., 1955. Estimation of uterine blood flow in normal human pregnancy at term. *J. Clin. Invest.*, 34(11):1632–8. <http://dx.doi.org/10.1172/JCI103216>. URL: <<http://www.ncbi.nlm.nih.gov/pubmed/13271546>>.
- Metcalfe, J., Moll, W., and Bartels, H., 1964. Gas exchange across the placenta. *Fed. Proc.*, 23:774–80. URL: <<http://www.ncbi.nlm.nih.gov/pubmed/14195461>>.
- Middleman, S., 1972. *Transport Phenomena in the Cardiovascular System*. Wiley-Interscience, New York.
- Misra, D. P., Salafia, C. M., Charles, A. K., and Miller, R. K., 2010. Birth weights smaller or larger than the placenta predict BMI and blood pressure at age 7 years. *J. Dev. Orig. Health Dis.*, 1(02):123. <http://dx.doi.org/10.1017/S2040174410000139>. URL: <<http://www.ncbi.nlm.nih.gov/pubmed/25143066>>.
- Misra, D. P., Salafia, C. M., Charles, A. K., and Miller, R. K., 2012. Placental measurements associated with intelligence quotient at age 7 years. *J. Dev. Orig. Health Dis.*, 3(03):190–7. <http://dx.doi.org/10.1017/S2040174412000141>. URL: <<http://www.ncbi.nlm.nih.gov/pubmed/25102009>>.
- Moffett, A. and Loke, Y. W., 2004. The immunological paradox of pregnancy: a reappraisal. *Placenta*, 25(1):1–8. [http://dx.doi.org/10.1016/S0143-4004\(03\)00167-X](http://dx.doi.org/10.1016/S0143-4004(03)00167-X). URL: <<http://www.ncbi.nlm.nih.gov/pubmed/15013633>>.
- Moll, W. Gas exchange in concurrent, countercurrent and crosscurrent flow systems. The concept of the fetoplacental unit. In Longo, L. D. and Bartels, H., editors, *Respiratory Gas Exchange and Blood Flow in the Placenta*, pages 281–96, Bethesda, Maryland, 1972. National Institute of Child Health and Human Development.
- Moorcroft, D. M., Sitzel, J. D., Duma, G. G., and Duma, S. M., 2003. Computational model of the pregnant occupant: predicting the risk of injury in automobile crashes. *Am. J. Obstet. Gynecol.*, 189(2): 540–4. [http://dx.doi.org/10.1067/S0002-9378\(03\)00519-2](http://dx.doi.org/10.1067/S0002-9378(03)00519-2). URL: <<http://www.ncbi.nlm.nih.gov/pubmed/14520231>>.
- Moore, R. J., Issa, B., Tokarczuk, P., Duncan, K. R., Boulby, P., Baker, P. N., Bowtell, R. W., Worthington, B. S., Johnson, I. R., and Gowland, P. A., 2000a. In vivo intravoxel incoherent motion measurements in the human placenta using echo-planar imaging at 0.5 T. *Magn. Reson. Med.*, 43(2):295–302. [http://dx.doi.org/10.1002/\(SICI\)1522-2594\(200002\)43:2<295::AID-MRM18>3.0.CO;2-2](http://dx.doi.org/10.1002/(SICI)1522-2594(200002)43:2<295::AID-MRM18>3.0.CO;2-2). URL: <<http://www.ncbi.nlm.nih.gov/pubmed/10680695>>.
- Moore, R. J., Strachan, B. K., Tyler, D. J., Duncan, K. R., Baker, P. N., Worthington, B. S., Johnson, I. R., and Gowland, P. A., 2000b. In utero perfusing fraction maps in normal and growth restricted pregnancy measured using IVIM echo-planar MRI. *Placenta*, 21(7):726–32. <http://dx.doi.org/10.1053/plac.2000.0567>. URL: <<http://www.ncbi.nlm.nih.gov/pubmed/10985977>>.

- Morel, O., Pachy, F., Chavatte-Palmer, P., Bonneau, M., Gayat, E., Laigre, P., Evain-Brion, D., and Tsatsaris, V., 2010. Correlation between uteroplacental three-dimensional power Doppler indices and true uterine blood flow: evaluation in a pregnant sheep model. *Ultrasound Obstet. Gynecol.*, 36(5):635–40. <http://dx.doi.org/10.1002/uog.7741>. URL: <<http://www.ncbi.nlm.nih.gov/pubmed/20617508>>.
- Morel, O., Grangé, G., Fresson, J., Schaaps, J. P., Foidart, J. M., Cabrol, D., and Tsatsaris, V., 2011. Vascularization of the placenta and the sub-placental myometrium: feasibility and reproducibility of a three-dimensional power Doppler ultrasound quantification technique. A pilot study. *J. Matern. Fetal. Neonatal Med.*, 24(2):284–90. <http://dx.doi.org/10.3109/14767058.2010.486845>. URL: <<http://www.ncbi.nlm.nih.gov/pubmed/20476879>>.
- Morrison, L. W., Bekey, G., Brinkman, C. R., and Assali, N. S., 1970. Computer simulation of fetal baroreceptor function. *Comput. Biomed. Res.*, 3(6):561–74. [http://dx.doi.org/10.1016/0010-4809\(70\)90026-1](http://dx.doi.org/10.1016/0010-4809(70)90026-1). URL: <<http://www.ncbi.nlm.nih.gov/pubmed/5508343>>.
- Mossman, H. W., 1926. The rabbit placenta and the problem of placental transmission. *Am. J. Anat.*, 37(3):433–97. <http://dx.doi.org/10.1002/aja.1000370303>.
- Mossman, H. W., 1937. Comparative morphogenesis of the fetal membranes and accessory uterine structures. *Carnegie Contrib. Embryol.*, 26:129–246.
- Myers, L. J. and Capper, W. L., 2002. A transmission line model of the human foetal circulatory system. *Med. Eng. Phys.*, 24(4):285–94. [http://dx.doi.org/10.1016/S1350-4533\(02\)00019-X](http://dx.doi.org/10.1016/S1350-4533(02)00019-X). URL: <<http://www.ncbi.nlm.nih.gov/pubmed/11996847>>.
- Nelson, S. M., Coan, P. M., Burton, G. J., and Lindsay, R. S., 2009. Placental structure in type 1 diabetes: relation to fetal insulin, leptin, and IGF-I. *Diabetes*, 58(11):2634–41. <http://dx.doi.org/10.2337/db09-0739>. URL: <<http://www.ncbi.nlm.nih.gov/pubmed/19690062>>.
- Nguyen, D., Nguyen, C., Yacobozzi, M., Bsat, F., and Rakita, D., 2012. Imaging of the placenta with pathologic correlation. *Semin. Ultrasound. CT. MR*, 33(1):65–77. <http://dx.doi.org/10.1053/j.sult.2011.10.003>. URL: <<http://www.ncbi.nlm.nih.gov/pubmed/22264904>>.
- Nguyen, D. K. Segmentation and Statistical Analysis of Placental Cross-Sectional Images. Internship report, Laboratoire de Physique de la Matière Condensée — Laboratoire de Physique de la Matière Condensée — École Polytechnique, Palaiseau, FR, Palaiseau, 2014.
- Ockleford, C. D., Wakely, J., and Badley, R. A., 1981. Morphogenesis of human placental chorionic villi: cytoskeletal, syncytioskeletal and extracellular matrix proteins. *Proc. R. Soc. Lond. B. Biol. Sci.*, 212(1188):305–16. URL: <<http://www.ncbi.nlm.nih.gov/pubmed/6115395>>.
- Opitz, E. and Thews, G., 1952. Einfluß von Frequenz und Faserdicke auf die Sauerstoffversorgung des menschlichen Herzmuskels. *Arch. Kreislaufforsch.*, 18(5-6):137–52. <http://dx.doi.org/10.1007/BF02119166>.
- Owers, N. O., 1960. The endothelio-endothelial placenta of the Indian musk shrew, *Suncus murinus*: A new interpretation. *Am. J. Anat.*, 106:1–25.
- Page, K., 1993. *The Physiology of the Human Placenta*. University College, London.
- Panigel, M. and Pascaud, M., 1968. Les orifices artériels d'entrée du sang maternel dans la chambre intervillieuse du placenta humain. *Bull. Assoc. Anat. 53rd Congr. (Tours No. 142)*, pages 1287–98.
- Panitchob, N., Widdows, K. L., Crocker, I. P., Hanson, M. A., Johnstone, E. D., Please, C. P., Sibley, C. P., Glazier, J. D., Lewis, R. M., and Sengers, B. G., 2014. Computational modelling of amino acid exchange and facilitated transport in placental membrane vesicles. *J. Theor. Biol.*, 365C:352–64. <http://dx.doi.org/10.1016/j.jtbi.2014.10.042>. URL: <<http://www.ncbi.nlm.nih.gov/pubmed/25451528>>.
- Papoutsakis, E., Ramkrishna, D., and Lim, H. C., 1980. The extended Graetz problem with Dirichlet wall boundary conditions. *Appl. Sci. Res.*, 36(1):13–34. <http://dx.doi.org/10.1007/BF00420067>.
- Pasanen, M., 1999. The expression and regulation of drug metabolism in human placenta. *Adv. Drug Deliv. Rev.*, 38(1):81–97. [http://dx.doi.org/10.1016/S0169-409X\(99\)00008-3](http://dx.doi.org/10.1016/S0169-409X(99)00008-3). URL: <<http://www.ncbi.nlm.nih.gov/pubmed/10837748>>.
- Pfarrer, C. D., Winther, H., Leiser, R., and Dantzer, V., 1999. The development of the endotheliochorial mink placenta: light microscopy and scanning electron microscopical morphometry of maternal vascular casts. *Anat. Embryol. (Berl.)*, 199(1):63–74. <http://dx.doi.org/10.1007/s004290050210>. URL: <<http://www.ncbi.nlm.nih.gov/pubmed/9924936>>.
- Pfarrer, C. D., Ebert, B., Miglino, M. A., Klisch, K., and Leiser, R., 2001. The three-dimensional feto-maternal vascular interrelationship during early bovine placental development: a scanning electron microscopical study. *J. Anat.*, 198(5):591–602. <http://dx.doi.org/10.1046/j.1469-7580.2001.19850591.x>. URL:

- <http://www.ncbi.nlm.nih.gov/pubmed/11430698>.
- Piotrowicz, B., Niebrój, T. K., and Sieroń, G., 1969. The morphology and histochemistry of the full term placenta in anaemic patients. *Folia Histochem. Cytochem. (Krakow)*, 7(4):435–44. URL: <http://www.ncbi.nlm.nih.gov/pubmed/5378213>.
- Poon, L. C. and Nicolaides, K. H., 2014. Early prediction of preeclampsia. *Obstet. Gynecol. Int.*, 2014: 297397. <http://dx.doi.org/10.1155/2014/297397>. URL: <http://www.ncbi.nlm.nih.gov/pubmed/25136369>.
- Potter, M. C., Wiggert, D. C., and Ramadan, B. H., 2012. *Mechanics of Fluids*. CL Engineering, Stamford, CT, 4-th edition.
- Power, G. G. and Jenkins, F., 1975. Factors affecting O₂ transfer in sheep and rabbit placenta perfused in situ. *Am. J. Physiol.*, 229(4):1147–53. URL: <http://www.ncbi.nlm.nih.gov/pubmed/1190329>.
- Power, G. G. and Longo, L. D., 1969. Graphical analysis of maternal and fetal exchange of O₂ and CO₂. *J. Appl. Physiol.*, 26(1):38–47. URL: <http://www.ncbi.nlm.nih.gov/pubmed/5762874>.
- Power, G. G. and Longo, L. D., 1975. Fetal circulation times and their implications for tissue oxygenation. *Gynecol. Invest.*, 6:342–55. <http://dx.doi.org/10.1159/000301534>. URL: <http://www.ncbi.nlm.nih.gov/pubmed/765235>.
- Power, G. G., Hill, E. P., and Longo, L. D., 1972a. Analysis of uneven distribution of diffusing capacity and blood flow in the placenta. *Am. J. Physiol.*, 222(3):740–6. URL: <http://www.ncbi.nlm.nih.gov/pubmed/5022688>.
- Power, G. G., Hill, E. P., and Longo, L. D. A mathematical model of carbon dioxide transfer in the placenta. In Longo, L. D. and Bartels, H., editors, *Respiratory Gas Exchange and Blood Flow in the Placenta*, pages 395–418, Bethesda, Maryland, 1972b. National Institute of Child Health and Human Development.
- Power, M. L. and Schulkin, J., 2012. *The Evolution of the Human Placenta*. Johns Hopkins University Press, Baltimore, MD, 1st edition.
- Pratt, W. K., 1991. *Digital Image Processing*. Wiley-Interscience, New York, 2nd edition.
- Prausnitz, J. M., Lichtenthaler, R. N., and de Azevedo, E. G., 1998. *Molecular Thermodynamics of Fluid-Phase Equilibria*. Prentice Hall, Upper Saddle River, NJ, 3rd edition.
- Ragavendra, N. and Tarantal, A. F., 2001. Intervillous blood flow in the third trimester gravid rhesus monkey (*Macaca mulatta*): use of sonographic contrast agent and harmonic imaging. *Placenta*, 22(2-3):200–5. <http://dx.doi.org/10.1053/plac.2000.0605>. URL: <http://www.ncbi.nlm.nih.gov/pubmed/11170824>.
- Rainey, A. and Mayhew, T. M., 2010. Volumes and numbers of intervillous pores and villous domains in placentas associated with intrauterine growth restriction and/or pre-eclampsia. *Placenta*, 31(7):602–6. <http://dx.doi.org/10.1016/j.placenta.2010.04.005>. URL: <http://www.ncbi.nlm.nih.gov/pubmed/20444500>.
- Ramsey, E. M., 1962. Circulation in the intervillous space of the primate placenta. *Am. J. Obstet. Gynecol.*, 84:1649–63. URL: <http://www.ncbi.nlm.nih.gov/pubmed/13990709>.
- Ramsey, E. M., 1982. *The Placenta — Human and Animal*. Praeger, New York.
- Ramsey, E. M., Corner, G. W., and Donner, M. W., 1963. Serial and cineradioangiographic visualization of maternal circulation in the primate (hemochorial) placenta. *Am. J. Obstet. Gynecol.*, 86:213–25. URL: <http://www.ncbi.nlm.nih.gov/pubmed/13990708>.
- Rankin, J. H. The effects of shunted and unevenly distributed blood flows on crosscurrent exchange in the sheep placenta. In Longo, L. D. and Bartels, H., editors, *Respiratory Gas Exchange and Blood Flow in the Placenta*, pages 207–29, Bethesda, Maryland, 1972. Nat. Inst. Child Health Hum. Dev.
- Rankin, J. H. and Peterson, E. N., 1969. Application of the theory of heat exchangers to a physiological study of the goat placenta. *Circ. Res.*, 24(2):235–50. <http://dx.doi.org/10.1161/01.RES.24.2.235>. URL: <http://www.ncbi.nlm.nih.gov/pubmed/5764584>.
- Rasmussen, A. S., Lauridsen, H., Laustsen, C., Jensen, B. G., Pedersen, S. F., Uhrenholt, L., Boel, L. W. T., Uldbjerg, N., Wang, T., and Pedersen, M., 2010. High-resolution ex vivo magnetic resonance angiography: a feasibility study on biological and medical tissues. *BMC Physiol.*, 10(1):3. <http://dx.doi.org/10.1186/1472-6793-10-3>. URL: <http://www.ncbi.nlm.nih.gov/pubmed/20226038>.
- Rasmussen, A. S., Stær Hansen, E., Lauridsen, H., Uldbjerg, N., and Pedersen, M., 2014. MR angiography demonstrates a positive correlation between placental blood vessel volume and fetal size. *Arch. Gynecol. Obstet.* <http://dx.doi.org/10.1007/s00404-014-3341-2>. URL: <http://www.ncbi.nlm.nih.gov/pubmed/24444500>.

- [gov/pubmed/25033715](http://www.ncbi.nlm.nih.gov/pubmed/25033715)>.
- Rejniak, K. A., Kliman, H. J., and Fauci, L. J., 2004. A computational model of the mechanics of growth of the villous trophoblast bilayer. *Bull. Math. Biol.*, 66(2):199–232. <http://dx.doi.org/10.1016/j.bulm.2003.06.001>. URL: <<http://www.ncbi.nlm.nih.gov/pubmed/14871565>>.
- Reneau, D. D., Bruley, D. F., and Knisely, M. H. A mathematical simulation of oxygen release, diffusion and consumption in the capillaries and tissue of the human brain. In Hershey, D., editor, *Chem. Eng. Med. Biol.*, pages 135–241. Plenum, New York, 1967.
- Reneau, D. D., Guilbeau, E. J., and Cameron, J. M., 1974. A theoretical analysis of the dynamics of oxygen transport and exchange in the placental-fetal system. *Microvasc. Res.*, 8(3):346–61. [http://dx.doi.org/10.1016/S0026-2862\(74\)80009-9](http://dx.doi.org/10.1016/S0026-2862(74)80009-9). URL: <<http://www.ncbi.nlm.nih.gov/pubmed/4437412>>.
- Rennie, M. Y., Whiteley, K. J., Kulandavelu, S., Adamson, S. L., and Sled, J. G., 2007. 3D visualisation and quantification by microcomputed tomography of late gestational changes in the arterial and venous fetoplacental vasculature of the mouse. *Placenta*, 28(8-9):833–40. <http://dx.doi.org/10.1016/j.placenta.2006.12.005>. URL: <<http://www.ncbi.nlm.nih.gov/pubmed/17324457>>.
- Rennie, M. Y., Detmar, J., Whiteley, K. J., Jurisicova, A., Adamson, S. L., and Sled, J. G., 2012. Expansion of the fetoplacental vasculature in late gestation is strain dependent in mice. *Am. J. Physiol. Heart Circ. Physiol.*, 302(6):H1261–73. <http://dx.doi.org/10.1152/ajpheart.00776.2011>. URL: <<http://www.ncbi.nlm.nih.gov/pubmed/22268107>>.
- Resta, L., Capobianco, C., Marzullo, A., Piscitelli, D., Sanguedolce, F., Schena, F. P., and Gesualdo, L., 2006. Confocal laser scanning microscope study of terminal villi vessels in normal term and pre-eclamptic placentas. *Placenta*, 27(6-7):735–9. <http://dx.doi.org/10.1016/j.placenta.2005.07.006>. URL: <<http://www.ncbi.nlm.nih.gov/pubmed/16242771>>.
- Rodesch, F., Simon, P., Donner, C., and Jauniaux, E., 1992. Oxygen measurements in endometrial and trophoblastic tissues during early pregnancy. *Obstet. Gynecol.*, 80(2):283–285. URL: <<http://www.ncbi.nlm.nih.gov/pubmed/1635745>>.
- Rossant, J. and Cross, J. C., 2001. Placental development: lessons from mouse mutants. *Nat. Rev. Genet.*, 2(7):538–48. <http://dx.doi.org/10.1038/35080570>. URL: <<http://www.ncbi.nlm.nih.gov/pubmed/11433360>>.
- Roughton, F. J. W. and Forster, R. E., 1957. Relative importance of diffusion and chemical reaction rates in determining rate of exchange of gases in the human lung, with special reference to true diffusing capacity of pulmonary membrane and volume of blood in the lung capillaries. *J Appl Physiol*, 11(2):290–302. URL: <<http://www.ncbi.nlm.nih.gov/pubmed/13475180>>.
- Rubin, J. M., Adler, R. S., Fowlkes, J. B., Spratt, S., Pallister, J. E., Chen, J. F., and Carson, P. L., 1995. Fractional moving blood volume: estimation with power Doppler US. *Radiology*, 197(1):183–90. <http://dx.doi.org/10.1148/radiology.197.1.7568820>. URL: <<http://www.ncbi.nlm.nih.gov/pubmed/7568820>>.
- Sadava, D., Heller, H. C., Orians, G. H., Purves, W. K., and Hills, D. M., 2007. *Life: The science of biology*. Sinauer Associates, Sunderland, MA.
- Saghri, J. A. and Freeman, A., 1981. Analysis of the precision of generalized chain codes for the representation of planar curves. *IEEE Trans. Pattern Anal. Mach. Intell.*, 3(5):533–9. <http://dx.doi.org/10.1109/TPAMI.1981.4767146>. URL: <<http://www.ncbi.nlm.nih.gov/pubmed/21868973>>.
- Sala, M. A., Matheus, M., and Valeri, V., 1984. A stereologic study on the thickness of the trophoblastic layer and its regional variation in the human term placenta. *Anat. Anz.*, 157(4):257–60. URL: <<http://www.ncbi.nlm.nih.gov/pubmed/6397079>>.
- Salafia, C. M., Maas, E., Thorp, J. M., Eucker, B., Pezzullo, J. C., and Savitz, D. A., 2005. Measures of placental growth in relation to birth weight and gestational age. *Am. J. Epidemiol.*, 162(10):991–8. <http://dx.doi.org/10.1093/aje/kwi305>. URL: <<http://www.ncbi.nlm.nih.gov/pubmed/16192346>>.
- Salafia, C. M., Zhang, J., Charles, A. K., Bresnahan, M., Shrout, P., Sun, W., and Maas, E. M., 2008. Placental characteristics and birthweight. *Paediatr. Perinat. Epidemiol.*, 22(3):229–39. <http://dx.doi.org/10.1111/j.1365-3016.2008.00935.x>. URL: <<http://www.ncbi.nlm.nih.gov/pubmed/18426518>>.
- Salafia, C. M., Yampolsky, M., Shlakhter, A., Mandel, D. H., and Schwartz, N., 2012. Variety in placental shape: When does it originate? *Placenta*, 33(3):164–70. <http://dx.doi.org/10.1016/j.placenta.2011.12.002>. URL: <<http://www.ncbi.nlm.nih.gov/pubmed/22217910>>.
- Salomon, L. J., Siauve, N., Balvay, D., Cuénod, C. A., Vayssettes, C., Luciani, A., Frija, G., Ville, Y., and

- Clément, O., 2005. Placental perfusion MR imaging with contrast agents in a mouse model. *Radiology*, 235(1):73–80. <http://dx.doi.org/10.1148/radiol.2351040192>. URL: <<http://www.ncbi.nlm.nih.gov/pubmed/15695621>>.
- Samson, J. E., Mari, G., Dick, E. J., Hubbard, G. B., Ferry, R. J., and Schlambritz-Loutsevitch, N. E., 2011. The morphometry of materno-fetal oxygen exchange barrier in a baboon model of obesity. *Placenta*, 32(11):845–51. <http://dx.doi.org/10.1016/j.placenta.2011.07.083>. URL: <<http://www.ncbi.nlm.nih.gov/pubmed/21872927>>.
- Sapoval, B., Filoche, M., and Weibel, E. R., 2002. Smaller is better – but not too small: a physical scale for the design of the mammalian pulmonary acinus. *Proc. Natl. Acad. Sci. U. S. A.*, 99(16):10411–6. <http://dx.doi.org/10.1073/pnas.122352499>. URL: <<http://www.ncbi.nlm.nih.gov/pubmed/12136124>>.
- Sattin, F., 2008. Fick's law and Fokker–Planck equation in inhomogeneous environments. *Phys. Lett. A*, 372(22):3941–3945. <http://dx.doi.org/10.1016/j.physleta.2008.03.014>.
- Schmid-Schönbein, H., 1988. Conceptual proposition for a specific microcirculatory problem: maternal blood flow in hemochorial multivillous placentae as percolation of a "porous medium". *Trophobl. Res.*, 3: 17–38. http://dx.doi.org/10.1007/978-1-4615-8109-3_2.
- Schneider, H., 2009. Tolerance of human placental tissue to severe hypoxia and its relevance for dual ex vivo perfusion. *Placenta*, 30 Suppl A:S71–6. <http://dx.doi.org/10.1016/j.placenta.2008.11.004>. URL: <<http://www.ncbi.nlm.nih.gov/pubmed/19064287>>.
- Schröder, H. Structural and functional organization of the placenta from the physiological point of view. In Kaufmann, P. and King, B. F., editors, *Struct. Funct. Organ. Placenta*, pages 4–12. Karger, Basel, 1982. URL: <<http://www.ncbi.nlm.nih.gov/pubmed/7126150>>.
- Sebire, N. J., Jain, V., and Talbert, D. G., 2004. Spiral artery associated restricted growth (SPAARG): a computer model of pathophysiology resulting from low intervillous pressure having fetal programming implications. *Pathophysiology*, 11(2):87–94. <http://dx.doi.org/10.1016/j.pathophys.2004.06.003>. URL: <<http://www.ncbi.nlm.nih.gov/pubmed/15364119>>.
- Sen, D. K., Kaufmann, P., and Schweikhart, G., 1979. Classification of human placental villi. II. Morphometry. *Cell Tissue Res.*, 200(3):425–34. <http://dx.doi.org/10.1007/BF00234853>. URL: <<http://www.ncbi.nlm.nih.gov/pubmed/487408>>.
- Sengers, B. G., Please, C. P., and Lewis, R. M., 2010. Computational modelling of amino acid transfer interactions in the placenta. *Exp. Physiol.*, 95(7):829–40. <http://dx.doi.org/10.1113/expphysiol.2010.052902>. URL: <<http://www.ncbi.nlm.nih.gov/pubmed/20418347>>.
- Sengupta, A., Biswas, P., Jayaraman, G., and Guha, S. K., 1997. Understanding utero-placental blood flow in normal and hypertensive pregnancy through a mathematical model. *Med. Biol. Eng. Comput.*, 35(3):223–30. <http://dx.doi.org/10.1007/BF02530042>. URL: <<http://www.ncbi.nlm.nih.gov/pubmed/9246856>>.
- Serov, A. S., Salafia, C. M., Brownbill, P., Grebenkov, D. S., and Filoche, M., 2015a. Optimal villi density for maximal oxygen uptake in the human placenta. *J. Theor. Biol.*, 364:383–96. <http://dx.doi.org/10.1016/j.jtbi.2014.09.022>. URL: <<http://www.ncbi.nlm.nih.gov/pubmed/25261730>>.
- Serov, A. S., Salafia, C. M., Filoche, M., and Grebenkov, D. S., 2015b. Analytical theory of oxygen transfer in the human placenta. *J. Theor. Biol.*, 368:133–44. <http://dx.doi.org/10.1016/j.jtbi.2014.12.016>. URL: <<http://www.ncbi.nlm.nih.gov/pubmed/25580015>>.
- Serra, J., 1982. *Image Analysis and Mathematical Morphology*. Academic Press, New York.
- Severinghaus, J. W., 1979. Simple, accurate equations for human blood O₂ dissociation computations. *J. Appl. Physiol.*, 46(3):599–602. URL: <<http://www.ncbi.nlm.nih.gov/pubmed/35496>>.
- Shapiro, N. Z., Kirschbaum, T. H., and Assali, N. S., 1967. Mental exercises in placental transfer. *Am. J. Obstet. Gynecol.*, 97(1):130–7. URL: <<http://www.ncbi.nlm.nih.gov/pubmed/6068096>>.
- Shennan, D. B. and Boyd, C. A., 1987. Ion transport by the placenta: a review of membrane transport systems. *Biochim. Biophys. Acta*, 906(3):437–57. URL: <<http://www.ncbi.nlm.nih.gov/pubmed/3307921>>.
- Shih, F. Y., 2009. *Image Processing and Mathematical Morphology: Fundamentals and Applications*. CRC Press, Taylor & Francis Group, LLC, Boca Raton, FL.
- Shih, F. Y. and Wong, W.-T., 1992. A new single-pass algorithm for extracting the mid-crack codes of multiple regions. *J. Vis. Commun. Image Represent.*, 3(3):217–24. [http://dx.doi.org/10.1016/1047-3203\(92\)90018-0](http://dx.doi.org/10.1016/1047-3203(92)90018-0). URL: <<http://linkinghub.elsevier.com/retrieve/pii/1047320392900180>>.
- Sibley, C. P., Glazier, J. D., Greenwood, S. L., Lacey, H., Mynett, K., Speake, P., Jansson, T., Johansson, M., and Powell, T. L., 2002. Regulation of placental transfer: the Na⁽⁺⁾/H⁽⁺⁾ exchanger—a review. *Placenta*,

- 23 Suppl A:S39–46. <http://dx.doi.org/10.1053/plac.2002.0790>. URL: <http://www.ncbi.nlm.nih.gov/pubmed/11978058>.
- Silver, M., Steven, D. H., and Comline, R. S. Placental exchange and morphology in ruminants and the mare. In Comline, K. S., Cross, K. W., Dawes, G. S., and Nathanielz, P. W., editors, *Foetal Neonatal Physiol.*, pages 245–71, Cambridge, 1973. Cambridge University Press.
- Singh, S. N., 1958. The determination of eigen-functions of a certain Sturm-Liouville equation and its application to problems of heat-transfer. *Appl. Sci. Res. Sect. A*, 7(4):237–250. <http://dx.doi.org/10.1007/BF03185050>. URL: <http://link.springer.com/article/10.1007%2FBF03185050>.
- Sisson, T. R. C. Blood volume. In Stave, U., editor, *Perinat. Physiol.*, pages 181–198. Plenum Medical, New York, 1978.
- Sørensen, A., Peters, D., Fründ, E., Lingman, G., Christiansen, O., and Uldbjerg, N., 2013a. Changes in human placental oxygenation during maternal hyperoxia estimated by blood oxygen level-dependent magnetic resonance imaging (BOLD MRI). *Radiology*, 42(3):310–4. <http://dx.doi.org/10.1002/uog.12395>. URL: <http://www.ncbi.nlm.nih.gov/pubmed/23303592>.
- Sørensen, A., Peters, D., Simonsen, C., Pedersen, M., Stausbøl-Grøn, B., Christiansen, O. B., Lingman, G., and Uldbjerg, N., 2013b. Changes in human fetal oxygenation during maternal hyperoxia as estimated by BOLD MRI. *Prenat. Diagn.*, 33(2):141–5. <http://dx.doi.org/10.1002/pd.4025>. URL: <http://www.ncbi.nlm.nih.gov/pubmed/23233459>.
- Specht, E. Packomania web-site (<http://packomania.com>), 2009. URL: <http://packomania.com>. (Last accessed: 2015-09-09).
- Stevenson, G. N., Collins, S. L., Welsh, A. W., Impey, L. W., and Noble, J. A., 2015. A technique for the estimation of fractional moving blood volume by using three-dimensional power doppler US. *Radiology*, 274(1):132363. <http://dx.doi.org/10.1148/radiol.14132363>. URL: <http://www.ncbi.nlm.nih.gov/pubmed/25117590>.
- Stulc, J., 1997. Placental transfer of inorganic ions and water. *Physiol. Rev.*, 77(3):805–36.
- Surat, D. R. and Adamson, S. L., 1996. Downstream determinants of pulsatility of the mean velocity waveform in the umbilical artery as predicted by a computer model. *Ultrasound Med. Biol.*, 22(6):707–17. [http://dx.doi.org/10.1016/0301-5629\(96\)00041-5](http://dx.doi.org/10.1016/0301-5629(96)00041-5). URL: <http://www.ncbi.nlm.nih.gov/pubmed/8865566>.
- Talbert, D. G. and Sebire, N. J., 2004. The dynamic placenta: I. Hypothetical model of a placental mechanism matching local fetal blood flow to local intervillous oxygen delivery. *Med. Hypotheses*, 62(4):511–9. <http://dx.doi.org/10.1016/j.mehy.2003.10.025>. URL: <http://www.ncbi.nlm.nih.gov/pubmed/15050098>.
- Tariel, V. *Image Analysis of Cement Paste: Relation to Diffusion Transport*. Ph.D. Thesis, Laboratoire de Physique de la Matière Condensée — École Polytechnique, Palaiseau, 2009. URL: <https://pastel.archives-ouvertes.fr/tel-00516939>.
- Taylor, J. R., 1996. *An introduction to error analysis: the study of uncertainties in physical measurements*. University Science Books, Sausalito, CA, 2nd edition.
- Teasdale, F., 1978. Functional significance of the zonal morphologic differences in the normal human placenta. A morphometric study. *Am. J. Obstet. Gynecol.*, 130(7):773–81. URL: <http://www.ncbi.nlm.nih.gov/pubmed/637100>.
- Teasdale, F., 1980. Gestational changes in the functional structure of the human placenta in relation to fetal growth: a morphometric study. *Am. J. Obstet. Gynecol.*, 137(5):560–8. URL: <http://www.ncbi.nlm.nih.gov/pubmed/7386550>.
- Teasdale, F., 1981. Histomorphometry of the placenta of the diabetic women: class A diabetes mellitus. *Placenta*, 2(3):241–51. [http://dx.doi.org/10.1016/S0143-4004\(81\)80007-0](http://dx.doi.org/10.1016/S0143-4004(81)80007-0). URL: <http://www.ncbi.nlm.nih.gov/pubmed/7279877>.
- Teasdale, F. Morphometric evaluation. In Soma, H., editor, *Contrib. to Gynecol. Obstet. vol. 9, Morphol. Funct. Asp. Placent. Dysfunct.*, volume 9, pages 17–28. Karger, Basel, 1982. URL: <http://www.ncbi.nlm.nih.gov/pubmed/7140298>.
- Teasdale, F., 1983. Histomorphometry of the human placenta in Class B diabetes mellitus. *Placenta*, 4(1):1–12. [http://dx.doi.org/10.1016/S0143-4004\(83\)80012-5](http://dx.doi.org/10.1016/S0143-4004(83)80012-5). URL: <http://www.ncbi.nlm.nih.gov/pubmed/6856585>.
- Teasdale, F., 1984. Idiopathic intrauterine growth retardation: Histomorphometry of the human placenta.

- Placenta*, 5(1):83–92. [http://dx.doi.org/10.1016/S0143-4004\(84\)80051-X](http://dx.doi.org/10.1016/S0143-4004(84)80051-X). URL: <http://www.ncbi.nlm.nih.gov/pubmed/6728834>.
- Teasdale, F., 1985a. Histomorphometry of the human placenta in Class C diabetes mellitus. *Placenta*, 6(1): 69–81. [http://dx.doi.org/10.1016/S0143-4004\(83\)80012-5](http://dx.doi.org/10.1016/S0143-4004(83)80012-5). URL: <http://www.ncbi.nlm.nih.gov/pubmed/3991476>.
- Teasdale, F., 1985b. Histomorphometry of the human placenta in maternal preeclampsia. *Am. J. Obstet. Gynecol.*, 152(1):25–31. [http://dx.doi.org/10.1016/S0002-9378\(85\)80170-8](http://dx.doi.org/10.1016/S0002-9378(85)80170-8). URL: <http://www.ncbi.nlm.nih.gov/pubmed/3993710>.
- Teasdale, F., 1987. Histomorphometry of the human placenta in pre-eclampsia associated with severe intrauterine growth retardation. *Placenta*, 8(2):119–28. [http://dx.doi.org/10.1016/0143-4004\(87\)90015-4](http://dx.doi.org/10.1016/0143-4004(87)90015-4). URL: <http://www.ncbi.nlm.nih.gov/pubmed/3615372>.
- Teasdale, F. and Jean-Jacques, G., 1985. Morphometric evaluation of the microvillous surface enlargement factor in the human placenta from mid-gestation to term. *Placenta*, 6(5):375–81. [http://dx.doi.org/10.1016/S0143-4004\(85\)80014-X](http://dx.doi.org/10.1016/S0143-4004(85)80014-X). URL: <http://www.ncbi.nlm.nih.gov/pubmed/4070179>.
- Teasdale, F. and Jean-Jacques, G., 1986. Morphometry of the microvillous membrane of the human placenta in maternal diabetes mellitus. *Placenta*, 7(1):81–8. [http://dx.doi.org/10.1016/S0143-4004\(86\)80020-0](http://dx.doi.org/10.1016/S0143-4004(86)80020-0). URL: <http://www.ncbi.nlm.nih.gov/pubmed/3703835>.
- Teasdale, F. and Jean-Jacques, G., 1988. Intrauterine growth retardation: morphometry of the microvillous membrane of the human placenta. *Placenta*, 9(1):47–55. [http://dx.doi.org/10.1016/0143-4004\(88\)90072-0](http://dx.doi.org/10.1016/0143-4004(88)90072-0). URL: <http://www.ncbi.nlm.nih.gov/pubmed/3362793>.
- Thompson, R. S. and Trudinger, B. J., 1990. Doppler waveform pulsatility index and resistance, pressure and flow in the umbilical placental circulation: An investigation using a mathematical model. *Ultrasound Med. Biol.*, 16(5):449–58. [http://dx.doi.org/10.1016/0301-5629\(90\)90167-B](http://dx.doi.org/10.1016/0301-5629(90)90167-B). URL: <http://www.ncbi.nlm.nih.gov/pubmed/2238251>.
- Thoumsin, H. J., Albert, A., and Duvivier, J., 1978. Preliminary clinical application of a mathematical model for interpreting dehydroepiandrosterone-sulfate loading test in late pregnancy. *J. Perinat. Med.*, 6(1):32–8. <http://dx.doi.org/10.1515/jpme.1978.6.1.32>. URL: <http://www.ncbi.nlm.nih.gov/pubmed/149846>.
- Todros, T., Guiot, C., and Piantà, P. G., 1992. Modelling the feto-placental circulation: 2. A continuous approach to explain normal and abnormal flow velocity waveforms in the umbilical arteries. *Ultrasound Med. Biol.*, 18(6-7):545–51. [http://dx.doi.org/10.1016/0301-5629\(92\)90069-M](http://dx.doi.org/10.1016/0301-5629(92)90069-M). URL: <http://www.ncbi.nlm.nih.gov/pubmed/1413266>.
- Todros, T., Sciarrone, A., Piccoli, E., Guiot, C., Kaufmann, P., and Kingdom, J., 1999. Umbilical Doppler waveforms and placental villous angiogenesis in pregnancies complicated by fetal growth restriction. *Obstet. Gynecol.*, 93(4):499–503. [http://dx.doi.org/10.1016/S00029-7844\(98\)00440-2](http://dx.doi.org/10.1016/S00029-7844(98)00440-2). URL: <http://www.ncbi.nlm.nih.gov/pubmed/10214822>.
- Tominaga, T. and Page, E. W., 1966. Accommodation of the human placenta to hypoxia. *Am. J. Obstet. Gynecol.*, 94(5):679–91. URL: <http://www.ncbi.nlm.nih.gov/pubmed/5906591>.
- Tsutsumi, Y., 1962. The vascular pattern of the placenta in farm animals (horse, pig, cow, sheep and rabbit). *J. Agric. Hokkaido Imp. Univ.*, 52:372–482.
- van den Wijngaard, J. P. H. M., Westerhof, B. E., Ross, M. G., and van Gemert, M. J. C., 2007. A mathematical model of twin-twin transfusion syndrome with pulsatile arterial circulations. *Am. J. Physiol. Regul. Integr. Comp. Physiol.*, 292(4):R1519–31. <http://dx.doi.org/10.1152/ajpregu.00534.2006>. URL: <http://www.ncbi.nlm.nih.gov/pubmed/17158266>.
- van der Velde, W. J., Copius Peereboom-Stegeman, J. H., Treffers, P. E., and James, J., 1983. Structural changes in the placenta of smoking mothers: A quantitative study. *Placenta*, 4(3):231–40. [http://dx.doi.org/10.1016/S0143-4004\(83\)80002-2](http://dx.doi.org/10.1016/S0143-4004(83)80002-2). URL: <http://www.ncbi.nlm.nih.gov/pubmed/6622428>.
- van Milligen, B. P., Carreras, B. A., and Sánchez, R., 2005. The foundations of diffusion revisited. *Plasma Phys. Control. Fusion*, 47(12B):B743–B754. <http://dx.doi.org/10.1088/0741-3335/47/12B/S56>.
- Voigt, S., Kaufmann, P., and Schweikhart, G., 1978. Problems of distinction of normal, artificial, and pathological structures in mature human placental villi. II. Morphometrical studies on the influence of the mode of fixation (in German). *Arch. Gynecol.*, 226(4):347–362. URL: <http://www.ncbi.nlm.nih.gov/pubmed/367290>.
- Vossepoel, A. and Smeulders, A., 1982. Vector code probability and metrication error in the representation of straight lines of finite length. *Comput. Graph. Image Process.*, 20(4):347–64. <http://dx.doi.org/>

- 10.1016/0146-664X(82)90057-0.
- Walker, P. G. T., ter Kuile, F. O., Garske, T., Menendez, C., and Ghani, A. C., 2014. Estimated risk of placental infection and low birthweight attributable to *Plasmodium falciparum* malaria in Africa in 2010: a modelling study. *Lancet. Glob. Heal.*, 2(8):460–7. [http://dx.doi.org/10.1016/S2214-109X\(14\)70256-6](http://dx.doi.org/10.1016/S2214-109X(14)70256-6). URL: <<http://www.ncbi.nlm.nih.gov/pubmed/25103519>>.
- Weibel, E. R. Morphometry and lung models. In Weibel, E. R. and Elias, H., editors, *Quantitative Methods in Morphology / Quantitative Methoden in der Morphologie*, pages 253–67. Springer, Berlin, Heidelberg, 1967. <http://dx.doi.org/10.1007/978-3-642-50130-2>.
- Weibel, E. R., 1970. Morphometric estimation of pulmonary diffusion capacity. I. Model and method. *Respir. Physiol.*, 11(1):54–75. [http://dx.doi.org/10.1016/0034-5687\(70\)90102-7](http://dx.doi.org/10.1016/0034-5687(70)90102-7). URL: <<http://www.ncbi.nlm.nih.gov/pubmed/4992513>>.
- Weibel, E. R., 1984. *The Pathway for Oxygen*. Harvard University Press, Cambridge, Massachusetts.
- Weibel, E. R., 2009. What makes a good lung? *Swiss Med. Wkly.*, 139(27-28):375–386. <http://dx.doi.org/smw-12270>. URL: <<http://www.ncbi.nlm.nih.gov/pubmed/19629765>>.
- Wessler, I., Kilbinger, H., Bittinger, F., Unger, R., and Kirkpatrick, C. J., 2003. The non-neuronal cholinergic system in humans: expression, function and pathophysiology. *Life Sci.*, 72(18-19):2055–61. [http://dx.doi.org/10.1016/S0024-3205\(03\)00083-3](http://dx.doi.org/10.1016/S0024-3205(03)00083-3). URL: <<http://www.ncbi.nlm.nih.gov/pubmed/12628456>>.
- West, J. B., 2008. *Respiratory Physiology: The Essentials*. Lippincott Williams & Wilkins, Baltimore, MD, 8 edition.
- Wigglesworth, J. S., 1969. Vascular anatomy of the human placenta and its significance for placental pathology. *J. Obstet. Gynaecol. Br. Commonw.*, 76(11):979–89. URL: <<http://www.ncbi.nlm.nih.gov/pubmed/5355382>>.
- Wilbur, W. J., Power, G. G., and Longo, L. D., 1978. Water exchange in the placenta: a mathematical model. *Am. J. Physiol.*, 235(3):R181–99. URL: <<http://www.ncbi.nlm.nih.gov/pubmed/567941>>.
- Wilkening, R. B. and Meschia, G., 1992. Current topic: Comparative physiology of placental oxygen transport. *Placenta*, 13(1):1–15. [http://dx.doi.org/10.1016/0143-4004\(92\)90002-B](http://dx.doi.org/10.1016/0143-4004(92)90002-B). URL: <<http://www.ncbi.nlm.nih.gov/pubmed/1502133>>.
- Wilkin, P. Les théories explicatives du mécanisme des échanges transplacentaires. In Snoeck, J., editor, *Le Placenta Hum.*, pages 248–79. Masson et Cie, Paris, 1958.
- Wills, L., Hill, G., Bingham, K., Miall, M., and Wrigley, J., 1947. Haemoglobin levels in pregnancy: The effect of the rationing scheme and routine administration of iron. *Br. J. Nutr.*, 1(2-3):126–138. <http://dx.doi.org/10.1079/BJN19470024>. URL: <<http://www.ncbi.nlm.nih.gov/pubmed/http://www.ncbi.nlm.nih.gov/pubmed/18907917>>.
- Wise, D. L. and Houghton, G., 1969. Solubilities and diffusivities of oxygen in hemolyzed human blood solutions. *Biophys. J.*, 9(1):36–53. [http://dx.doi.org/10.1016/S0006-3495\(69\)86367-8](http://dx.doi.org/10.1016/S0006-3495(69)86367-8). URL: <<http://www.ncbi.nlm.nih.gov/pubmed/5782894>>.
- Wooding, P. and Burton, G. J., 2008. *Comparative Placentation: Structures, Functions and Evolution*. Springer-Verlag, Berlin, Heidelberg.
- Xia, Q. and Salafia, C. M., 2014. Transport efficiency of the human placenta. *J. Coupled Syst. Multiscale Dyn.*, 2(1):1–8. <http://dx.doi.org/10.1166/jcsmd.2014.1038>.
- Yamaguchi, K., Nguyen-Phu, D., Scheid, P., and Piiper, J., 1985. Kinetics of O₂ uptake and release by human erythrocytes studied by a stopped-flow technique. *J. Appl. Physiol.*, 58(4):1215–24. URL: <<http://www.ncbi.nlm.nih.gov/pubmed/3988677>>.
- Yampolsky, M., Salafia, C. M., Shlakhter, O., Haas, D., Eucker, B., and Thorp, J., 2008. Modeling the variability of shapes of a human placenta. *Placenta*, 29(9):790–7. <http://dx.doi.org/10.1016/j.placenta.2008.06.005>. URL: <<http://www.ncbi.nlm.nih.gov/pubmed/18674815>>.
- Yampolsky, M., Salafia, C. M., Shlakhter, O., Haas, D., Eucker, B., and Thorp, J., 2009. Centrality of the umbilical cord insertion in a human placenta influences the placental efficiency. *Placenta*, 30(12):1058–64. <http://dx.doi.org/10.1016/j.placenta.2009.10.001>. URL: <<http://www.ncbi.nlm.nih.gov/pubmed/19879649>>.
- Yang, L., Albrechtsen, F., Lønnestad, T., and Grøttum, P. Areas and perimeters of blob-like objects: A comparison. In *IAPR Work. Mach. Vis. Appl. Dec. 13-15, 1994*, page 272276, Kawasaki, 1994.
- Yeh, B. M., 2006. Has the time arrived to image placental perfusion? *Radiology*, 241(3):633–4. <http://dx.doi.org/10.1148/radiol.2413061104>. URL: <<http://www.ncbi.nlm.nih.gov/pubmed/17114613>>.

- You, Z. *Digital Image Analysis of Human Placenta Cross-Sections*. M. Sc. Thesis, Laboratoire de Physique de la Matière Condensée — Laboratoire de Physique de la Matière Condensée — École Polytechnique, Palaiseau, FR, 2014.
- Yudilevich, D. L. and Sweiry, J. H., 1985. Transport of amino acids in the placenta. *Biochim Biophys Acta*, 822:169–201.